



**Pacific Northwest**  
NATIONAL LABORATORY

*Proudly Operated by Battelle Since 1965*

# Second Year Report of the Atmosphere to Electrons Mesoscale to Microscale Coupling Project: Nonstationary Modeling Techniques and Assessment

**February 2017**

SE Haupt  
R Kotamarthi  
Y Feng  
JD Mirocha  
E Koo  
R Linn  
B Kosovic  
B Brown

A Anderson  
MJ Churchfield  
C Draxi  
E Quon  
W Shaw  
L Berg  
R Rai  
BL Ennis

## DISCLAIMER

This report was prepared as an account of work sponsored by an agency of the United States Government. Neither the United States Government nor any agency thereof, nor Battelle Memorial Institute, nor any of their employees, makes **any warranty, express or implied, or assumes any legal liability or responsibility for the accuracy, completeness, or usefulness of any information, apparatus, product, or process disclosed, or represents that its use would not infringe privately owned rights.** Reference herein to any specific commercial product, process, or service by trade name, trademark, manufacturer, or otherwise does not necessarily constitute or imply its endorsement, recommendation, or favoring by the United States Government or any agency thereof, or Battelle Memorial Institute. The views and opinions of authors expressed herein do not necessarily state or reflect those of the United States Government or any agency thereof.

PACIFIC NORTHWEST NATIONAL LABORATORY  
*operated by*  
BATTELLE  
*for the*  
UNITED STATES DEPARTMENT OF ENERGY  
*under Contract DE-AC05-76RL01830*

Printed in the United States of America

Available to DOE and DOE contractors from the  
Office of Scientific and Technical Information,  
P.O. Box 62, Oak Ridge, TN 37831-0062;  
ph: (865) 576-8401  
fax: (865) 576-5728  
email: [reports@adonis.osti.gov](mailto:reports@adonis.osti.gov)

Available to the public from the National Technical Information Service  
5301 Shawnee Rd., Alexandria, VA 22312  
ph: (800) 553-NTIS (6847)  
email: [orders@ntis.gov](mailto:orders@ntis.gov) <<http://www.ntis.gov/about/form.aspx>>  
Online ordering: <http://www.ntis.gov>



This document was printed on recycled paper.

(8/2010)

# **Second Year Report of the Atmosphere to Electrons Mesoscale to Microscale Coupling Project: Nonstationary Modeling Techniques and Assessment**

## **Argonne National Lab**

Rao Kotamarthi  
Yan Feng

## **National Renewable Energy Lab**

Matthew J. Churchfield  
Caroline Draxl  
Eliot Quon

## **Lawrence Livermore National Lab**

Jeffrey D. Mirocha

## **Pacific Northwest National Laboratory**

Larry Berg  
Raj Rai  
William Shaw

## **Los Alamos National Lab**

Eunmo Koo  
Rod Linn

## **Sandia National Laboratories**

Brandon L. Ennis

## **National Center for Atmospheric Research**

Sue Ellen Haupt<sup>1</sup>  
Branko Kosovic  
Barbara Brown  
Amanda Anderson

February 2017

Prepared for  
the U.S. Department of Energy  
under Contract DE-AC05-76RL01830

Pacific Northwest National Laboratory  
Richland, Washington 99352

---

<sup>1</sup> Project PI and Primary Author



## Abstract

The purpose of the Mesoscale-Microscale Coupling (MMC) Project is to develop, verify, and validate physical models and modeling techniques that bridge the most important atmospheric scales that determine wind plant performance and reliability. Without appropriate larger scale forcing, microscale models cannot correctly capture the meteorologically dependent flow details required to optimize siting, operations, controls, and the integration of wind-generated electricity. Incorporating meteorological forcing into wind plant simulation tools, on the other hand, will significantly improve viability of wind power to meet the emerging domestic and global demands for reliable, efficient, and cost-competitive energy sources. As part of the U.S. Department of Energy's Atmosphere to Electrons (A2e) program, the MMC project seeks to create a new predictive numerical simulation capability that is able to represent the full range of atmospheric flow conditions impacting wind plant performance.

In FY16, the focus of MMC was on nonstationary conditions over flat terrain, namely, the Scaled Wind Farm Technology (SWiFT) facility site. These nonstationary cases are critical for wind energy and represent a primary need for mesoscale meteorological forcing of the microscale models. The MMC team modeled two types of nonstationary cases: 1) diurnal cycles in which the daytime convective boundary layer collapses with the setting of the sun when the surface heat flux changes from positive to negative, passing through a brief period of neutral stability before becoming stable, with smaller scale turbulence and the potential for low level jet (LLJ) formation; and 2) frontal passage as an example of a synoptic weather event that may cause relatively rapid changes in wind speed and direction.

The team compared and contrasted two primary techniques for nonstationary forcing of the microscale by the mesoscale model. The first is to use the tendencies from the mesoscale model to directly force the microscale mode. The second method is to couple not only the microscale domain's internal forcing parameters, but also its lateral boundaries, to a mesoscale simulation. While the boundary coupled approach provides the greatest generality, since the mesoscale flow information providing the lateral boundary information for the microscale domain contains no explicit turbulence information, the approach requires methods to accelerate turbulence production at the microscale domain's inflow boundaries. Forefront assessment strategies, including comparing spectra and cospectra, were used to evaluate the techniques.

During FY16, the MMC team also completed the downselection of models for further study and application, choosing the Weather Research and Forecasting (WRF) model as the mesoscale model. Nalu was chosen by the high fidelity modeling team as the microscale model; the MMC team is helping to transition Nalu to the needed capabilities for wind plant simulations. It is yet to be determined how far to apply nesting in WRF before the hand-off to Nalu, a topic for year 3 of the project.

The MMC team continued testing methods to initialize turbulence at the microscale. In addition, the team studied the impact of the *terra incognita*, the region between the mesoscale and microscale, on application of the coupling techniques.

These advances will help industry better understand how the mesoscale forcing can induce changes in the wind plant and will lead to integrating the techniques developed here into high-performance modeling tools being developed as part of A2e.



## **Acknowledgments**

The MMC project is supported at the participating laboratories by the Wind Energy Technologies Office within the U.S. Department of Energy's Office of Energy Efficiency and Renewable Energy through the Atmosphere to Electrons program. The collaborators on this project also thank Texas Tech University for providing the high-quality historical atmospheric data set from DOE's SWiFT facility.



## Acronyms and Abbreviations

ABL	atmospheric boundary layer
AMS	American Meteorological Society
CDT	central daylight time
CFD	computational fluid dynamics
DAP	Data Access Portal
DOE	Department of Energy
GABLS	GEWEX Atmospheric Boundary-Layer Study
GEWEX	Global Energy and Water Exchange
HFM	high-fidelity modeling
HIGRAD	high gradient
HPC	high-performance computing
HPM	high-performance modeling
IEA	International Energy Agency
IEC	International Electrotechnical Commission
LANL	Los Alamos National Laboratory
LASD	Lagrangian-averaged scale-dependent
LBC	lateral boundary conditions
LES	large-eddy simulation
LLJ	low level jet
LLNL	Lawrence Livermore National Laboratory
MAE	mean absolute error
MMC	mesoscale-microscale coupling
MPAS	Model for Prediction Across Scales
MYNN	Mellor-Yamada-Nakanishi-Niino
NCAR	National Center for Atmospheric Research
NREL	National Renewable Energy Laboratory
NWI	National Wind Institute
NWP	numerical weather prediction
OpenFOAM	Open-source Field Operations And Manipulations
PBL	planetary boundary layer
PNNL	Pacific Northwest National Laboratory
POT	potential temperature
R&D	research and development
RMSE	root mean square error
RWP	radar wind profiler
SGS	subgrid scale

SMAG	Smagorinsky model
SNL	Sandia National Laboratories
SOWFA	Simulator fOr Wind Farm Applications
SWiFT	Scaled Wind Farm Technology
TKE	turbulent kinetic energy
TMP	air temperature
TTU	Texas Tech University
UTC	Coordinated Universal Time
V&V	verification and validation
VPTMP	virtual potential temperature
WENO	weighted essentially non-oscillatory
WFIP2	Wind Forecasting Improvement Project 2
WRF	Weather Research and Forecasting model
WSPD	wind speed
YSU	Yonsei University

# Contents

Abstract.....	iii
Acknowledgments.....	v
Acronyms and Abbreviations .....	vii
1.0 Introduction .....	1.1
1.1 Mesoscale to Microscale Coupling Project.....	1.1
1.2 Context within A2e .....	1.2
1.3 Progression of the MMC Project.....	1.3
1.4 Background and Motivation.....	1.5
1.5 Year 2 Emphasis: Nonstationary Conditions .....	1.7
1.6 Expected Impacts to Industry .....	1.8
2.0 Model Downselect from Year 1 Work .....	2.1
2.1 The WRF Model.....	2.1
2.2 Microscale Model Selection.....	2.1
2.2.1 WRF-LES.....	2.2
2.2.2 SOWFA.....	2.2
2.2.3 HIGRAD .....	2.3
2.2.4 Downselection of Microscale Models.....	2.3
2.3 Mesoscale Model Selection.....	2.3
2.3.1 WRF Model.....	2.4
2.3.2 MPAS.....	2.5
2.3.3 Mesoscale Model Comparison .....	2.5
2.3.4 Results from WRF and MPAS Comparison.....	2.8
2.3.5 Downselection of Mesoscale Models.....	2.14
3.0 Data and Case Selection .....	3.1
3.1 SWiFT Site and Instrumentation.....	3.1
3.2 Case Selection and Description.....	3.2
3.2.1 Case 1: Quiescent Diurnal Cycle; November 8–9, 2013.....	3.3
3.2.2 Case 2: Cold-Frontal Passage; May 12–13, 2014 .....	3.7
3.3 Metrics Plan .....	3.10
4.0 Analyzing the <i>terra incognita</i> .....	4.1
4.1 Qualitative Evidence from Plots.....	4.1
4.2 Formal Assessment .....	4.9
4.2.1 Time Series.....	4.9
4.2.2 Vertical Profiles.....	4.14
4.2.3 Quantitative Metrics.....	4.17
4.3 Interpretation of Results.....	4.18

5.0	Analyzing Microscale Simulations of Nonstationary Cases.....	5.1
5.1	Source Term Forcing with Mesoscale Tendencies.....	5.3
5.2	Extraction of Mesoscale Tendencies from a Mesoscale Simulation.....	5.5
5.3	Testing Coupling Methods.....	5.9
5.3.1	Use of Mesoscale Tendencies to Force the Microscale Simulations.....	5.9
5.3.2	Boundary Forcing with Conditions Interpolated from a Mesoscale Simulation.....	5.10
5.4	GABLS3 Case, Internal Mesoscale Forcing Derived from Observations.....	5.10
5.5	SWiFT Site November 8, 2011 Case, Mesoscale Forcing Derived from a Mesoscale Simulation.....	5.14
5.5.1	Mesoscale Forcing Through Internal Source Terms – SOWFA.....	5.14
5.5.2	Comparison of Internal Mesoscale Tendency Versus Boundary Forcing using WRF.....	5.18
5.5.3	Formal Assessment of November 8, 2013 Diurnal Case.....	5.21
5.6	Frontal Passage Case Forcing Through Online Boundary Conditions and Mesoscale Tendencies.....	5.27
5.6.1	Case Modeling.....	5.27
5.6.2	Large-Scale Assessment of Frontal Passage Case.....	5.29
5.6.3	Assessment of Microscale Properties of the Frontal Passage Case.....	5.37
5.7	Spectral Analysis of Canonical ABLs.....	5.42
6.0	Turbulence Generation Methods.....	6.1
6.1	TurbSim Approach.....	6.2
6.1.1	Coupling Framework.....	6.2
6.1.2	Coupling Evaluation.....	6.3
6.1.3	Results.....	6.4
6.2	Stochastic Cell Perturbation Method.....	6.7
6.3	Discussion.....	6.17
7.0	Summary, Context, Next Steps.....	7.1
7.1	Summary of Results.....	7.1
7.2	Assessment of Modeling Nonstationary Cases.....	7.3
7.3	Context in A2e, Community, and Next Steps.....	7.3
8.0	References.....	8.1
	Appendix A – Contributions of Individual Laboratories.....	A.1

# Figures

1.1	Diagram of Project Approach.....	1.2
2.1	WRF Simulation Domains at a 27, 9, and 3 km Resolution.....	2.4
2.2	Depiction of the Approximate Vertical Grid Spacing for the Mesoscale Simulations; Pressure from the Standard Atmosphere as a Function of Height .....	2.5
2.3	Observed Virtual Temperature Profiles during the Near-Neutral Conditions at Approximately 0000 to 0100 UTC on August 17 at the SWiFT Site.....	2.6
2.4	The Model Domain used in WRF-3DVAR Simulations.....	2.7
2.5	The ~15 km Variable Mesh Generated for the MPAS Resolution and the Vertical Resolution of the Model.....	2.8
2.6	Surface Weather Maps for August 17 and 18 2012.....	2.9
2.7	Results from MPAS and WRF Model Simulations for August 17 at 7 p.m. ....	2.9
2.8	Simulated Wind Velocity Profiles at Various Times between 0000 UTC and 0100 UTC, using the WRF Model, WRF-3DVAR, and MPAS .....	2.10
2.9	Potential Temperature Profiles Calculated with the WRF, WRF-3DVAR, and MPAS Models for August 17 at the SWiFT Site.....	2.11
2.10	Wind and Potential Temperature Profiles from WRF-LES at 0030 UTC on August 18 .....	2.12
2.11	PBL Heights Calculated by MPAS, WRF, and WRF-3DVAR.....	2.12
2.12	Comparison of Sensible Heat Flux from WRF 3D-VAR and MPAS for 12:00, 18:00, and 01:00 Local Time.....	2.13
2.13	Comparison of Latent Heat Flux from WRF 3D-VAR and MPAS for 12 p.m., 6 p.m., and 1 a.m. Local Time.....	2.14
3.1	SWiFT Facility with Adjacent TTU Atmospheric Facilities.....	3.1
3.2	Relevant TTU Atmospheric Facilities; 200 m Tower, Radar Profiler, and Mesonet .....	3.2
3.3	November 8–9, 2013 Near-Neutral Transition Profiles from the TTU 200 m tower .....	3.4
3.4	November 8–9, 2013 Diurnal Cycle Time-History .....	3.5
3.5	Surface Weather Map Valid at 1813 UTC on November 8, 2013 and 0013 UTC on November 9 .....	3.6
3.6	Time-Height Cross Section of Wind Speed and Wind Direction Measured at the TTU RWP for November 8, 2013 .....	3.7
3.7	May 12–13, 2014 Near-Neutral Transition Profiles from the TTU 200 m tower .....	3.7
3.8	May 12–13, 2014 Diurnal Cycle Time-History.....	3.8
3.9	Surface Weather Map Valid at 0323 UTC on May 12, 2014 and 0807 UTC on May 12, 2014 ....	3.9
3.10	Time-Height Cross Section of Wind Speed and Wind Direction Measured at the TTU RWP for May 12, 2013.....	3.10
4.1	Time Series of Wind Speed Obtained from Locations within the LES Domain used by Rai et al. using the MYNN PBL Scheme and YSU PBL Scheme for Different Horizontal Grid Spacing ...	4.1
4.2	Time Series of Vertical Wind Speed at 117 m, Horizontal Wind Speed at 117 m, Wind Direction at 117 m, Potential Temperature, TKE, Surface Momentum Flux, Simulated Boundary Layer Depth, Simulated Latent Heat Fluxes and Sensible Heat Fluxes, and Pressure at 117 m .....	4.3

4.3	Time Series of Vertical Wind Speed at 117 m, Horizontal Wind Speed at 117 m, Wind Direction at 117 m, Potential Temperature, TKE, Surface Momentum Flux, Simulated Boundary Layer Depth, Simulated Latent Heat Fluxes and Sensible Heat Fluxes, and Pressure at 117 m .....	4.4
4.4	Horizontal Wind Speed at 21 UTC on November 8, 2013 at 117 m in Domain 3, Domain 4, and Domain 5 .....	4.5
4.5	Horizontal Wind Speed at 18 UTC on November 8, 2013 at 117 m in Domain 3, Domain 4, and Domain 5 .....	4.6
4.6	Spectra of Horizontal Wind Speed for Two Hours during Stable Conditions between 4 and 6 UTC on November 9, the Convective Conditions between 1600 and 1800 UTC on November 8, and the Transition between 2000 UTC and 0000 UTC on November 8.....	4.6
4.7	Horizontal Wind Speed at 2100 UTC on November 8, 2013 at 117 m in Domain 3, Domain 4, and Domain 5 for Simulations with the YSU Boundary Layer Scheme .....	4.7
4.8	Spectra of Horizontal Wind Speed for Two Hours during Stable Conditions between 0400 and 0600 UTC on November 9, the Convective Conditions between 1600 and 1800 UTC on November 8, and the Transition between 2000 UTC and 0000 UTC on November 8 .....	4.7
4.9	Vertical Profiles of Virtual Potential Temperature for the MYNN Boundary Layer Scheme and YSU Scheme for the Domain with 3 km Grid Spacing and 333 m Grid Spacing.....	4.8
4.10	Time Series of Virtual Potential Temperature for the Three Different Domains and for Multiple Altitudes, with the MYNN and YSU Parameterizations .....	4.11
4.11	Time Series of Wind Speed for the Three Different Domains and for Multiple Altitudes, with the MYNN and YSU Parameterizations.....	4.12
4.12	Time Series of Wind Direction for the Three Different Domains and for Multiple Altitudes, with the MYNN and YSU Parameterizations.....	4.13
4.13	Vertical Profiles of Virtual Potential Temperature for the Convective, Stable, and Neutral Cases with the MYNN and YSU Parameterizations.....	4.15
4.14	Vertical Profiles of Wind Speed for the Convective, Stable, and Neutral Cases with MYNN and YSU Parameterizations .....	4.16
4.15	Vertical Profiles of Wind Direction for the Convective, Stable, and Neutral Cases, for the MYNN Boundary Layer Parameterization, and the Three Model Domains .....	4.17
5.1	A Schematic Diagram of the Two Coupling Approaches used in these Microscale Simulations..	5.3
5.2	Instantaneous Time-Height Plots of Zonal Wind Speed, and the Tendency Terms Presented in Equation (2): the Tendency $U_{tend}$ , the Pressure Gradient Force, Advection, Coriolis Acceleration, and SGS Effects Occurring from November 8 0000 UTC to November 10 0000 UTC, taken from the Closest Grid Point to the SWiFT Site; right: Same as Left, but Averaged over 2 Hours.....	5.6
5.3	Profiles of Wind Speed, Wind Speed Tendency Contributions of Pressure Gradient, Advection, and Pressure Gradient and Advection Combined at the Nearest Grid Point to the SWiFT Site ....	5.6
5.4	Instantaneous Time-Height Plots of Zonal Wind Speed, and the Tendency Terms Presented in Equation (2): the Tendency $U_{tend}$ , the Pressure Gradient Force, Advection, Coriolis Acceleration, and SGS Effects, Occurring from November 8 0000 UTC to November 10 0000 UTC and Averaged over 2x2 Grid Points Surrounding the SWiFT Site; Right: Same as Left, but Additionally Averaged over 1 Hour.....	5.7
5.5	Instantaneous Time-Height Plots of Zonal Wind Speed, and the Tendency Terms Presented in Equation (2): the Tendency $U_{tend}$ , the Pressure Gradient Force, Advection, Coriolis Acceleration, and SGS Effects, Occurring from November 8 0000 UTC to November 10 0000 UTC and	

	Averaged over 5x5 Grid Points Surrounding the SWiFT Site; Right: Same as Left, but Additionally Averaged over 1 Hour.....	5.8
5.6	Profiles of Wind Speed, Wind Speed Tendency Contributions of Pressure Gradient, Advection, and Pressure Gradient and Advection Combined.....	5.8
5.7	Profiles of Wind Speed, Wind Speed Tendency Contributions of Pressure Gradient, Advection, and Pressure Gradient and Advection Combined.....	5.9
5.8	Tendencies from the GABLS3 Case as Provided by Bosveld et al.....	5.11
5.9	Time-Height Contours of TKE from the GABLS3 Simulation as Calculated with SOWFA .....	5.12
5.10	Time-Height Contours of Horizontal Wind Speed for the GABLS3 Case as Computed with WRF- LES and SOWFA .....	5.12
5.11	Time Histories of Horizontal Wind Speed at Different Vertical Levels as Computed by the Microscale Models for the GABLS3 Case, and as Measured at the Cabauw Tower.....	5.13
5.12	Time-Height Contours of Computed Horizontal Wind Speed for the GABLS3 Case using SOWFA.....	5.14
5.13	Time-Height Histories of Horizontal Wind Speed of the November 8 SWiFT Case from the WRF- Mesoscale Simulation and the Planar-Averaged Horizontal Wind Speed from SOWFA.....	5.15
5.14	Time-History of the 85 m Horizontal Wind Speed and Potential Temperature from WRF and SOWFA; the SOWFA Results are Planar Averaged.....	5.16
5.15	Horizontal Slices at 80 m above the Surface of Instantaneous Horizontal Velocity from the SOWFA SWiFT November 8 Simulation at Various Times of Day.....	5.17
5.16	Computational Domains for Mesoscale Simulations and LES with Terrain Elevation and State Boundaries.....	5.18
5.17	Simulated Wind Speed Approximately 90 m Above the Surface for Domains 5 and 6 using a Nested LES Configuration with a 90 and 30 m Horizontal Resolution and Periodic LES with a 10 m Horizontal Resolution during Periods with Convective, Neutral, and Stable Conditions.....	5.19
5.18	Vertical Profiles of Wind Speed during the Evening of November 8 from the WRF-Mesoscale, Online Coupled LES, and Offline Periodic LES with the Noise Removed from the Lower Portion of the Geostrophic Wind Profiles, as Described in the Text .....	5.21
5.19	Wind Speed—Diurnal Case Based on Observations on November 8, 2013; SWiFT Facility Tower Sonic Anemometer Measurements, SOWFA LES, and WRF-LES .....	5.22
5.20	Wind Direction—Diurnal Case Based on Observations on November 8, 2013; SWiFT Facility Tower Sonic Anemometer Measurements, SOWFA LES, and WRF-LES.....	5.23
5.21	Temperature—Diurnal Case Based on Observations on November 8, 2013; SWiFT Facility Tower Measurements; SOWFA LES; and WRF-LES.....	5.24
5.22	TKE—Diurnal Case Based on Observations on November 8, 2013; SWiFT Facility Measurements, SOWFA LES, and WRF-LES.....	5.25
5.23	Turbulent Stress—Diurnal Case Based on Observations on November 8, 2013; SWiFT Facility Measurements, SOWFA LES, and WRF-LES.....	5.25
5.24	Turbulent Sensible Heat Flux—Diurnal Case Based on Observations on November 8, 2013; SWiFT Facility Measurements, SOWFA LES, WRF-LES.....	5.26
5.25	Simulated Time-Height Cross Section of Wind Speed, Wind Direction, and Temperature at the SWiFT Site.....	5.27

5.26	Simulated Wind Speed Approximately 90 m Above the Surface for Domains 5 and 6 using a Nested LES Configuration with a 90 and 30 m Horizontal Resolution and periodic LES with a 10 m Horizontal Resolution Before, During, and After the Frontal Passage .....	5.29
5.27	Time Series of Virtual Potential Temperature from Three WRF Domains and the SWiFT Location Tower on May 12, 2014 .....	5.31
5.28	Vertical Profiles of Virtual Potential Temperature from Three WRF Domains and the SWiFT Location Tower on May 12, 2014 .....	5.32
5.29	Time Series of Wind Direction from Three WRF Domains and the SWiFT Location Tower on May 12, 2014.....	5.33
5.30	Time Series of Wind Speed from Three WRF Domains and the SWiFT Location Tower on May 12, 2014 .....	5.34
5.31	Vertical Profiles of Wind Direction from Three WRF Domains and the SWiFT Location Tower on May 12, 2014.....	5.35
5.32	Vertical Profiles of Wind Direction from Three WRF Domains and the SWiFT Location Tower on May 12, 2014.....	5.36
5.33	Wind Speed—Frontal Passage Observed on May 12, 2014; SWiFT Facility Anemometer Measurements, WRF-LES with Periodic Boundary Conditions Forced with Output from a Mesoscale Simulation, and the WRF-LES Nested in a Mesoscale Simulation.....	5.38
5.34	Wind Direction—Frontal Passage Observed on May 12, 2014; SWiFT Facility Anemometer Measurements, WRF-LES with Periodic Boundary Conditions Forced with Output from a Mesoscale Simulation, and the WRF-LES Nested in a Mesoscale Simulation.....	5.39
5.35	Temperature—Frontal Passage Observed on May 12, 2014; SWiFT Facility Measurements, WRF-LES with Periodic Boundary Conditions Forced with Output from a Mesoscale Simulation, WRF-LES Nested in a Mesoscale Simulation.....	5.40
5.36	TKE—Frontal Passage Observed on May 12, 2014; SWiFT Facility Measurements, WRF-LES with Periodic Boundary Conditions Forced with Output from a Mesoscale Simulation, and the WRF-LES Nested in a Mesoscale Simulation.....	5.41
5.37	Turbulent Stress—Frontal Passage Observed on May 12, 2014; SWiFT Facility Measurements, WRF-LES with Periodic Boundary Conditions Forced with Output from a Mesoscale Simulation, and the WRF-LES Nested in a Mesoscale Simulation .....	5.41
5.38	Turbulent Sensible Heat Flux—Frontal Passage Observed on May 12, 2014; SWiFT Facility Measurements, WRF-LES with Periodic Boundary Conditions Forced with Output from a Mesoscale Simulation, WRF-LES Nested in a Mesoscale Simulation .....	5.42
5.39	Comparison of Measured and Simulated Frequency Spectra under Unstable Stratification; Streamwise Velocity Spectra, Cross-Stream Velocity Spectra, Vertical Velocity Spectra, and Temperature Spectra.....	5.43
5.40	Comparison of Measured and Simulated Frequency Spectra under Unstable Stratification; Streamwise Velocity Spectra, Cross-Stream Velocity Spectra, Vertical Velocity Spectra, and Temperature Spectra.....	5.44
5.41	Comparison of Measured and Simulated Frequency Spectra under Neutral Stratification; Streamwise Velocity Spectra, Cross-Stream Velocity Spectra, Vertical Velocity Spectra, and Temperature Spectra.....	5.45
5.42	Comparison of Measured and Simulated Frequency Spectra under Neutral Stratification; Streamwise Velocity Spectra, Cross-Stream Velocity Spectra, Vertical Velocity Spectra, and Temperature Spectra.....	5.46

5.43	Comparison of Measured and Simulated Frequency Spectra under Stable Stratification; Streamwise Velocity Spectra, Cross-Stream Velocity Spectra, Vertical Velocity Spectra, and Temperature Spectra.....	5.47
5.44	Comparison of Measured and Simulated Frequency Spectra under Stable Stratification; Streamwise Velocity Spectra, Cross-Stream Velocity Spectra, Vertical Velocity Spectra, and Temperature Spectra.....	5.48
6.1	Scaling of the Synthetic Turbulence Applied to the MMC Coupling as a Function of Height.....	6.3
6.2	Downstream Profiles of Turbulence Intensity and Reynolds Shear Stress for a Variety of Synthetic Turbulence-Based Perturbation Approaches.....	6.5
6.3	The Reference Fully-Developed Flow, Compared with the Mean Flow Superimposed with Correlated TurbSim Perturbations Applied at the Inlet.....	6.6
6.4	Computational Setup used to Evaluate the Stochastic Cell Perturbation Method Showing Nested and Stand-Alone LES Domains, along with the Number of Grid Cells in each Direction on each Domain, the Location of the Nested LES within the Mesoscale Domain, and Approximate Locations within the Nested Domain from which Flow Statistics were Examined .....	6.7
6.5	Plan View Contours of Wind Speed in Stand-Alone and Nested LES Domains at 100 m Above the Surface, from the Convective Simulations, with Stand-Alone Periodic LES, Nested Domains with No Perturbations, and via the Cell Perturbation Method, using both the SMAG and LASD SGS Models.....	6.9
6.6	Mean Vertical Profiles of Wind Speed and Direction during Neutral Simulations, from Mesoscale, Stand-Alone LES, and Nested LES, from $i = 400$ Grid Cells from the Inflow, using Different Cell Perturbations, as Described in the Text .....	6.10
6.7	Vertical Profiles of Resolved Turbulence Kinetic Energy $K$ and Friction Velocity $u^*$ on Nested LES Domains versus the Stand-Alone Value at 400 Grid Cells from the Inflow during Neutral Simulations using Cell Perturbation of Different Vertical Dimensions, as Described in the Text.....	6.11
6.8	Vertical Profiles of Resolved Turbulence Kinetic Energy $K$ and Friction Velocity $U^*$ on Nested LES Domains versus the Stand-Alone Value as Function of Inflow Distance, using Cell Perturbation Sizes of $N\delta z=6$ and 8 from the SMAG and LASD SGS Models.....	6.12
6.9	Plan View Contours of Wind Speed in Stand-Alone and Nested LES Domains at 100 m above the Surface, as in Figure 6.5, Under Convective Forcing.....	6.13
6.10	Vertical Profiles of Resolved Turbulence Wind Speed and Direction, as in Figure 6.6, from the Convective Simulations.....	6.14
6.11	Vertical Profiles of Resolved Turbulence Kinetic Energy $K$ and Friction Velocity $u^*$ as in Figure 6.7, during Convective Conditions.....	6.15
6.12	Vertical Profiles of Resolved Turbulence Kinetic Energy $K$ and Friction Velocity $u^*$ , as a Function of Inflow Distance, as in Figure 6.8, from Convective Simulations, with No Perturbations.....	6.16
6.13	Vertical Profiles of Resolved Turbulence Kinetic Energy $K$ and Friction Velocity $u^*$ , as a Function of Inflow Distance, as in Figure 6.12, from Convective Simulations, with Perturbations.....	6.17

# Tables

1.1	Details of MMC Project Progression and Milestones .....	1.4
1.2	Assessment of Stakeholder Use and Assessment Strategies to Determine if the MMC Modeling Provides Useful Information for that Use.....	1.9
3.1	TTU 200 m Tower Instrumentation.....	3.2
3.2	Metrics used for Evaluation of Variables .....	3.11
4.1	Overall Verification Results for the November 8 Case.....	4.18
5.1	Metrics for the May 12 Case .....	5.37

# 1.0 Introduction

## 1.1 Mesoscale to Microscale Coupling Project

The purpose of the Mesoscale-Microscale Coupling (MMC) Project is to develop, verify, and validate physical models and modeling techniques that bridge the most important atmospheric scales that determine wind plant performance and reliability. Without appropriate larger scale forcing, microscale models cannot correctly capture the meteorologically dependent flow details required to optimize siting, operations, controls and the integration of wind-generated electricity. Incorporating meteorological forcing into wind plant simulation tools, on the other hand, will significantly improve viability of wind power to meet the emerging domestic and global demands for reliable, efficient, and cost-competitive energy sources. As part of U.S. Department of Energy's (DOE's) Atmosphere to Electrons (A2e) program, the MMC project seeks to create a new predictive numerical simulation capability that is able to represent the full range of atmospheric flow conditions impacting wind plant performance.

The goal of the MMC project is to create a new predictive numerical simulation capability that is able to represent the full range of atmospheric flow conditions impacting wind plant performance. While wind power is ultimately generated from the mesoscale flow field (i.e., the atmospheric boundary-layer winds), microscale flow characteristics, including turbulence, complex distribution of wind speed and direction, and significant short-term time variability, impact both power generation and turbine component reliability. These features are ultimately driven by a myriad of environmental and weather factors not traditionally represented within microscale wind plant simulations. Coupling microscale wind plant simulation tools with mesoscale atmospheric models is an emerging approach to incorporate these important meteorological and environmental drivers of microscale variability into the microscale simulation codes used throughout the wind power industry, providing improved characterization, prediction, and understanding of wind plant performance under a wide range of realistic operating conditions. Having robust, well-characterized MMC methods is widely seen by industry as a significant need for future wind plant simulation capabilities. It will enable industry to perform better forensic analysis of anomalous wind plant behavior. It will also enable tailoring turbines and control systems to specific sites subject to specific mesoscale and environmental effects. Researchers will be able to better explore next-generation wind plant concepts composed of larger, more flexible turbines. These are just a few examples of the possible benefits of the enhanced wind plant predictive capability that MMC will enable, thus saving the wind energy industry money, enabling more investment in wind plants.

To achieve the MMC project goal, the overarching objective is the creation, assessment, and validation of state-of-the-science atmospheric simulation methodologies to incorporate important mesoscale flow characteristics into microscale wind plant simulations. MMC project objectives include those listed below.

- Compare existing physics models' ability to fully characterize the meso/micro atmospheric boundary layer (ABL) characteristics, including plant inflows, wake flows, and interactions with the boundaries. Identified deficiencies will provide rationale for next steps for improvement.
- Establish field data baseline cases as part of the verification and validation (V&V) process for existing models. Thus, improvements can be grounded in data.
- Downselect from the existing modeling suite for future implementation to improve development efficiencies using a common high-fidelity modeling (HFM) framework. This process will enable a tool that is usable by industry.

- Establish research and development (R&D) requirements to improve ABL model performance. This initiative will identify specific areas for improvement and how they will impact the microscale modeling initiative in the HFM environment.
- Advance development issues including nonstationarity, boundary interactions, coupling strategies, *terra incognita* issues, modeling in complex terrain, and beyond. It is necessary to make improvements in all of these issues if the HFM framework is expected to correctly represent critical mesoscale forcings.
- Transition existing model and physics requirements to the HFM development environment by working closely with the HFM team.

Realizing these objectives will enable simulation of the full suite of mesoscale and microscale flow characteristics affecting turbine and wind plant uncertainties and performance, thus allowing substantive improvements in wind plant design, operation, and performance projections. Accomplishing these goals will achieve substantive improvements in wind plant design, operation, and performance projections. Figure 1.1 diagrams the MMC approach to the project, taking into account the objectives described above.

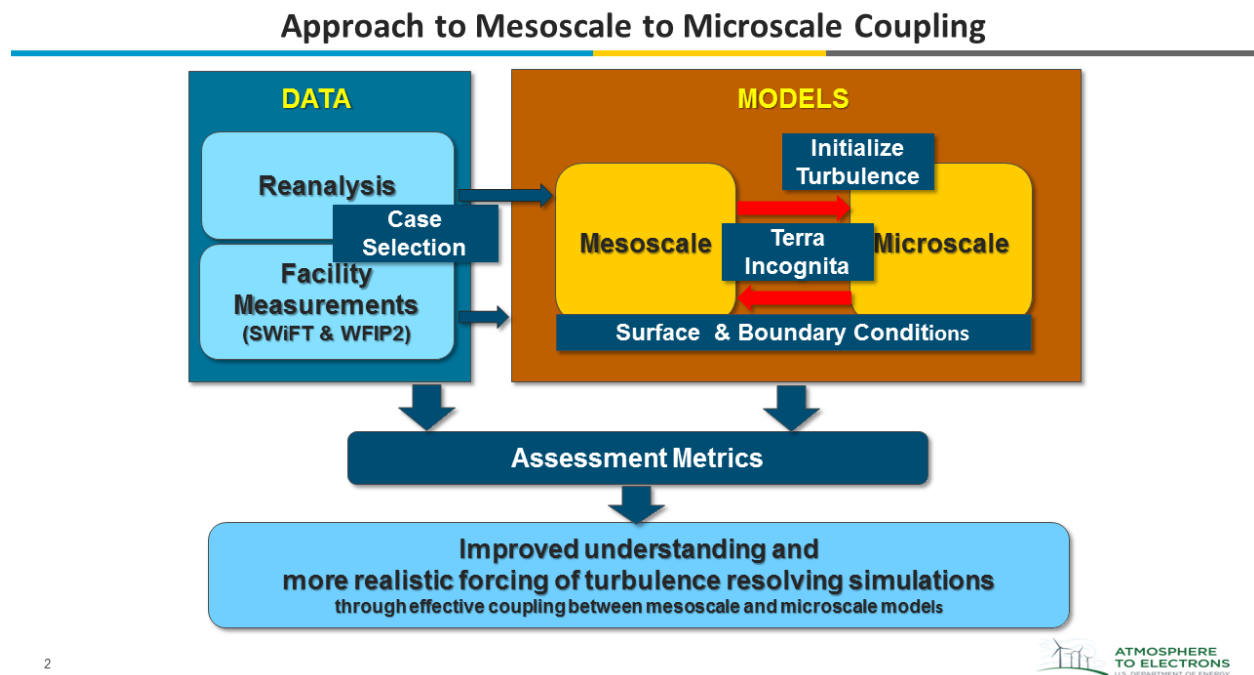


Figure 1.1. Diagram of Project Approach

## 1.2 Context within A2e

The A2e Initiative is an effort within the Wind Energy Technologies Office (WETO) of DOE’s Energy Efficiency and Renewable Energy Office with the goal of optimizing power production from wind plants as a whole. To that end, the initiative is explicitly integrating advances in atmospheric sciences, wind plant aerodynamics, and wind plant control technologies, taking advantage of current and emerging capabilities for high-performance computing. Because the atmospheric inflow is the fuel that powers wind plants, containing both the energy available for conversion into electricity, as well as characteristics that modulate that conversion, the development and validation of first-principles based, high-fidelity physics models within an open-source simulation environment has been identified as a crucial part of A2e science

goals and objectives. Furthermore, there has been an overwhelming consensus within the research community that these models must be developed and systematically validated using a formal V&V process. The MMC task was intended to provide an initial demonstration of the V&V-guided approach to model development specifically applied to the mesoscale-microscale coupling problem and to provide the foundation for the ultimate selection of a common framework for the development of atmospheric and wind plant modeling within A2e. It has been a joint collaborative project between six DOE national laboratories, with National Center for Atmospheric Research (NCAR) leadership as a formal subcontractor, as well as incorporating external feedback from other A2e team members, industry, DOE leadership, and other stakeholders.

The MMC project is grounded in data provided by other A2e facilities. For the first two years, that has included measurements taken at the Sandia National Laboratories (SNL) Scaled Wind Farm Technology (SWiFT) facility in Lubbock, Texas. The MMC modeling has helped characterize and inform the wake dynamics experiments being accomplished at that site and its results are expected to contribute to modeling the wake dynamics. As the project moves toward coupled modeling in complex terrain in year 3, the data will be derived from the observations currently being taken in the Pacific Northwest as part of the A2e project, Wind Forecasting Improvement Project 2 (WFIP2). Including the mesoscale forcing in the microscale models will also become critical to the success of the A2e project focusing on wind plant controls. Most prominently, the very specific coupling and modeling philosophies and technologies being developed in MMC are necessary for building the HFM tools. The results of MMC modeling and case studies are being archived in the Data Archive and Portal (DAP).

Thus, because the wind plant exists within the ABL, improved understanding and modeling of the ABL constitutes a core requirement of improving wind plant performance. Improved ABL modeling inherently requires that the details of the mesoscale forcing be coupled to the microscale models that are used for the wake modeling and development of robust new control methods. Improved ABL simulation capabilities must therefore be incorporated into the new HFM facility along with the other wind plant simulation tools. Without the ability to include the physics, land surface interactions, coupling to the large-scale atmospheric dynamics, nonstationarity, and inhomogeneity of the atmospheric flow, any microscale model cannot be a true representation of the flow impacting a wind plant and its turbines. Therefore, developing these new strategies and tools is integral to realizing the goal of improved modeling that makes a difference in power output, which will reduce the levelized cost of energy from wind.

### 1.3 Progression of the MMC Project

The MMC project was designed to systematically progress from simulation of canonical quasi-steady cases through the full complexity of nonstationarity and complex terrain. The plans are grounded in V&V based on comparing model cases to observations. Specifically, the plans for the three years of the project are listed below.

**FY15:** Couple mesoscale to microscale models for canonical steady flow conditions, to include neutral, stable, and convective conditions for flat terrain and compare to SWiFT site measurements.

**FY16:** Couple mesoscale to microscale models for nonstationary conditions, also for a flat terrain site, and devise coupling strategies where the mesoscale forcing causes the microscale models to follow through the temporal changes, and compare to SWiFT site measurements.

**FY17:** Couple mesoscale to microscale models for representative meteorological conditions occurring over a complex terrain site, where the mesoscale forcing causes the microscale models to follow through the temporal changes, and compare to WFIP2 site measurements.

An overarching goal for these three years has been to downselect which models and MMC techniques to implement within the HFM environment. At this point, downselection of the computational solvers has been accomplished—the mesoscale model will be the Weather Research and Forecasting (WRF) model and the microscale model will be Nalu. Section 2.0 discusses the assessment of the model options and rationale for the decisions. Downselection of coupling techniques, based upon efforts begun during FY16, and discussed throughout this report, will be completed by the end of FY17.

As part of each of the three years, there have been four specific objectives that are being addressed, including:

1. to define V&V procedures and benchmarks,
2. to develop and assess microscale turbulence generation methods,
3. to assess current surface-layer and boundary-layer parameterizations, and
4. to develop and assess approaches for coupling mesoscale to microscale models.

The plans beyond FY17 are necessarily more vague, as they depend on the results of the first three years of the project. However, the team expects to continue to add complexity, explicitly compare microscale simulations with and without mesoscale forcing focusing on metrics important to wind plan operation, feedback findings into low order models that can be used rapidly by industry, improve turbulence models for industry, work with the HFM team to provide fast mesoscale modeling capabilities and couple them to Nalu, and feed the results into other A2e projects including controls and others. Table 1.1 summarizes the project progression.

**Table 1.1.** Details of MMC Project Progression and Milestones

Fiscal Year	FY15		FY16				FY17			
Milestone	Q3	Q4	Q1	Q2	Q3	Q4	Q1	Q2	Q3	Q4
<b>Case Selection</b>										
Select Canonical Cases at SWiFT Site										
Select Nonstationary Cases at SWiFT Site										
Characterize SWiFT Site										
Select Complex Terrain Cases from WFIP2 Site										
<b>Downselect Mesoscale Models</b>										
WRF Model/Physics Sensitivity										
WRF Model/Boundary Conditions Sensitivity										
WRF Model/Grid Resolution Sensitivity										
MPAS Model/Suitability for Mesoscale Simulations										
Development of Evaluation Metrics/Evaluation										
<b>Mesoscale Model Selection</b>										
<b>Downselect Microscale Models</b>										
WRF-LES/Steady State										
WRF-LES/Neutral										
SOWFA/Steady State										
SOWFA/Neutral										
HIGRAD										
Development of Evaluation Metrics/Evaluation										
<b>Model Selection/ WRF-LES &amp; Nalu</b>										
<b>Test Microscale Model/Forcing Strategies</b>										
WRF-LES / Fixed Geostrophic Forcing										

Fiscal Year	FY15		FY16				FY17			
Milestone	Q3	Q4	Q1	Q2	Q3	Q4	Q1	Q2	Q3	Q4
WRF-LES / Tendency Forcing										
SOWFA										
<b>Selection of Forcing Strategy</b>										
<b>Testing terra incognita Modeling Strategy</b>										
WRF – Multiresolution Modeling										
<b>Group Recommendation</b>										
<b>Complex Terrain Modeling/Evaluation</b>										
WRF-LES										
Nalu / SOWFA										
Development of Metrics/Case Studies/ Evaluation										
<b>Recommend Best Practices</b>										
<b>Test Coupling Strategies</b>										
WRF-LES/WRF Online										
WRF-LES/ WRF Offline										
WRF-LES/ Asynchronous										
Nalu/ WRF Offline Coupling/Forcing Strategy										
Development of Metrics for Evaluation/Evaluation										
<b>Coupling Strategy Recommendation</b>										
<b>Recommend Best Practices</b>										

Acronyms and abbreviations are defined as: SWiFT: Scaled Wind Farm Technology, WFIP2: Wind Forecasting Improvement Project 2, WRF: Weather Research and Forecasting model, MPAS: Model for Prediction Across Scales, LES: large-eddy simulation, SOWFA: Simulator fOr Wind Farm Applications, HIGRAD: high gradient.

Color Key	
	All
	National Center for Atmospheric Research
	Argonne National Laboratory
	Lawrence Livermore National Laboratory
	National Renewable Energy Laboratory
	Pacific Northwest National Laboratory
	Los Alamos National Laboratory
	Sandia National Laboratories

## 1.4 Background and Motivation

This work is motivated by the fact that the current generation of tools is insufficient to adequately simulate winds and turbulence on all of the atmospheric scales that drive wind plant performance. This project has brought together a team of subject-matter experts to address these modeling gaps. It is widely reported that many wind plants in complex operating environments continue to underperform by 30–40% relative to annual production estimates. According to a survey conducted by AWS Truepower, LLC.

(Bailey 2013), the three largest factors contributing to performance losses, as well as four of the eight uncertainty sources, are impacted by the quality of the numerical simulation tools used for turbine and wind plant performance estimates.

A significant fraction of wind plant underperformance and uncertainty can be attributed to design, siting, and operational strategies based upon inaccurate assessment of environmental conditions, as well as an underestimation of the importance of the environmental (mesoscale) influence on the microscale environment in which wind turbines operate. Wind turbine design, plant construction, and operations all rely on a suite of simulation design tools of varying levels of complexity and fidelity, targeting different phases of wind energy planning, deployment, and production. These computational tools span a range of applications, including flow characterization, power production, fatigue loading, wake effects, and the impacts of complex terrain (e.g., Shaw et al. 2009).

Crucially, these tools all suffer from an inability to adequately address the impacts of the complexity of the mesoscale flow and the physical understanding and modeling of the weather phenomena that strongly influence turbine operation (Sanderson et al. 2011; Troldborg et al. 2011; Mehta et al. 2014). While recent advances have been made to the engineering models used to estimate wakes and loads, and to examine control strategies to improve plant production or mitigate fatigue, (e.g., National Renewable Energy Laboratory's [NREL's] Simulator fOr Wind Farm Applications (SOWFA) and FAST toolkits and Los Alamos National Laboratory's [LANL's] WindBlade model), the applicability of these models to turbine operations in the real world is limited by the low fidelity of the atmospheric flow fields represented within their simulation frameworks. Further rationale and details of the needs are described in the report on the results of year 1 efforts of this team (Haupt et al. 2015).

High levels of wind plant power production uncertainty and underperformance threaten the viability of wind power to meet aggressive future domestic renewable energy targets. A key contributor to both of these threats is industry reliance on a suite of inadequate design tools. These tools, largely developed for idealized conditions and based on a range of simplifying assumptions, do not adequately incorporate the influences of mesoscale variability and other environmental factors that drive important characteristics of the microscale flow field impacting turbine and plant operations. The lack of representation of these important environmental drivers in design tools has led to incorrect assessments of flow characteristics, turbine response, and plant behavior, thereby impacting the performance, reliability, and ultimately the profitability of wind energy projects. MMC allows for the use of time-varying mesoscale boundary conditions (derived from either model output or data) to drive the microscale model simulations. These simulations will allow for microscale simulations that represent a wide range of important meteorological phenomena, such as frontal passages, over the wind plant. This project will document how to best perform MMC and in what situations it is beneficial.

A difficulty with MMC is that it bridges a wide span in spatial and temporal scales. Mesoscale models were designed for horizontal resolutions on the order of kilometers with time-scales ranging from days to hours. Microscale models have resolutions typically ranging from ten meters to a few meters, depending on the stability and desired resolution, and they resolve time-scales ranging from hours to seconds. Spanning these scales involves resolving a wide range of disparate phenomena and turbulence with different fundamental characteristics.

Examples of wind energy applications that would benefit from MMC include single wind turbine loads, power, and controls estimation (by creating more realistic microscale inflow under a variety of conditions for turbine simulators); wind plant siting (by providing more site-specific inflow profiles under the full diurnal cycle in different seasons or terrain-induced flow behavior); wind plant power forecasting and operation (through higher-resolution wind plant-local forecasting); wind plant-level control system design (by testing these controls under more realistic mesoscale-forced situations rather than just applying simple

canonical cases); and wake modeling (through microscale wake simulations in more realistic situations than the canonical ones). All have differing needs for representations of the microscale. For example, it is possible that for loads analysis, the primary factor is employing more realistic mean wind profiles forced by the mesoscale as opposed to the power or log law typically used today. Having site-specific profiles from different times of day and different types of common mesoscale-driven events could greatly improve loads calculations. On the other hand, performing forensics as to why certain turbines failed in a wind plant in complex terrain during a mesoscale weather event will likely require a sophisticated mesoscale-microscale coupled simulation. Wind plant controls experts have been requesting more realistic mesoscale-forced microscale inflow to study because they realize that canonical microscale inflow may not exercise their control systems rigorously enough. Some of those industry experts are developing their own MMC frameworks because the current, more basic frameworks are not sufficient. This MMC project is directly addressing these known deficiencies common to industry research and design tools by assessing and validating mesoscale-microscale coupling strategies.

Thus, MMC is a key enabling technology required for the replacement of many of the inadequate idealizations and simplifications limiting the applicability of current microscale simulation tools. MMC will replace these with environmental forcing obtained from mesoscale simulations. Incorporation of these important environmental drivers will enable simulation of critical microscale flow characteristics impacting turbine and wind plant performance and uncertainties.

## **1.5 Year 2 Emphasis: Nonstationary Conditions**

MMC presents the most promising approach to address the key limitations of current wind plant simulation techniques. The MMC project has been evaluating and developing methods and tools to replace the existing highly idealized or steady-state forcing parameters, periodic lateral boundary conditions, and other simplifications typically employed in wind farm simulation tools. The key to these improved methods is dynamic input from mesoscale weather models that can provide important meteorological, topographical, and other environmental drivers of microscale variability.

In FY16, the focus has been on nonstationary conditions over flat terrain, namely the SWiFT site. These nonstationary cases are critical for wind energy and represent a primary need for mesoscale meteorological forcing of the microscale models. These mesoscale forcings are of two primary types. The first is the well-documented diurnal cycle (Stull 1988) in which the daytime convective boundary layer collapses with the setting of the sun when the surface heat flux changes from positive to negative, passing through a brief period of neutral stability before becoming stable, with smaller-scale turbulence and the potential for low level jet (LLJ) formation. The year 1 report (Haupt et al. 2015) documents the predominance of stable conditions at the SWiFT site and LLJs are a common nocturnal phenomenon there that contributes to the region's renown as a wind power area. While LLJs can substantially enhance wind power production due to increased wind speeds over the spans of contemporary tall turbine rotor swept areas, LLJs also feature large wind speed and direction changes over those heights, as well as increased turbulence, all of which can augment stress loading on turbine components. Further, small changes in LLJ characteristics, such as the height and thickness of the jet nose (region of maximum wind speed) can significantly impact the power available for conversion. Then, in the morning as the surface heating increases, the convection begins to increase, leading to convective rolls that can become convective cells depending upon the relative magnitudes of the mean wind speed and surface buoyant forcing. Both processes lead to increasing depth of the ABL throughout the morning and afternoon hours. Coupled modeling of such conditions has been limited. Talbot et al. (2012) found that the impact of the mesoscale WRF simulation on the nested large-eddy simulations (LES) was the most important driving force on the microscale results. The International Energy Agency Wakebench team has been modeling a diurnal case at the Cabauw tower in the Netherlands in a project known as the Global Energy and Water

Exchange (GEWEX ) Atmospheric Boundary-Layer Study (GABLS) 3 that includes participation from some of the MMC team members. That team is taking an approach of determining forcing tendencies from the mesoscale model and using that as a forcing for the microscale model (Rodrigo et al. 2016a,b). The MMC team has been testing both the nesting approach and the forcing tendency approach. The details of both methods are described in section 5.0 of this report, which also presents the MMC team results for both the GABLS3 diurnal case and a typical diurnal case day from the SWiFT site of November 8, 2013 (see section 3.0 for the case description).

The second type of nonstationary case is any type of synoptic weather event that may cause relatively rapid changes in wind speed and direction, as well as other ABL characteristics, such as those caused by frontal passages, thunderstorm outflows, sea breezes, and other large-scale forced events. These types of cases can cause ramping conditions at wind farms, which can lead to rapid changes in the power output, making the wind power difficult to integrate into the electric grid and utility operations. Modeling such synoptic nonstationary events at the microscale certainly requires the mesoscale output to be able to capture changes in wind speed and direction as well as the other variables (including turbulence intensity, heating rate, etc.) that impact the wind park operations. The Danish Technical University partnered with the University of Hamburg (Pedersen et al. 2013) to study LES models forced by variable pressure gradients from observations. They found that it was important to include the baroclinic height variations in addition to the temporal variations in order to capture the variability of the forcing correctly. The work described in section 5.0 reinforces this result. Jayaraman et al. (2016) used forcing from a WRF simulation to drive changes in surface heating and due to a frontal passage combined with diurnal variations in a case study over southern Kansas.

The MMC team tested running WRF in two modes to assess the ability of coupling the microscale to the mesoscale for the case of a frontal passage on May 12, 2013. The case day is described in section 3.2.2 and the modeling results are presented in section 5.6. This case was modeled both by using the forcing tendency approach and by fully nesting WRF smoothly from the mesoscale through the microscale as described in detail in section 5.6.

The MMC team has also initiated the process for building a turbulence model simulation library that could eventually be used for seeding turbulence in microscale models with asynchronous coupling to a mesoscale model. Also, in FY16, an industry survey was created and feedback received about the view of the value of meso-micro coupling. Additionally, a summary was created of the various meso-micro coupling-related validation quantities of interest and metrics and how different wind energy application areas would use such quantities and metrics.

## **1.6 Expected Impacts to Industry**

The overall role of the MMC project is to advance the science and engineering of coupled mesoscale-microscale modeling in order to provide industry with more advanced wind plant optimization capabilities. Industry stakeholders have made it clear that this must be done in terms of better modeling of power output. This issue is complex and involves many factors beyond applying a simple power curve to a simulated mean wind speed, with small adjustments for turbulence. Uncertainties come from many different aspects of the coupling, including interannual variability due to the longer term climatic variability, variability in the outer scales that are resolved by the mesoscale models, variability due to wake effects, inner variability due to the heterogeneity within the wind plant, variability due to coherent structures, inherent uncertainty due to the chaotic nature of turbulent flow, and impacts through the surface-layer treatment and its interactions with characteristics of the underlying surface. This MMC project addresses these issues directly, and over the course of the multi-year project will be able to provide specific guidance. The team developed Table 1.2 as a list of various uses of the MMC approach,

the stakeholder(s) who are most interested in that use, quantities and metrics to assess for that use, and the type of uncertainty analysis that will impact power output. The “current list” metrics referred to in the table are provided in detail in Table 3.2 of section 3.3.

**Table 1.2.** Assessment of Stakeholder Use and Assessment Strategies to Determine if the MMC Modeling Provides Useful Information for that Use

MMC Use	Stakeholder	Quantity to Measure	Metrics	Uncertainty Analysis for Power Curve
Basic understanding of physics	Scientists/ Engineers	Current list + evaluate structures	Current list plus below	Ensembles – physics, ICs, BCs
Micrositing	Developers/ Contractors/OEMs	Binned WS, spectra, spatial variability	PDF structures, spatial corr	Distribution corr, spatial corr, covar
Turbine siting	Developers/ Contractors/OEMs	Binned WS, spectra, spatial variability	PDF structures, spatial corr	Distribution corr, spatial corr, covar
Turbine reliability & design + forensics		Turbulence stats, Shear, coherent structures	Correlate structures to loads	Distribution extremes, WD variability
Ops & management, controls, loads		Slow variations, even variation, binned WS, accurate turb stats + characterize structures	Use spatial & temporal filters	Time dependent stats & variability
Inform low order models - Mass consistent - Steady RANS	Developers/ Contractors/OEMs	- 3D avg wind & surf fluxes - Full 3D fields, TKE, selected cases	Spatial correlations	All

Acronyms and abbreviations are defined as: IC: initial conditions, BC: boundary conditions, Corr: correlation, Covar: covariance, WS: wind speed, OEMs: original equipment manufacturers, WD: wind direction, Stats: statistics, RANS: Reynolds-Averaged Navier-Stokes, TKE: turbulence kinetic energy, 3D: three-dimensional, .Pdf: probability density function.

Both the improved computational methodologies and the knowledge gained through their assessment and validation will enable substantive improvements in wind plant design, operation, and performance projections, all of which are required to attract continued investment in wind power as a viable means to meet national goals of mitigating climate change and establishing energy independence.

The successful outcome of this project will result in an improved computer simulation capability that accurately incorporates the impact of mesoscale weather on wind power plant performance. Meeting this goal will require microscale simulations driven with realistic mesoscale forcing, a knowledge of when the additional complexity of mesoscale coupling provides a benefit, and recommendations for best practices for modeling across spatial and temporal scales. Over the course of this multi-year project, the tools and knowledge developed at each phase, outlined above, will be made available to both industry and the broader research community. Experimental inputs and numerical results will be made available via the DOE DAP according to the DAP format for data.

The team has engaged with industry through inviting industry representatives to the first year workshop in September 2015 at NCAR, where they were invited to comment on the approach and the results as well as

to suggest changes in the course of the project. In FY16, the MMC team conducted an industry survey. In FY17, the team plans to further engage industry during bimonthly teleconferences, and some industry members will be invited to exercise their models on case studies.

As described in more detail in the sections to follow, each of the models and techniques used in this study is validated against a range of metrics to determine their accuracy for a mix of wind energy related applications. **A key outcome of this project is to provide concrete guidance to both industry and research communities regarding the potential strengths and weaknesses of various MMC approaches.** Additionally, the best performing of the approaches assessed will be incorporated into the A2e high-performance modeling (HPM) environment for future design and testing. A set of metrics has been defined in the project, but continues to be refined further as the project progresses into additional realms of modeling.

The remainder of this report provides detailed documentation of the results of the year 2 effort. The performance metrics were defined at the beginning of the project and updated as further needs for these nonstationary cases became evident. The need for uncertainty quantification has been an intentional part of the metrics development and plans for model runs in the future.

Section 2.0 begins with discussing the downselection of models that resulted from the team's year 1 results. Data and case selection for the nonstationary cases of year 2 are described in section 3.0. Section 4.0 deals with analyzing the issues related to the *terra incognita*. Details of the microscale model simulations are analyzed and assessed in section 5.0. Analysis of turbulence generation methods appears in section 6.0. Section 7.0 provides a summary of the results, assessment of the models' ability to model nonstationarity, and the use of these methods in the context of the planned HFM system and of the greater community, given the stakeholder needs discussed above.

## 2.0 Model Downselect from Year 1 Work

This section discusses the team's efforts in downselecting the models chosen for microscale and mesoscale simulations. The WRF model is described in detail below, as it is recommended for both mesoscale and microscale simulations, and is a complete mesoscale to microscale weather tool. We further discuss the microscale models WRF-LES, SOWFA, and HIGRAD, and connect their characteristics to the microscale model chosen for the HPM framework, Nalu. Lastly, the Model for Prediction Across Scales (MPAS) is compared to WRF and WRF-LES as a potential candidate for a mesoscale model.

### 2.1 The WRF Model

The WRF model (Skamarock et al. 2008) is a community model maintained by NCAR in collaboration with universities and other users. It includes a data assimilation system and an LES system, among many other capabilities, which have been used in the meso- to microscale coupling modeling efforts of this project. While primarily used for weather applications, mesoscale wind farm parameterizations are currently available within the public release (Fitch et al. 2012). Microscale wind turbine parameterizations have also been successfully implemented within WRF (Mirocha et al. 2014), however, they are not yet available in the public release (as of V3.7).

WRF uses finite differencing to solve the compressible Euler equations, using a split time stepping algorithm within the Runge-Kutta time integration scheme, and a filter for acoustic modes. Users may specify from among third- and fourth-order Runge-Kutta methods and the number of the small time-steps within each Runge-Kutta cycle, with default values being third-order and six small steps, respectively. Users may also specify the order of accuracy of the advection scheme. The options are second- through fifth-order in the horizontal and second- or third-order in the vertical, with default values of fifth and third, respectively. There are also options for positive-definite and weighted essentially non-oscillatory (WENO) advection schemes. Other user-specifiable parameters of the solution method may be employed to control instabilities, including both internal weighting parameters and several external damping options.

The WRF model uses a Cartesian mesh, with the horizontal grid spacing specified in meters, and the vertical mesh spacing specified in terms of a terrain-following pressure-based eta coordinate,  $\eta(z) = (p(z) - p_T)/(p_S - p_T)$ . Here,  $p$  is pressure,  $z$  is height above the surface, and subscript  $S$  and  $T$  define the surface and model top. The heights of gridcells above the surface can be approximately specified in meters using the hypsometric equation,  $p(z) = p_S \exp(-gz/(R\bar{T}))$  (Holton 1980), using standard atmosphere values for  $\bar{T}$ , the average value of temperature over a vertical layer of depth,  $\Delta z$ . Here,  $g = 9.81 \text{ m s}^{-2}$ , the gravitational acceleration, and  $R = 287 \text{ J kg}^{-1} \text{ K}^{-1}$ , the gas constant for dry air. Initial eta values may be prescribed to identify specific height values; however, those values are not maintained precisely during a simulation due to changes in the thermodynamic state. Model variables are specified on an Arakawa "C" grid.

WRF-LES is described and compared to other microscale models in the next section, and the use of WRF as a mesoscale solver is detailed in section 2.3.

### 2.2 Microscale Model Selection

The microscale solvers used in this work are the WRF model applied in LES (WRF-LES) model, SOWFA, and the high gradient applications (HIGRAD) model. WRF-LES is developed primarily at

NCAR, SOWFA is developed at the NREL, and HIGRAD is developed at LANL. WRF is a complete mesoscale to microscale weather tool, whereas SOWFA and HIGRAD are microscale computational fluid dynamics (CFD) tools that each have the ability to couple to independent mesoscale models by using mesoscale model output as input to their simulations. The following sections briefly review the model characteristics and section 2.2.4 discusses the path forward given the results of year 1 and year 2 of the MMC effort.

### 2.2.1 WRF-LES

This section describes the use of WRF in this MMC project as a microscale solver by employing its LES capabilities. Besides the characteristics of WRF outlined above, for LES, the current WRF release (version 3.7.1) includes four subgrid-scale (SGS) turbulence options. A range of lateral boundary condition options are available, including periodic, open, symmetric, specified, or nested. Mesh refinement is provided via block rectangular nesting, with integer ratios for the horizontal mesh and time stepping ratios. Vertical mesh refinement is available either as an external postprocessing step, or, as of version 3.6, can be activated for concurrent simulation. Nesting can be either one- or two-way, with two-way restricted to concurrent simulation with only horizontal, but not vertical, mesh refinement. At the model top, WRF imposes a free-slip upper boundary condition for  $u$  and  $v$ , and  $w = 0$ . The Monin-Obukhov-based surface boundary condition can be applied, as with the other two codes described below (SOWFA in section 2.2.2 and HIGRAD in section 2.2.3). An advantage of WRF-LES is the ability to use the physics parameterizations inherent in WRF throughout the LES nests.

### 2.2.2 SOWFA

SOWFA is a collection of flow solvers, turbulence models, turbine models, boundary conditions, and utilities used specifically for computing wind plant flows (SOWFA 2015). The complete toolset is meant to span from the mesoscale down to the turbine scale, providing interfaces between tools of different scales.

The SOWFA microscale solver is built upon the Open-source Field Operations And Manipulations (OpenFOAM) CFD Toolbox (OpenFOAM 2105), a popular, open-source, freely available set of C++ libraries for solving partial differential equations. OpenFOAM comes with a variety of standard solvers, turbulence models, boundary conditions, and other physics models, and because of its open-source nature, it is easy to build new solvers, boundary conditions, and other parameters. OpenFOAM, and hence SOWFA, uses an unstructured mesh, finite-volume formulation for solving the governing equations. There are a variety of options for spatial discretization, and typically, second-order central differencing is used for the advective and diffusive terms. Time advancement is also second-order accurate with Crank-Nicolson-implicit discretization. SOWFA's microscale flow solver is incompressible, but uses the Boussinesq approximation for buoyancy. All variables are located at cell centers, and to avoid velocity-pressure decoupling, a Rhie-Chow-like interpolation of velocity flux to cell faces is used. A number of SGS turbulence models are available in SOWFA. SOWFA includes Schumann's boundary condition for surface stress and also boundary conditions for surface temperature flux or cooling rate. The solver can be used over flat or complex terrain. Because of the unstructured nature of the mesh, regions of increased refinement can be added where necessary, such as in turbine wakes and around regions of highly complex terrain.

### 2.2.3 HIGRAD

The HIGRAD LES model (Sauer 2013) discretizes the fully-compressible, nonhydrostatic Euler equations using the finite-volume technique on an Arakawa “A” grid. A variety of advection schemes are available—upstream, QUICK, FCT, and WENO, as well as two different time-marching methods—method of averages (MOA) and Runge-Kutta (1<sup>st</sup> to 4<sup>th</sup> order accurate). Two SGS model options can be chosen, Lilly and a multi-scale turbulent kinetic energy (TKE) closure, the latest specifically designed for wildland fire applications. The grid is fixed in physical space, with several options for different local refinements both in the horizontal and vertical directions. A range of lateral boundary condition options are available, including periodic, open, symmetric, specified, or nested. Mesh refinement is provided via block rectangular one-way nesting, with arbitrary ratios for the horizontal and vertical grid spacing and domain extent in all of the three directions (bounded within the corresponding parent domain). Additionally, the WindBlade turbine model developed at LANL (Linn and Koo 2008) is embedded in HIGRAD. The WindBlade model represents rotating turbine blades using an actuator-line type of model in an Eulerian-Lagrangian framework that allows calculation of the two-way interactions between turbines and local wind fields, including resulting fluctuations of aerodynamic loads on the blades and turbine power output.

### 2.2.4 Downselection of Microscale Models

The three microscale models described above were compared with varying grid spacings, order of the advection schemes, turbulence schemes, geostrophic wind speed, roughness height, aspect ratio, and a variety of other parameterizations for convective and neutral conditions in the flat terrain cases from the SWiFT site in the year 1 report (Haupt et al. 2015). All models were successful at reproducing some of the basic features of the cases, but also showed discrepancies, particularly on capturing specific profile and turbulence characteristics. In general, errors in most variables are within the variability of the measurements. Sensitivity to different parameterizations and forcings were evident, and reinforce the notion that one must carefully construct the current combination of parameters to correctly model a case. Turbulence quantities and spectra and cospectra were additionally assessed. A major finding was that when tuned for the cases, the models performed similarly and the differences between models was smaller than the variability in the SWiFT tower data that was being used for comparison. It was also found that it is quite difficult to set up a high-quality stable boundary layer case with the appropriate characteristics as a canonical case.

In moving toward a HPM framework, a more important consideration for the team was identifying a model that is amenable to exascale computing. The choice was made to work with the model Nalu, which is currently being equipped with the physics for wind plant modeling that is already embedded in SOWFA. This enhanced version of Nalu will become the microscale model for the HPM framework.

Note, however, that the MMC team still believes that it may be critical to carry the physics inherent in WRF through the *terra incognita* and into the microscale. Thus, the MMC team plans to continue to assess how far WRF should be nested before handing off to Nalu in the fully coupled HPM framework that is being developed.

## 2.3 Mesoscale Model Selection

Two mesoscale models were considered to provide the mesoscale simulations for the project: the WRF model (in several configurations) and the newer MPAS. Both are described below and an assessment is provided that is derived from Kotamarthi and Feng (2016).

### 2.3.1 WRF Model

The results of the year 1 report (Haupt et al. 2015), as well as those presented in the following sections, indicate that the WRF model represents the mesoscale flow well. Its other advantages include the large number of physics packages available, the large number of users who have successfully applied WRF in research and in operations, its ease of use for a trained numerical weather prediction (NWP) modeler, and its use by many companies in the wind industry. Additionally, its improvement for wind forecasting within the WFIP2 make it the mesoscale model of choice.

FY15 efforts made use of WRF version 3.6.1, whereas FY16 efforts used version 3.7.1. Most simulations were initialized daily at 0000 Coordinated Universal Time (UTC) to run for 36 hours. The first 12 hours were discarded to allow for spin up. The outermost domain has a 27 km grid spacing, and was nested down through 9 km, to an inner domain with a 3 km grid spacing (Figure 2.1) and a size of 354 x 300 km. To investigate *terra incognita* issues, the WRF was further downscaled in mesoscale mode to 1 km and 333 m. The time-step was set to 15 s with model output saved every 5 min of model time. A total of 88 model levels were used, and were spaced approximately 5 m apart in the lowest 20 m, and stretched continuously beyond that (Figure 2.2).

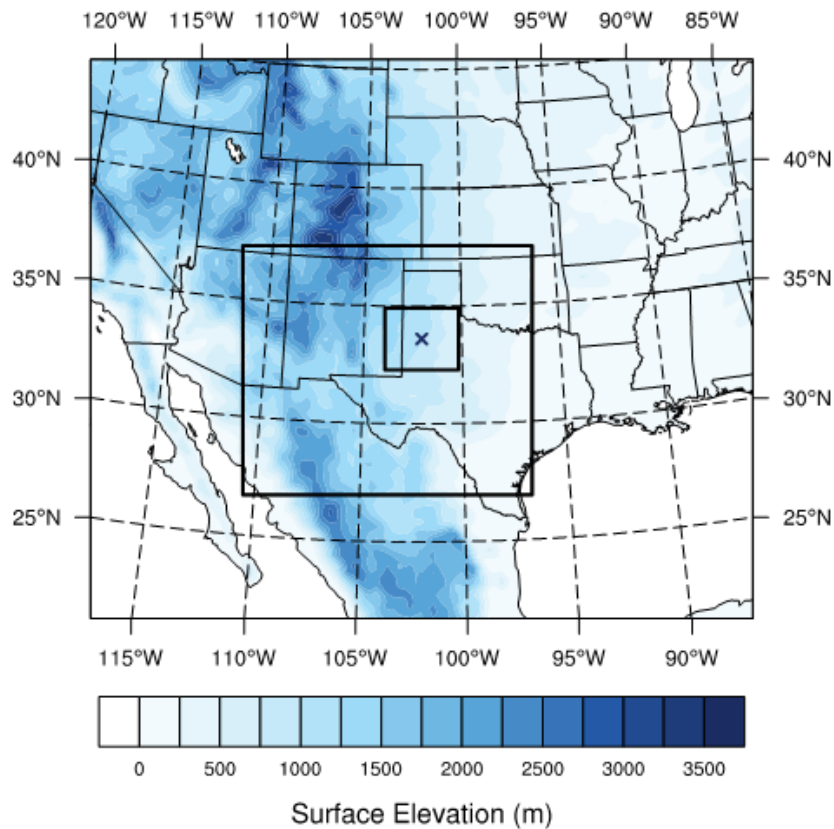


**Figure 2.1.** WRF Simulation Domains at a 27, 9, and 3 km Resolution

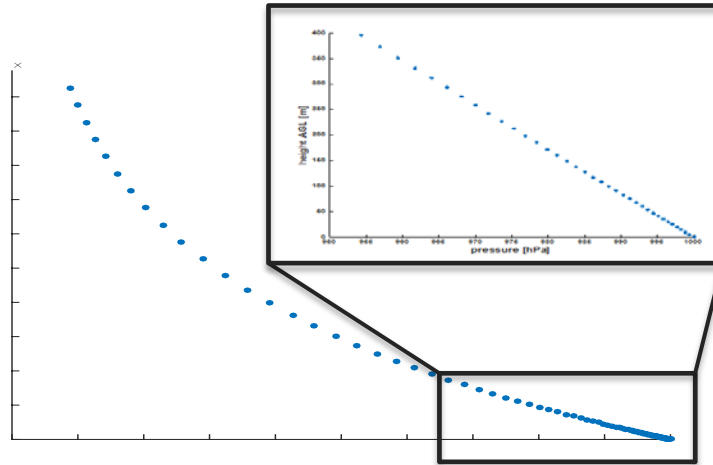


**Figure 2.2.** Depiction of the Approximate Vertical Grid Spacing for the Mesoscale Simulations; Pressure from the Standard Atmosphere as a Function of Height

### 2.3.2 MPAS

The MPAS is a continuously refinable variable mesh model with dynamic core and physics options adopted from WRF (Skamarock and Klemp 2008). The model uses the Yonsei University (YSU) planetary boundary layer (PBL) scheme (Noh et al. 2003), the Noah land surface model (Chen and Dudhia 2001), the Kain-Fritsch convection scheme (Kain 2004), and the Rapid Radiative Transfer Model-global (RRTMg; <http://rtweb.aer.com>) for radiative transfer. The surface layer is parameterized using Monin-Obhukov parameterizations. Its advantage is that its grid can be continuously refined.

Our primary interest in evaluating the MPAS model is its potential for providing a solution to some challenges researchers face when using the WRF model for mesoscale simulation coupled with WRF-LES. The scale-down ratio of 1:3—recommended and widely used for WRF—achieves a large refinement in resolution by using a number of nested domains; however, it introduces numerical stability and convergence problems at each of the nesting boundaries (Gill and Pyle 2011). The newer dynamical core with unstructured mesh (MPAS) has been tested over the last few years (Skamarock et al. 2008), and a version of the MPAS model implemented with WRF physics is now available. The nest-down options provided by MPAS, which allow for a continuous grid refinement, are likely superior to those currently available with WRF. This work was initiated to evaluate the suitability of using MPAS to reach higher spatial resolutions (<3 km) for mesoscale phenomena.

### 2.3.3 Mesoscale Model Comparison

Argonne National Laboratory (Argonne) investigated the capability of WRF and MPAS models under various configurations to simulate an observed neutral boundary layer case using data collected at the SWIFT facility at the Texas Tech University (TTU) National Wind Institute (Kelly and Ennis 2016) as described further in section 3.0 and in the year 1 report (Haupt et al. 2015).

Simulations were performed using three-dimensional variational data assimilation (WRF-3DVAR), WRF-LES, and MPAS for August 2011 for the vicinity of the SWIFT site. This period was identified as experiencing neutral boundary layer conditions from approximately 0000 UTC to 0100 UTC (7 p.m. to 8 p.m. Central Daylight Time [CDT]) on August 17 and 18 of 2012. The observations capture this

transition to neutral stability (Figure 2.3). We tested the ability of WRF-3DVAR, WRF-LES, and MPAS models to reproduce these conditions. The model setup, initial conditions, and boundary conditions used for each of these exercises are discussed in sections 2.3.3.1, 2.3.3.2, and 2.3.3.3.

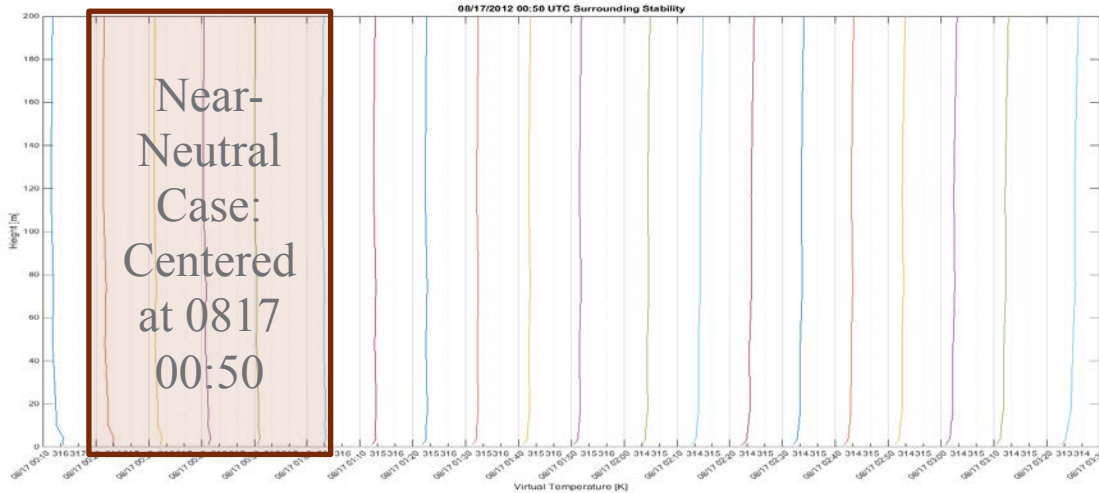


**Figure 2.3.** Observed Virtual Temperature Profiles during the Near-Neutral Conditions at Approximately 0000 to 0100 UTC (7–8 p.m. CDT) on August 17 at the SWiFT Site

### 2.3.3.1 WRF/WRF-3DVAR Setup

Data assimilation has the potential to improve surface wind velocity and wind direction forecasts in mesoscale models. A preliminary assessment was performed to assess the impact of assimilating observations on WRF forecasts. The evaluation used observational data from the Texas Mesonet (<http://www.mesonet.ttu.edu>) for the August 17 neutral case. A total of 54 stations were identified in the region surrounding the SWiFT site (Figure 2.4). WRF was initialized with observations using WRF-3DVAR, which is a WRF configuration that uses three-dimensional variational data assimilation to constrain the model, to create an initial conditions field and modified boundary conditions at two starting times: 12 pm the previous day and 00 hours on the day of the observed neutral case. The simulations that assimilated data one hour or less before the target time produce results that are closer to observations than those initialized with observational data 12 hours ahead of the time when the neutral conditions were observed. This shows that assimilating observations at frequencies with 1 hour gaps produces more accurate surface wind fields. Calculations were also performed using the WRF model without the 3DVAR and with the same initial, boundary, and physics parameterizations.

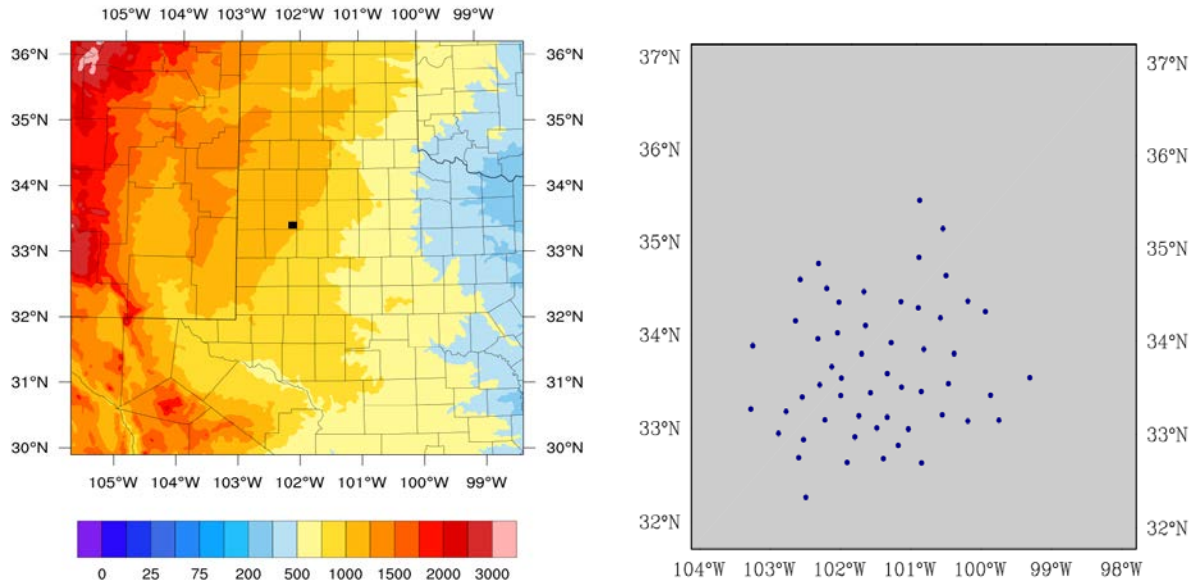


**Figure 2.4.** The Model Domain used in WRF-3DVAR Simulations. The black square in the figure on the left shows the approximate location of the SWiFT site and the colored contours are the terrain heights. The figure on the right covers a similar domain and shows the Mesonet stations used for assimilation in the 3D-VAR simulations.

### 2.3.3.2 MPAS Setup

The MPAS model used here is global and has a spatial resolution of 15 km, 41 vertical layers, and the model top is set at 30 km (Figure 2.5). The model initial conditions are set using NNRP (NCEP<sup>1</sup>/NCAR Reanalysis Project) and the surface conditions (including the sea surface temperature) are updated every 6 hours. The model was used to simulate the entire month of August 2012. The model simulations were compared with a limited area simulation performed with WRF for a region that includes the SWiFT site at Texas Tech University.

<sup>1</sup> National Centers for Environmental Prediction

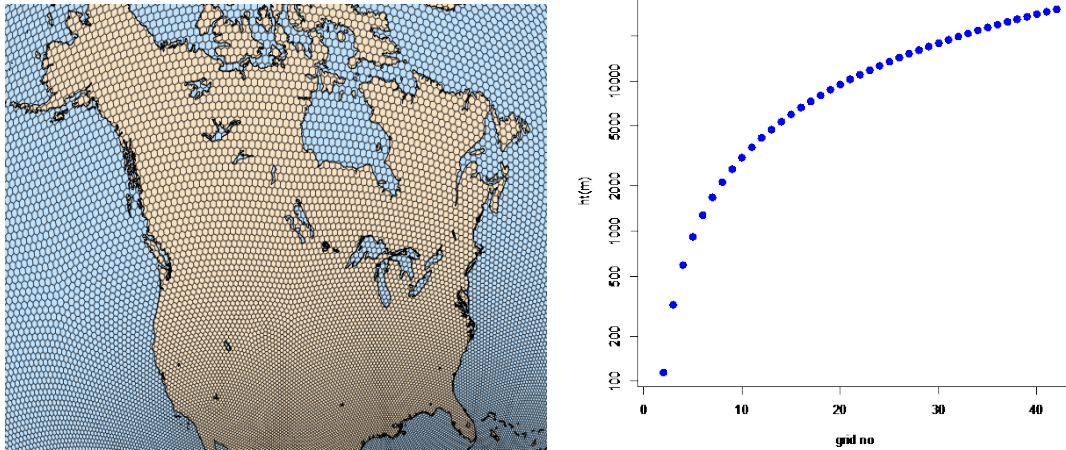


**Figure 2.5.** The  $\sim 15$  km Variable Mesh Generated for the MPAS Resolution (left) and the Vertical Resolution of the Model (right). The vertical resolution is approximately 150 m in the lower atmosphere.

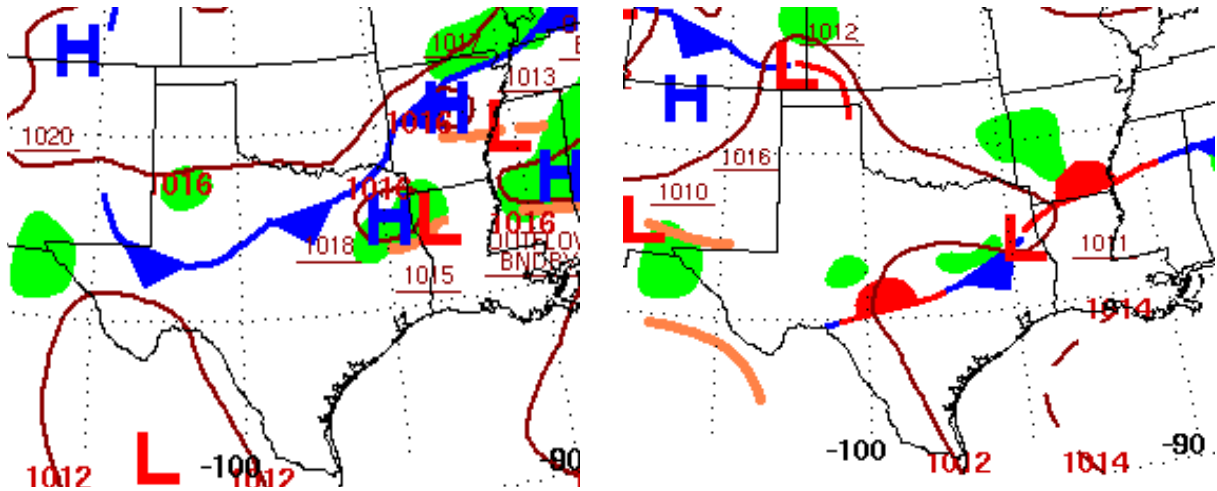
### 2.3.3.3 WRF-LES Setup

WRF-LES simulations were also performed for the neutral boundary layer case during the late evening (0020–0220 UTC) of August 17, 2012, using WRF 3.6 in LES mode. The simulations were run over a domain of  $2.4 \text{ km} \times 2.4 \text{ km} \times 2 \text{ km}$ , with a horizontal resolution of 25 m and a resolution of 7.5 m below 500 m in the vertical direction. The baseline case uses the Lilly SGS model (Lilly 1967) with a surface roughness ( $z_0$ ) of 0.05 m. Model sensitivity to using the Smagorinsky SGS model (Smagorinsky 1963) and other model configurations were also performed for the neutral case (Kotamarthi and Feng 2016). The idealized LES simulations were initialized with sounding profiles that approximated the tower observations at the SWiFT site. The wind components were initialized as geostrophic wind values. The initial temperature was specified to be consistent with potential temperature profiles of  $\theta(z) = \theta_B + a(z) + a'(z)$ . Here,  $\theta(z) = [P_0/p(z)]^{0.286}$ , where  $P_0 = 1000$ , hPa is a reference pressure,  $\theta_B$  is a background constant value,  $a(z)$  specifies an inversion of 500 m with a rate of 10 K/km, to prevent turbulence from reaching the model top, and  $a'(z)$  is small perturbations  $\in [\pm 0.25 \text{ K}]$ , drawn from a uniform distribution, and scaled as a decreasing cubic function of height from the surface up to specified height. These small perturbations are applied only to the initial condition to seed turbulence.

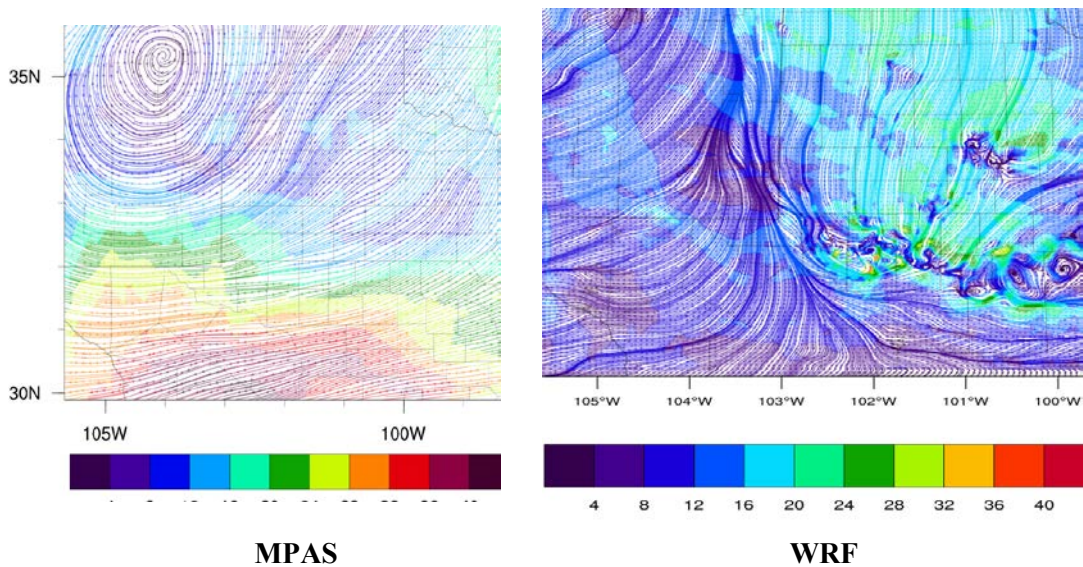
## 2.3.4 Results from WRF and MPAS Comparison

### 2.3.4.1 General Meteorological Conditions

A cold front was positioned to the west of the SWiFT site on the morning of August 17, 2012; it moved over the site by early morning the next day (Figure 2.6). To the east and in front of the cold front was a high-pressure system that moved out of the domain the following day. Another high-pressure system was located west of the site on both days, with its location moving closer to the site on August 18. Figure 2.7 shows the results obtained from the WRF and MPAS models 5 km above the ground. The MPAS and WRF models had approximately the same wind velocities over most of the domain. The MPAS model located the high-pressure system farther to the east and south compared to the WRF model. The low-pressure region to the south and east of the SWiFT site (lower right corner of the domain) is not a prominent feature of the MPAS model, as compared to the WRF results. These features are similar to the conditions observed, as shown in Figure 2.6.



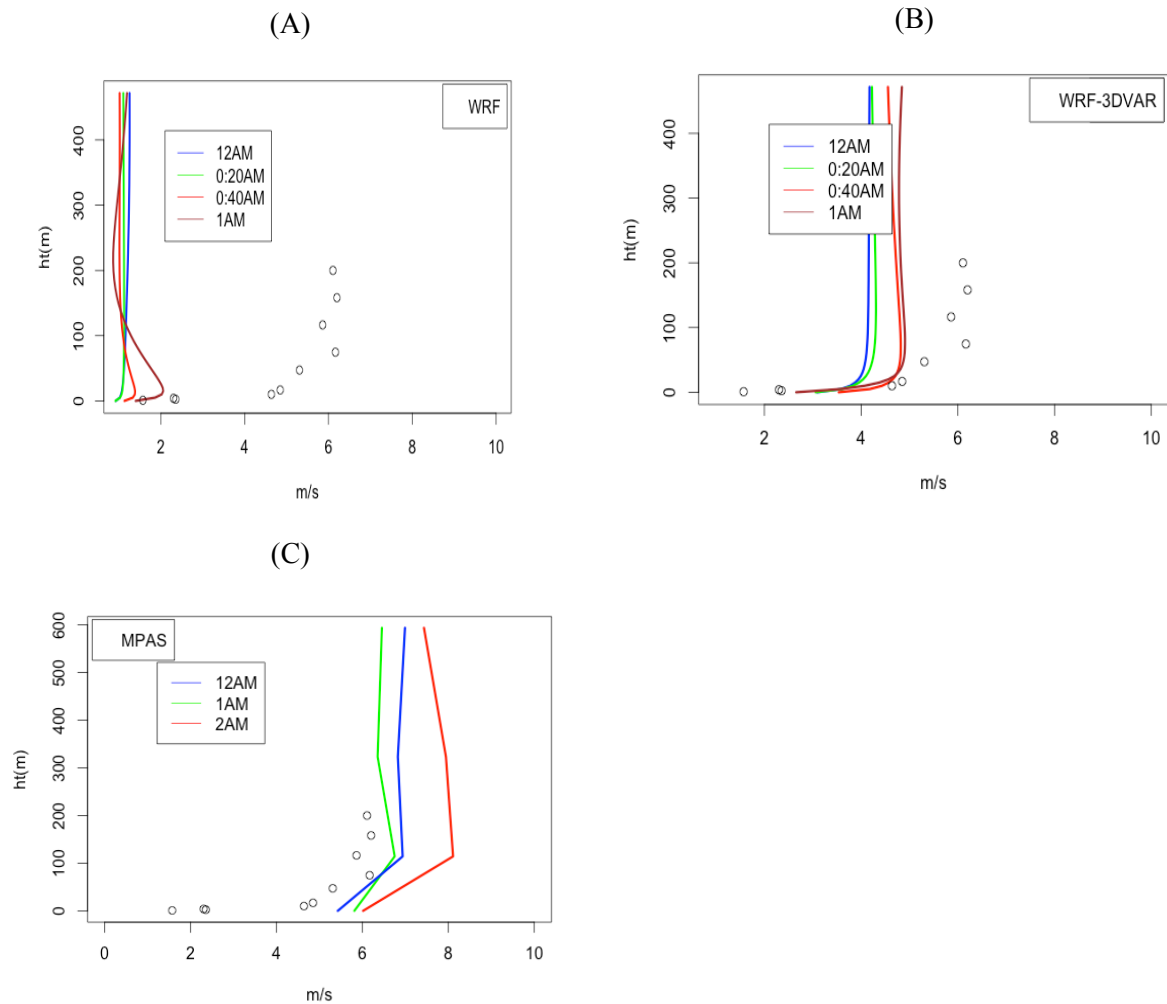
**Figure 2.6.** Surface Weather Maps for August 17 (left) and 18 (right) 2012. The neutral case we are exploring occurred between and 7 and 8 p.m. on August 17.



**Figure 2.7.** Results from MPAS and WRF Model Simulations for August 17 at 7 p.m. The color coding indicates the wind speeds (m/s). The domains shown are approximately the same size and cover the SWiFT site.

### 2.3.4.2 Wind Profiles for the Neutral Case

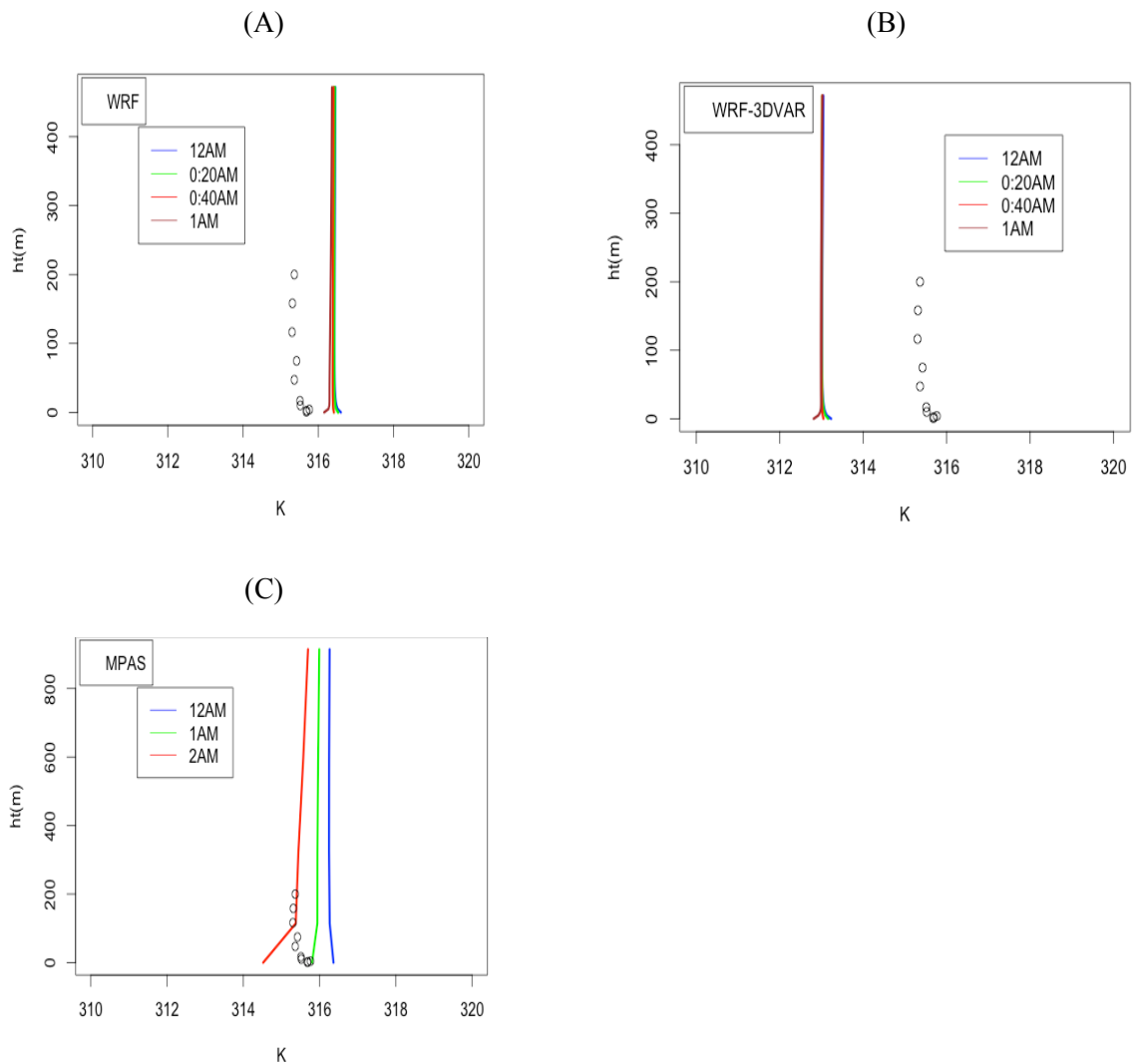
The simulated wind profiles were saved every 5 min for the entire simulation period with the WRF and WRF-3DVAR configurations, and every hour with the MPAS model at the SWiFT site. Figure 2.8 shows the results from these simulations. The WRF model underestimates the wind velocities by a factor of 2 to 3 and the wind profiles start moving away from neutral conditions by 0100 UTC. The WRF-3DVAR wind velocities are closer to the observed wind profile. The profile is similar to observations and remains neutral near the surface for the entire time period. Figure 2.8(c) shows results from 1200, 0100, and 0200 UTC from the MPAS simulations. The MPAS model simulates the neutral profile; however, the model vertical resolution is coarse and there are only about six layers in the lower 200 m of the model. The model produces higher velocities than either WRF or WRF-3DVAR.



**Figure 2.8.** Simulated Wind Velocity Profiles at Various Times between 0000 UTC and 0100 UTC, using the (A) WRF Model, (B) WRF-3DVAR, and (C) MPAS. The circles shown are the measurements from the 200 m tower at the SWiFT site.

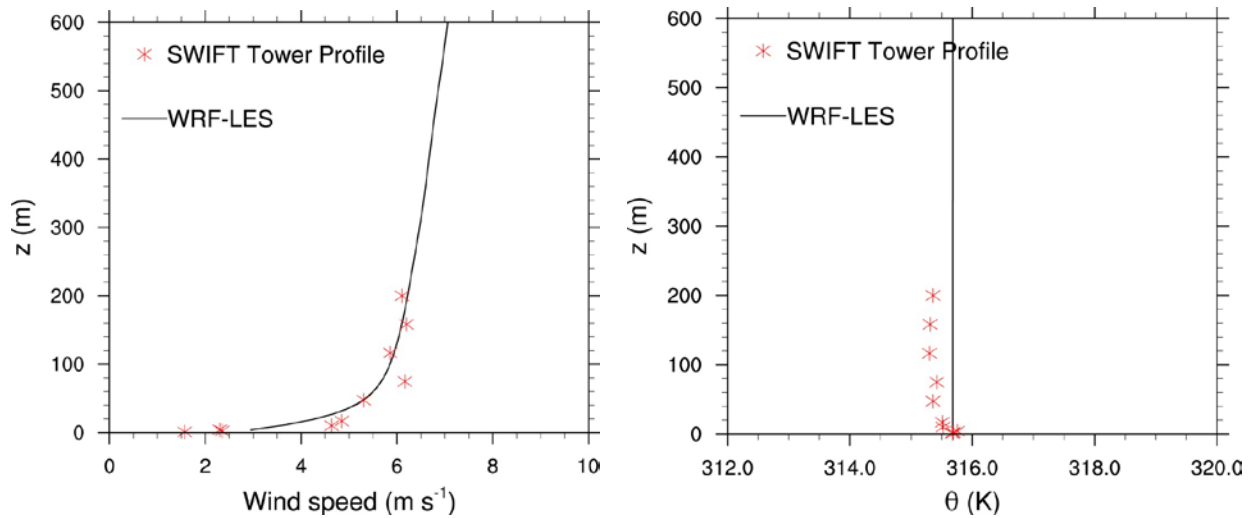
### 2.3.4.3 Potential Temperature

Figure 2.9 shows a similar comparison for the calculated potential temperatures from the models. The WRF model estimates a higher potential temperature than observed by approximately  $1^{\circ}\text{C}$ , and the WRF-3DVAR configuration underestimates the potential temperature by more than a degree. The MPAS model results at 0100 UTC are approximately the same as observations at the surface, but lower at higher altitude. The WRF-3DVAR shows temperature profiles that are closer to the neutral case at the surface, and the WRF output indicates a transition to an unsteady state at the surface by 0100 UTC. The MPAS temperature profiles at 12 and 0100 UTC indicate neutral conditions.



**Figure 2.9.** Potential Temperature Profiles Calculated with the (A) WRF, (B) WRF-3DVAR, and (C) MPAS Models for August 17 at the SWiFT Site. The open circles are observed potential temperatures from a 200 m tower at the site.

Results from the WRF-LES are shown in Figure 2.10. The model was initialized with the observed temperature at the surface and geostrophic forcing estimated from the observations at the tower. After 16 hrs of simulation, the boundary layer turbulence was fully spun up, reaching a nearly steady state for the baseline neutral case, as identified by the occurrence of the first maximum in horizontal velocity at 80 m above the surface. The model simulates both the temperature and wind profiles with greater accuracy, although the potential temperature estimated was slightly higher than observed and is similar to the WRF model.



**Figure 2.10.** Wind and Potential Temperature Profiles from WRF-LES at 0030 UTC on August 18

### 2.3.4.4 PBL Height

The PBL heights calculated from the WRF, WRF-3DVAR, and MPAS models are shown in Figure 2.11. The PBL height estimated by the MPAS model is similar to that of the WRF model; it also produces a higher peak than the WRF-3DVAR model and a smaller peak than the WRF model. The peak PBL heights produced by the WRF and MPAS models are similar at approximately the same time (20 UTC, ~2 p.m. CDT). The WRF-3DVAR PBL height is lower and appears an hour later than in the WRF and MPAS models. Some of the differences between the MPAS and WRF models can be explained by the differences in model spatial resolution in both the vertical and horizontal dimensions. Although the MPAS model is global in scope and was initialized on August 1 (with sea surface temperature updates every 6 hrs), the model compares favorably with WRF. It should also be noted that all three models use the same PBL scheme and other relevant physical parameterizations.

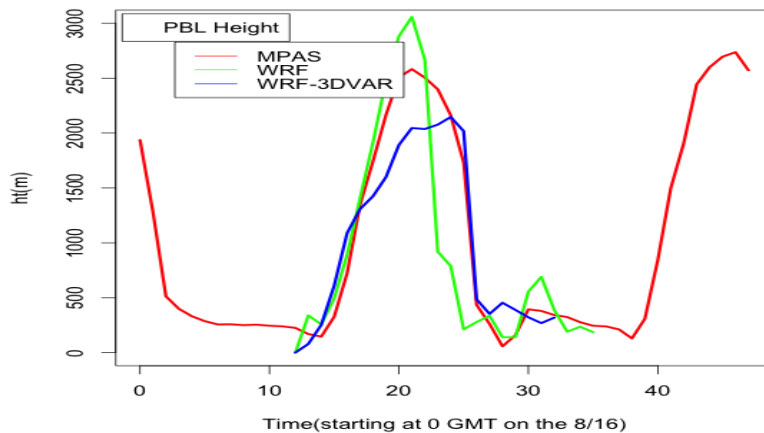


**Figure 2.11.** PBL Heights Calculated by MPAS (red line), WRF (green line), and WRF-3DVAR (blue line). Results are shown from 0000 UTC on August 16 to 0000 UTC on August 19.

### 2.3.4.5 Surface Fluxes

We also compared surface sensible heat flux calculated by the different models over this region. Figure 2.12 shows the heat flux calculated in WRF-3DVAR (top row) and MPAS (bottom row). The WRF-3DVAR model simulates smaller sensible heat flux at 12:00 and 18:00 local time over the western half of the model compared to MPAS. This could be related to the location of clouds in the model around the cold front and location of the high pressure over the west. Although the eastern and southern halves of the domain are similar, the MPAS model estimates higher sensible heat fluxes over a larger domain in the south than does the WRF-3DVAR. Compared to the MPAS model, the location of the low-pressure system and the movement of the cold front and cloud cover in the lower eastern corner in the WRF and WRF-3DVAR models (which does not show the low-pressure system in the lower part of the domain) could explain the differences. Both models show nearly zero sensible heat fluxes at night, as expected.

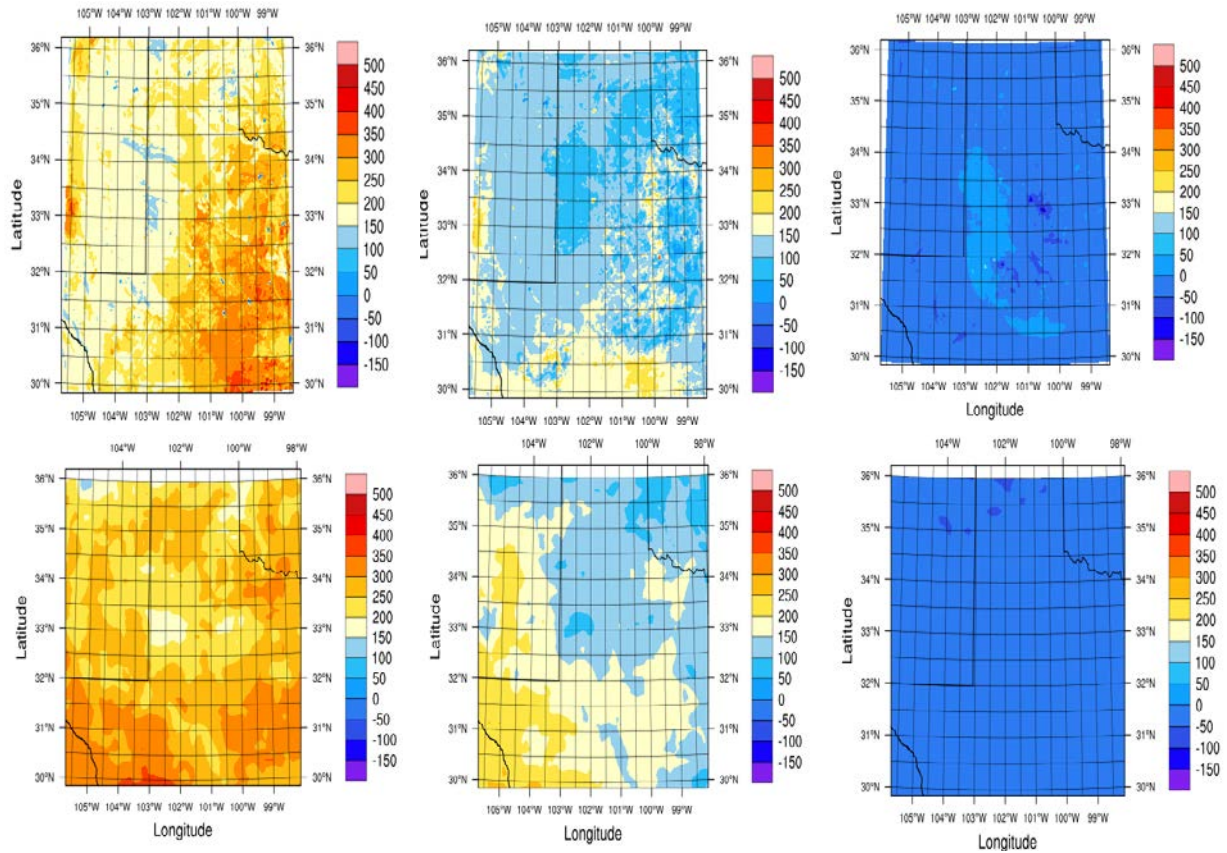


**Figure 2.12.** Comparison of Sensible Heat Flux (in  $\text{W m}^{-2}$ ) from WRF 3D-VAR (top row) and MPAS (bottom row) for 12:00 (left), 18:00 (middle), and 01:00 (right) Local Time

Comparison of latent heat fluxes leads to similar conclusions, as shown in Figure 2.13. The higher latent fluxes in the WRF-3DVAR correspond to clouds/precipitation and overlap the regions with low sensible heat fluxes in Figure 2.12. The region around the location of the front in the lower eastern portion of the domain leads to precipitation and latent heat fluxes that are not captured by the MPAS model. This region is still experiencing enhanced latent fluxes later in the night that are absent in the MPAS model. It is likely that the spatial resolution of the MPAS model compared to the WRF-3DVAR contributes to lower amounts of clouds/precipitation in the model as compared to WRF-3DVAR.

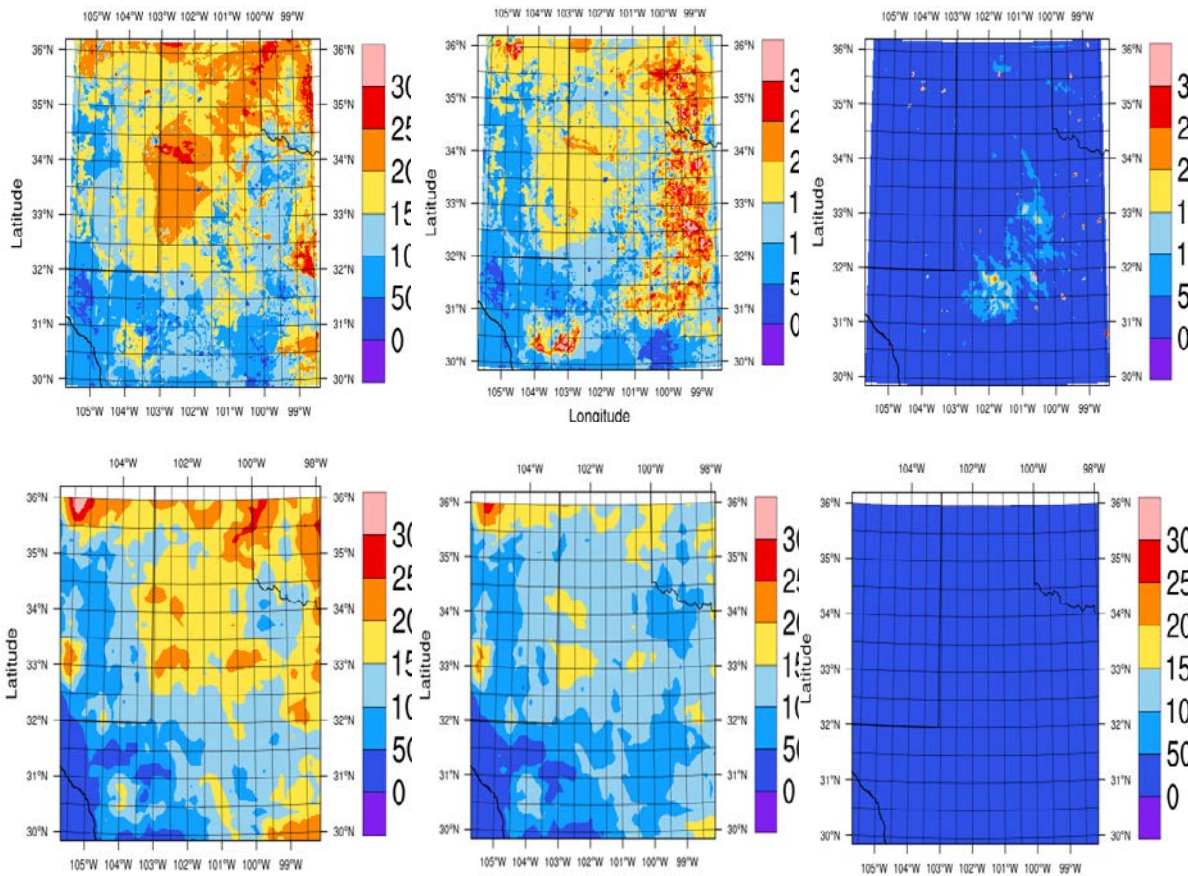


**Figure 2.13.** Comparison of Latent Heat Flux (in  $\text{W m}^{-2}$ ) from WRF 3D-VAR (top row) and MPAS (bottom row) for 12 p.m. (left), 6 p.m. (middle), and 1 a.m. (right) Local Time

### 2.3.5 Downselection of Mesoscale Models

The performance of MPAS was compared to that of WRF for a neutral stability case observed during the night of August 17, 2012, for the SWiFT site. Observations of temperature profiles and wind speeds made from a 200 m tower were used for the model evaluations. From these calculations, we have shown that (a) surface heat fluxes calculated by WRF and MPAS are similar for the selected neutral case; (b) boundary-layer vertical profiles of wind speed calculated for the neutral case with MPAS were similar to the WRF mesoscale models; (c) assimilating wind profiles with initialization the hour before the event produced the best comparison to the observed winds; (d) potential temperature profiles for all three cases show a neutral profile at the time when the observations were made; (e) WRF 3D-VAR and LES produced the closest reproduction of the observations; and (f) the PBL heights calculated by the three models differ by several hundred meters during the daytime but show similar diurnal transitions.

A thorough evaluation of the physical drivers behind these differences is beyond the scope of this report. However, we can conclude that higher vertical resolution in the MPAS model could alleviate some of the observed differences. Another challenge in using MPAS was the data volumes from the MPAS model at a spatial resolution of 15 km and finer. At a 15 km spatial resolution, the model produces more than 500 GB of output per calendar day of model simulations when saved once every hour. Very few plotting and analysis tools are useful for handling this amount of output; we would need parallel processing tools

(e.g., Paraview), which poses a challenge in terms of obtaining the computational/visualization resources and the effort needed for analysis. Developing a regional version of MPAS and better visualization and analysis tools in the model's native coordinates will be required to fully utilize the model for the MMC project. Thus, the capabilities of MPAS are not sufficiently developed at this time to make it a viable option for the HPM framework.

As noted in section 2.1, WRF has many advantages, including the large number of users (especially in the energy industry), availability of a series of choices of physics parameterizations, success in many research and operational applications, and ease of use by an experienced NWP modeler. For these reasons as well as due to the limitations of MPAS described above, the MMC team recommends that WRF be used as the base mesoscale model for the A2e systems.



### 3.0 Data and Case Selection

Year 2 goals of the MMC project are to model nonstationary cases, including a complete diurnal cycle of the atmosphere as seen in the daily operation of a wind turbine as well as an example of frontal passage. For this effort, the DOE/SNL SWiFT facility was again selected as the test site, as was true for the year 1 efforts (Haupt et al. 2015). Simulating nonstationary cases such as diurnal cycles and frontal passages at this site is a continuation of the previous year’s work and the next step in increasing simulation complexity before including complex terrain effects. The SWiFT site was chosen for its flat terrain, relevance to wind energy installations in the United States, and the adjacent atmospheric measurement facilities hosted by Texas Tech University’s (TTU) National Wind Institute (NWI).

#### 3.1 SWiFT Site and Instrumentation

A picture of the SWiFT site and relative location of the TTU 200 m meteorological tower are shown in Figure 3.1. The SWiFT site is located within the Southern Great Plains with very minor terrain changes and no significant geographic features for hundreds of miles.

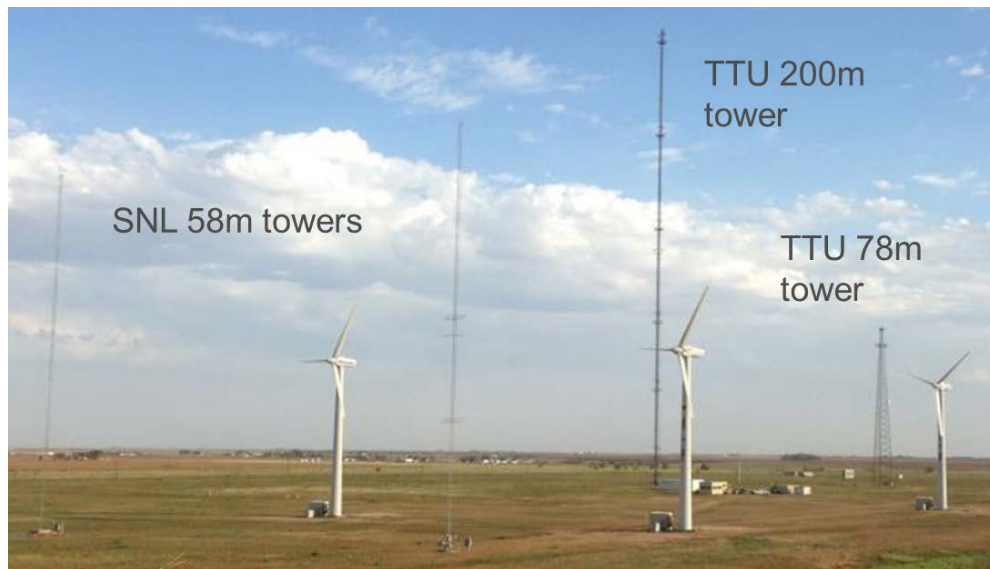


**Figure 3.1.** SWiFT Facility with Adjacent TTU Atmospheric Facilities

Historical data sets from this site are used to find the benchmark cases from TTU’s NWI facilities. The subset of TTU facilities used for this initial effort includes the 200 m meteorological tower, radar wind profiler (RWP), and data from the TTU operated West Texas Mesonet. Historical data from weather stations in the surrounding area from the DOE WFIP1 experiment were also available for analysis. The utilized TTU facilities are shown in Figure 3.2. The tall tower data are analyzed as described by Kelley and Ennis (2016) and used to identify potential cases. Raw data from the 200 m tower are saved at a sample rate of 50 Hz dating back to July 2012 for the current hardware configuration. The mesonet and sodar networks are used for mesoscale model reanalysis and to understand the regional atmospheric conditions. The West Texas Mesonet has historical data sets saved in 5 min logs for common atmospheric measurements and 15 min logs of surface/soil measurements. The RWP data are used to determine the geostrophic forcing that drives the microscale flow conditions. The RWP logs profiles of wind speed, direction, and radio acoustic sounding system (RASS) virtual temperature every 20 min, with a spatial resolution of 60 m between 150–2,000 m and 200 m between 600–6,000 m above ground level. The radar

profiler is approximately 540 m to the southeast of the 200 m tower. More information can be found on the NWI facilities in the facilities report by Hirth and Schroeder (2014).



**Figure 3.2.** Relevant TTU Atmospheric Facilities; 200 m Tower (left), Radar Profiler (center), and Mesonet (right)

The 200 m tower data set contains the most detailed atmospheric measurements for microscale simulation comparison. The tower has 10 stations ranging from 0.9 m to 200 m heights, and a sensor package as shown in Table 3.1. For wind speed and direction, the sonic anemometers are used as the more accurate measurement, which also provides turbulence quantification as a non-inertial measurement of velocity. Analog temperature and barometric pressure are used to calculate the potential temperature, and the relative humidity sensor is used with the calculated potential temperature to determine the virtual potential temperature for atmospheric stability characterization using the Bulk Richardson number. The Bulk Richardson number is calculated using gradients between the 2.4 and 10.1 m measurement stations.

**Table 3.1.** TTU 200 m Tower Instrumentation

Sensor Package	Tower Sensor Heights	
	[ft]	[m]
	3	0.9
	8	2.4
3D sonic anemometer with	13	4.0
virtual temperature, temperature,	33	10.1
relative humidity, barometric	55	16.8
pressure, and 3D propeller	155	47.3
anemometer*	245	74.7
	382	116.5
	519	158.2
	656	200.0

\*No propeller anemometers below 4.0 m

### 3.2 Case Selection and Description

The data used for case identification includes the range from June 23, 2012 to December 31, 2014, which contains 731 days of high-quality meteorological tower data where the complete measurement package was available. The data are used to search for quiescent diurnal cycles by first searching for a consistent 1 hour, near-neutral atmospheric stability condition, and then requiring that the surrounding 24 hours have

fairly consistent wind speed and wind direction, which was done to remove cases with significant frontal passages. The details of the case identification process and requirements are listed below.

Step 1: Add filters to identify consistent 1 hour, near-neutral stability cases:

- **Evening transitions only**; restrict to near-neutral cases occurring between 12:00–24:00 local time.
- **Near-neutral atmospheric stability**; Bulk Richardson average magnitude is less than 0.01, with the time series difference less than 0.01.
- **Relevance for wind energy applications**; wind speed 1 hour average at 47 m greater than 5 m/s; wind speed 1 hour average at 116 m less than 15 m/s.
- **Consistent wind speed**; wind speed time series difference less than 2 m/s at all heights.
- **Data quality assurance**; full resolution wind direction never from [110, 170] deg. to exclude the data affected by the meteorological tower wake.
- **Radar profiler data available**; only consider dates in which RWP data are available.

Step 2: Add filters to verify that the surrounding 24 hours have quiescent conditions:

- **Consistent wind speed**; difference in the average wind speed over 24-hrs is less than 15 m/s.
- **Consistent wind direction**; average wind direction standard deviation over 24 hrs is less than 40 deg.

After performing this analysis, there were 36 days that met the set of conditions above. Out of these candidates, two cases were selected for detailed testing and analysis of the different MMC approaches. The first case was the evening transition on November 8, 2013, which had fairly quiescent conditions. The second case was May 12, 2014 and included a frontal passage. Both of these cases were modeled and are reported on in later sections (sections 3.2, 5.5, and 5.6). In addition to these two selected cases, by relaxing some of the filter conditions, a third case that included thunderstorm outflow was also identified in the evening transition on September 9, 2014. This last case was not included in the modeling. The full data for these cases can be found on the DOE DAP website, <https://a2e.energy.gov/about/dap>.

### **3.2.1 Case 1: Quiescent Diurnal Cycle; November 8–9, 2013**

The team selected November 8, 2013 as the primary diurnal cycle case to model because it represents a quiescent day that includes typical morning and evening transitions and makes a good first test case with common conditions that are important for wind energy. The 1 hour, near-neutral transition is centered around 2230 UTC, with profiles shown in Figure 3.3. The diurnal cycle, convective-neutral-stable atmospheric transition is shown for the 24 hours centered on the near-neutral transition in Figure 3.4.

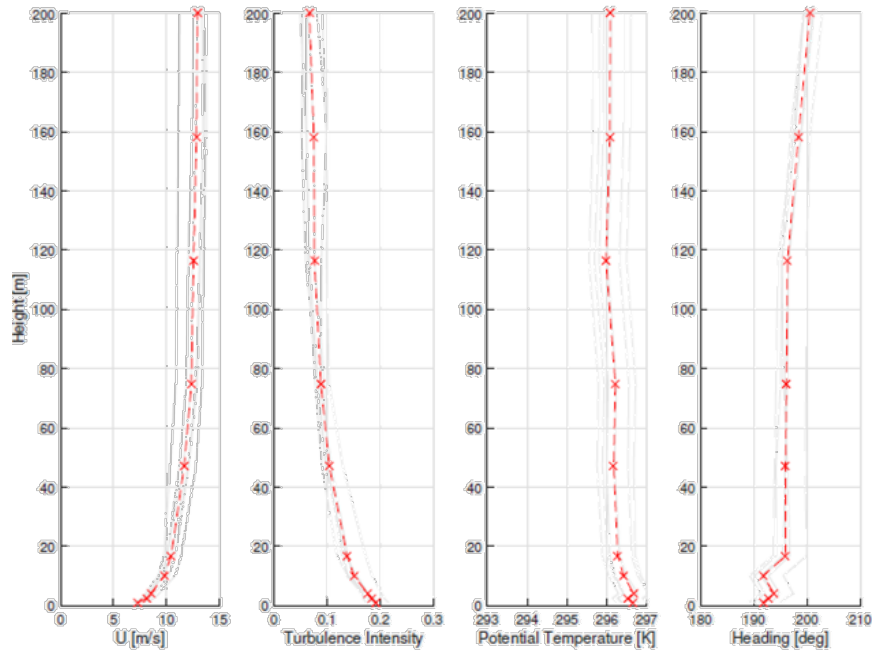


**Figure 3.3.** November 8–9, 2013 Near-Neutral Transition Profiles from the TTU 200 m tower. Gray profiles are the 10 min averages, and the red profile is the 1 hour average.

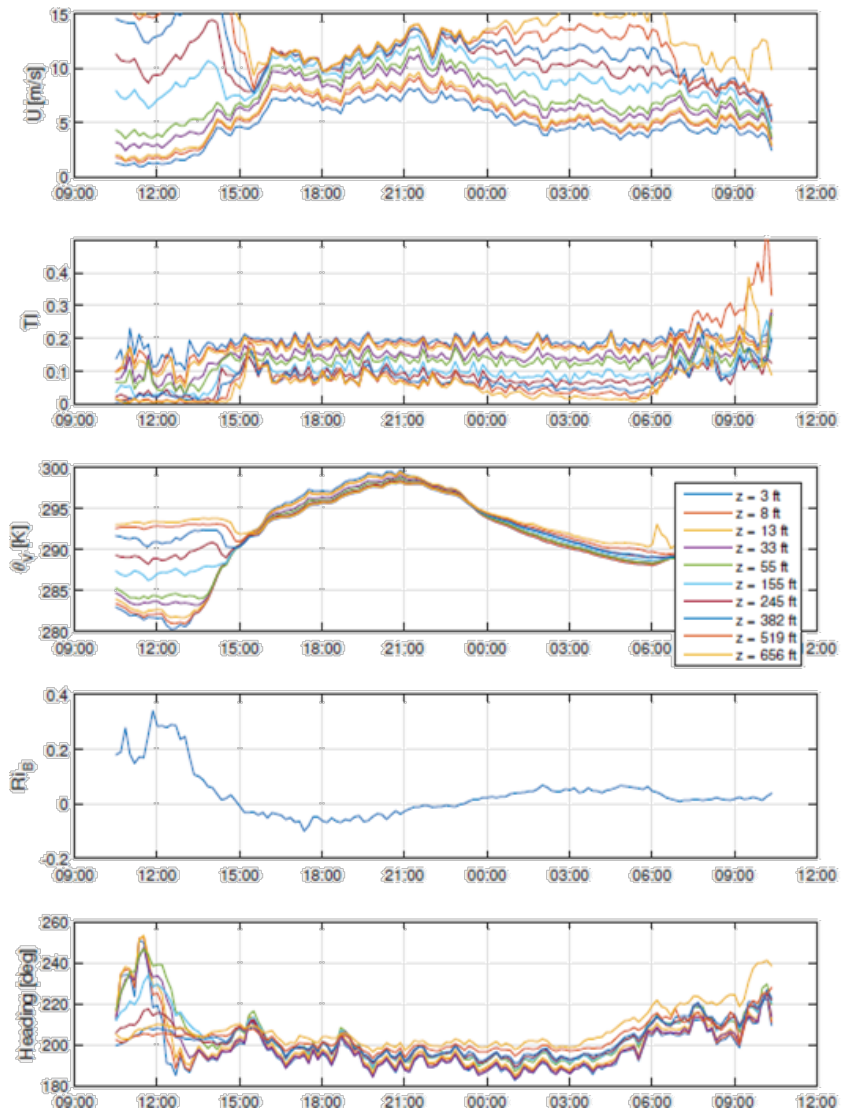


**Figure 3.4.** November 8–9, 2013 Diurnal Cycle Time-History

This period was marked by strong southwesterly winds over the West Texas panhandle and generally clear conditions (Figure 3.5). Data from the TTU RWP operated at the SWiFT site show that the winds at the lowest altitudes are consistently south-southwesterly over the course of the day (Figure 3.6).

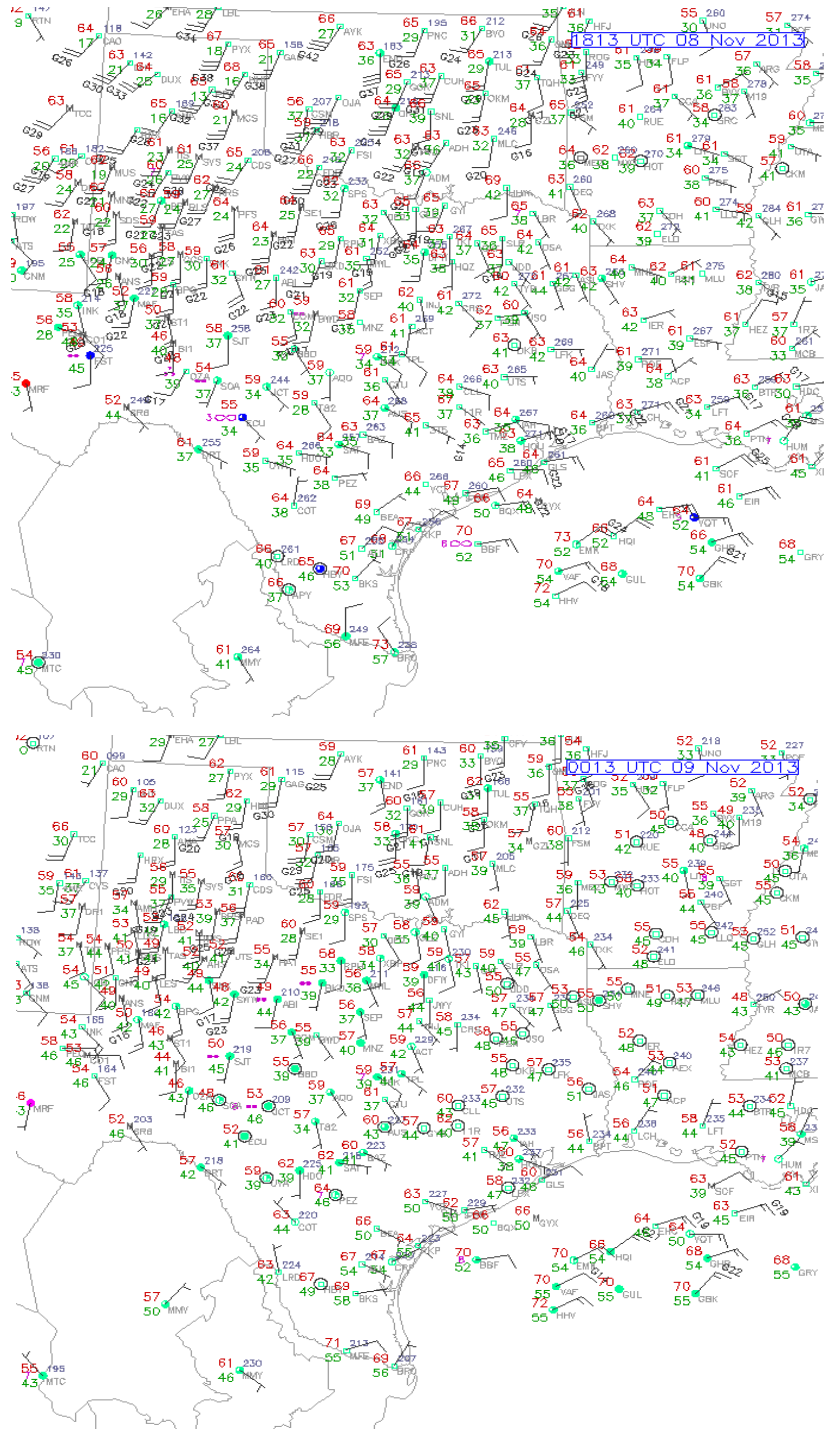


**Figure 3.5.** Surface Weather Map Valid at 1813 UTC (1213 CST) on November 8, 2013 (left) and 0013 UTC (1813 CST) on November 9 (right)

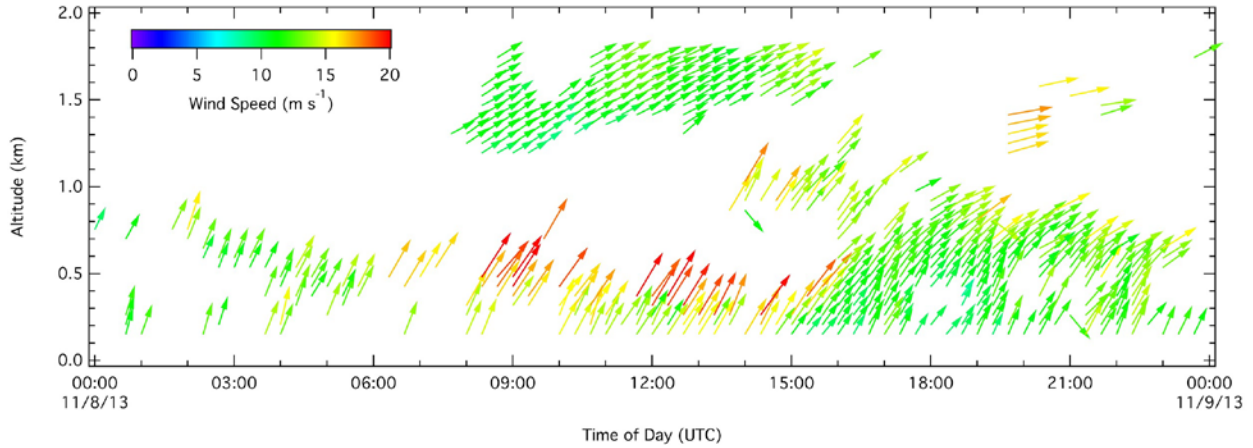


**Figure 3.6.** Time-Height Cross Section of Wind Speed and Wind Direction Measured at the TTU RWP for November 8, 2013

### 3.2.2 Case 2: Cold-Frontal Passage; May 12–13, 2014

A cold-frontal passage on May 12, 2014 was selected as a test case that is representative of periods with rapidly changing synoptic and mesoscale conditions that can have a large impact on both the wind resource and the operation of a wind farm. The near-neutral portion of this diurnal cycle is centered around 0130 UTC, but extends much further into the overnight portion, in which there is only a slightly stable overnight. The plots for the 1 hour near-neutral profiles and the surrounding diurnal cycle are shown in Figure 3.7 and Figure 3.8.

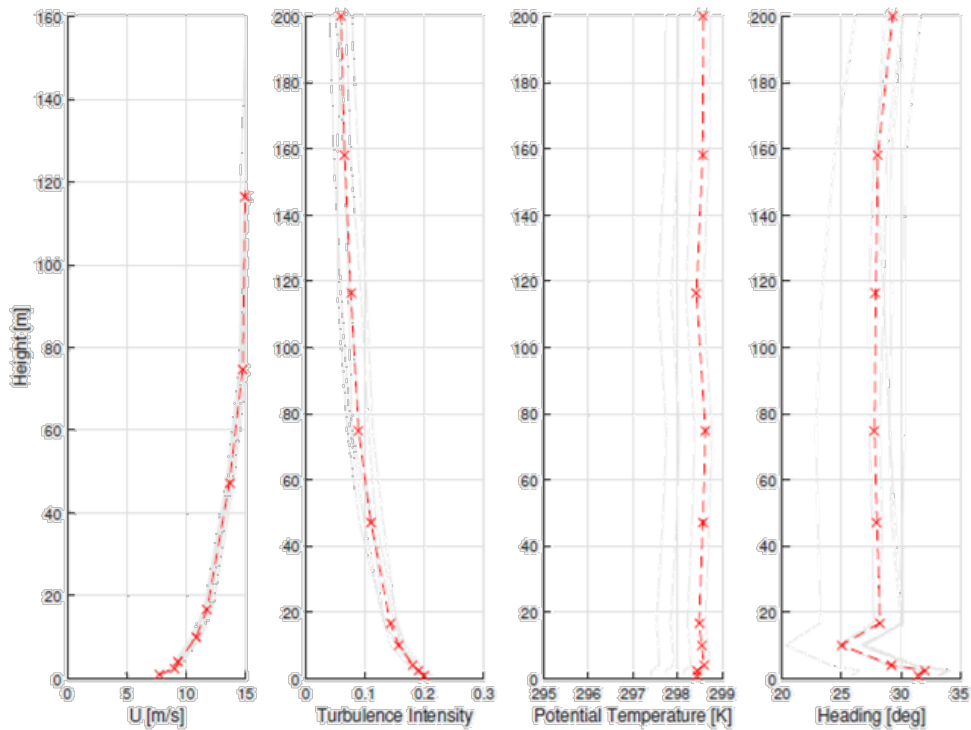


**Figure 3.7.** May 12–13, 2014 Near-Neutral Transition Profiles from the TTU 200 m tower. Gray profiles are the 10 min averages, and the red profile is the 1 hour average.

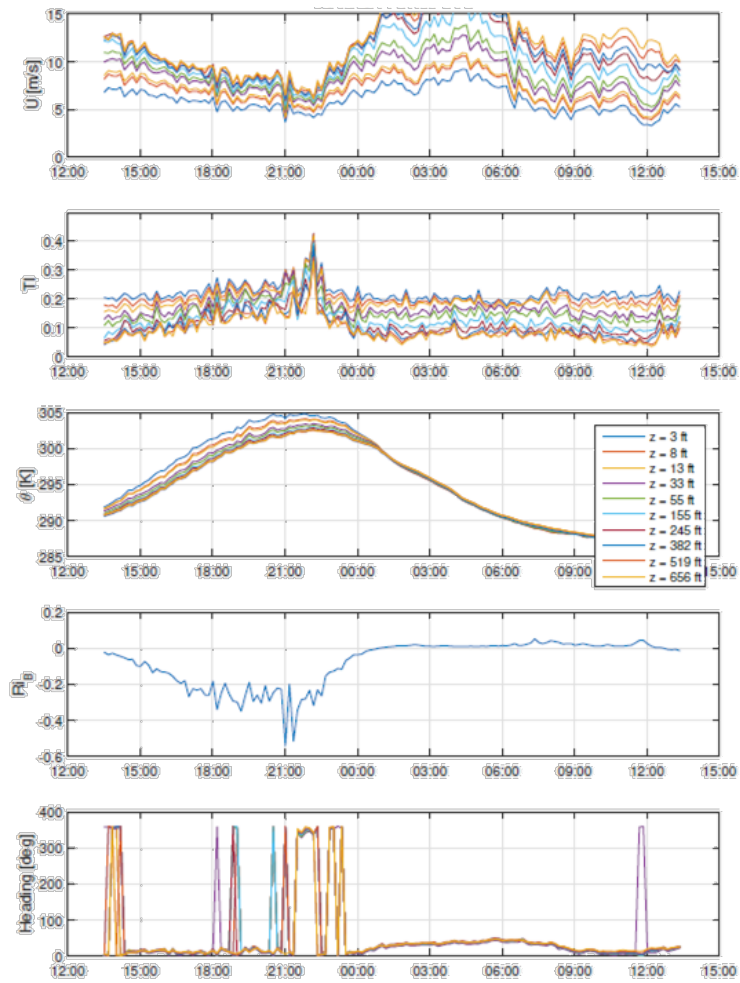


**Figure 3.8.** May 12–13, 2014 Diurnal Cycle Time-History

Early in the day on May 12, 2014, the winds over the SWiFT site were southerly ahead of the approaching cold front (Figure 3.9). Between 0800 and 0900 UTC, the winds shifted from southerly to northerly and there is a rapid decrease in temperature at the site, with strong northerly winds found behind the front. A time-height cross section of wind speed observed from the TTU RWP is found in Figure 3.10. Based on these observations, the front passes through the site around 0800 UTC, as indicated by the rapid change in wind direction at that time.

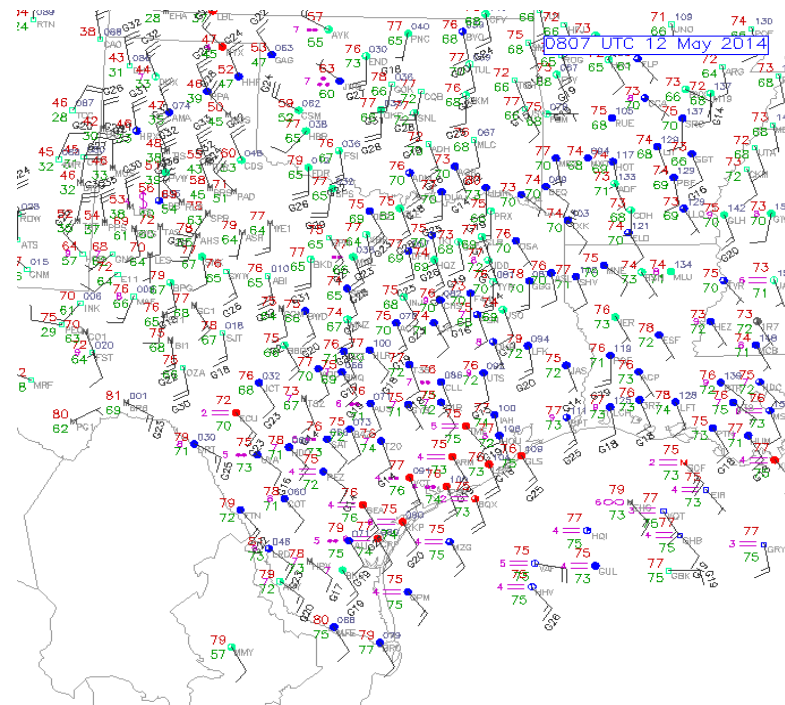
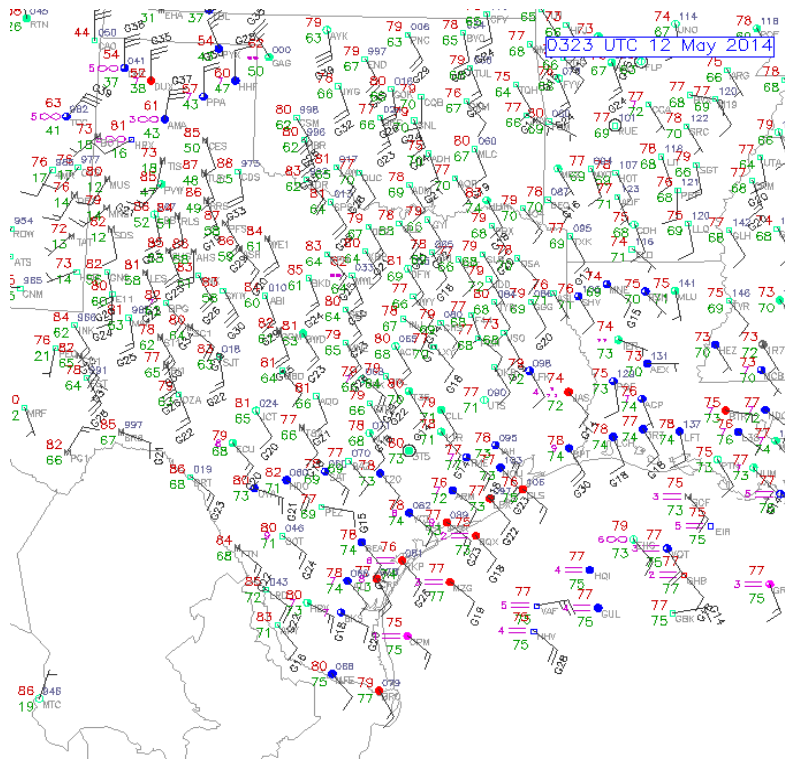


**Figure 3.9.** Surface Weather Map Valid at 0323 UTC (21:23 CST) on May 12, 2014 (left) and 0807 UTC (02:07 CST) on May 12, 2014 (right)

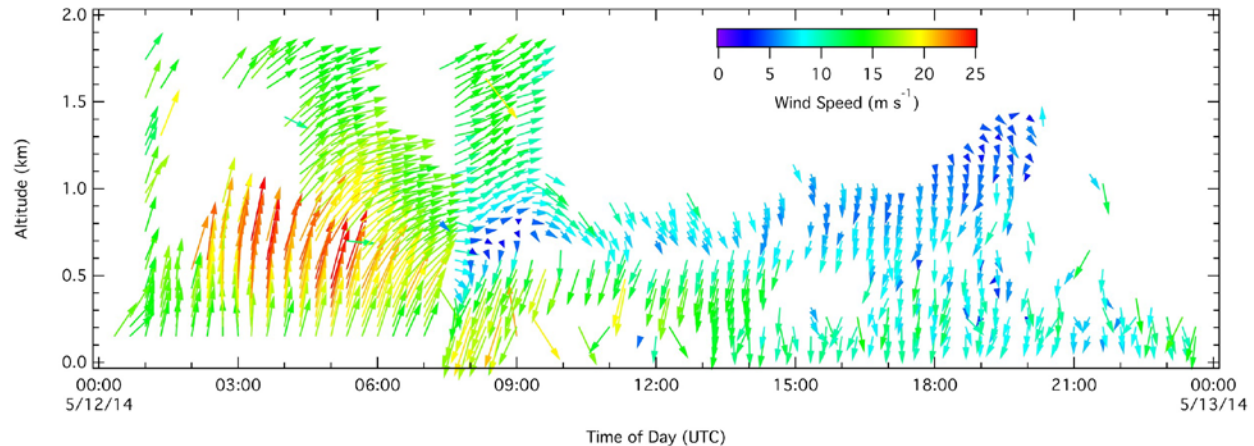


**Figure 3.10.** Time-Height Cross Section of Wind Speed and Wind Direction Measured at the TTU RWP for May 12, 2013

### 3.3 Metrics Plan

The focus of the metrics applied in year 2 is the assessment of the microscale models' ability to reproduce microscale features in wind, temperature, turbulence, and associated variables, including spectra and cospectra. Given that the goal is to model a nonstationary period with a diurnal cycle or frontal passage, the ability of the microscale model to capture the transitions from the mesoscale model input is emphasized.

The models were assessed relative to observations at the SWIFT site, which are considered verification data for the exercise. Profiles available from the 200 m tower were used for the assessment.

Assessments were made based on observations made on November 8, 2013, as well as other potential case studies, including May 12, 2014. The goal is to simulate the diurnal evolution of surface heat flux, wind speed and direction, potential temperature, and TKE profiles. In addition to the diurnal evolution, the assessment focused on three periods of the diurnal cycle, identified as:

- stable conditions,
- near-neutral conditions associated with the evening transition, and
- unstable/convective conditions.

For the entire diurnal period, modeling teams provided 1 min temporal resolution data at the coordinates of the tower for predefined vertical levels. Modeling teams provided relevant variables (velocity components  $[u, v, w]$ , potential temperature  $\theta$ , and SGS TKE, when available) at the native vertical resolution. For three periods characterized by different stability conditions, nominal temporal resolution from the microscale models for computation of spectra, and other variables were 1 s. Derived variables were assessed at averaging times as specified in Table 3.2. High temporal resolution data was saved for 60 min starting at 0400 UTC for stable conditions, 90 min starting at 2130 UTC for neutral conditions, and 120 min starting at 1800 UTC for convective conditions to allow for a sufficient number of eddy turnovers. For relevant variables, NCAR will evaluate the time series of each variable and compare the mean, median, and standard deviation, and possibly other summary measures, with the observational data using the metrics in Table 3.2. Confidence intervals can be used where appropriate to quantify uncertainty and evaluate differences between distributions and statistical measures. Taylor diagrams could be used to

summarize continuous verification results (e.g., root mean square error [RMSE]), and performance diagrams could be used to summarize verification of event statistics

Variables to be assessed include the following.

- Wind speed at each level of wind speed measurement of the tower or range gate of the profiler.
- Wind direction at each level of wind measurement of the tower or range gate of the profiler.
- Temperature at each level of measurement of the tower or range gate of the profiler.
- TKE at each level of wind measurement of the tower.
- Velocity spectra at each level of wind speed measurement of the tower; NCAR personnel computed spectra based on data supplied by modeling teams.
- Velocity cospectra ( $Co(u,w)$ ) and vertical/horizontal wind speed joint spectra ( $Co(v,w)$ ) at each level of wind speed measurement of the tower; NCAR personnel computed cospectra based on data supplied by modeling teams.
- Boundary layer depth—the verifying measurement was the depth determined by Pacific Northwest National Laboratory (PNNL) personnel based on wind profiler data (the ABL depth from simulation output defined as the level where, starting from the surface, turbulent stress ( $\langle uw \rangle$ ) crosses the zero line for the first time for the convective case or as the level of the peak of the jet for stable cases).
- Surface flux of heat at tower coordinates.
- Surface flux of momentum at tower coordinates.
- Turbulent spatial coherence, which will be evaluated depending on data availability from nearby towers.

**Table 3.2.** Metrics used for Evaluation of Variables

Variable	Averaging Period	Basic Metrics	Additional Metrics
Wind speed time series – mean, median, stdev	10 min	RMSE, mean absolute error (MAE); statistics associated with time series differences	Distribution, deviation from profile (integrated area in error curve)
Wind direction	10 min	RMSE, MAE; statistics associated with time series differences	RMSE in area of profile Ekman spiral “hodograph”
Temperature	10 min	RMSE, MAE; statistics associated with time series differences	Distribution, deviation from profile (integrated area in error curve)
TKE	10 min	RMSE, MAE; statistics associated with time series differences	Distribution, deviation from profile (integrated area in error curve)
Velocity spectra	10/15/20 min time series then spectra averaged over 60/90/120 min periods <sup>a</sup>	Frequency of peak, match to slope, frequency of drop-off	Differences in areas under curves, and statistical uncertainty information, as available

<b>Variable</b>	<b>Averaging Period</b>	<b>Basic Metrics</b>	<b>Additional Metrics</b>
Velocity cospectra	10/15/20 min time series then spectra averaged over 60/90/120 min periods <sup>a</sup>	Frequency of peak, match to slope, frequency of drop-off	Differences in areas under curves, and statistical uncertainty information, as available
ABL depth	10 min	MAE	TBD
Heat flux	10 min	MAE	TBD
Momentum flux	10 min	MAE	TBD
Nondimensional shear in surface layer	10 min	MAE	TBD
Shear across the rotor (40 m–120 m)	10 min	MAE	TBD
Veer across the rotor (40 m–120 m)	10 min	MAE	TBD
Turbulence intensity across the rotor (40 m–120 m)	10 min	MAE	TBD

<sup>a</sup> averaging period for stable / neutral / convective periods respectively.

## 4.0 Analyzing the *terra incognita*

Boundary-layer parameterizations used in the current generation of mesoscale models utilize the assumption that no turbulent eddies are explicitly resolved. This assumption can be violated when the horizontal resolution of the mesoscale model is shrunk past some critical value, the so-called “*terra incognita*” (Wyngaard 2004). At this point, some, but not all, aspects of the eddies are explicitly resolved by the mesoscale model in a way that is independent of the turbulence parameterization, leading to erroneous results.

### 4.1 Qualitative Evidence from Plots

The *terra incognita* is important in the context of MMC, particularly when using a model configuration that includes nesting. In such an application, the horizontal grid spacing of one or more of the nested mesoscale domains is likely to fall within the *terra incognita*. For example, Rai et al. (2016) show that their nested simulations produce unrealistic oscillations in the wind speed when using the Mellor-Yamada-Nakanishi-Niino (MYNN; Nakanishi et al. 2004) parameterization and horizontal grid spacing of 1.2, 1.0, and 0.8 km (Figure 4.1). Based on their analysis of this case over complex terrain, they configured the horizontal grid spacing of their domains such that the finest mesoscale domain utilized a horizontal grid spacing of 1.37 km and the coarsest LES domain applies a horizontal grid spacing of 0.27 km. These particular values are likely case specific, and it may be critical to make the horizontal grid spacing of the mesoscale domain greater than the boundary-layer depth.

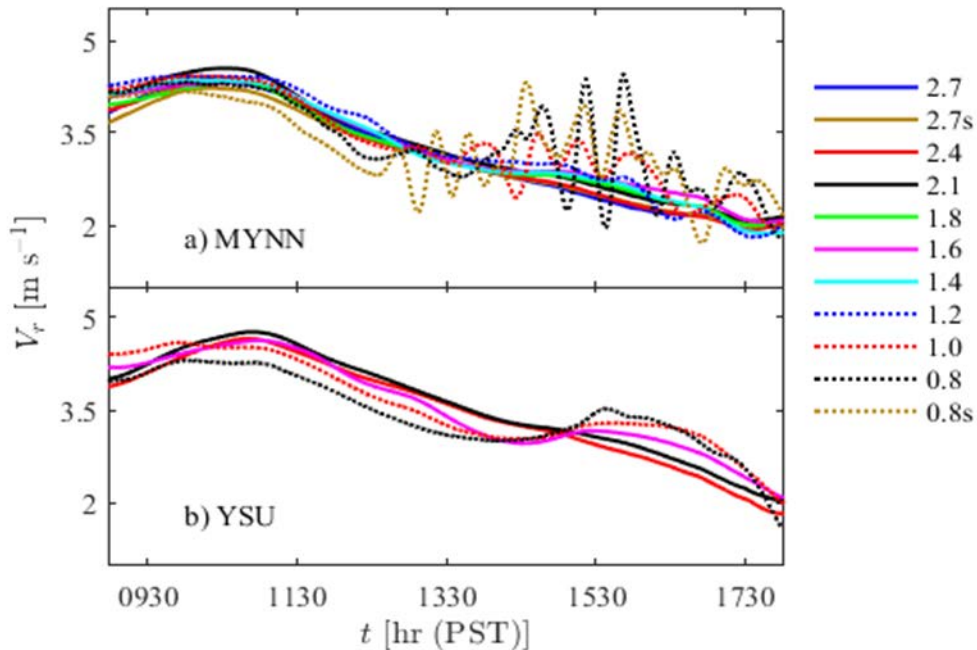


**Figure 4.1.** Time Series of Wind Speed Obtained from Locations within the LES Domain used by Rai et al. (2016) using the a) MYNN PBL Scheme and b) YSU PBL Scheme for Different Horizontal Grid Spacing (colors). The lines for “0.8s” and “2.7s” indicate WRF model simulation.

Additional effort to investigate the impact of the *terra incognita* included a sensitivity study at the SWiFT site, using two WRF PBL parameterizations at horizontal resolutions less than the typical 3–5 km, namely

at 3 km, 1 km, and 333 m. The aim was to tease out potential issues in terms of wind speed and turbulence characteristics that may result from using grid spacing within the *terra incognita* in an area with simple terrain.

The efforts included WRF simulations for the case study of November 8, 2013, which was identified by the MMC team and is described in section 3.2.1. This day is marked by relatively quiescent conditions and has a nice diurnal cycle with atmospheric stability conditions ranging from a dry convective boundary layer, a clean transition to a neutral boundary layer at 2230 UTC, to the onset of stable conditions during the nighttime (see Figure 2.3). Looking at the entire diurnal cycle should indicate *terra incognita* issues at different times of the day, because turbulence length scales, boundary layer (PBL) height, and the scale of the *terra incognita* change within a diurnal cycle.

The WRF setup is similar to that used in FY15 efforts (Haupt et al. 2015). The effort used 88 vertical levels, with 5–10 m vertical grid spacing in the lower levels of the atmosphere, including the turbine layer. Global Forecast System (GFS) Final analyses were used as boundary conditions. The model was run from November 8, 2013 at 00 UTC to November 10, 2013 at 00 UTC. The first 12 hours were discarded to eliminate model spin up. Output from the 10 min instantaneous model from three domains (with grid spacing of 3, 1, and 0.333 km) using the MYNN and YSU turbulence parameterizations was used for the analyses presented here. The MYNN scheme was chosen because it is currently being extensively modified within the WFIP 2 project, and because it is a local TKE-based scheme. The YSU scheme was chosen because it is a widely used scheme, is available in MPAS, and is nonlocal and first order. In contrast to the MYNN parameterization, the YSU scheme is not TKE-based. The YSU scheme has been found to behave differently in the *terra incognita* than TKE-based models (Ching et al. 2014).

The findings from the MYNN PBL scheme are shown in Figure 4.2 and Figure 4.3. In general, for Domain 3 (horizontal grid spacing of 3 km, which is outside the *terra incognita*), the model output is smoother than observed for all quantities (Figure 4.2). The simulated diurnal cycle of vertical wind speed is uniform, and the deviations to the observations might derive from the wind sensor being tilted. For most other quantities, there is good agreement between the simulation and observations. For the formal microscale verification (described in section 5.0), the sensor tilt was calculated and then removed for the computation of the turbulence quantities.

In Domain 5 (Figure 4.3), with a grid spacing of 333 m (which is within the *terra incognita*), the same characteristics are found in terms of matching the diurnal cycle; however between ~20 – 00 UTC (14-18 local standard time) on November 8 and 9, the simulations (green) exhibit some noise (or wiggles). This behavior is most pronounced for vertical wind speed, horizontal wind speed, TKE, surface flux of momentum, and boundary layer depth. The temperature shows some noise as well during that time. The wiggles in PBL depth are assumed to be a coincidental agreement, and MMC team members have seen similar signals in the PBL depth in previous *terra incognita* simulations. Domain 4 shows similar behavior to that of Domain 5 (not shown), indicating *terra incognita* issues even at a grid spacing of 1 km. Note that PBL depth drops below 1 km during this time period.

Next, the patterns of wind speed in the region are considered by looking at planar plot views. Figure 4.4 to Figure 4.7 show wind speeds at 117 m in the 36 x 21 km surrounding the SWiFT site. Overlaid in these figures is the grid spacing. Figure 4.4 shows horizontal wind speeds at 21 UTC, which is within the time window where the noise occurs in the time series (Figure 4.2). The wind field is smooth in Domain 3, but exhibits horizontal rolls in Domain 4, which become more distinct in Domain 5. The same is partially true for 18 UTC (Figure 4.5); however, no rolls or cells are observed during the stable conditions throughout the night hours of November 9 (not shown). The rolls span the domain and affect all the wind and turbulence parameters, as well as the heat flux, PBL depth, and pressure (not shown). These findings agree with those of Ching et al. (2014), who found that convectively induced secondary circulations

develop in the *terra incognita* when the PBL depth is of the same order of magnitude as the length scales. They also state that wind fields of modeled convectively induced secondary circulations impact surface fluxes and complicate the interaction between the resolved physics and subgrid physics.

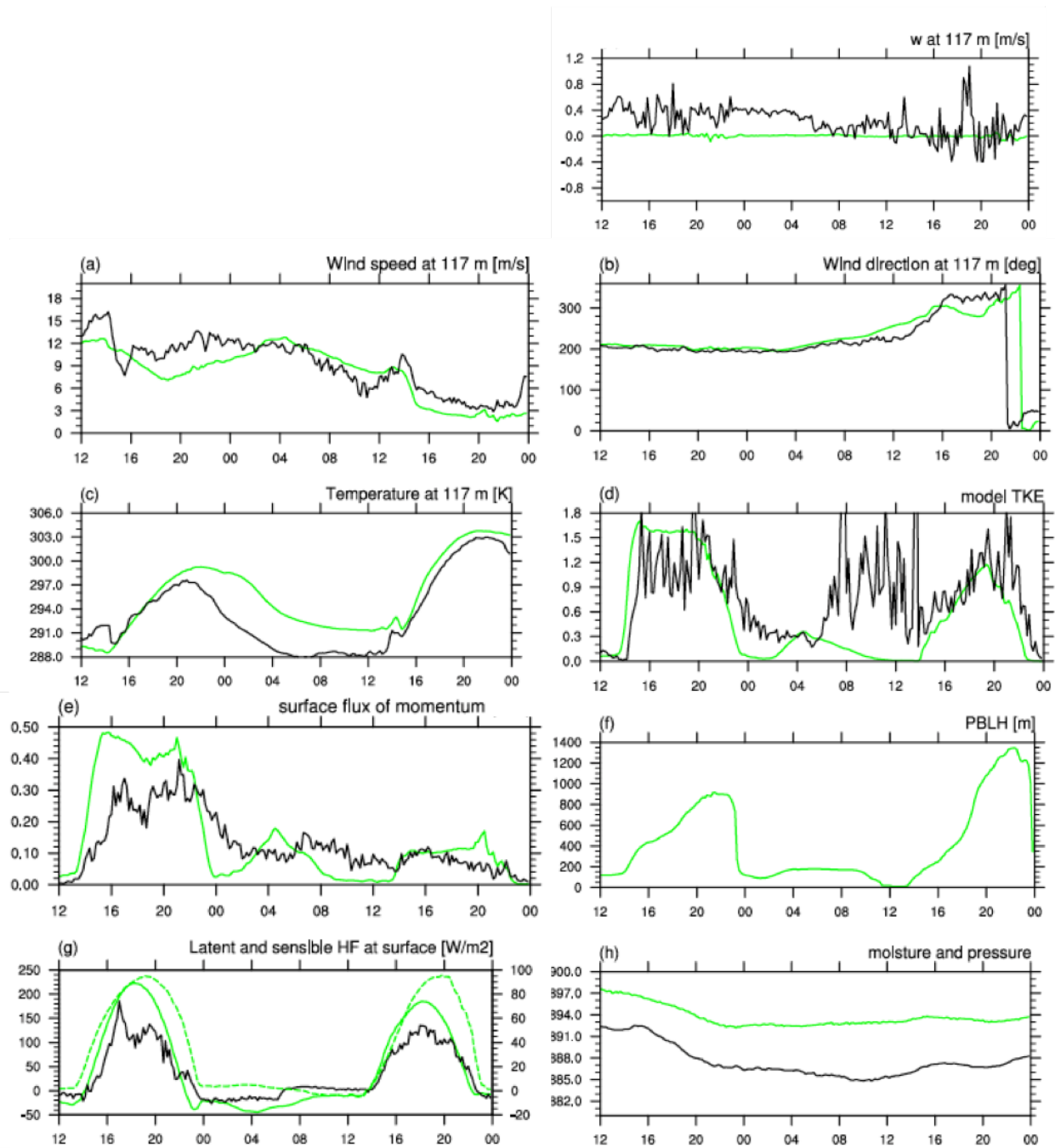


**Figure 4.2.** Time Series of (top right) Vertical Wind Speed at 117 m, (a) Horizontal Wind Speed at 117 m, (b) Wind Direction at 117 m, (c) Potential Temperature, (d) TKE, (e) Surface Momentum Flux, (f) Simulated Boundary Layer Depth, (g) Simulated Latent Heat Fluxes (dashed lines and y-axis on right) and Sensible Heat Fluxes (solid), and (h) Pressure at 117 m. Simulations use the MYNN PBL scheme and are in green, observations in black. Valid for Domain 3 with a grid spacing of 3 km.

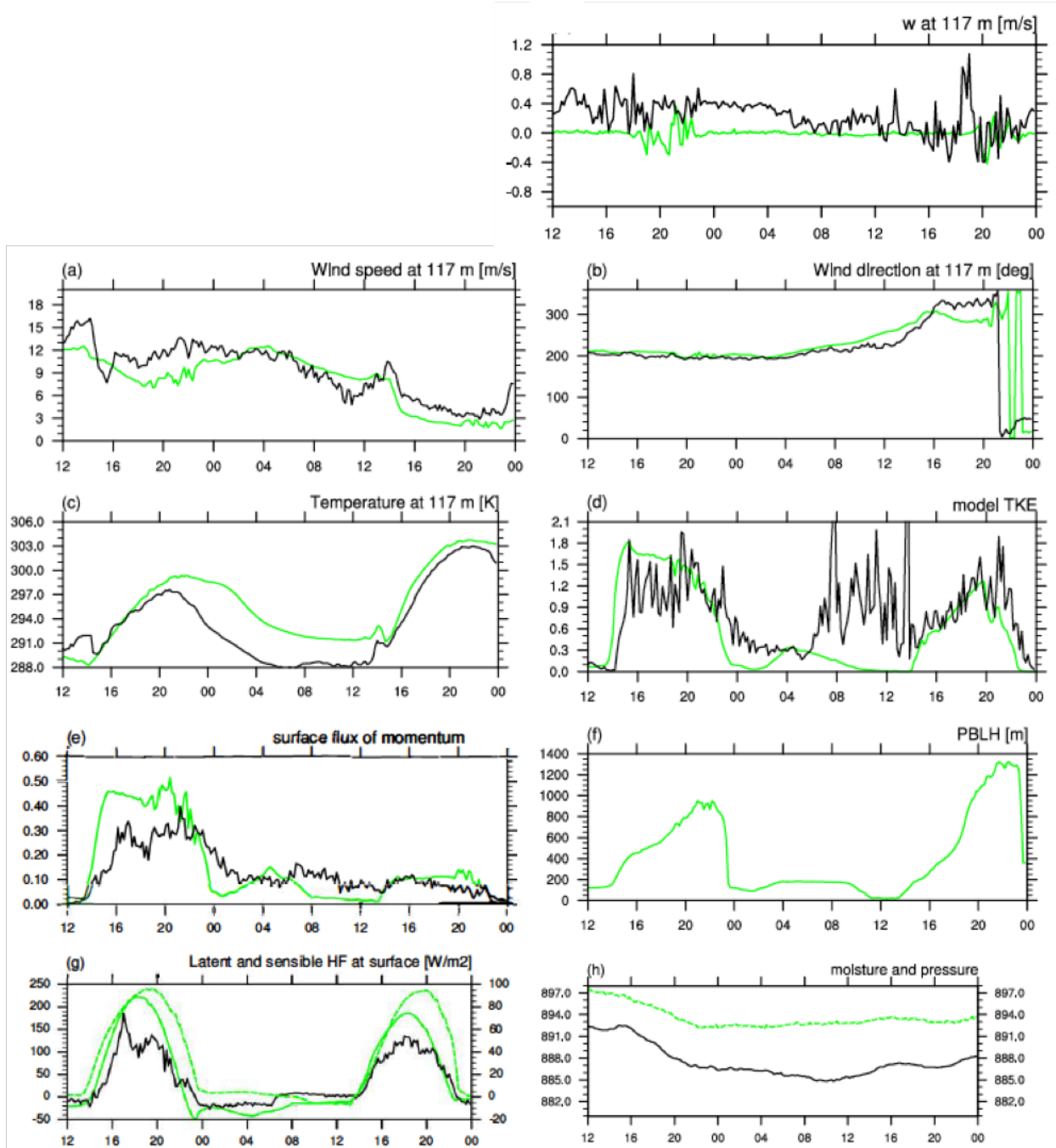


**Figure 4.3.** Time Series of (top right) Vertical Wind Speed at 117 m, (a) Horizontal Wind Speed at 117 m, (b) Wind Direction at 117 m, (c) Potential Temperature, (d) TKE, (e) Surface Momentum Flux, (f) Simulated Boundary Layer Depth, (g) Simulated Latent Heat Fluxes (dashed lines and y-axis on right) and Sensible Heat Fluxes (solid), and (h) Pressure at 117 m. Simulations use the MYNN PBL scheme and are in green, observations in black. Valid for Domain 5 with a grid spacing of 333 m.

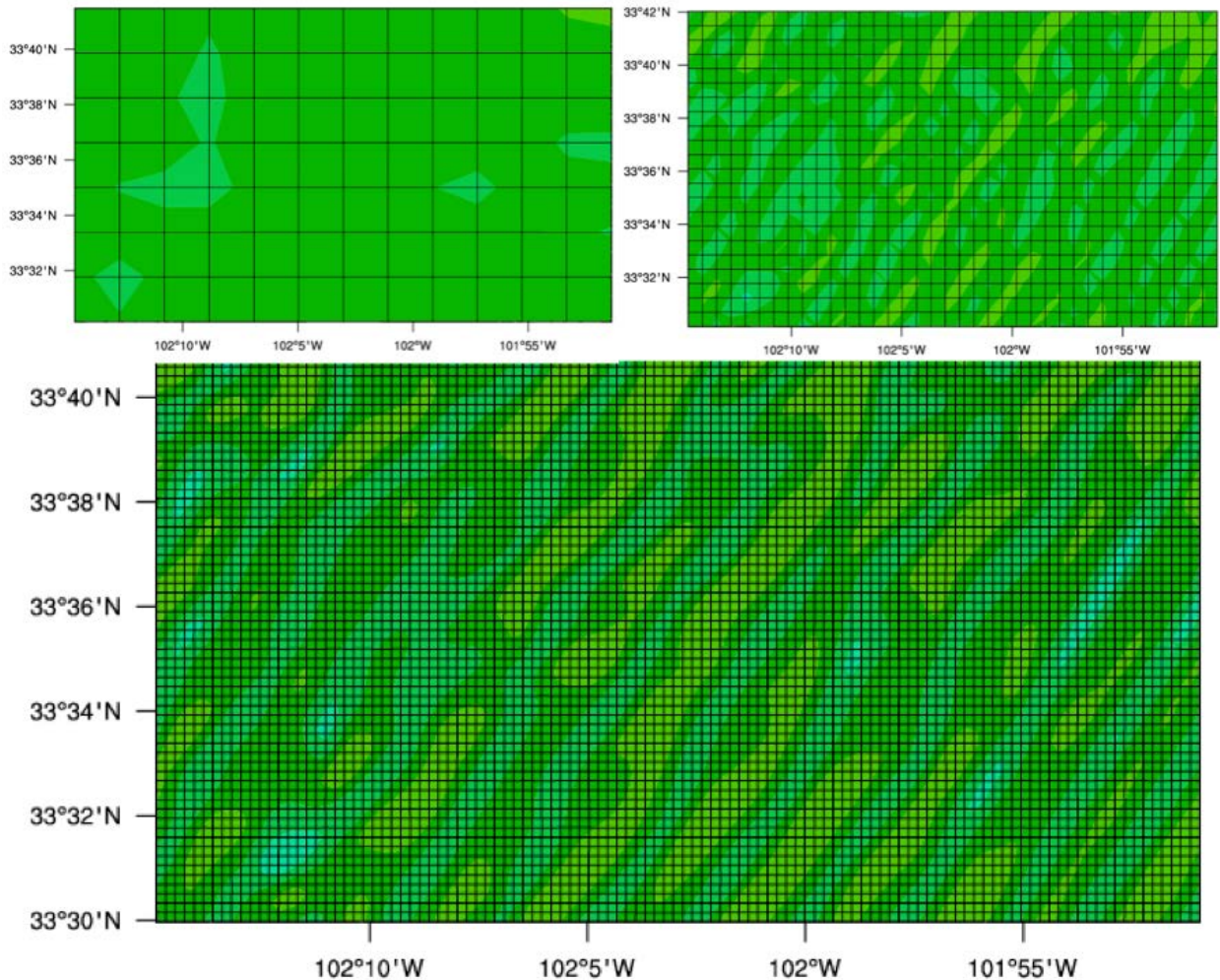


**Figure 4.4.** Horizontal Wind Speed at 21 UTC on November 8, 2013 at 117 m in Domain 3 (top left), Domain 4 (top right), and Domain 5 (bottom). All the plots portray the same horizontal extent of 36x21 km. Colors are in 1 m/s increments.

Spectra of horizontal and vertical wind speed show how energy is resolved (or not) by the model in the three domains, and can be compared to the observations. Figure 4.6 shows that the amount of energy captured by the model is much smaller than is observed, which is expected in a mesoscale model at the frequencies that are plotted. A mesoscale model does not resolve the energy associated with the small-scale features of the flow. In addition, it can be observed that the amount of energy is a function of the stability regime, also across grid spacing. During the transition period, the resolved energy is similar to the observations, which is likely due to the energy created by the rolls and cells in Domain 5. Even though the simulated time series of wind speed exhibit more energy at this finer resolution and compare better with the observations, this increase of energy occurs for the wrong reasons and would lead to erroneous input into a microscale model. In contrast, runs with the YSU scheme (Figure 4.7) do not exhibit these rolls (again, in line with Ching et al. 2014), and the YSU spectra shows the expected behavior (Figure 4.8); for each regime and in each domain, the resolved energy is smaller than in the observations due to the lack of ability of the mesoscale model to resolve those microscale features.

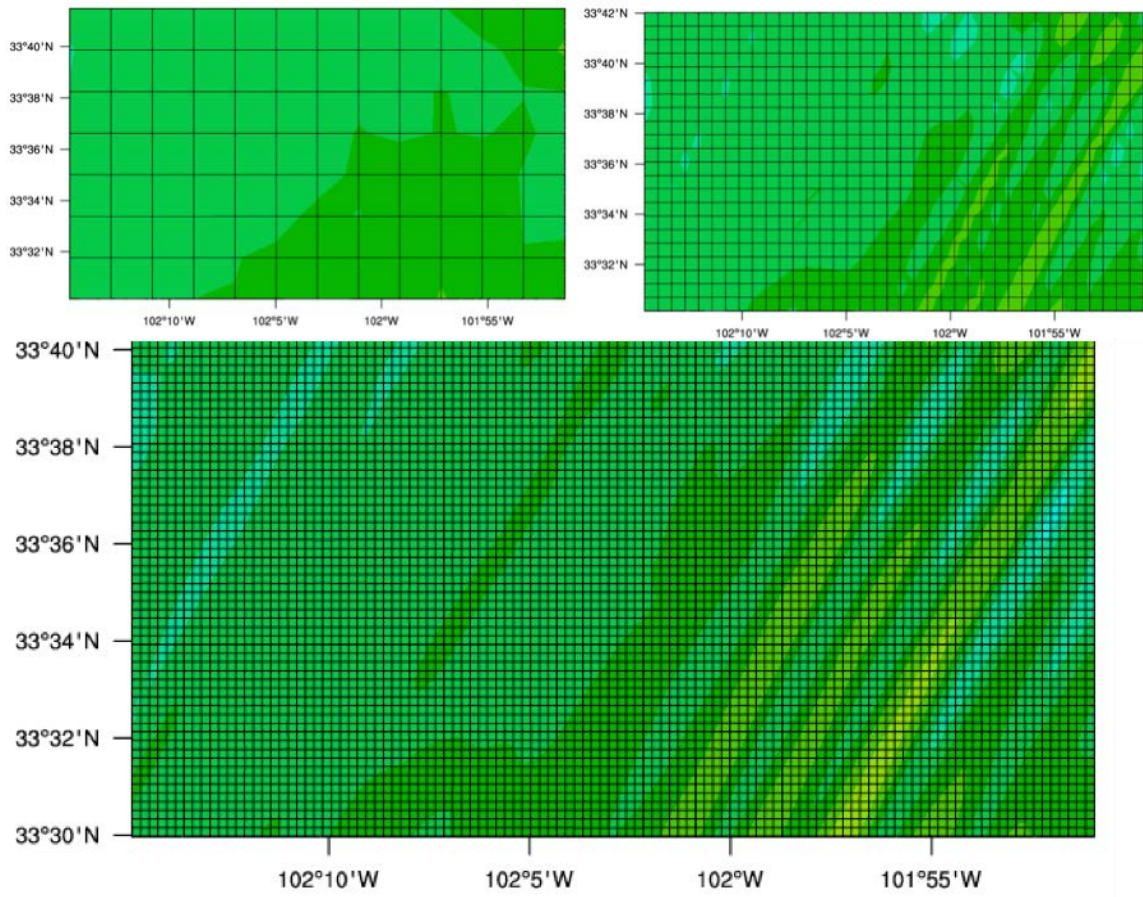


**Figure 4.5.** Horizontal Wind Speed at 18 UTC on November 8, 2013 at 117 m in Domain 3 (top left), Domain 4 (top right), and Domain 5 (bottom). All the plots portray the same horizontal extent of 36 x 21 km. Colors are in 1 m/s increments.

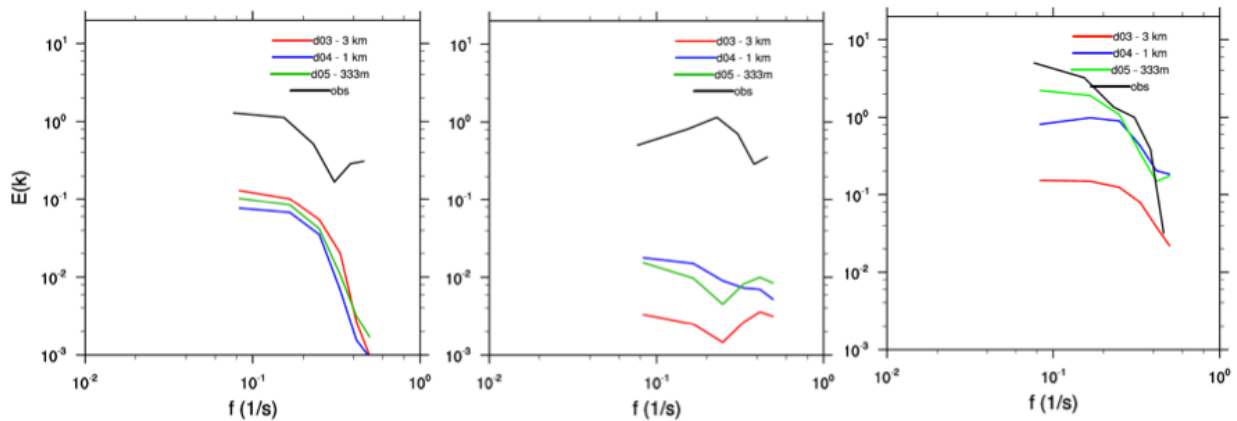


**Figure 4.6.** Spectra of Horizontal Wind Speed for Two Hours during Stable Conditions between 4 and 6 UTC on November 9 (left), the Convective Conditions between 1600 and 1800 UTC on November 8 (middle), and the Transition between 2000 UTC and 0000 UTC on November 8 (right). The observations are shown in black, simulations with the MYNN PBL scheme for Domain 3 in red, Domain 4 in blue, and Domain 5 in green.

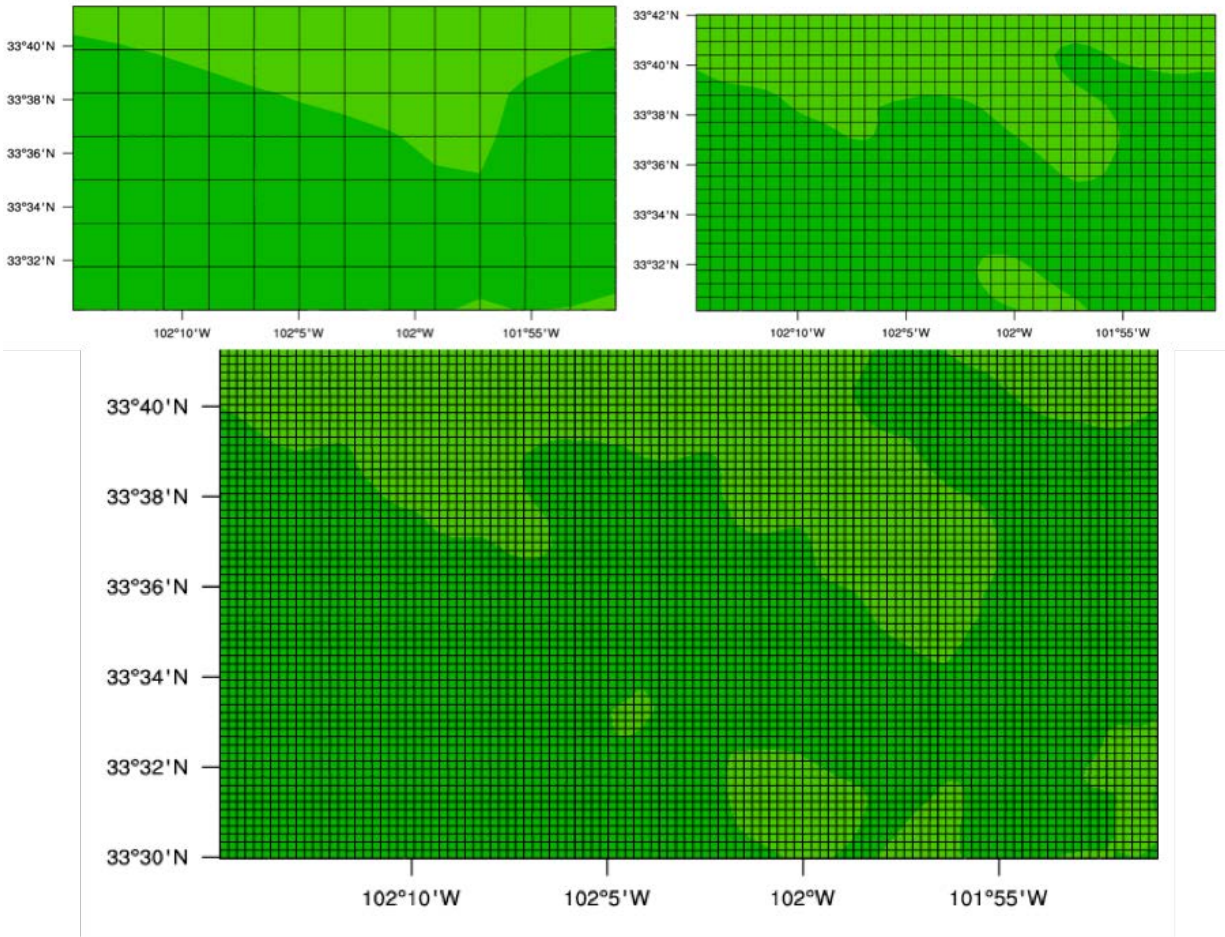


**Figure 4.7.** Horizontal Wind Speed at 2100 UTC on November 8, 2013 at 117 m in Domain 3 (top left), Domain 4 (top right), and Domain 5 (bottom) for Simulations with the YSU Boundary Layer Scheme. All the plots portray the same horizontal extent of 36 x 21 km. Colors are in 1 m/s increments.

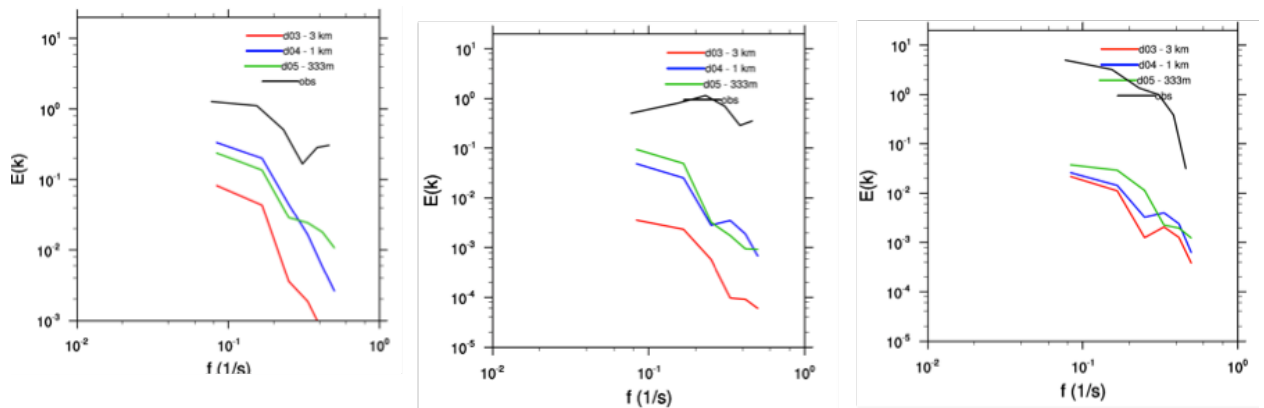


**Figure 4.8.** Spectra of Horizontal Wind Speed for Two Hours during Stable Conditions between 0400 and 0600 UTC on November 9 (left), the Convective Conditions between 1600 and 1800 UTC on November 8 (middle), and the Transition between 2000 UTC and 0000 UTC on November 8 (right). The observations are shown in black, simulations with the YSU PBL scheme for Domain 3 in red, Domain 4 in blue, and Domain 5 in green.

The analysis shows that during the time when the rolls developed, a superadiabatic layer formed in the simulations at the surface (Figure 4.9), similar to the results presented by Ching et al. (2014). While the virtual potential temperature profiles show near-neutral lapse rates (straight vertical lines) in the boundary layer in the 3 km domain, the profiles for the 333 m domain maintained a superadiabatic lapse rate throughout the boundary layer (Figure 4.10; compare to Fig. 6 in Ching et al. 2014). For the YSU simulations, straight vertical lines indicate a neutral stratification throughout the boundary layer. This behavior is very likely attributed to the difference in the two schemes. While the MYNN scheme is based on the assumption of downgradient diffusion, where vertical fluxes are negatively proportional to the local vertical gradient, the YSU scheme uses nonlocal mixing through entrainment fluxes; these fluxes do not depend on the local vertical gradient.

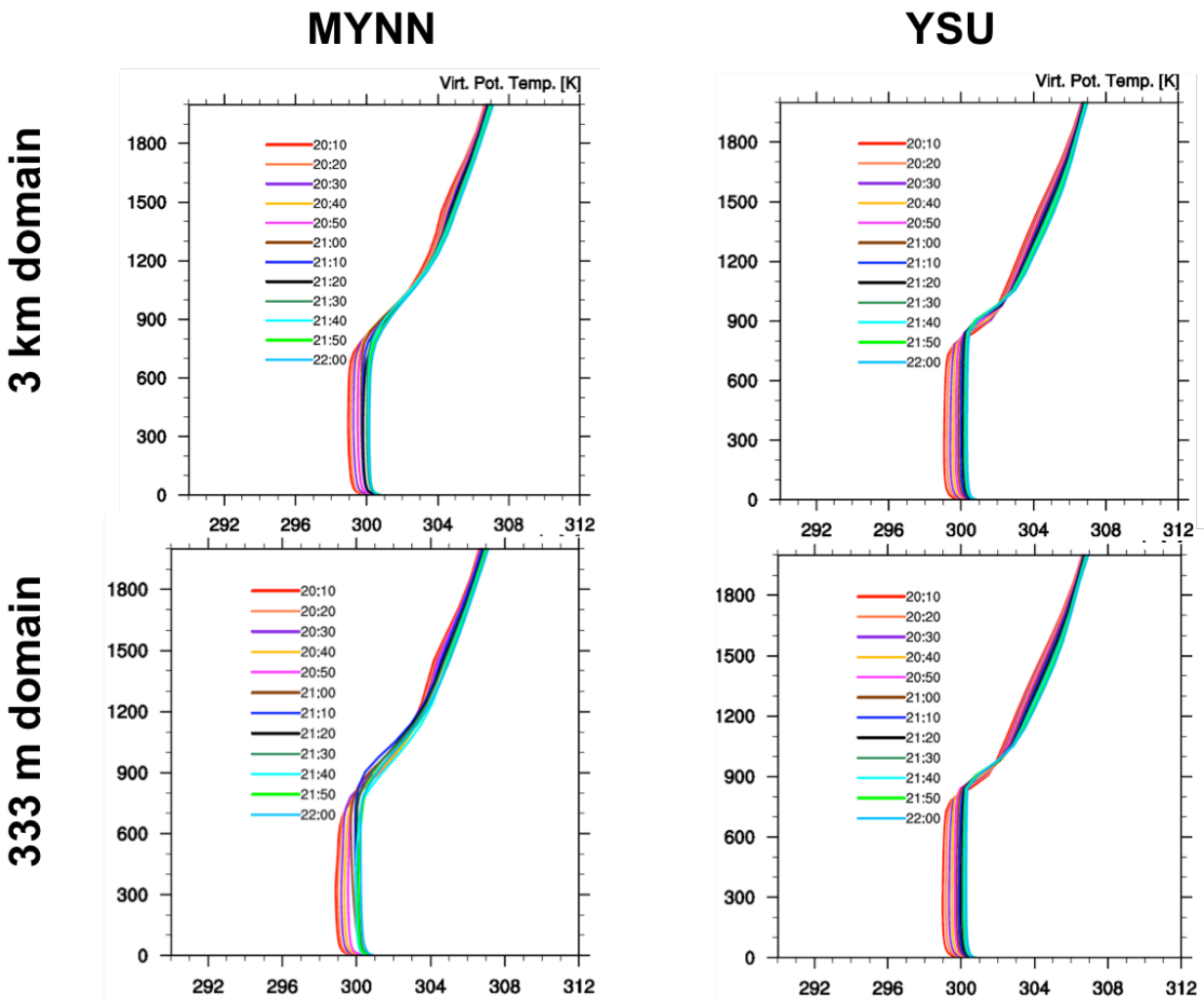


**Figure 4.9.** Vertical Profiles of Virtual Potential Temperature for the MYNN Boundary Layer Scheme (left column) and YSU Scheme (right column) for the Domain with 3 km Grid Spacing (upper row) and 333 m Grid Spacing (bottom row)

The results show that unrealistic rolls and cells form when using *terra incognita* grid spacings of 1 km and 333 m when using the MYNN PBL scheme and during convective/neutral atmospheric stability conditions. However, when using the YSU boundary layer scheme, no *terra incognita* issues were found; this is in line with previous findings. However, as Ching et al. (2014) point out, this observation is due to

the fact that the YSU scheme uses a downgradient diffusion with an additional nonlocal term to account for countergradient transport that in turn accounts for the turbulent fluxes. Although this might avoid the spurious convective rolls, it may not necessarily imply that it is more correct.

The issues associated with the *terra incognita* are challenging to providing accurate boundary or forcing conditions to the microscale model. One approach is to carefully select the mesoscale model grid spacing so as to avoid *terra incognita*, which will require a more careful definition of the scale of that region during different conditions. A second promising approach is to use new parameterizations, such as the new 3D-PBL scheme, which is currently under development by NCAR and the National Oceanic and Atmospheric Administration within the WFIP2 project. It is recommended to test the cases discussed herein with these new 3D-PBL schemes. The current analysis should also continue to look at more quantities (e.g., profiles of shown quantities, analyzing model output from time-steps rather than 10 min output), and then be carried it out in complex terrain.

## 4.2 Formal Assessment

A formal assessment of the mesoscale model runs was performed for the November 8 case from the GFS-forced WRF simulations using the MYNN and the YSU boundary layer parameterizations; LES was not considered here, only the mesoscale model output. Three model resolutions (domains) were analyzed: 3,000 m, 1,000 m, and 333 m. To produce the matched pairs for the formal comparison, the closest gridpoint to the SWiFT tower site from the WRF model output was chosen and vertical levels were linearly interpolated to match the tower levels. Unfortunately, because the analysis is limited to the observation location at the tower, it is not possible to evaluate the spatial structure of the wind field; only characteristics of the time evolution of the variables and the vertical structures at the tower can be considered.

The variables assessed were virtual potential temperature (VPTMP), wind speed, and wind direction. The assessment included examining and comparing vertical profiles and time series, as well as evaluating some basic verification metrics.

For these analyses, the three periods of interest represented in the observations are identified at the following times:

- Convective: November 08, 2013, 2000 to 2200 UTC
- Neutral: November 08, 2013, 2130 to 2300 UTC
- Stable: November 09, 2013, 0400 to 0500 UTC.

### 4.2.1 Time Series

Time series of VPTMP are shown in Figure 4.10 for the three domains, for both boundary layer parameterizations, and for 10 levels on the TTU tower. In general, the series for the two parameterizations do not differ greatly. However, both differ from the tower results in some important respects. In particular, the peak VPTMP in the first half of the series is more extreme for both model configurations than for the TTU tower. In addition, the TTU measurements tend to flatten out at most levels in the latter part of the series as the atmosphere stabilizes, whereas the model temperatures remain more widely spread out. The model does capture the consistent homogeneous vertical temperature profile in the period prior to the start of the convective period, but the timing of this feature is earlier than observed at the tower. Variations among the time series for different model resolutions are minimal.

Time series of wind speed are shown in Figure 4.11. The TTU tower measurements for wind speed are quite variable with time, compared to the relatively smooth variations produced by the models. However, it is notable that the peak upper level wind associated with the stable period is overestimated significantly by the YSU model configuration; in contrast, the MYNN configuration appears to capture the timing and magnitude of this peak fairly well. Both configurations of the model seem to indicate more homogeneity in wind speed with height than was observed. Variations in predictions as a function of model resolution are small.

Wind direction time series are shown in Figure 4.12. In general, the forecast and observed profiles are in fairly good agreement, except for some excursions to more westerly directions at midlevels exhibited by the YSU model configuration (and to a lesser extent the MYNN configuration) at later times in the simulations, particularly for the higher-resolution versions of the model. These shifts are not reflected in the observations.

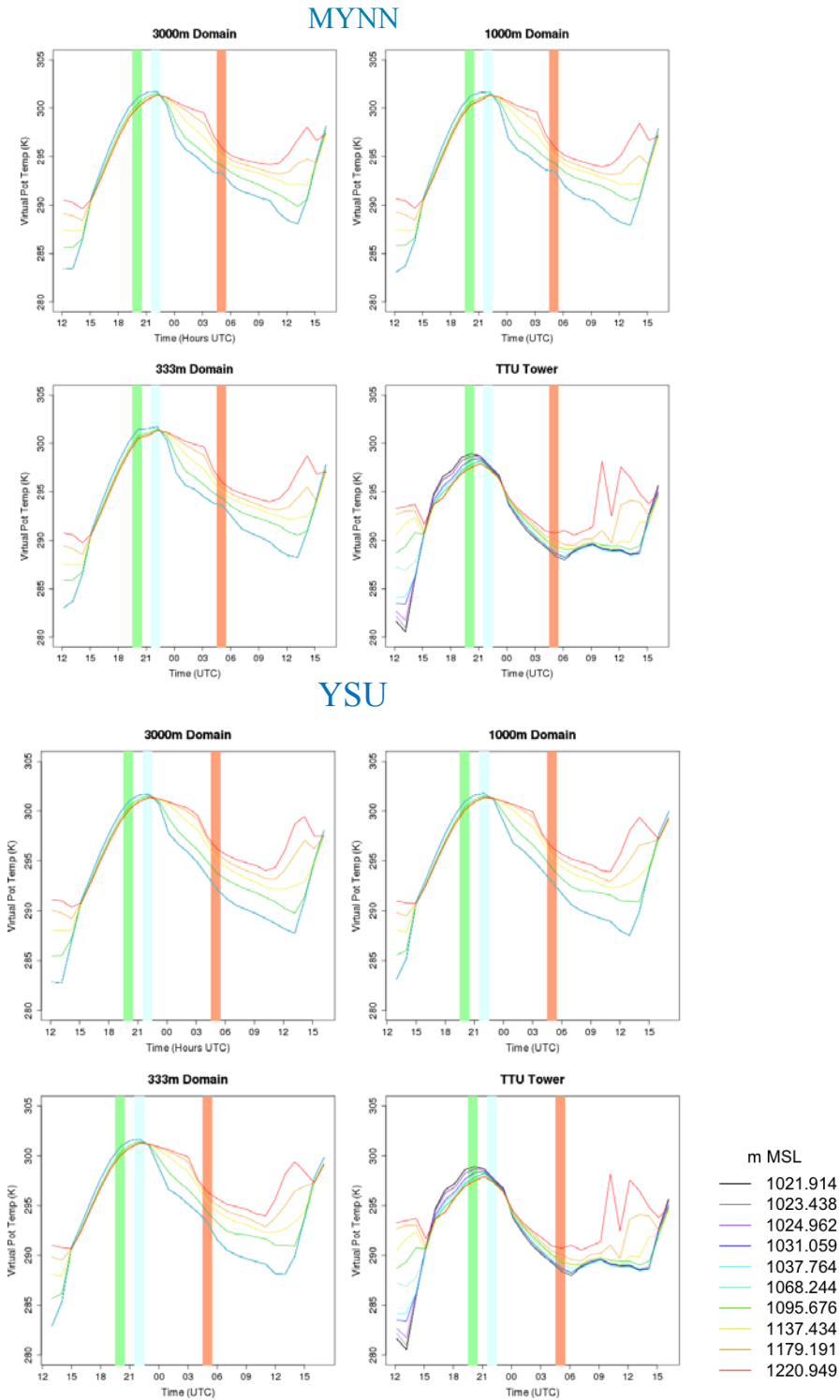


**Figure 4.10.** Time Series of Virtual Potential Temperature for the Three Different Domains and for Multiple Altitudes, with the MYNN (top four panels) and YSU (bottom four panels) Parameterizations. Within each group of four, the top left is the 3,000 m grid spacing, top right is 1,000 m, bottom left is 333 m spacing, and bottom right is from the TTU tower. The green period is convective, blue is neutral, and orange is stable.

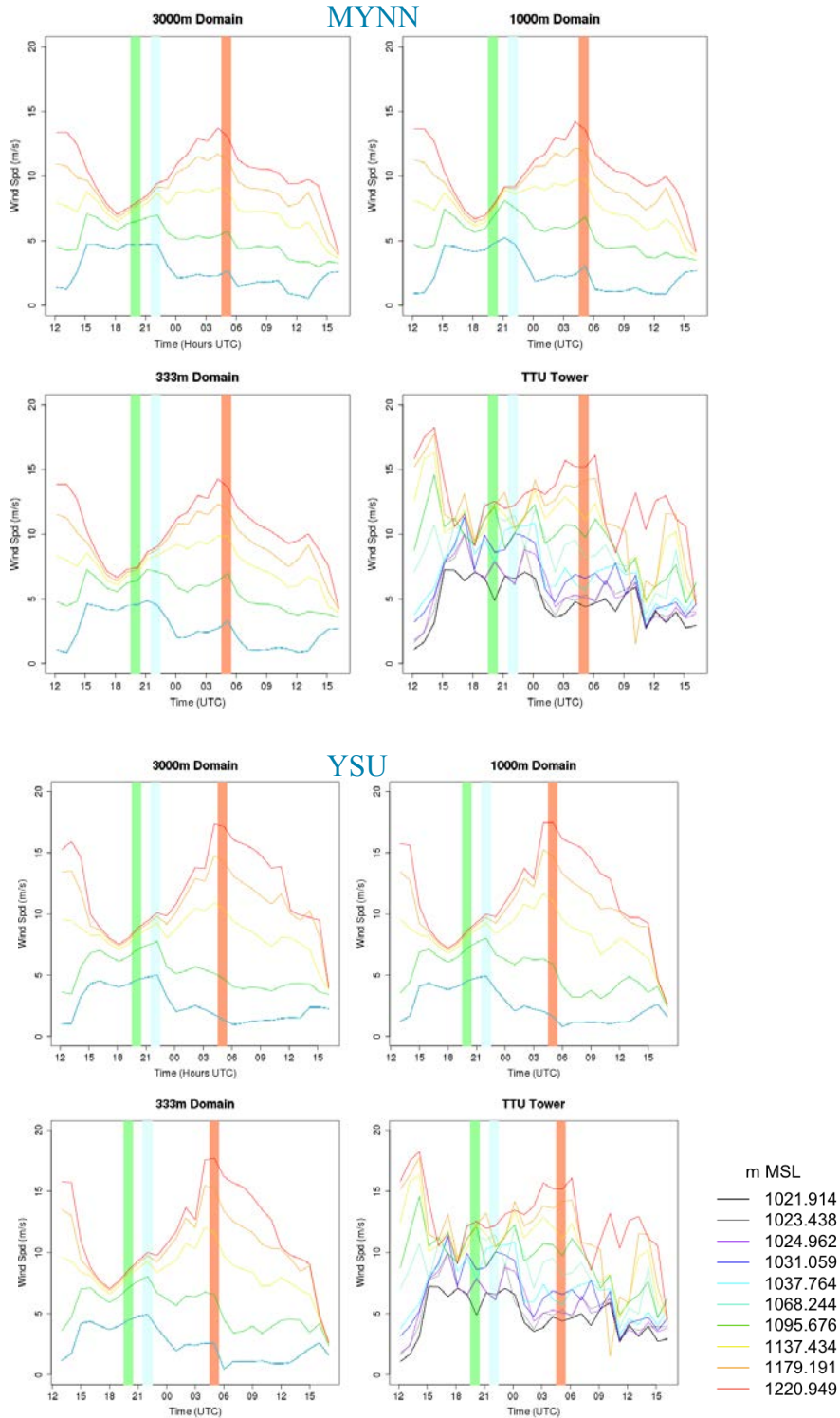


**Figure 4.11.** Time Series of Wind Speed for the Three Different Domains and for Multiple Altitudes, with the MYNN (top four panels) and YSU (bottom four panels) Parameterizations. Within each group of four, the top left is the 3,000 m grid spacing, top right is 1,000 m, bottom left is 333 m spacing, and bottom right is from the TTU tower. The green period is convective, blue is neutral, and orange is stable.

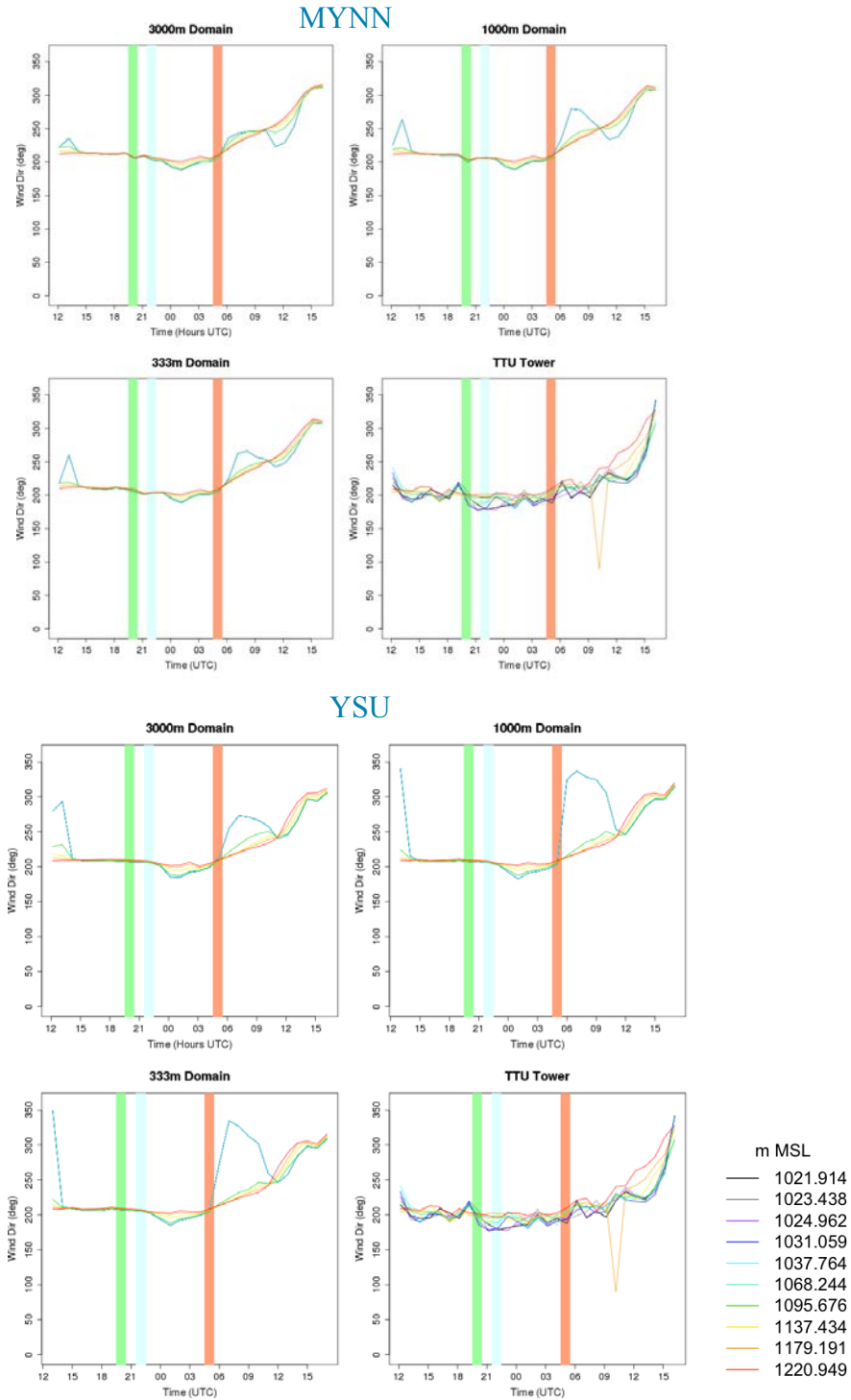


**Figure 4.12.** Time Series of Wind Direction for the Three Different Domains and for Multiple Altitudes, with the MYNN (top four panels) and YSU (bottom four panels) Parameterizations. Within each group of four, the top left is the 3,000 m grid spacing, top right is 1,000 m, bottom left is 333 m spacing, and bottom right is from the TTU tower. The green period is convective, blue is neutral, and orange is stable.

## 4.2.2 Vertical Profiles

Vertical profiles of virtual potential temperature (VPTMP) are shown in Figure 4.13 for both PBL parameterizations and the three model resolutions/domains. The profiles focus on representative times for the three phases: convective (2010 UTC), neutral (2110), and stable (0510 on November 9). The most striking result is the positive bias that is apparent at all levels, at all three times and for both model configurations. The bias is not impacted by increases in resolution, except for the YSU configuration for the stable case in which the lower resolution output is slightly less biased.

The profiles of wind speed (WSPD) are shown in Figure 4.14. For both model configurations and each of the three time windows, the forecasts generally predicted speeds that were too small at all levels. The exception is the YSU model output for the stable case at higher levels. In addition, for both model configurations, the predicted low-level winds do not represent the apparent low-level inversion in the observations for the convective and neutral times. For the stable case with the YSU boundary layer scheme, some differences among the model domains are apparent, with the highest resolution output associated with slightly less bias.

Wind direction profiles are shown in Figure 4.15 for the MYNN model output. The YSU results are almost identical and are not shown here. The biases in wind direction are very small, with only very small errors exhibited for all three cases at the times selected.

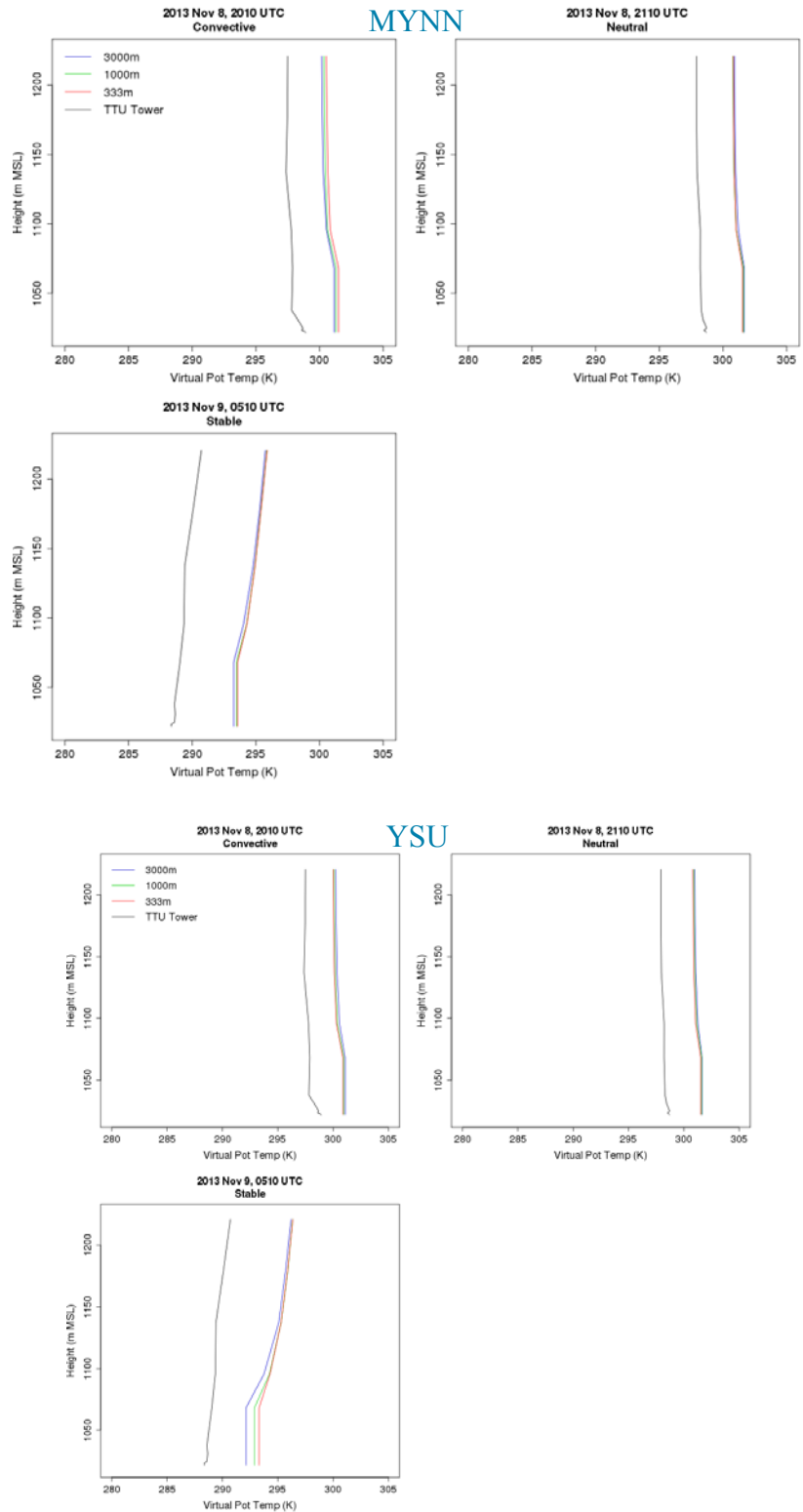


**Figure 4.13.** Vertical Profiles of Virtual Potential Temperature for the Convective, Stable, and Neutral Cases with the MYNN (top three panels) and YSU (bottom three panels) Parameterizations. Within each group of three, the top left is the 3,000 m grid spacing, top right is 1,000 m, and bottom left is 333 m spacing.

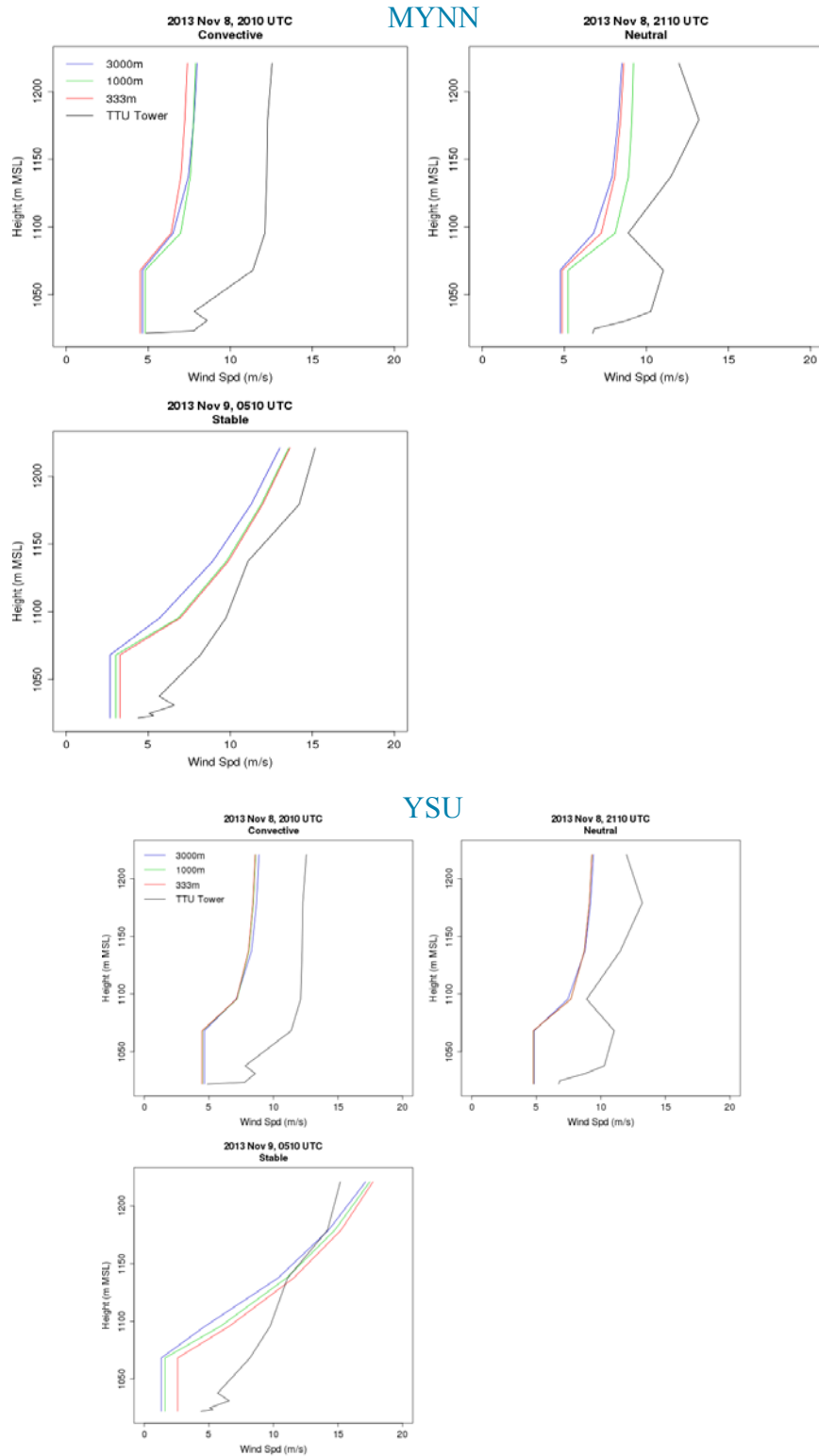


**Figure 4.14.** Vertical Profiles of Wind Speed for the Convective, Stable, and Neutral Cases with MYNN (top three panels) and YSU (bottom three panels) Parameterizations. Within each group of three, the top left is the 3,000 m grid spacing, top right is 1,000 m, and bottom left is 333 m spacing.

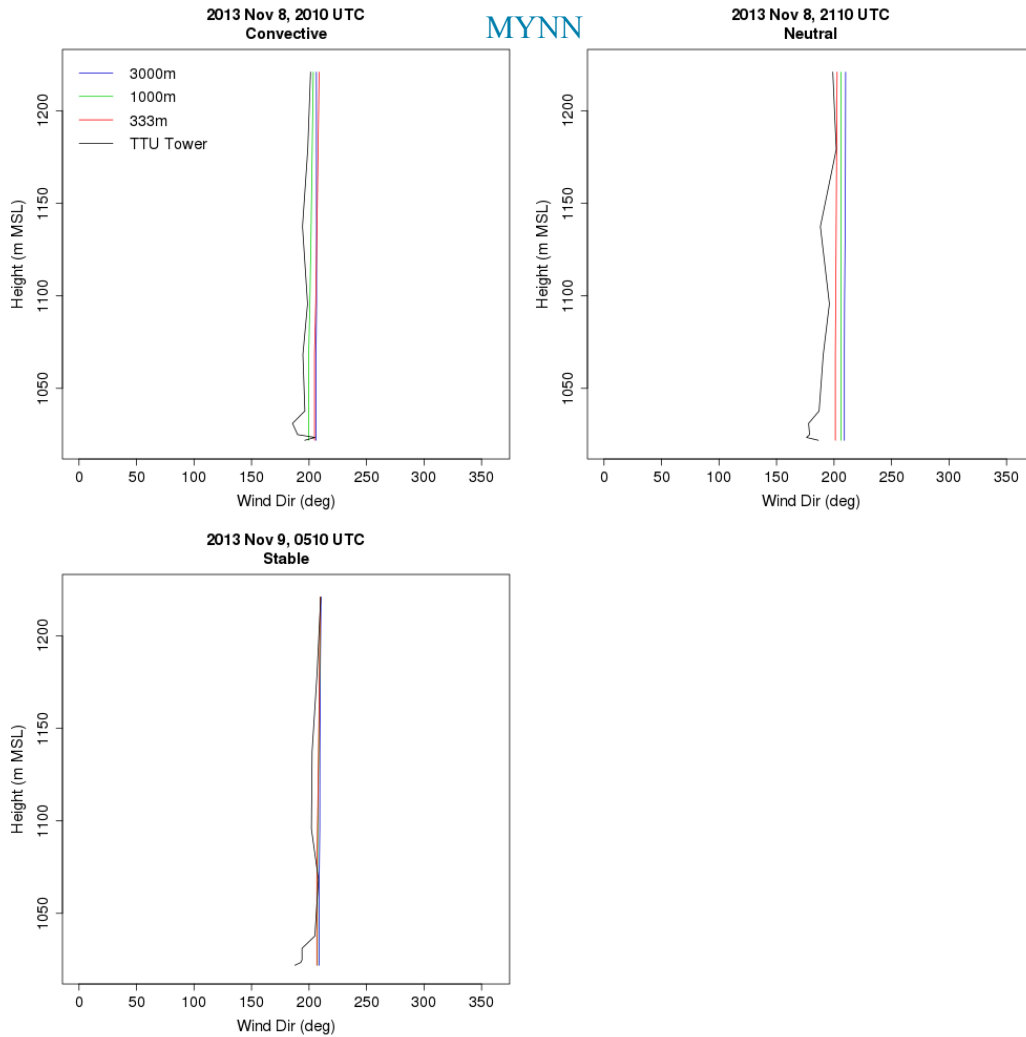


**Figure 4.15.** Vertical Profiles of Wind Direction for the Convective, Stable, and Neutral Cases, for the MYNN Boundary Layer Parameterization, and the Three Model Domains. The top left is the 3,000 m grid spacing, top right is 1,000 m, bottom left is 333 m spacing.

### 4.2.3 Quantitative Metrics

The following quantitative metrics were calculated over the simulated time period.

- Mean error (ME): a measure of bias between the forecast and observed values.
- Mean absolute error (MAE): a measure of the difference between the forecast and observed values that does not take bias (sign) into account.
- Root mean square error (RMSE): a measure of the standard deviation of errors.
- Correlation coefficient (CC): a measure of the relationship between forecast and observed values, which will be nearer to 1.0 if the two behave similarly in time and profile regardless of the magnitude of difference between the two.

The metrics were computed for all forecasts and observation pairs across the entire case, combining all levels. Thus, these metrics provide a “bulk” overview of the model performance. Because only a single case was considered, it is difficult to ascribe statistical significance to these results, so confidence intervals are not shown.

Table 4.1 presents the overall verification results for the November 8 case. The U- and V-components of the wind are shown instead of the wind direction, to avoid some difficulties associated with summarizing statistics of wind direction.

**Table 4.1.** Overall Verification Results for the November 8 Case

Variable	Domain	Parametrization	ME	MAE	RMSE	CC
VPTMP	d03	MYNN	1.88	2.33	2.88	0.92
	d03	YSU	1.95	2.39	2.99	0.92
	d04	MYNN	1.86	2.32	2.89	0.92
	d04	YSU	2.07	2.37	3.00	0.92
	d05	MYNN	2.18	2.68	3.21	0.87
	d05	YSU	2.08	2.35	3.00	0.92
WSPD	d03	MYNN	-3.14	3.22	3.75	0.83
	d03	YSU	-2.78	3.11	3.71	0.79
	d04	MYNN	-3.12	3.2	3.75	0.83
	d04	YSU	-2.6	2.93	3.60	0.79
	d05	MYNN	-3.45	3.54	4.05	0.81
	d05	YSU	-2.64	2.96	3.62	0.79
U	d03	MYNN	6.99	8.17	9.69	-0.49
	d03	YSU	6.98	8.41	9.90	-0.47
	d04	MYNN	6.94	8.16	9.67	-0.49
	d04	YSU	6.64	8.11	9.76	-0.51
	d05	MYNN	9.31	9.42	10.64	-0.24
	d05	YSU	7.04	8.14	9.81	-0.46
V	d03	MYNN	-0.73	2.81	3.65	0.33
	d03	YSU	-0.57	3.09	4.02	0.36
	d04	MYNN	-0.75	2.93	3.76	0.32
	d04	YSU	-0.46	3.13	4.03	0.38
	d05	MYNN	-0.35	2.97	3.91	0.14
	d05	YSU	-0.41	3.16	4.05	0.33

The results in Table 4.1 confirm many of the observations associated with Figure 4.9 through Figure 4.14. For example, VPTMP is consistently biased positively (as shown by ME), and wind speed is consistently biased negatively. Biases in WSPD are somewhat smaller for the YSU configuration than for the MYNN. Correlations are strong for VPTMP and WSPD, but the biases result in fairly large MAE and RMSE values. The U- and V-components are also associated with large MAE and RMSE, and negative (positive) correlations for the U (V) components. In general, the errors (MAE, RMSE) are approximately equivalent for all three domains for all variables.

### 4.3 Interpretation of Results

This section has examined the effect of mesoscale modeling through the *terra incognita*. Qualitative evidence has been presented showing that the expected effects—the appearance of convective rolls at incorrect scales—indeed are present in the simulations at the 333 m grid spacing and, to a lesser extent, at 1,000 m. These spurious numerically induced rolls are more apparent when applying the TKE-based MYNN PBL scheme than in the YSU scheme. This observation is consistent with that of Ching et al.

(2014). As stated there, the PBL schemes assume that the horizontal gradients of turbulent fluxes are much smaller than the vertical gradients and are thus neglected. When these Reynolds-averaged Navier-Stokes (RANS) models are run at this fine resolution, the assumptions are violated. The WFIP2 team is working on a new fully 3D version of the boundary layer scheme that may alleviate these issues. It will be difficult to determine whether there are rolls in the real atmosphere for this case day without additional horizontal measurements and if so, to determine the actual appropriate scales.

The formal assessment showed that, in general, the wind speed is underpredicted by the models and they do not sufficiently capture the transition to the LLJ during the stable conditions. This underprediction is expected to result in a corresponding underprediction when the mesoscale runs are used as forcing for the microscale runs in section 5.0. The VPTMP tends to be overpredicted for this case day, particularly the spread during the most stable portions of the day, suggesting that the model is predicting too strong an inversion.



## 5.0 Analyzing Microscale Simulations of Nonstationary Cases

As introduced in section 1.0, several MMC methods have been developed to suit a variety of applications, computational setup requirements, and fidelity needs, ranging from semi-idealized stand-alone LES to fully lateral boundary-coupled MMC simulations, either within the same computational solver (internal), or using separate solvers (modular) for the mesoscale and microscale domains. This section presents results from simulations using a range of increasingly complex and general MMC approaches.

The simplest MMC method representing the lowest order of coupling involves conducting a stand-alone LES with periodic lateral boundary conditions (LBCs) driven by representative mesoscale forcing parameters (Deardorff 1970a,b, 1972; Andren 1994; Kosović 1997; Kosović and Curry 2000; Chow et al. 2005; and described extensively in the FY15 MMC project report by Haupt et al. 2015). The use of periodic LBCs permits development of the classical 3D turbulence energy cascade relative to the applied forcing. Such forcing typically consists of a geostrophic wind,  $U_g = [u_g, v_g]$ , which represents the large-scale pressure gradient force driving the flow, and surface parameters, such as roughness length,  $z_0$ , which controls frictional drag, and heat flux,  $H_S$ , or skin temperature,  $T_S$ , which control surface-driven buoyancy.

Normally, in this periodic LES approach, forcing parameters are held constant in space and time, allowing the simulated flow to approach statistically steady-state equilibrium with the constant forcing. While this standard approach is restricted to steady flow conditions, we demonstrate here that a class of nonequilibrium ABLs can be simulated using the same setup, incorporating nonconstant values of various forcing parameters. A requirement of the applied forcing used in any stand-alone microscale setup with periodic LBCs is that it obeys periodicity in the lateral directions. This requires either forcing that is uniform in the horizontal direction throughout the domain, or that maintains periodicity about any horizontal heterogeneity that is captured. Herein, nonsteady forcing that obeys these restrictions is incorporated and the efficacy of the approach in simulations of two diurnal cycles and a semi-idealized frontal passage is tested. It is shown, however, that this approach does not capture the mesoscale forcing as well as fully nested coupling.

In addition to standard forcing variables, additional physical factors not captured within the LES domain, such as large-scale advection of momentum, temperature, or other scalars, can also be incorporated into the LES domain by including source terms in the prognostic equations. The time variability of these additional forcing parameters can be obtained either from observations, or from a mesoscale simulation for retrospective analyses. Note, however, that the full range of forcing variables is seldom available from observations. Any forecasting would require model coupling.

The use of periodic LBCs has been extended somewhat to a handful of specific quasi-nonperiodic applications via various techniques, including rescaling the outflow turbulence characteristics before flow reenters the domain as inflow (Mayor et al. 2002; Morgan et al. 2011), use of precursor simulation domains to provide turbulent inflow, and other methods (see review in Tabor and Baba-Ahmadi 2010). However, those approaches are not easily generalizable or applicable to situations with significant departures from periodicity, such as those that are likely to be encountered in realistic meteorological conditions—including complex terrain—and hence are not examined further herein.

When nonperiodicity (such as of terrain or meteorology) prevents use of periodic LBCs, then LBCs must be otherwise specified. An emerging method for specification of microscale LBCs is to execute a mesoscale simulation over the region of interest and extract flow information at the microscale domain location, in addition to providing state variable values at the microscale domain boundaries. This

approach also supplies forcing terms required within the microscale domain, such as geostrophic winds, for compatibility with the mesoscale LBCs.

The most straightforward way to incorporate mesoscale forcing into a microscale simulation is to use a unified computational solver that supports both mesh refinement and scale-appropriate physics modules. This method provides both the LBCs and any internal forcing terms, including geostrophic wind forcing and its variability, as well as surface information, at the microscale domain model timestep. Other physical forcing factors, such as large-scale advection, are automatically incorporated into the microscale domain.

An alternative to conducting unified MMC within the same solver is the modular MMC approach, which uses separate mesoscale and microscale solvers. Modular MMC requires specification of forcing parameters at the lateral domain boundaries, the model surface and top, and internally (e.g., geostrophic forcing), all of which can be obtained from a mesoscale simulation. Modular MMC could involve a full, direct coupling, in which the simulation domains exchange parameter values at each model time step (as required for both upscale and downscale information exchange), execution of the mesoscale simulation ahead of the microscale simulation, the output from which can provide variables for the microscale domains, or use of precomputed libraries that can be linked to a mesoscale event or simulation to specify quasi-idealized forcing parameters.

A major undertaking of the MMC project is the examination of representatives of these previously described approaches, to understand the applicability, benefits, and drawbacks of each approach, as well as to advise selection of the best methods for incorporation into the ModSim environment. While the work in FY15 assessed the simplest approaches of steady, periodic forcing using stand-alone LES, the focus of FY16 was to perform more sophisticated mesoscale-coupled microscale simulations under nonstationary forcing conditions.

Two main coupling approaches are described herein: the application of mesoscale forcing 1) internally through source terms, and 2) at the boundaries through appropriate surface and LBCs. The latter approach is examined using both internal coupling within the WRF solver, and modular coupling between WRF and OpenFOAM. These approaches are contrasted schematically in Figure 5.1. Both methods were tested on two diurnal variation cases—the GABLS3 diurnal cycle at the Cabauw site in the Netherlands and the November 8, 2013 case at the SWiFT site. In section 5.6, an additional case study representing a strongly nonperiodic meteorological situation involving a frontal passage that could not be handled through a simulation using periodic LBCs is also explored.

The formal assessment of the microscale simulations is performed in three steps. The first step involves focusing on the assessment of simulations of a diurnal cycle observed on November 8, 2013 and microscale simulations carried out using LES with SOWFA and WRF models (section 5.5). The second step includes the frontal passage observed on May 12, 2014 and the comparison of realistically forced stand-alone LES and LES nested in mesoscale simulations to observations (section 5.6). A large-scale look at the simulations is presented followed by a look at the features that assess the ability to correctly capture the microscale aspects of the flow. Finally, the spectral properties of simulated flows were studied in comparison to observations in the frequency domain for three near-canonical cases (convective, neutrally stratified, and stably stratified periods) observed on November 8, 2013 (section 5.7).

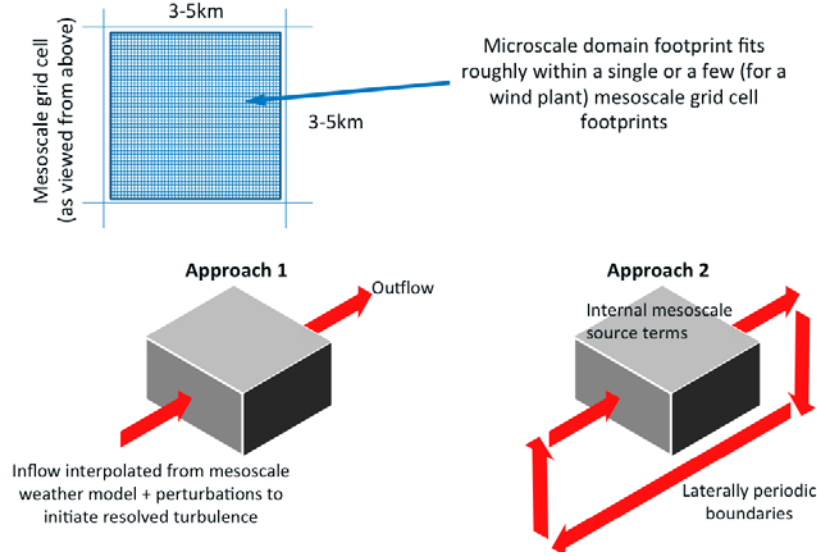


**Figure 5.1.** A Schematic Diagram of the Two Coupling Approaches used in these Microscale Simulations. Approach 1 is boundary forcing using microscale boundary conditions interpolated from the mesoscale simulation; Approach 2 is the internal source term forcing a schematic diagram of the two coupling approaches used in these microscale simulations.

## 5.1 Source Term Forcing with Mesoscale Tendencies

The evolution of zonal momentum in atmospheric simulation models can be expressed as

$$\frac{\partial u}{\partial t} = - \left( u \frac{\partial u}{\partial x} + v \frac{\partial u}{\partial y} + w \frac{\partial u}{\partial z} \right) + f v - \frac{1}{\rho} \frac{\partial p}{\partial x} - \left( \frac{\partial}{\partial x} \tau_{11} + \frac{\partial}{\partial y} \tau_{21} + \frac{\partial}{\partial z} \tau_{13} \right) + F. \quad (1)$$

Here,  $u$ ,  $v$ , and  $w$  are the zonal, meridional, and vertical components of velocity, respectively;  $f = 2\Omega \sin\phi$  is the Coriolis acceleration parameter, with  $\Omega$  Earth's angular rotation rate, and  $\phi$  the latitude;  $\frac{1}{\rho} \frac{\partial p}{\partial x}$  represents the component of the horizontal pressure gradient force acting in the zonal direction, with  $p$  the pressure, and  $\rho$  the density;  $\tau_{ij}$  represents fluxes arising from SGS motions (those too small to be resolved on the computational mesh); and  $F$  represents any external forcing.

Denoting the time rate of change as the tendency, we can express the tendency as depending on the terms on the right-hand side, which represent, in order, advection, Coriolis acceleration, the pressure gradient force, SGS effects, and external forces,

$$U_{tend} = U_{adv} + U_{cor} + U_{pg} + U_{sgs} + U_F. \quad (2)$$

For mesoscale simulations,  $u$ ,  $v$ , and  $w$  represent slowly-varying, large-scale velocity components, with turbulence motions filtered from the flow by the coarse mesh spacing. The effects of unresolved turbulence motions on the evolution of the resolved flow components are commonly represented as  $U_{sgs} = \frac{\partial}{\partial z} \overline{u'w'}$  (with the horizontal SGS components  $\frac{\partial}{\partial x} \tau_{11}$  and  $\frac{\partial}{\partial y} \tau_{21}$  assumed to be zero on the premise of horizontal homogeneity of the SGS velocity field). The remaining term represents the vertical component of the Reynolds stress, which controls the vertical distribution of momentum, hence wind speed and direction, within the ABL. As with the advectons, the pressure gradient term likewise represents synoptic-scale pressure variability driving the mean flow. Finally,  $U_F$  is typically 0 in

mesoscale simulations, but could represent drag from a mesoscale wind farm parameterization, as an example.

For microscale simulations, equation (1) still holds; however, the interpretation of various terms is a bit different. First, microscale computational domains are too small to represent large-scale advections due to synoptic-scale air mass motions or other meteorological features captured by mesoscale simulations. Therefore, in a microscale simulation,  $u$ ,  $v$ , and  $w$  represent the small-scale motions comprising the turbulence production and inertial scales, captured within the flow in this case. Turbulence motions are modulated primarily through nonlinear advective interactions, with SGS dissipation primarily representing mean dissipation of energy from those resolved structures. Due to the highly 3D structure of the flow field, SGS stress closures are also 3D. For the same reason that large-scale advection cannot be captured in small microscale domains, neither can the large-scale pressure gradient force driving the mean flow. Therefore, the pressure gradient term in microscale simulations represents resolved pressure fluctuations due to turbulence and interactions of the flow with features such as terrain or other objects, including wind turbines. For this reason, the large-scale pressure gradient driving the mean flow is applied as an external forcing term,  $F$ .

In nonatmospheric microscale simulations, Coriolis accelerations are typically ignored ( $f = 0$ ) due to their impacts requiring larger spatiotemporal scales than typically captured in microscale domains. However, for atmospheric microscale simulations, Coriolis effects are critical to relevant impacts, including the large changes in wind direction often observed within the ABL.

Often, the large-scale pressure gradient used to force a microscale ABL flow simulation is represented using the geostrophic wind, in which the zonal component is given by

$$v_g = \frac{1}{f\rho} \frac{\partial p}{\partial x}. \quad (3)$$

Using equation (3) in equation (1) gives

$$\frac{\partial u}{\partial t} = - \left( u \frac{\partial u}{\partial x} + v \frac{\partial u}{\partial y} + w \frac{\partial u}{\partial z} \right) + f(v - v_g) - \frac{1}{\rho} \frac{\partial p}{\partial x} - \left( \frac{\partial}{\partial x} \tau_{11} + \frac{\partial}{\partial y} \tau_{21} + \frac{\partial}{\partial z} \tau_{13} \right) + F, \quad (4)$$

showing one manner in which the geostrophic winds (in units of  $\text{m s}^{-1}$ ) can be used to force microscale simulations. In this context,  $v_g$  represents the large-scale pressure gradient force, whereas  $\frac{1}{\rho} \frac{\partial p}{\partial x}$  represents the resolved-scale fluctuations captured within the microscale solver. A similar treatment applied to the meridional momentum equation yields a recipe for incorporating synoptic-scale horizontal pressure gradient forcing and Coriolis effects into microscale simulation domains.

In a similar manner, synoptic-scale advective tendencies can also be incorporated into microscale simulations to represent the synoptic-scale changes in mean forcing owing to meteorological variability with scales too large to be captured within microscale domains. This can be achieved simply by setting  $F = U_{adv}$  in equation (2), as applied within the microscale simulation domain.

Significant difficulties can arise in the measurement of both the geostrophic winds and advective tendencies, each of which requires the spatial distributions of wind speed, pressure, and other desired quantities such as temperature or moisture, with height. Geostrophic wind components, which represent the steady-state balance between pressure gradient and Coriolis accelerations in the absence of friction can be estimated from the velocity components occurring just above the ABL, where friction due to turbulence typically attenuates. However, such estimates may be inaccurate due to some remaining turbulence, as well as the observed wind field being influenced by other factors, including advection. Further, baroclinicity, the change of the geostrophic wind with height, is also difficult to estimate,

especially within the ABL, where frictional effects, due to turbulence, induce large departures of the observed winds from their geostrophic values. Therefore, estimation of geostrophic winds and advective tendencies from observations requires either a specialized observational campaign, or quasi-ideal synoptic meteorological conditions from which additional constraints can be inferred.

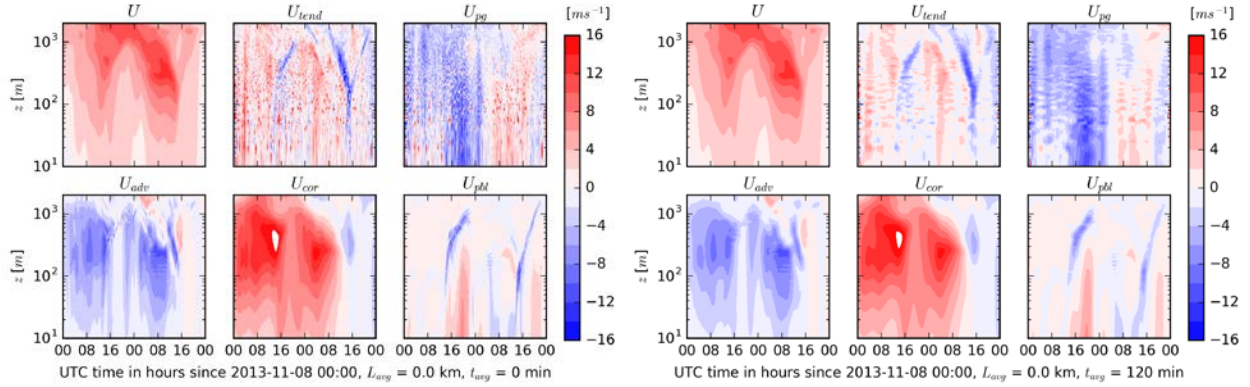
## 5.2 Extraction of Mesoscale Tendencies from a Mesoscale Simulation

As discussed in section 5.1, due to the explicit representation of meteorological parameters in both horizontal and vertical directions, as well as in time, mesoscale simulations can provide both the height and time dependence of these quantities critical to capturing ABL features impacting wind plant operations. One phenomenon often strongly influenced by baroclinicity and advection is the LLJ, the characteristics of which, including timing, magnitude, shear, and veer, strongly influence power production and fatigue loading.

The extraction of mesoscale forcing tendencies for use in microscale simulations is described in the context of a case study from the SWiFT facility occurring on November 8, 2013, which represents a typical diurnal cycle under quiescent synoptic-scale meteorological conditions. The case is described in section 3.0 and modeled through the *terra incognita* in section 4.0. This case is simulated using both the traditional MMC approach of direct coupling at the microscale domain lateral boundaries, and using the new approach described in this section. The extraction of mesoscale tendencies follows the examination of momentum and temperature budgets inspired by the GABLS3 model intercomparison exercise (Bosveld et al. 2014), which is now being used for benchmarking ABL models (Rodrigo et al. 2016b), and is also simulated herein.

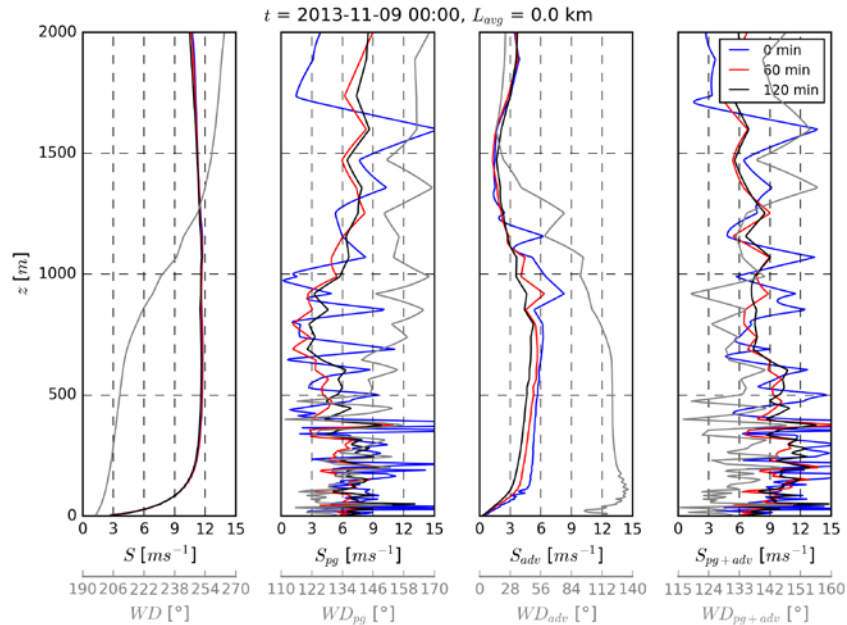
Figure 5.2 shows time-height sections of the zonal velocity, as well as several of the tendency terms presented in equation (2), within the lowest 1.2 km, over 48 hours from a WRF-mesoscale simulation with output every 10 min. Here,  $U_{pbl}$  represents  $U_{sgs}$ , denoting the use of a mesoscale PBL parameterization for the SGS momentum transport. Inspection of Figure 5.2 clearly shows not only the development of an LLJ each evening, but also the nontrivial magnitudes of synoptic-scale advective, pressure, and Coriolis tendencies that play strong roles in LLJ evolution, and must be captured for wind plant simulations.

Figure 5.2 also shows considerable small-scale spatiotemporal variability in the instantaneous profiles of these tendencies (left) that can be substantially ameliorated by averaging in time over two hours (right).



**Figure 5.2.** Instantaneous Time-Height Plots of Zonal Wind Speed ( $U$ ), and the Tendency Terms Presented in Equation (2): the Tendency  $U_{tend}$ , the Pressure Gradient Force, Advection, Coriolis Acceleration, and SGS Effects Occurring from November 8 0000 UTC to November 10 0000 UTC, taken from the Closest Grid Point to the SWiFT Site (left); (right) Same as Left, but Averaged over 2 Hours.

The small-scale spatiotemporal variability can also be seen when plotting a vertical profile at a certain time (e.g., Figure 5.3 for November 9 at 0000 UTC after the ABL has passed through neutral conditions and is beginning to stabilize). Panels from left to right in this figure show profiles up to 2,000 m of wind speed, wind speed tendency contribution of pressure gradient (here denoted as  $S_{pg}$ ), advection ( $S_{adv}$ ), and pressure gradient and advection combined ( $S_{pg+adv}$ ). The blue line shows instantaneous values, which have a reduction of variability increases with longer averaging intervals, shown here for averaging intervals of 60 min in red and 120 min in black.



**Figure 5.3.** Profiles of Wind Speed, Wind Speed Tendency Contributions of Pressure Gradient, Advection, and Pressure Gradient and Advection Combined at the Nearest Grid Point to the SWiFT Site. Tendencies of pressure gradient and advection are passed on to the microscale simulations. Overlaid are profiles of wind direction in grey.

The reduction of small-scale spatiotemporal variability was explored not only by averaging in time, but also in space, and in space and time combined. Figure 5.4 (left) shows time-height sections of the instantaneous zonal velocity, as well as several of the tendency terms presented in equation (2) averaged spatially over 2x2 grid points. Figure 5.4 (right) shows those same averages over 2x2 grid points but additionally averaged over 60 min. When no temporal averaging is performed (Figure 5.4 left), the  $U_{pg}$  component exhibits more variability than the other tendency components. Temporal averaging over 60 min (Figure 5.4, right) reduces the variability for all components further, except for  $U_{pg}$ , which still shows similar variability. When averaging over five grid points (Figure 5.5), the small-scale spatiotemporal variability decreases in all tendency components. Profiles of tendency components show reduced variability when averaged over 2x2 grid points (Figure 5.6) compared to tendency components extracted at one grid point (Figure 5.3), which is further reduced by averaging over time (averages of 60 min and 120 min shown in Figure 5.6). Spatial averages over 5x5 grid points and in time further increase this variability (Figure 5.7).

This analysis indicates that averaging in space is more effective at decreasing the variability than averaging in time. Profiles of tendency components still exhibit variability when averaging over 2x2 grid points even after 260 min (not shown). In our case of November 8–November 10, temporal averages over extended periods have the disadvantage of including higher wind speeds from the later-forming LLJ, which shifts the averaged profile to higher wind speeds (black line in Figure 5.6). On the other hand, when wind speeds and tendency components are spatially averaged, profiles are not shifted and are smoother (Figure 5.7).

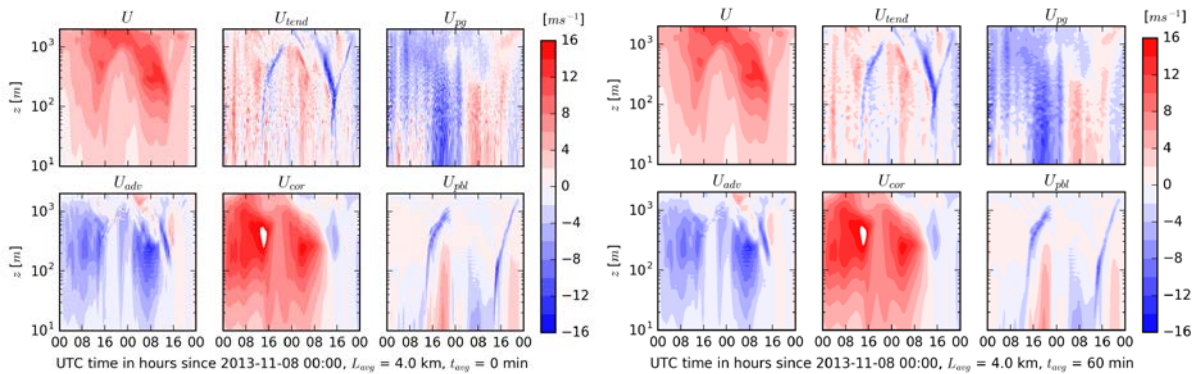


**Figure 5.4.** Instantaneous Time-Height Plots of Zonal Wind Speed ( $U$ ), and the Tendency Terms Presented in Equation (2): the Tendency  $U_{tend}$ , the Pressure Gradient Force, Advection, Coriolis Acceleration, and SGS Effects, Occurring from November 8 0000 UTC to November 10 0000 UTC and Averaged over 2x2 Grid Points Surrounding the SWiFT Site (left); Right: Same as Left, but Additionally Averaged over 1 Hour

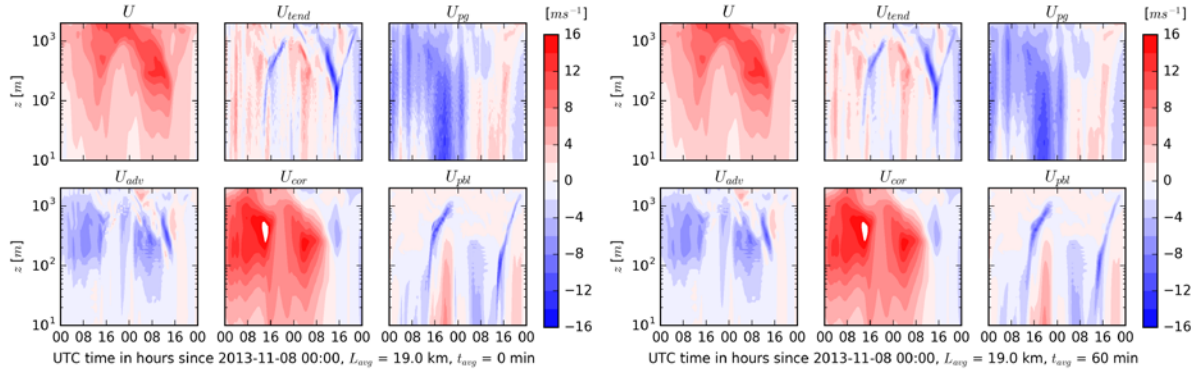


**Figure 5.5.** Instantaneous Time-Height Plots of Zonal Wind Speed ( $U$ ), and the Tendency Terms Presented in Equation (2): the Tendency  $U_{tend}$ , the Pressure Gradient Force, Advection, Coriolis Acceleration, and SGS Effects, Occurring from November 8 0000 UTC to November 10 0000 UTC and Averaged over  $5 \times 5$  Grid Points Surrounding the SWiFT Site (left); Right: Same as Left, but Additionally Averaged over 1 Hour

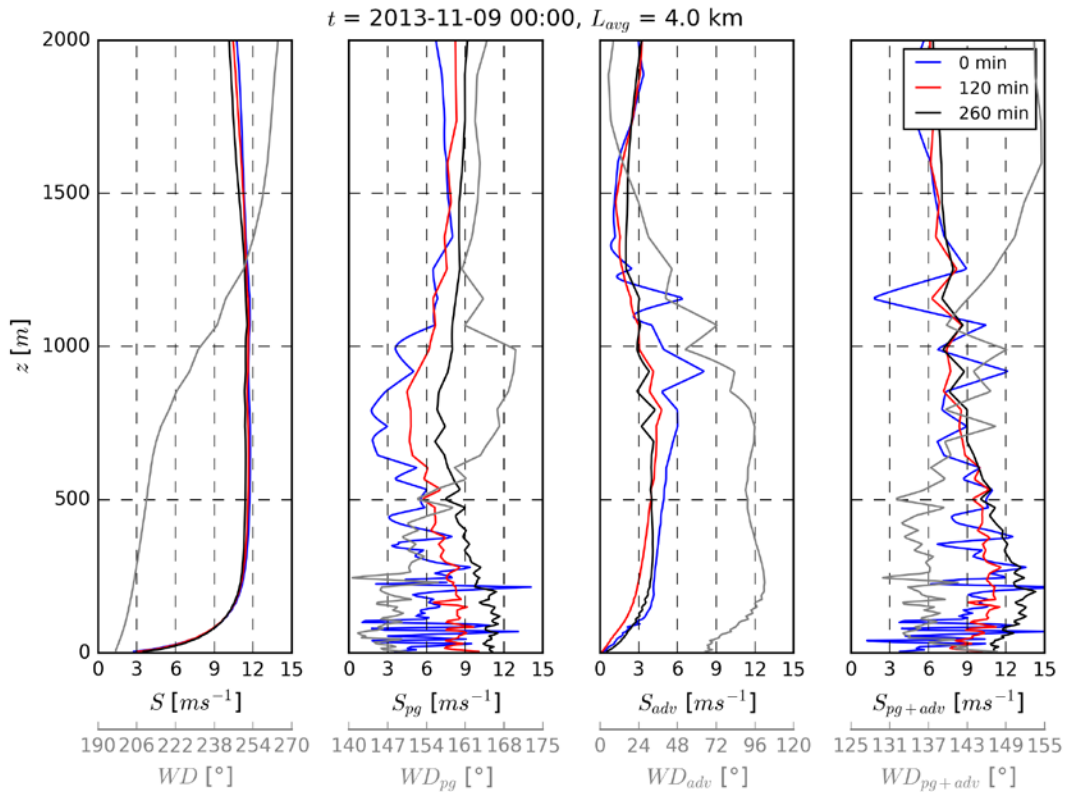


**Figure 5.6.** Profiles of Wind Speed, Wind Speed Tendency Contributions of Pressure Gradient, Advection, and Pressure Gradient and Advection Combined. Averaged over  $2 \times 2$  grid points: (blue) instantaneous model output, (red) 120 min average, (black) 260 min average. Overlaid are profiles of wind direction in grey.

One research question is whether emphasizing the spatiotemporal variability in the mesoscale model output when coupling to the microscale is desired. It could be argued that only numerical noise should be removed, not all signals in variability. Spatiotemporal variability is desired, for example, to preserve time-

varying features, which are eliminated when tendencies are averaged in time, such as is demonstrated in relation to offline coupled LES with part of the signal removed as described in section 5.5.1. In future work, we hope to explore whether nonaveraged or averaged tendency components yield more accurate results when coupled to the microscale.

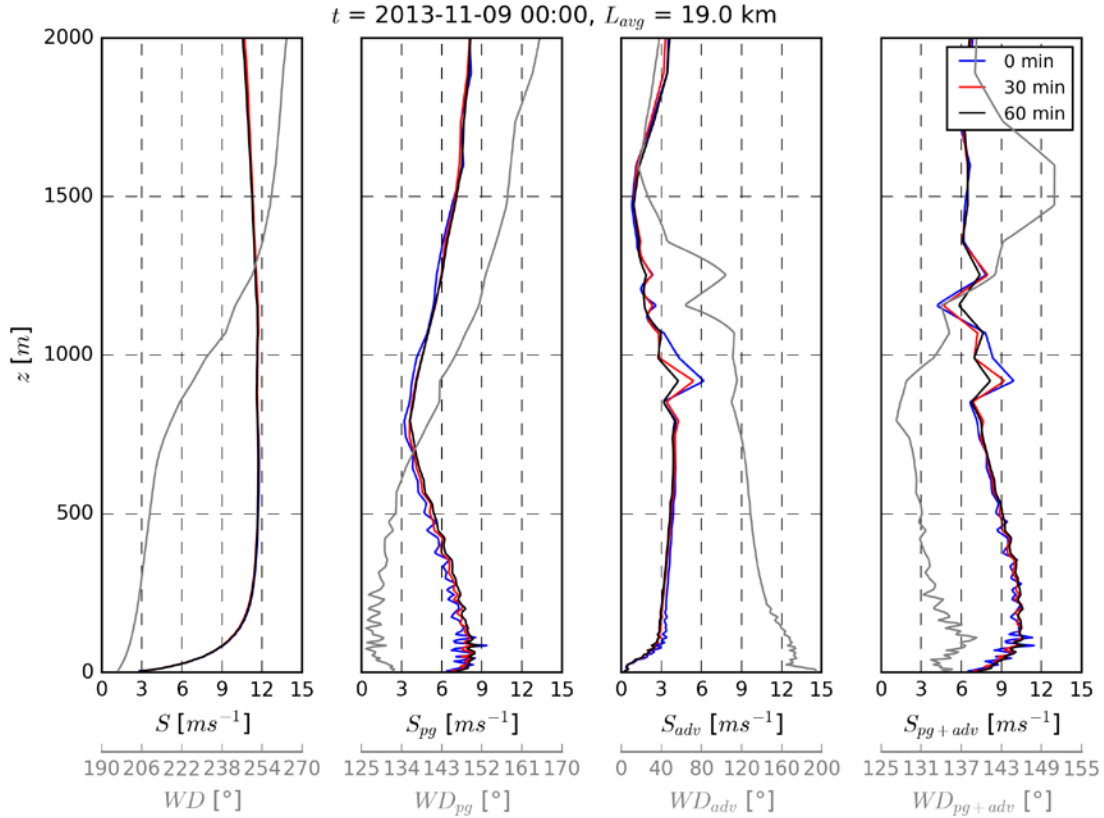


**Figure 5.7.** Profiles of Wind Speed, Wind Speed Tendency Contributions of Pressure Gradient, Advection, and Pressure Gradient and Advection Combined. Averaged over  $5 \times 5$  grid points: (blue) instantaneous model output, (red) 30 min average, (black) 60 min average. Overlaid are profiles of wind direction in grey.

## 5.3 Testing Coupling Methods

### 5.3.1 Use of Mesoscale Tendencies to Force the Microscale Simulations

An investigation was completed on the addition of mesoscale tendency forcing terms obtained both from observations and from mesoscale simulations into microscale simulations, via incorporation into the momentum and temperature equations. In the momentum equation, the source term accounts for the pressure gradient force and large-scale advection of momentum. In the temperature equation, the source term accounts for large-scale advection of temperature. These source terms can be implemented in two ways.

- The first and most natural way is to extract the corresponding tendencies from the mesoscale simulation as a function of time and height, and simply apply those directly to the governing equations.

- In the second method, which is akin to data assimilation, the mesoscale model time-height history of mean wind velocity and potential temperature is used by the microscale solver to compute source terms that cause the solver to return the same mean time-height history as the mesoscale solver.

The first approach above is examined using both WRF and SOWFA, whereas the second is examined within SOWFA only. Surface forcing, in the form of either a sensible heat flux,  $H_S$ , or a surface skin temperature,  $T_S$ , is also applied. These parameters can likewise be derived either from observations or mesoscale simulations, and each approach is investigated. Both observed and mesoscale-derived source terms are allowed to vary in height and time, but are held constant in both horizontal directions, due to use of periodic LBCs. This method of forcing therefore assumes horizontal homogeneity, which is valid for relatively flat sites with low spatial variability of the mesoscale weather. This is often applicable to sites like the SWiFT facility in Texas or the Cabauw site in the Netherlands. This coupling method is more easily understood by imagining a mesoscale warm air mass advecting toward an observer. If the gradient between the warmer and cooler air is not too strong, the observer will feel this advection of warm air as a simple warming of the local air. That effect is equally represented by a source term within the relatively small microscale domain warming the air at the same rate that it is truly being advected. Hence, no horizontal gradient in mean temperature ever appears within the microscale domain, the entire domain simply warms uniformly at the rate specified by the advective temperature tendency.

### 5.3.2 Boundary Forcing with Conditions Interpolated from a Mesoscale Simulation

For cases that do not permit the use of periodic LBCs, a mesoscale model can also be employed to provide lateral boundary information. Simulations using this approach internally within the WRF model are also examined. More generally, this approach can be extended to separate solvers, as described previously, using mesoscale time series data, like that of velocity and temperature, on planes within the mesoscale simulation that are coincident with the boundaries of the microscale domain. These time series of planes of data can then be used as boundary conditions for the microscale simulation domain. For example, on inflow boundaries of the microscale simulation, velocity and potential temperature Dirichlet conditions extracted from the mesoscale simulation are used as boundary conditions. On the surface, heat flux extracted from the mesoscale simulation is also used as a microscale boundary condition. As time advances, these boundary conditions update. The frequency that these boundary data are sampled from the mesoscale need not be as high as the microscale time step. The microscale solver can simply interpolate the boundary data in time. For example, the microscale solver time step may be on the order of 1 s, but the mesoscale boundary data is only saved every few minutes.

This method is valuable in that it does not assume horizontal homogeneity, but it has the added complexity that the mesoscale boundary information is smooth because the majority of the turbulence is parameterized. Consequently, the inflow must be perturbed in some way to allow for resolved-scale turbulence to form. This topic is addressed in section 6.0.

## 5.4 GABLS3 Case, Internal Mesoscale Forcing Derived from Observations

GABLS3 was selected for evaluation of MMC using the method discussed in section 5.2 in which internal source terms derived from observed mesoscale tendencies, like large-scale advection and the pressure gradient force, are used. Both WRF and SOWFA are used to conduct the microscale simulations, allowing comparison of similar techniques in two different microscale solver bases. The meteorological parameters used to force the microscale simulations of the GABLS case are derived from tower

measurements, radiosondes, surface pressure stations, and mesoscale model information; however, the forcings are idealized for ease of implementation. Example time-height histories of some of these idealized forcings are shown in Figure 5.8. The GABLS3 case study took place at Cabauw, the Netherlands on July 1–2, 2006. It consisted of 24 hours with clear skies with a nearly constant geostrophic wind of about  $7 \text{ m s}^{-1}$ , and a considerable wind shear in the vertical. Significant near-surface temperature inversion after sunset was found to aid formation of the LLJ. Detailed initial conditions, surface conditions, and dynamical forcings can be found in Bosveld et al. (2014).

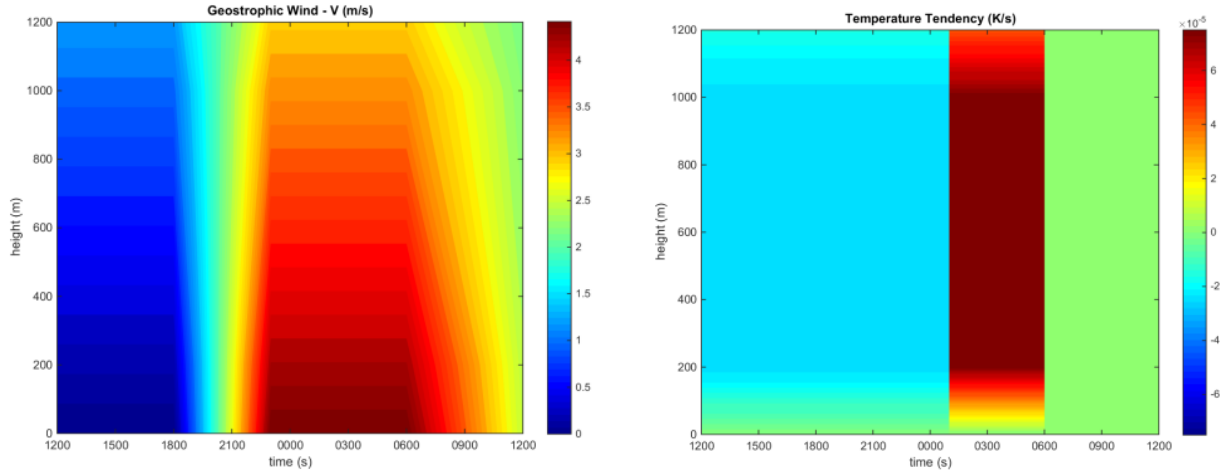
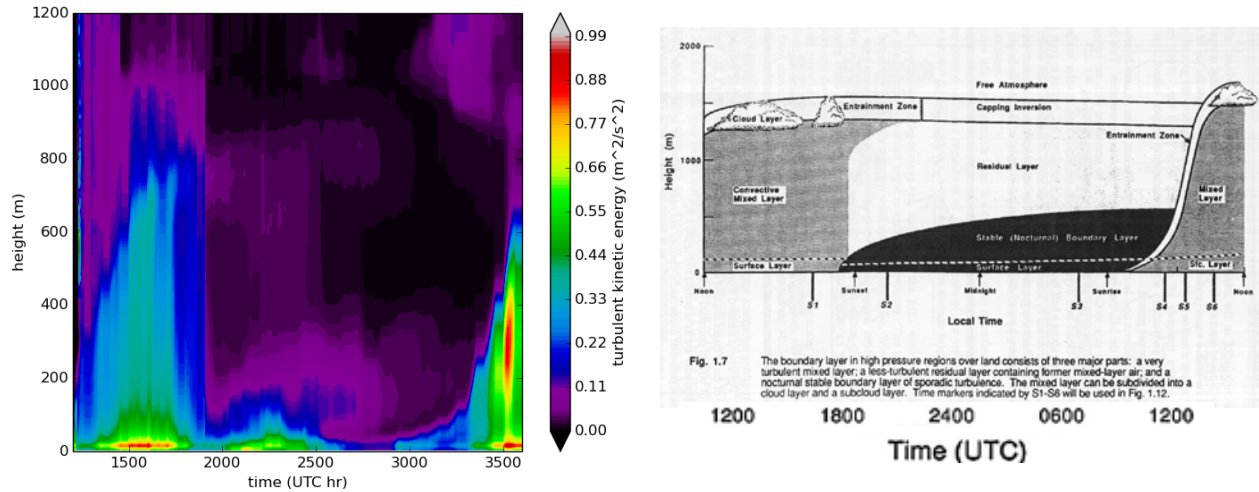


**Figure 5.8.** Tendencies from the GABLS3 Case as Provided by Bosveld et al. (2014). The V-component geostrophic wind time-height history is shown at the left and the large-scale advection of temperature time-height history is shown at the right.

A capability was added to the WRF-LES model allowing it to apply internal source terms based on the time-varying GABLS3 inputs, including horizontal advection and geostrophic wind tendencies available at 6 hour intervals interpolated to the model time step (0.25 s). Surface temperature was also prescribed as a function of time to modify the sensible heat flux from the surface. The WRF-LES model domain is configured as  $4 \text{ km} \times 4 \text{ km}$  horizontally with a resolution of 12.5 m and about 2.1 km in the vertical direction with a resolution of 7.5 m. The Lilly 1.5-order TKE (3D) scheme was used for the SGS parameterization. A damping layer of 500 m was applied at the top of the model domain.

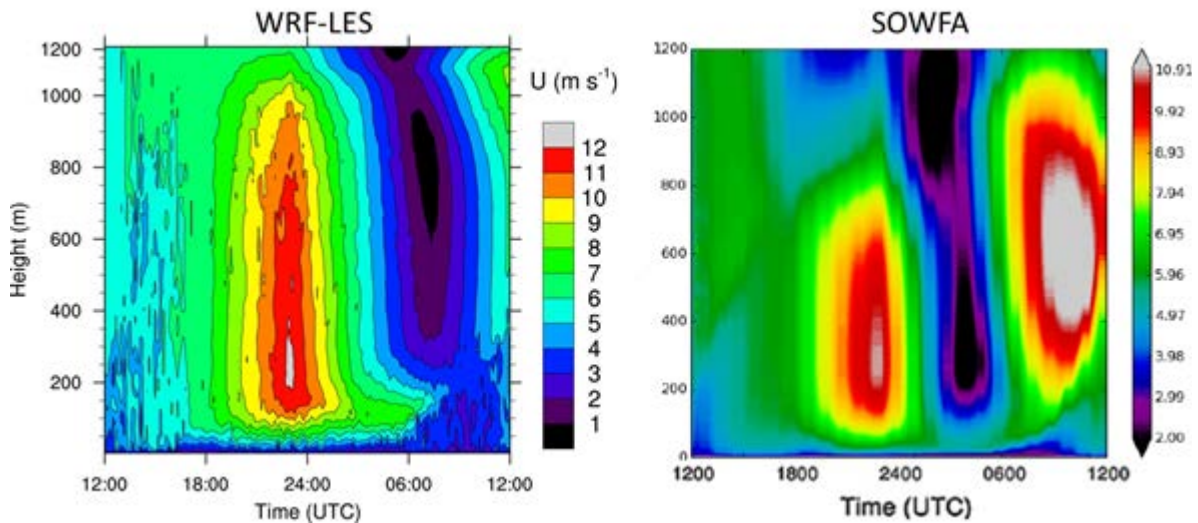
SOWFA was also used to simulate the GABLS3 case. As with WRF-LES, a capability was added to allow for the specification of mesoscale-derived internal source terms to provide the MMC. As with WRF-LES, a  $4 \text{ km} \times 4 \text{ km} \times 2 \text{ km}$  domain was used, but with uniform a 10 m resolution. The simulation was run from 1200 UTC of the first day to 1200 UTC of the second day. Lilly’s one-equation SGS turbulence model was used. The surface forcing was tried in two ways. First, the sensible heat flux was specified. Next, the surface temperature was provided, and a surface heat flux compatible with Monin-Obukhov scaling was derived by the solver and applied.

Figure 5.9 shows a time-height contour plot of TKE for the GABLS3 case as simulated with SOWFA. For comparison, the classic boundary layer diurnal structure schematic diagram of Stull (1988) is also shown. Ending at around 1800 UTC the first day and beginning around 0900 UTC the second day (3300 UTC in Figure 5.9), there is clear vertical development of TKE, indicating a convective daytime boundary layer. From 1800 UTC the first day to 0900 UTC the second day, the boundary layer collapsed because the sun had set and conditions were stable. Capturing diurnal behavior like this is a new capability within SOWFA that has resulted from the MMC project.



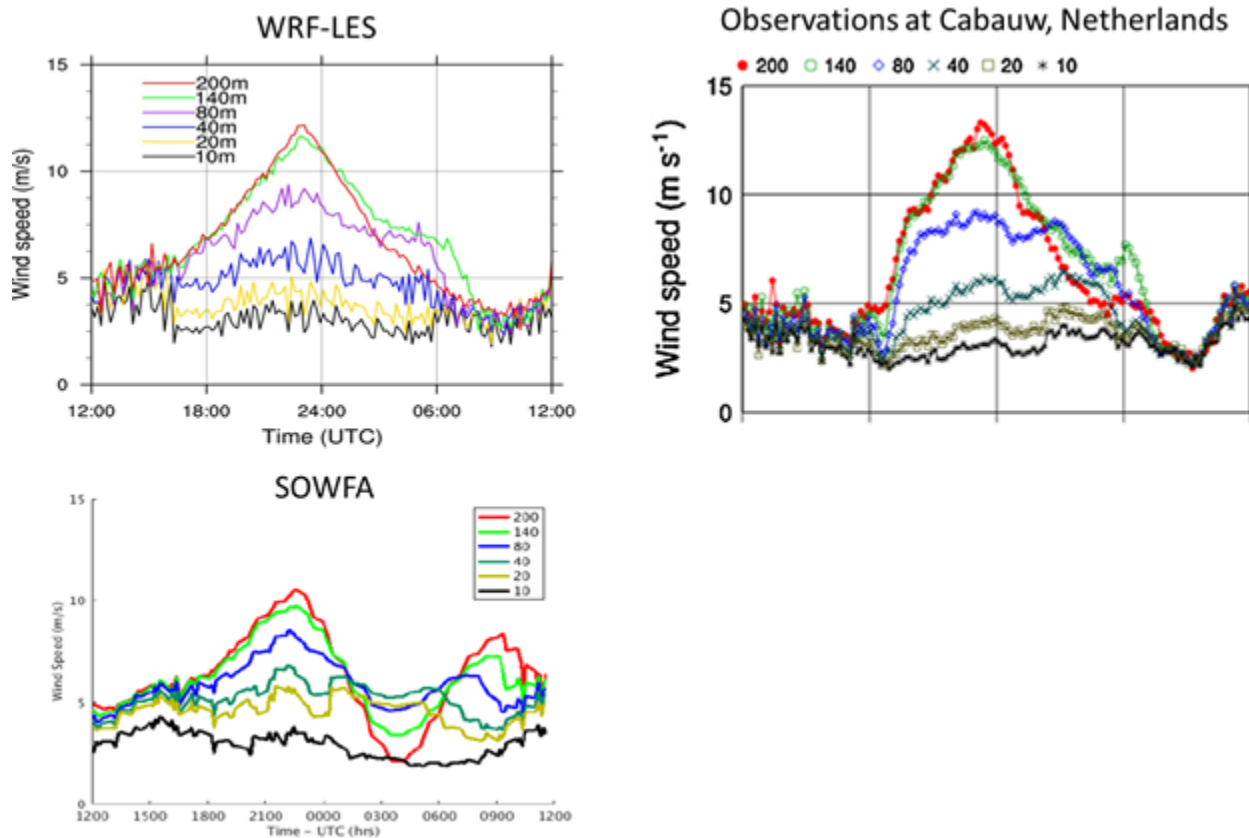
**Figure 5.9.** Time-Height Contours of TKE from the GABLS3 Simulation as Calculated with SOWFA (left). For comparison, the classic boundary layer structure diagram of Stull is shown (right).

In order to better compare the two microscale solvers applied to this case, Figure 5.10 shows the time-height contours of the horizontal wind speed. Both capture the diurnal cycle of wind speed forced with the observed mesoscale wind speed tendencies and surface heat fluxes. An LLJ developed in both model cases around 2300 UTC at about 200 m with a maximum wind speed of 12.5 m/s. One main difference between the WRF-LES and SOWFA results is that on the second day, the SOWFA simulation predicted higher wind speeds peaking around 600 m starting at about 0700 UTC.



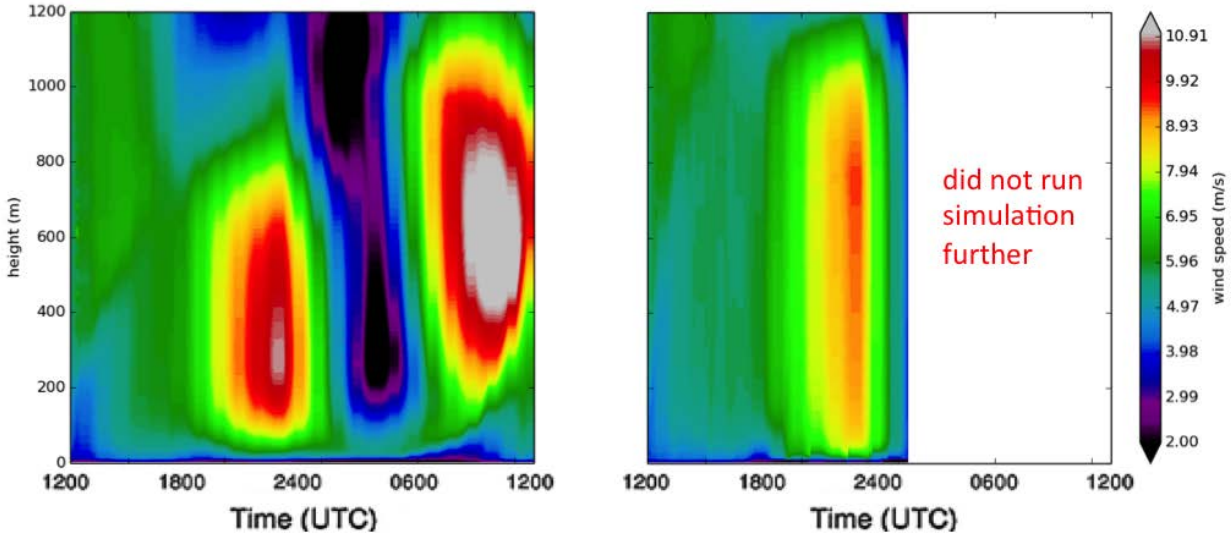
**Figure 5.10.** Time-Height Contours of Horizontal Wind Speed for the GABLS3 Case as Computed with WRF-LES (left) and SOWFA (right)

Figure 5.11 compares the horizontal wind speeds between the simulations and the Cabauw tower measurements at several altitudes. Both microscale models capture the overall diurnal evolution of the wind speeds near the surface. The wind shear on day 2 simulated by WRF-LES agrees better with the tower measurements than does that of SOWFA. The reason for the discrepancy between the WRF-LES and SOWFA results is unclear, but it may be caused by differences in the way the two models calculate surface heat flux given a surface temperature history.



**Figure 5.11.** Time Histories of Horizontal Wind Speed at Different Vertical Levels as Computed by the Microscale Models for the GABLS3 Case (left), and as Measured at the Cabauw Tower (right)

Using SOWFA, it was discovered that the results in the GABLS3 case are very sensitive to the way the surface heat flux is prescribed. Figure 5.12 compares the time-height contours of predicted horizontal wind speed using two different surface heat flux specification methods. For the left contour plot, the surface sensible heat flux that was recorded at the Cabauw site was directly specified. For the right contour plot, the 2 m potential temperature reading from the Cabauw site was used, along with the 5 m computed potential temperature to use Monin-Obukhov scaling to compute and specify a surface heat flux. This second method produces a much more realistic nocturnal LLJ at around 2300 UTC. However, whether the 2 m temperature or some measure of surface skin temperature should be used needs to be further investigated.



**Figure 5.12.** Time-Height Contours of Computed Horizontal Wind Speed for the GABLS3 Case using SOWFA. The left plot is when 2 m measured temperature along with 5 m computed temperature are used with Monin-Obukhov similarity theory to specify a surface heat flux. The right plot is when surface heat flux recorded at Cabauw is directly specified in the simulation.

## 5.5 SWiFT Site November 8, 2011 Case, Mesoscale Forcing Derived from a Mesoscale Simulation

The use of mesoscale forcing tendencies main case of interest for the MMC group’s FY16 work is a typical example of the diurnal variation at the SWiFT site for the November 8, 2011 case. That case was simulated using the two different MMC methods. In section 5.5.1, results from the SOWFA solver are presented in which the forcing is done through internal source terms. Here, the source terms are computed such that the time-history of the planar-averaged velocity and temperature match the time-history of those variables from the column of WRF data nearest the SWiFT site’s tall tower. In section 5.5.2, we present results from the WRF-LES solver. Here, the WRF-LES domain is embedded within the mesoscale WRF domain, and WRF-LES is forced at the boundaries in the usual way. Section 5.5.3 documents the formal assessment carried out by NCAR for all the SWiFT November 8 case simulations.

### 5.5.1 Mesoscale Forcing Through Internal Source Terms – SOWFA

Herein, we investigated the novel MMC method based on incorporating mesoscale simulation-derived synoptic-scale tendencies into stand-alone LES using periodic LBCs. The mesoscale simulations produced the time-height histories of wind speed, direction, and potential temperature, geostrophic winds, and advective tendencies along the model column nearest the SWiFT tall tower. These time-height histories were extracted as described in section 5.2.

Those data were then used as input to each model as described in section 5.1, with WRF driven directly with the mesoscale-derived fields, whereas SOWFA computed source terms that forced the microscale simulation planar-averaged profiles to match the mesoscale wind and potential temperature profiles. In each case, the time-history of planar-averaged microscale computed velocity and temperature fields match those of a WRF model column of interest, but the microscale model still resolves all the turbulence that results from those planar-averaged conditions.

The SOWFA microscale simulations were conducted on a 5 km x 5 km x 2 km domain with uniform 10 m resolution, resulting in 50 million grid cells. The simulation was initiated at 1200 UTC, which is 6:00 am local time. It was run through 0530 UTC the following day, so it covers the evening transition of interest. For this simulation, we used the one-equation Lilly SGS model. The time step size was 0.5 s. The case was driven by a 48 hour set of WRF results and run on 1,000 cores of NREL’s Peregrine high-performance computing system, requiring about four days of wall clock time.

Figure 5.13 shows time-height contours of horizontal wind speed as calculated by the WRF-mesoscale simulation in the model column (3 km x 3 km cells) nearest the SWiFT site (left) and as calculated by SOWFA during the period of interest (right). The SOWFA results are planar averaged at each height because that microscale solver resolves turbulence. SOWFA was run in a mode in which the source terms are computed to force the planar average profiles toward the WRF profiles; therefore, they match the WRF input. This is a novel, internally forced MMC method that is akin to data assimilation. It is powerful in that any mean profile time-history can be given to the solver and it will match that in the mean, but it will naturally develop turbulence that is compatible with these mean input profiles. Figure 5.14 shows the same simulation, but as time histories of wind speed and potential temperature at the 85 m level from both WRF and SOWFA. Again, the SOWFA results shown are the planar-averaged results. Locally, the SOWFA results contain resolved-scale turbulence.

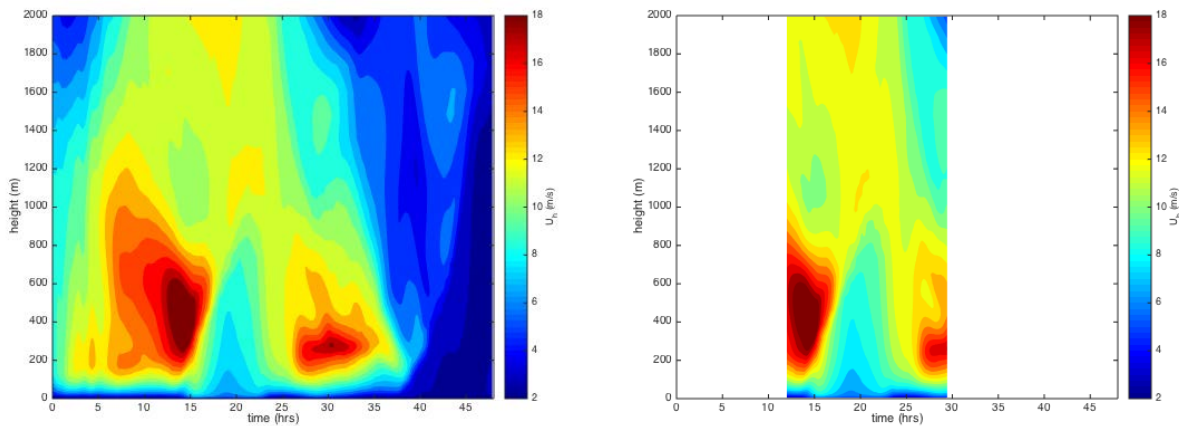


**Figure 5.13.** Time-Height Histories of Horizontal Wind Speed of the November 8 SWiFT Case from the WRF-Mesoscale Simulation (left) and the Planar-Averaged Horizontal Wind Speed from SOWFA (right)

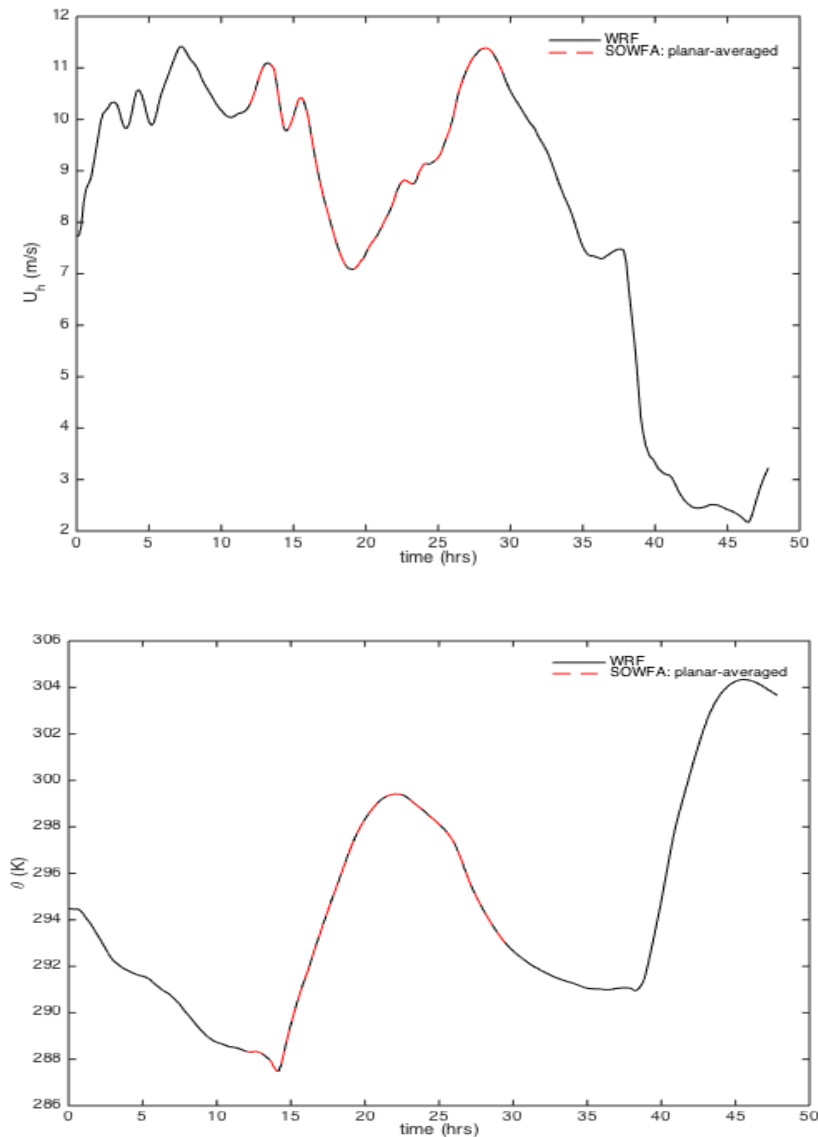


**Figure 5.14.** Time-History of the 85 m Horizontal Wind Speed (top) and Potential Temperature (bottom) from WRF and SOWFA; the SOWFA Results are Planar Averaged

To demonstrate the fact that the microscale solver, when run in this coupling mode, creates resolved-scale turbulence that is compatible with the mean input profiles of velocity and temperature, we show 80 m slices of instantaneous horizontal velocity at five different times of day (Figure 5.15). The first is 8:00 local time, just after the sun has risen. The stratification near the surface is still quite stable, as seen by the small-scale turbulent structures. The next is 10:00 local time. Here, long streaky structures are obvious that indicate long roll cells. These structures are realistic and occur in shear-driven, lightly convective conditions, such as this transitional time between stable and unstable stratification. Next, 14:00 local time is shown, and the conditions have become much more convective. The turbulent structures are large and patchy, which are indicative of moderately strong convection in the presence of shear. At 17:00 local time, the sun is about to set, and convection is weakening. The simulation here is in the evening transition. Again, we see the long streaks indicative of roll cells. Last, at 18:00 local time, the

stratification has again become stable near the surface, and the turbulence structure is again small in scale; however, there is some large-scale weak variation left over from the daytime turbulence.

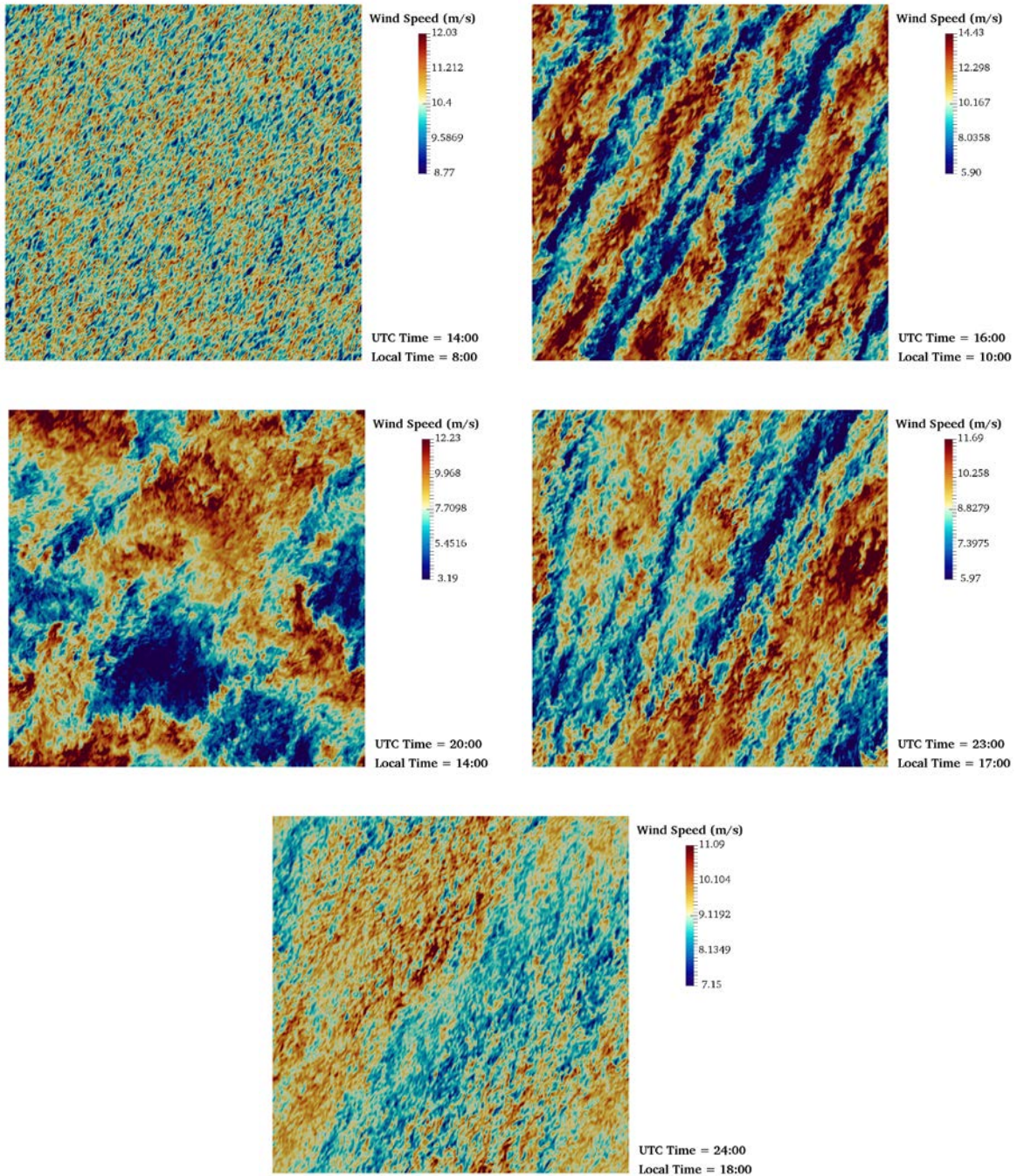


**Figure 5.15.** Horizontal Slices at 80 m above the Surface of Instantaneous Horizontal Velocity from the SOWFA SWiFT November 8 Simulation at Various Times of Day

## 5.5.2 Comparison of Internal Mesoscale Tendency Versus Boundary Forcing using WRF

Two nonstationary case studies are investigated with the WRF model using both fully boundary-coupled nested simulations and offline LES with periodic LBCs forced by mesoscale model derived forcing. The nesting approach used for the WRF boundary-coupled simulations is similar to that presented by Rai et al. (2016), with six telescoping WRF model domains (three mesoscale and three LES), starting with a horizontal resolution of 12.15 km down to a resolution of 30 m, as shown in Figure 5.16. Domains 1, 2, and 3 are WRF-mesoscale domains in which the model is run using a standard one-dimensional boundary-layer parameterization and horizontal grid spacing of 12.15, 4.05, and 1.35 km, respectively. Domains 4, 5, and 6 are the LES domains that use a standard 3D SGS turbulence parameterization to represent features of the flow that are SGS. The horizontal resolution of the WRF-LES domains are 270, 90, and 30 m, respectively. Other than the boundary-layer and convective parameterizations, the same suite of physics parameterizations is applied on each domain. Care has been taken when making the jump from the mesoscale to LES domains to avoid having a grid with resolution in *terra incognita* (see the description of *terra incognita* issues in section 4.0 of this report). In this setup, the LBCs for each nested domain are provided by the bounding domain. For the coarsest LES domain nested within the finest mesoscale domain, no treatment has been applied to accelerate the development of turbulence, as described in section 6.0; however, this remains as future work.

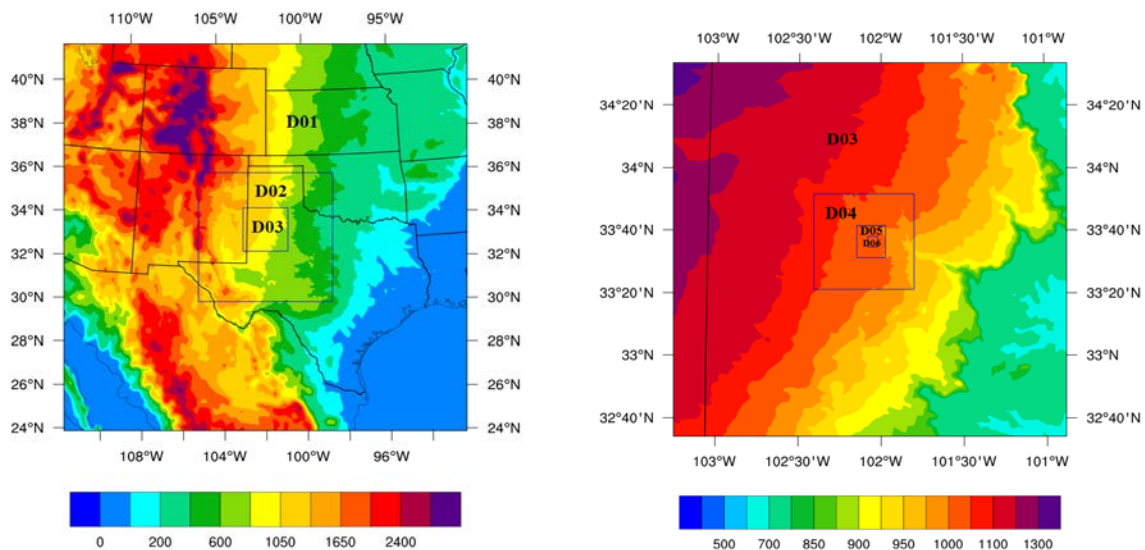


**Figure 5.16.** Computational Domains for Mesoscale Simulations (D01, D02, and D03; left) and LES (D04, D05, and D06; right) with Terrain Elevation (m; colors) and State Boundaries

The mesoscale-derived forcing parameters applied within the offline LES include geostrophic wind components and advective horizontal velocity and temperature tendencies extracted from the same mesoscale simulations used to force the nested simulations (performed in the manner described in section 5.1). While the mesoscale forcing parameters are allowed to vary in the vertical direction, homogeneity is enforced within each horizontal plane to obey the constraints imposed by the use of periodic LBCs.

Figure 5.17 shows instantaneous cross sections with the wind speed at approximately 90 m above the ground during three segments of the diurnal cycle case occurring on November 8. These cross sections represent convective (top), neutral (middle), and stable (bottom) conditions, from both the nested

simulations (Domains 5 and 6) as well as from a stand-alone LES using periodic LBCs, and forced with tendencies derived from the mesoscale simulations (as described in detail in section 5.2).

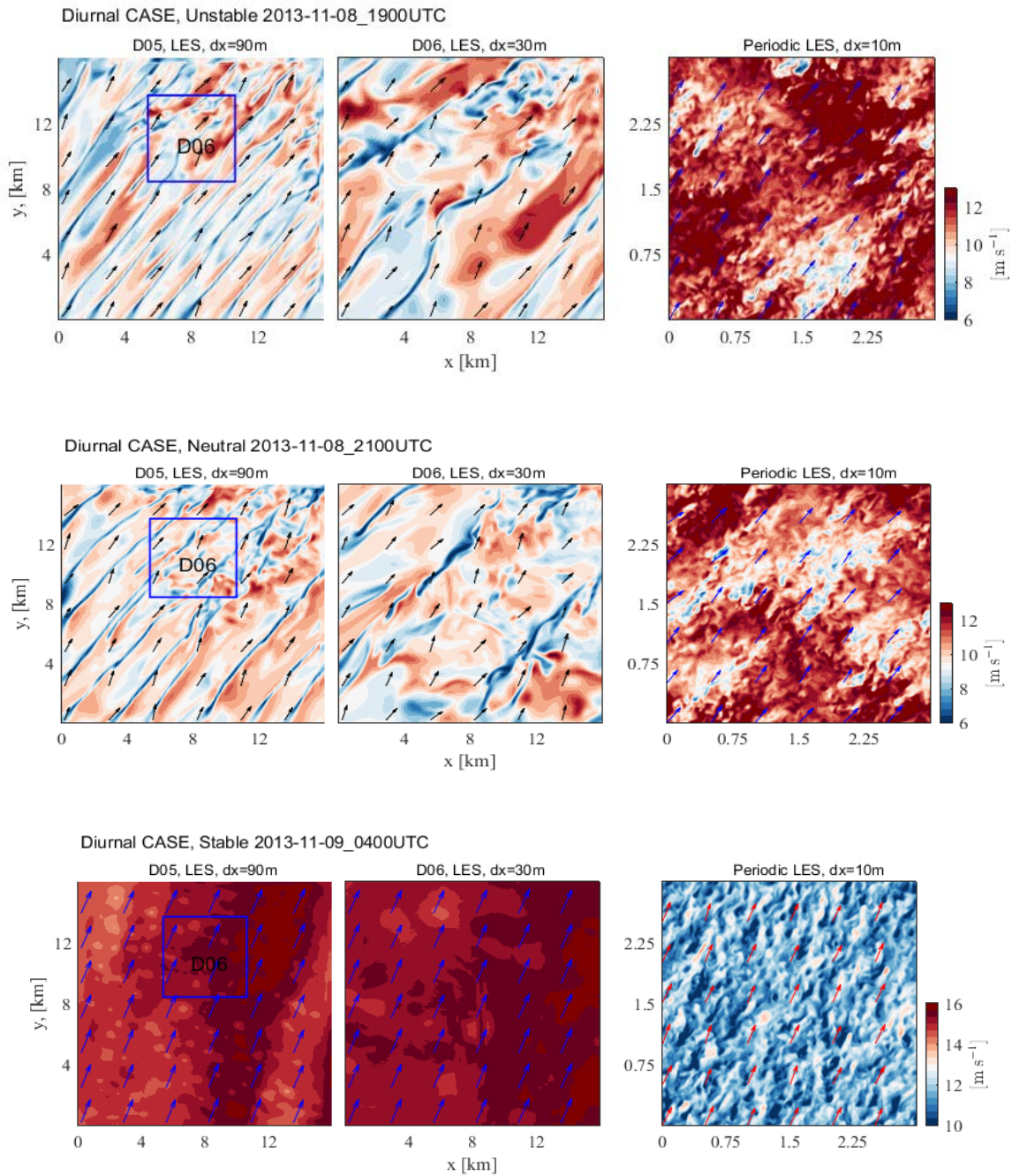


**Figure 5.17.** Simulated Wind Speed Approximately 90 m Above the Surface for Domains 5 and 6 using a Nested LES Configuration (left and center) with a 90 and 30 m Horizontal Resolution and Periodic LES with a 10 m Horizontal Resolution (right) during Periods with Convective (top), Neutral (middle), and Stable (bottom) Conditions

Figure 5.17 reveals significant differences in the morphology of the simulated flow field depending upon the type of coupling method employed, with the offline LES producing a fully-developed turbulence spectrum at all times, as opposed to the online coupled LES, which indicates the presence of elongated roll structures oriented in the streamwise direction advecting into the LES domains from the bounding mesoscale simulation, similar to those observed for the SOWFA model runs described previously. During convective and neutral conditions, these rolls slowly give rise to a 3D turbulence spectrum. While the large distance required for the emergence of 3D turbulence cascade is the subject of section 6.0, it is noted here that the roll structures do not appear in the LES using periodic LBCs, suggesting that either the offline LES domains are too small to capture these features, or that these structures might be artifacts of the mesoscale simulation (Ching et al. 2014). Little difference is observed between the nested and offline LES during convective and neutral conditions, except for the appearance of slightly higher peak velocities in the offline LES occurring during convective conditions due to increased downward transport of momentum.

The more significant differences appear during stable conditions. The online coupled simulations feature the disappearance of the roll structures and cessation of turbulence motions in general, accompanied by a dramatic increase in wind speed. The offline LES, on the contrary, maintains a resolved turbulence spectrum, albeit with smaller integral scales, and also depicts a significant reduction in mean wind speed. The reduction of wind speeds at 90 m above the surface is consistent with a reduction of downward momentum transport in the presence of less energetic turbulence, and is also at a height below the nose of the developing LLJ (not shown).

The precise reasons for the significant differences in mean wind speed between the two coupling methods are currently under investigation; however, a likely factor is the application of the mesoscale-derived tendencies. As shown in the section describing the extraction of the mesoscale tendencies (section 5.2), there can be nontrivial levels of noise contained in the mesoscale fields, requiring a method to average or smooth the fields. Examination of mean wind speed and direction profiles during the stable conditions occurring on November 8 indicated significant, unphysical variability occurring near the surface that was traced to the mesoscale geostrophic winds. Because the mesoscale geostrophic winds are computed directly from the resolved horizontal pressure gradients at each vertical level during a simulation (see equation (3)), small-scale pressure fluctuations near the surface do not represent the synoptic-scale pressure distribution, but rather arise from other atmospheric processes, and are incorrectly assigned to the geostrophic winds. One potential remedy is to instead use the value of the geostrophic wind occurring just above the ABL top throughout the entire ABL. However, this approach would remove baroclinic effects within the ABL that could be important for subsequent LLJ development. A better approach would be to develop a robust means of detecting and removing spurious variability near the surface, allowing for important baroclinic effects to be captured, while filtering out the noise.

Figure 5.18 provides an example of how the removal of both near-surface noise and real atmospheric forcing can influence ABL wind speed prediction. Vertical profiles of wind speed each hour during the evening transition and development of the LLJ on November 8 are shown from three simulations: the WRF-mesoscale (top), the online coupled LES (middle), and the offline periodic LES (bottom). Rather than using the mesoscale-derived tendencies at each model height throughout the ABL, these simulations instead used constant values of the geostrophic wind speeds, computed from just above the ABL height during the WRF-mesoscale simulations, throughout the depth of the ABL. This approach had the effect of removing much of the spurious noise, but also removed some of the real atmospheric forcing required to capture the correct evolution of the LLJ.

The boxes indicate wind speeds greater than  $14 \text{ m s}^{-1}$  between the surface and 300 m, representing rated power for most wind turbines, whereas the horizontal bars superimposed on the LES wind speed profiles indicate two standard deviations of the resolved variability within each domain over each hour of planar

averaging. The offline periodic LES in this case produces an LLJ that is weaker than either the online coupled or the mesoscale simulations, with a difference of approximately  $5 \text{ m s}^{-1}$  at the jet nose at 2000 CST. The weaker LLJ in the offline coupled LES underscores the importance of baroclinicity and advection within the ABL that were filtered from these simulations. Future efforts will seek to formulate a robust method for separating the signal from the noise in the preparation of mesoscale-derived fields for offline microscale forcing.

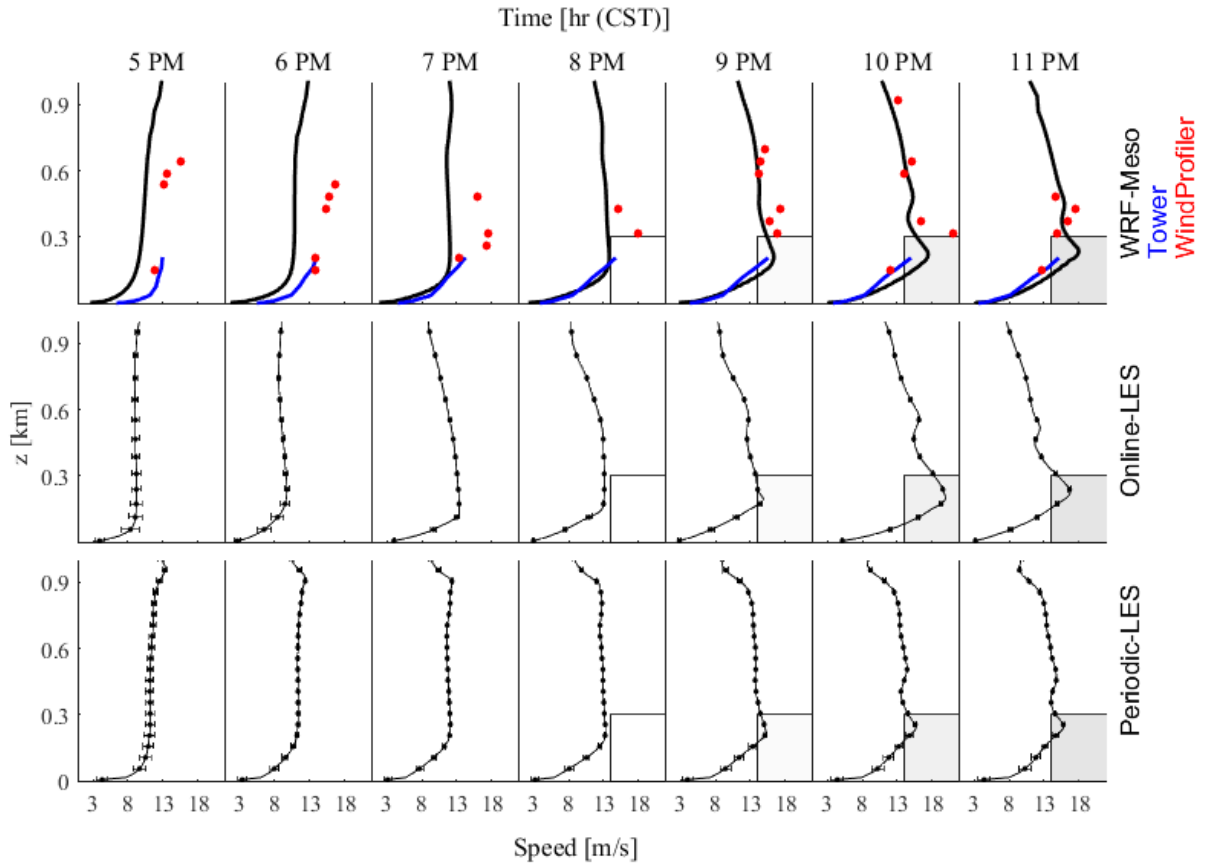


**Figure 5.18.** Vertical Profiles of Wind Speed during the Evening of November 8 from the WRF-Mesoscale (top), Online Coupled LES (middle), and Offline Periodic LES (bottom) with the Noise Removed from the Lower Portion of the Geostrophic Wind Profiles, as Described in the Text

### 5.5.3 Formal Assessment of November 8, 2013 Diurnal Case

As described previously, the simulations of diurnal evolution with nearly stationary synoptic forcing observed on November 8 were carried out by forcing LES with time-varying profiles of geostrophic wind and advection tendencies extracted from a precursor mesoscale simulation with WRF. 10 min running means of simulated wind speed, wind direction, temperature, TKE, turbulent stress, and sensible heat flux were interpolated to the levels of 4.0 m, 10.1 m, 16.8 m, 47.3 m, 74.7 m, 116.5 m, 158.2 m, and 200.0 m above the ground corresponding to the observations at the SWiFT facility tower.

In Figure 5.19 and Figure 5.20, observed wind speed and wind direction are compared to wind speed and direction simulated with SOWFA and WRF-LES. Both SOWFA and WRF capture the general evolution of the wind speed during a 12 hour period starting at 1200 UTC. Both WRF and SOWFA captured strong shear in the early-morning, stably stratified ABL well. However, following the morning transition, after 1400 UTC, WRF overpredicts and SOWFA underpredicts the wind speed. As can be observed from Figure 5.20, both models captured the wind direction accurately. Slight differences between simulated and observed wind direction are noticeable in the early morning when observations display more significant wind veer.

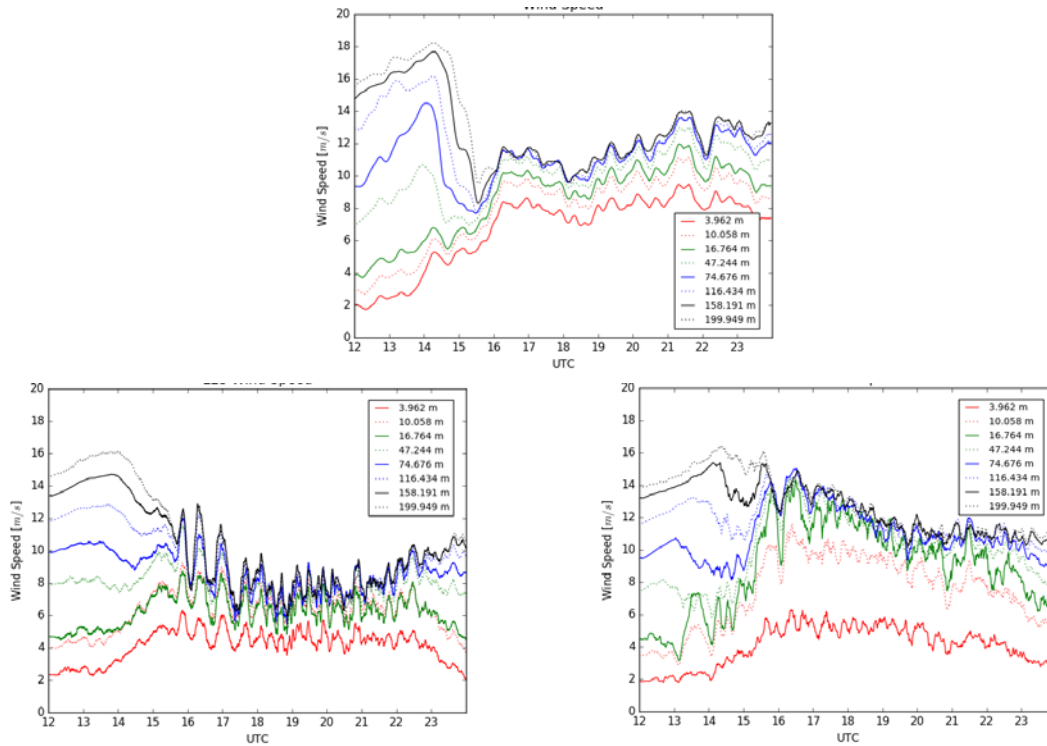


**Figure 5.19.** Wind Speed—Diurnal Case Based on Observations on November 8, 2013; SWiFT Facility Tower Sonic Anemometer Measurements (top), SOWFA LES (bottom left), and WRF-LES (bottom right)

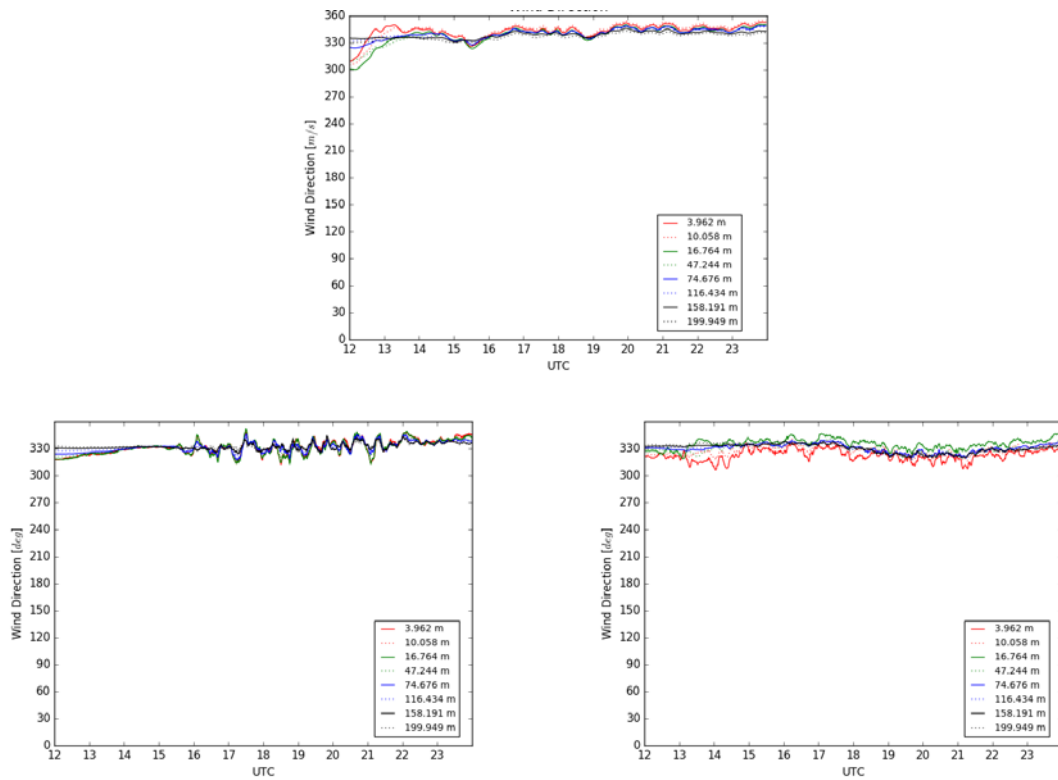


**Figure 5.20.** Wind Direction—Diurnal Case Based on Observations on November 8, 2013; SWiFT Facility Tower Sonic Anemometer Measurements (top), SOWFA LES (bottom left), and WRF-LES (bottom right)

Comparison of the evolution of temperature shown in Figure 5.21 demonstrates that both SOWFA and WRF have a significant bias of more than 5 kelvins (K). This bias is likely related to the bias in temperature prediction by a mesoscale simulation. Section 4.0 documented the underprediction of temperature in the mesoscale model simulations for this case day. Also noticeable is that the observed daytime superadiabatic surface layer is stronger than simulated, again as noted in the mesoscale runs of section 4.0. However, the trends in temperature evolution from stable stratification, through morning transition, to evolution of a convective ABL are captured well by both models, once again following the forcing of the mesoscale model.

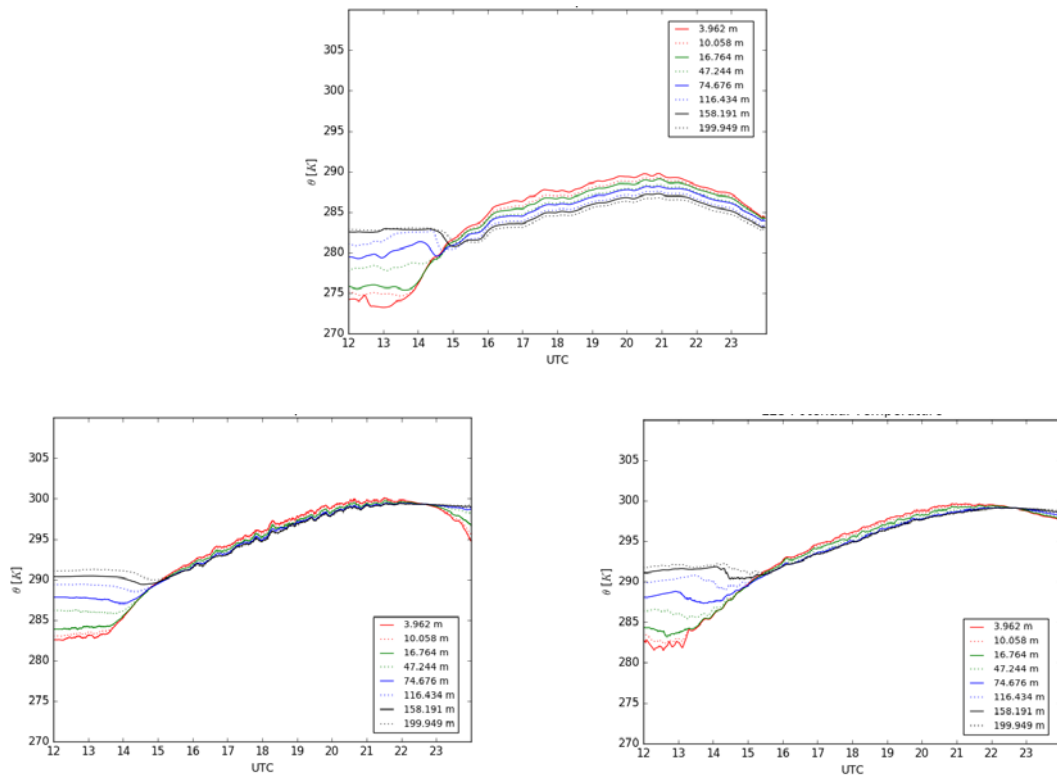


**Figure 5.21.** Temperature—Diurnal Case Based on Observations on November 8, 2013; SWiFT Facility Tower Measurements (top); SOWFA LES (bottom left); and WRF-LES (bottom right)

TKE levels in both LESs are higher by a factor of two or more than the observed TKE level as shown in Figure 5.22. While this may be attributed to a stronger low-level shear in LES with WRF, the cause is not obvious for the simulation with the SOWFA model. Similarly, turbulent stresses presented in Figure 5.23 are overpredicted by both models. Again, the SOWFA model overprediction is greater than that provided by WRF. While turbulent stresses are overpredicted, turbulent sensible heat fluxes are underpredicted (Figure 5.24). SOWFA significantly underpredicts sensible heat flux at all levels whereas WRF underpredicts fluxes at upper levels.

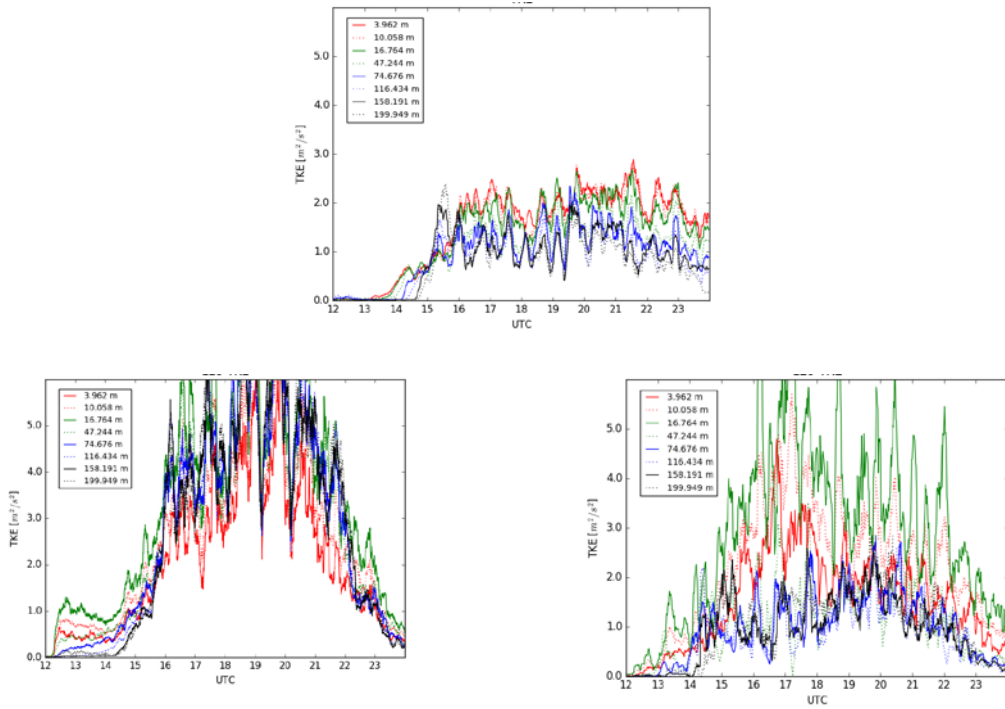


**Figure 5.22.** TKE—Diurnal Case Based on Observations on November 8, 2013; SWiFT Facility Measurements (top), SOWFA LES (bottom left), and WRF-LES (bottom right)

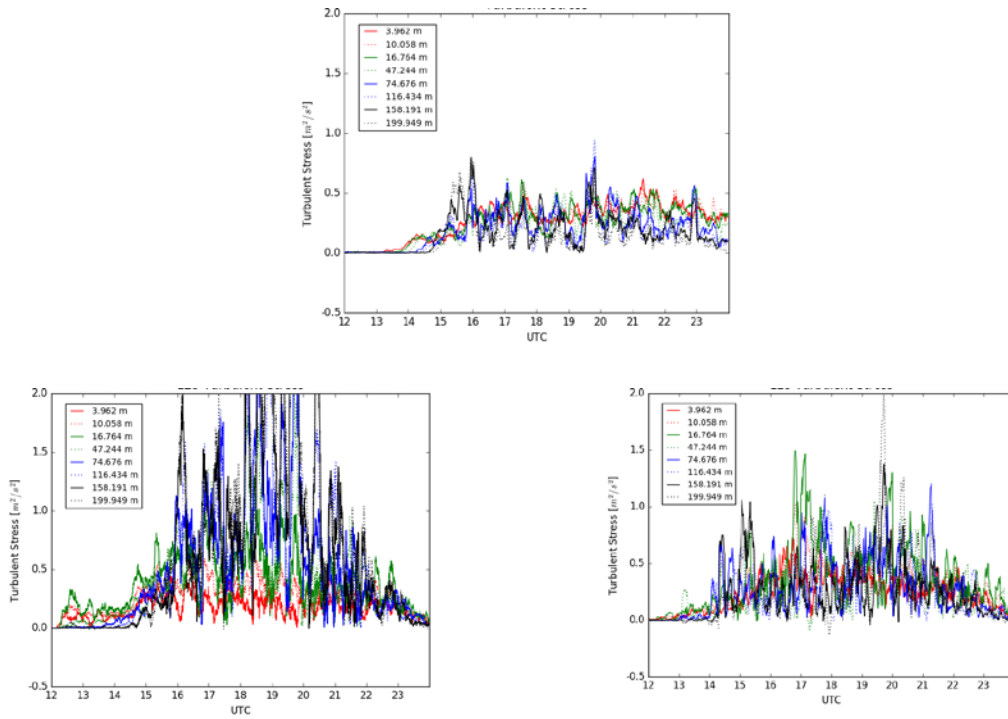


**Figure 5.23.** Turbulent Stress—Diurnal Case Based on Observations on November 8, 2013; SWiFT Facility Measurements (top), SOWFA LES (bottom left), and WRF-LES (bottom right)

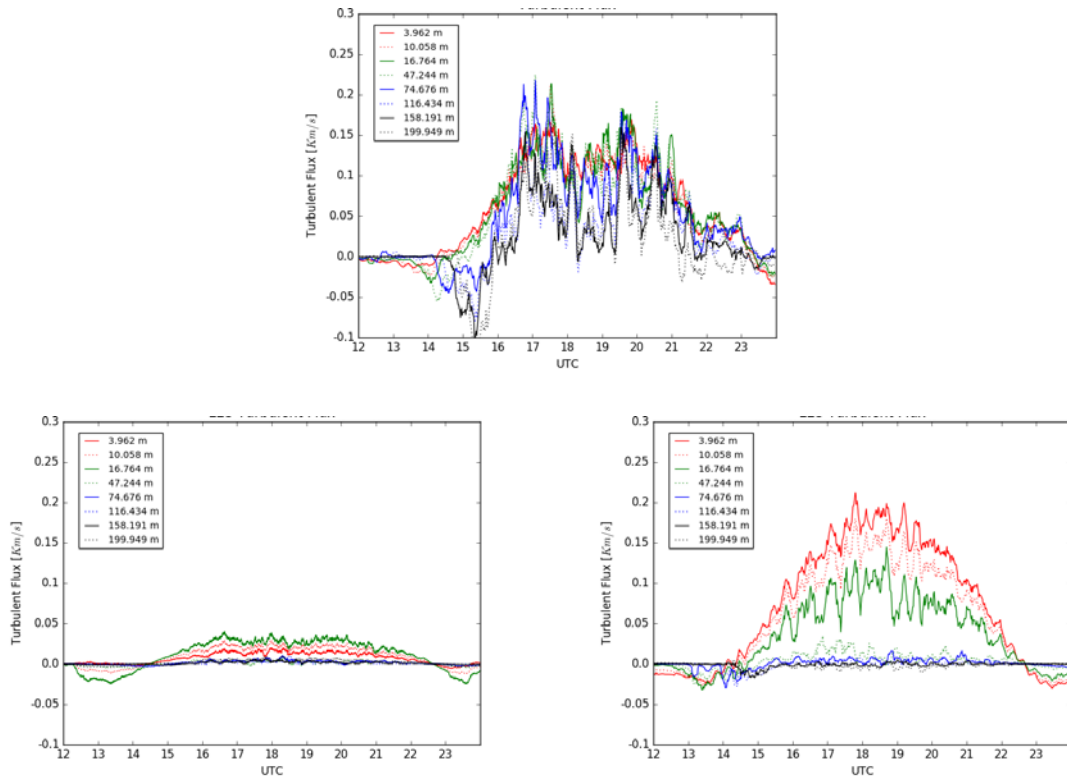


**Figure 5.24.** Turbulent Sensible Heat Flux—Diurnal Case Based on Observations on November 8, 2013; SWiFT Facility Measurements (top), SOWFA LES (bottom left), WRF-LES (bottom right)

The accuracy of LES depends on the precision of the external forcing and the representation of the internal unresolved processes that need to be parameterized. Without perfect external forcing, it is not possible to assess, in detail, the error resulting from parameterization of unresolved or underresolved processes such as turbulent mixing. However, based on the analysis of periodic LES forced with large-scale forcing derived from a precursor mesoscale simulation, it can be concluded that this is a viable approach to realistic microscale ABL simulations under slowly evolving synoptic forcing. While mean flow properties, mean wind speed and direction, and temperature evolution are captured well with LES, the turbulent quantities display larger discrepancies when compared to the observations. In the surface layer of an ABL, the accuracy of LES critically depends on the parameterization of the subgrid stresses and fluxes and their boundary conditions. Because it is impossible to resolve the viscous sublayer in LES, the imposed approximate surface boundary conditions are based on the Monin-Obukhov similarity theory linking mean wind and temperature to turbulent stress and sensible heat flux (see section 5.3). It is likely that the observed errors in representing turbulent stresses and fluxes can largely be attributed to the accuracy of these surface boundary conditions and the parameterization of unresolved and underresolved turbulent mixing, rather than to the accuracy of the imposed external forcing from a mesoscale simulation. This confirms the importance of including the mesoscale forcing as well as further studying the best way to incorporate the surface boundary conditions and resolve the turbulence—both topics of the following year’s efforts.

## 5.6 Frontal Passage Case Forcing Through Online Boundary Conditions and Mesoscale Tendencies

A frontal passage case that occurred on May 12, 2014 was selected as an additional test of various MMC techniques to show a situation with rapidly changing mesoscale conditions. The team selected a case of frontal passage, which is described in more detail in section 3.2.2.

### 5.6.1 Case Modeling

Two different model configurations have been used in this case: (1) full online one-way coupling in which three telescoping mesoscale and LES domains are applied, and (2) a configuration with periodic boundary conditions and forcing derived from the mesoscale model. A time-height cross section of conditions at the SWiFT facility is shown in Figure 5.25. This highlights the rapid change in temperature, wind direction, and hub-height wind speed as the simulated front passes around 0900 UTC.

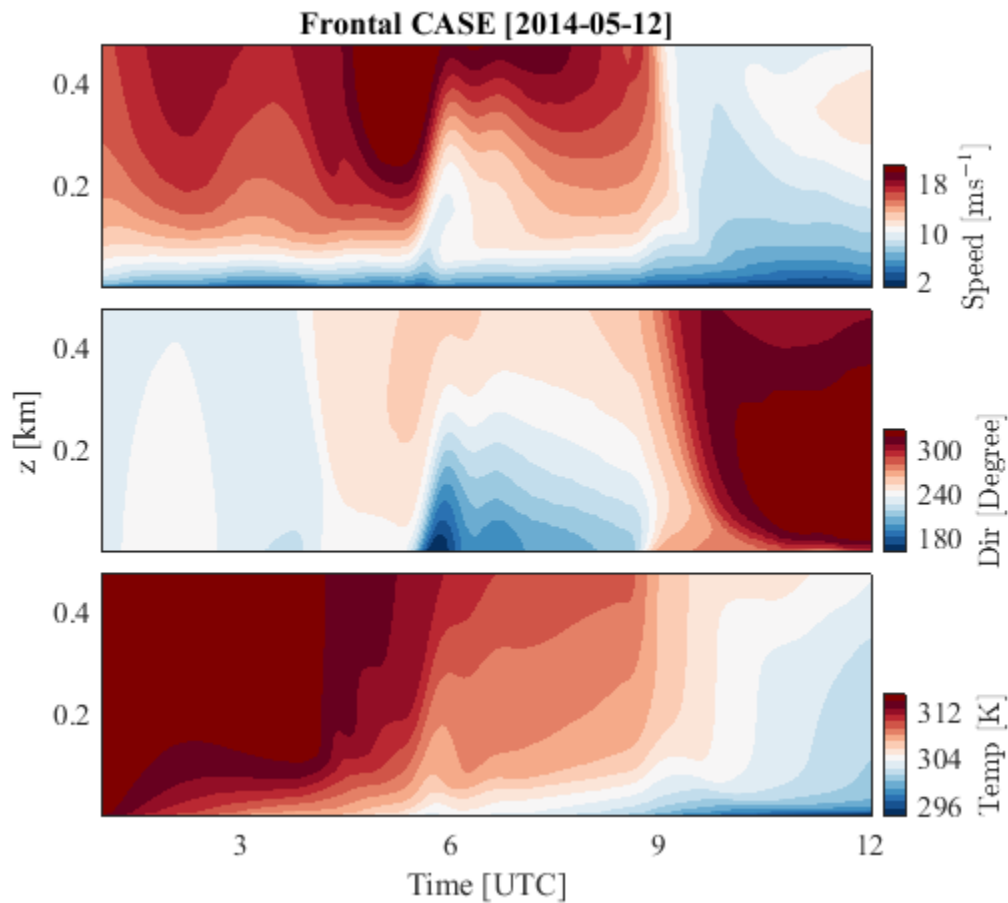


**Figure 5.25.** Simulated Time-Height Cross Section of Wind Speed (top), Wind Direction (center), and Temperature (bottom) at the SWiFT Site

Similar to our results for the November 8 case, there are large differences between the simulated wind speed in the nested LES configuration and the setup using periodic LBCs and forcing from the mesoscale model. In general, the nested LES produces streak-like structures, whereas the periodic configuration has cellular-like structures in the velocity field and includes a well-developed cascade of turbulence scales.

Note that random temperature perturbations are applied at the start of the simulation when using the period setup. There is more low-frequency variability captured with the nested configuration. For example, at 0800 UTC, the wind speed in the southeasterly part of Domain 5 is generally greater than  $10 \text{ m s}^{-1}$ , but there are streaks with much smaller and larger wind speed in the northwest and northeast corners, respectively, of the domain. The simulated wind speed is also much larger in the periodic case during the prefrontal period. As the front passes through the SWiFT site, the wind direction changes in both model configurations and the wind speed in the nested LES remains smaller than that found for the configuration using periodic boundary conditions. At this time, the streaks in the nested simulations become more obvious, and there are larger differences in the maximum and minimum wind speed in both Domains 5 and 6. After the frontal passage, the speed is larger in the simulation using the nested domains, and the streaks that were apparent before and during the frontal passage are less obvious. In contrast, the wind speed in the periodic configuration is much smaller after the frontal passage. Again, it is not clear to what extent these larger-scale roll structures represent reality or mesoscale artifacts.

The simulated wind speeds are also much larger in the periodic case during the prefrontal period. As the front passes through the SWiFT site, the wind direction changes in both model configurations and the wind speed in the nested LES remains smaller than that found for the configuration using periodic boundary conditions. At this time, the streaks in the nested simulations become more obvious, and there are larger differences in the maximum and minimum wind speed in both Domains 5 and 6. After the frontal passage, the wind speeds remain significantly greater in the nested domain simulation, and the streaks that were apparent before and during the frontal passage are less obvious, likely due to the cessation of convection occurring in the more stable postfrontal air mass.

As in the November 8 case, the wind speeds in the periodic configuration are much lower in the stable conditions (here following the frontal passage), likely due in part to reduced downward momentum transport supported by the weaker turbulence. However, the use of constant geostrophic wind values below the ABL top likely removed some of the baroclinity impacting low-altitude wind speed and direction changes, reinforcing the need to develop robust techniques for removing noise from the signal near the surface in mesoscale-derived forcing parameters.

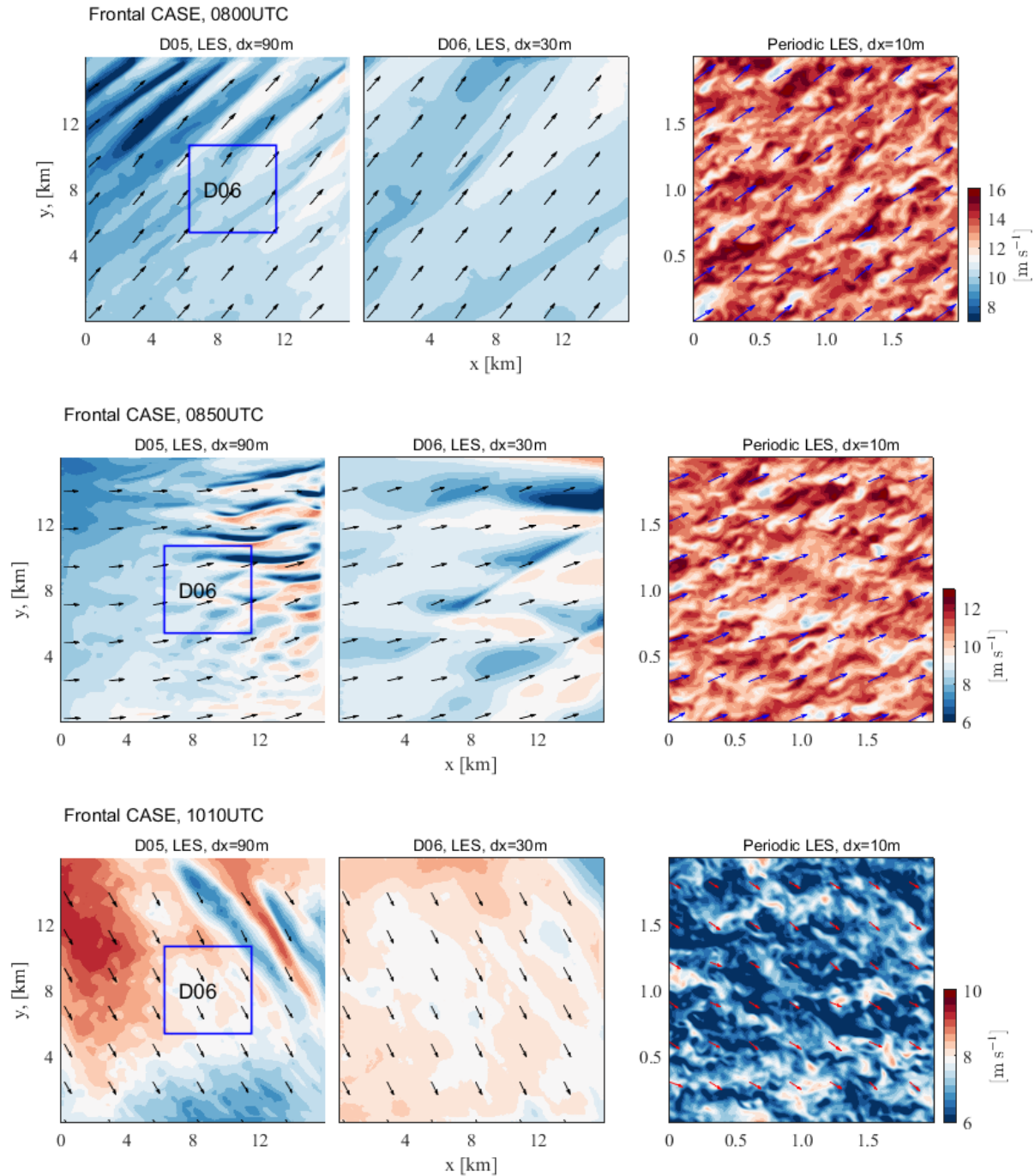


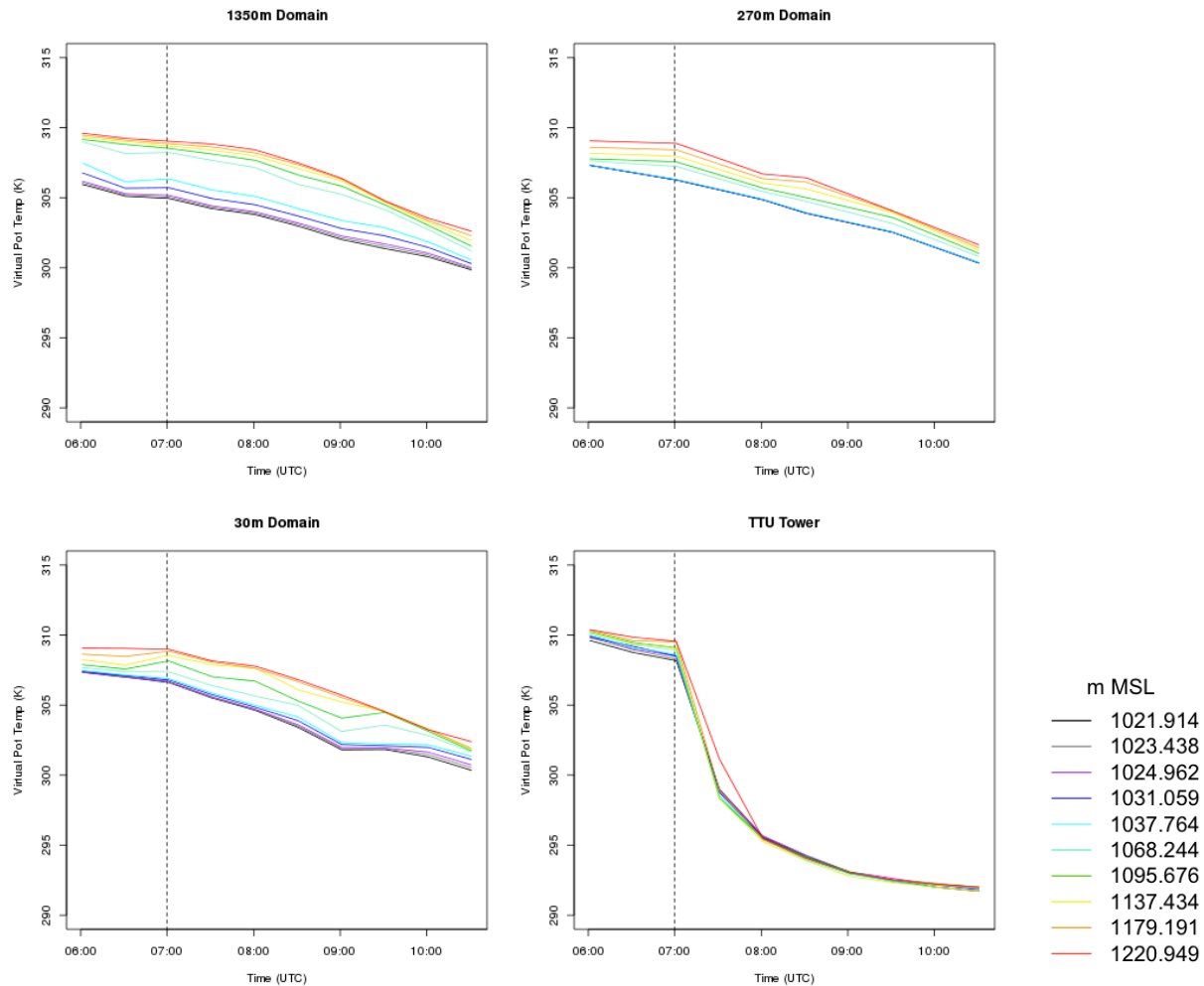
**Figure 5.26.** Simulated Wind Speed Approximately 90 m Above the Surface for Domains 5 and 6 using a Nested LES Configuration (left and center) with a 90 and 30 m Horizontal Resolution and periodic LES (right) with a 10 m Horizontal Resolution Before (top), During (middle), and After (bottom) the Frontal Passage

## 5.6.2 Large-Scale Assessment of Frontal Passage Case

The large-scale features of this frontal passage case were assessed for the period of 0600 UTC to 1100 UTC, with the passage of the front observed around 0700 UTC at the SWiFT tower compared to

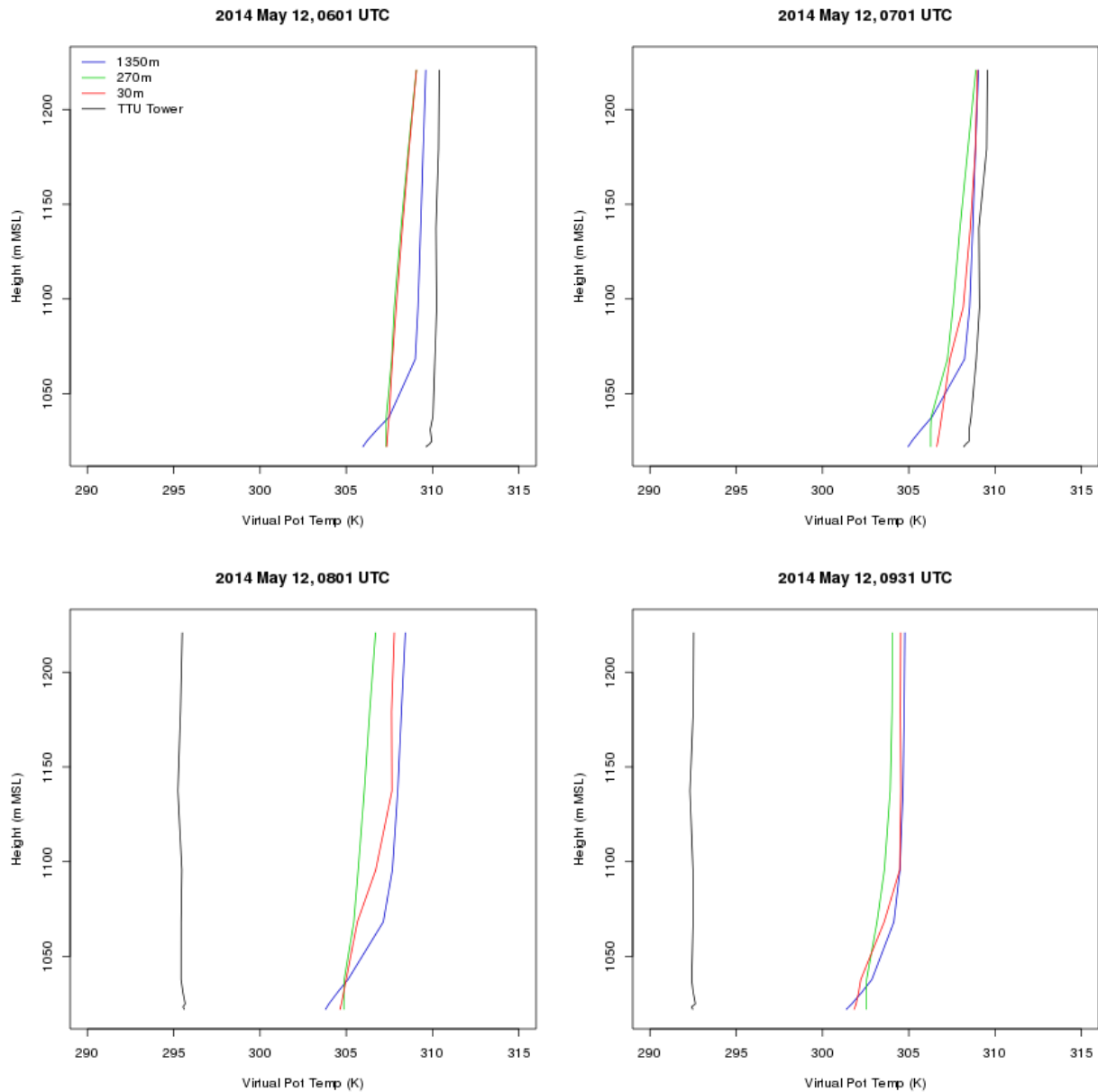
around 0900 UTC in the coupled simulations. Model data were from a GFS-forced WRF simulation using the MYNN boundary layer parameterization for the mesoscale-level simulations and a nested LES model. Three domains (resolutions) were analyzed: 1,350 m, which was a mesoscale-level simulation with boundary layer parameterization, and 270 m and 30 m, which were run as nested LES. To produce the matched pairs for comparison, the closest gridpoint to the SWiFT tower site from the WRF model output was chosen and vertical levels were linearly interpolated to match the tower levels.

Figure 5.27 displays a time series of the virtual potential temperature for each of these domains, at each vertical level. The cold-frontal passage is clearly visible in the tower observations (lower right) as seen in the rapid drop in virtual potential temperature at 0700 UTC. In contrast, the virtual potential temperatures in the three model domains, which start a few degrees cooler than the observations, decrease at a much slower rate over the period. There is some indication that the decrease in temperature did start around the time of frontal passage, but the strength of that passage in terms of temperature was not captured by the model. Given that the mesoscale grid did not capture the steep change, it is not surprising that the nested LES followed suit. Additionally, near-surface levels were cooler at the tower location in the model results than with the observations. The model results show a steeper lapse rate than the observations, where each level had similar virtual potential temperatures, particularly after the cold front passed. This variation in the temperature across levels was more pronounced in the mesoscale simulation (1,350 m) than in the LES simulations (270 m and 30 m).



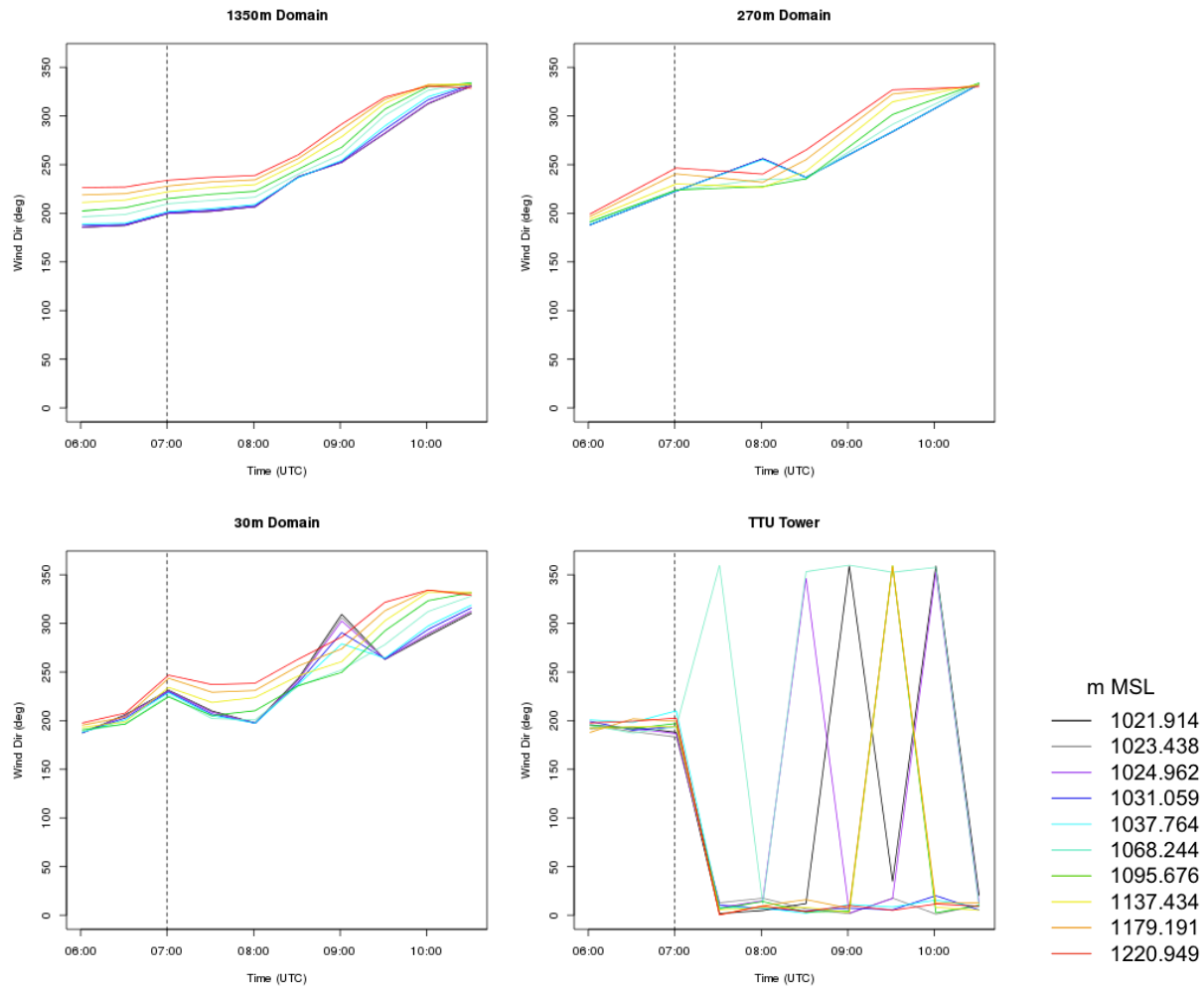
**Figure 5.27.** Time Series of Virtual Potential Temperature from Three WRF Domains and the SWiFT Location Tower on May 12, 2014. Approximate time of observed frontal passage is marked with a vertical dash line.

Vertical profiles were extracted at approximately hourly intervals before and after the observed frontal passage and are displayed in Figure 5.28. Prior to the observed frontal passage, the WRF output was slightly cooler at all levels and domains than the observed virtual potential temperature, but these differences were quite small (on the order of 2 K). The shape of the profile appears best matched in the LES simulations at 270 m and 30 m, with too much of a decrease in the virtual potential temperature with height observed in the 1,350 m mesoscale simulation. This low-level decrease was consistent both before and after the frontal passage. The two time periods after the frontal passage show the timing and strength error in the simulation with virtual potential temperature differences of nearly 10 K. The 270 m simulation, and to a lesser extent the 30 m simulation, more closely represent the isothermal nature of the virtual potential temperature profile observations for this case.



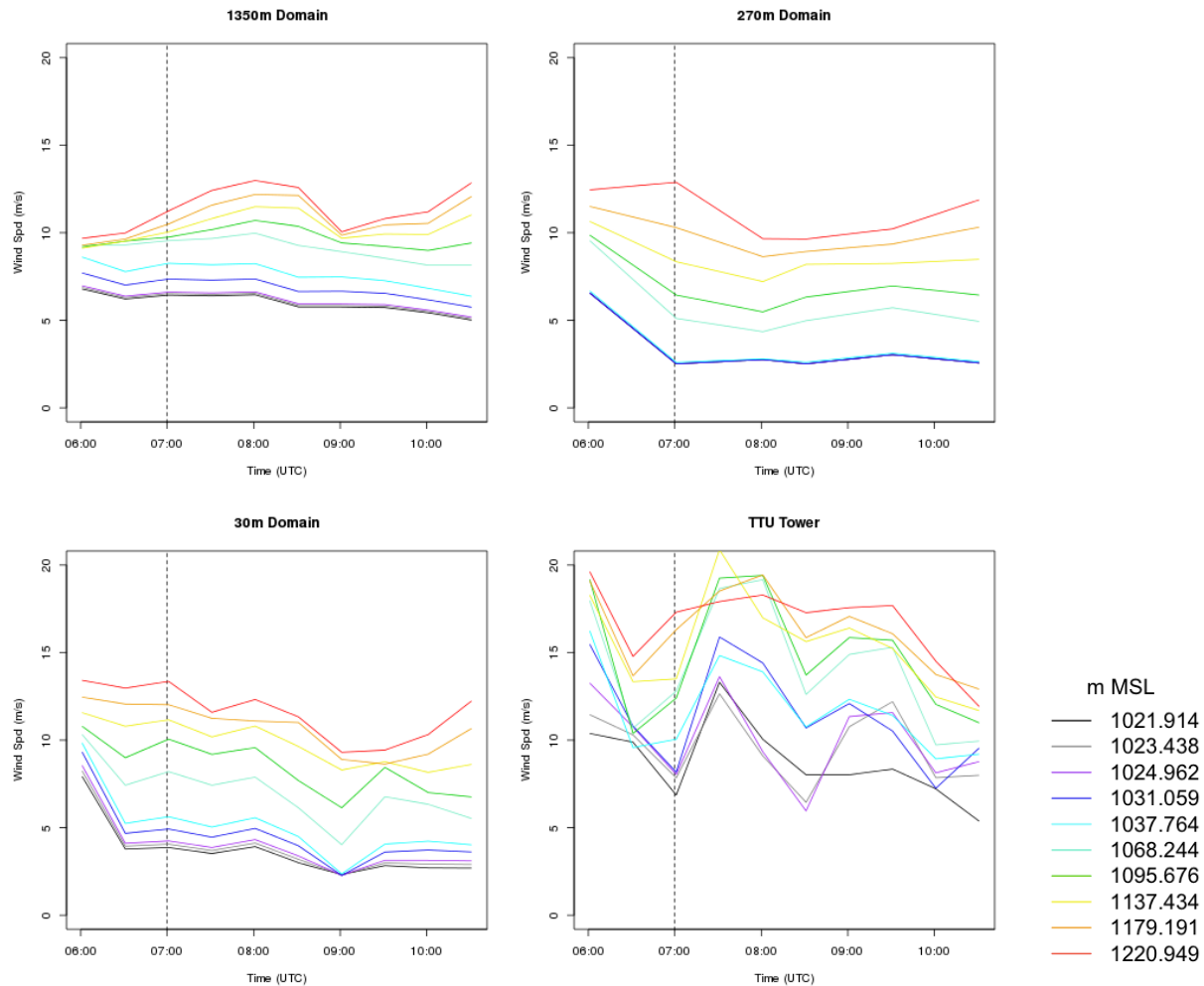
**Figure 5.28.** Vertical Profiles of Virtual Potential Temperature from Three WRF Domains and the SWiFT Location Tower on May 12, 2014. The top row provides profiles prior to the observed frontal passage and the bottom row provides profiles after the observed frontal passage.

Figure 5.29 is a time series of wind direction for the three model domains and the tower observations. The WRF output for wind direction suggests that frontal passage in the model may have been between 0800 UTC and 0900 UTC, where wind direction slowly veers from southwesterly to northwesterly (note that in section 5.5.1, we found evidence that model frontal passage was nearer to 0900 UTC). In contrast, wind direction was observed initially to be close to that of the model, but at 0700 UTC shifted to northerly with the passage of the front. In addition to the timing offset, the difference in the wind directions (more northwesterly in the model compared with closer to due north in the observations) may have had some impact on the relative lower intensity of the front in the model versus the observations.



**Figure 5.29.** Time Series of Wind Direction from Three WRF Domains and the SWiFT Location Tower on May 12, 2014. Approximate time of observed frontal passage is marked with a vertical dashed line.

The wind speed time series in Figure 5.30 indicates that, overall, the WRF simulations did not fully capture the magnitude of the observed wind speeds. Both before and after the observed frontal passage, the observed wind speed was 5–10 m/s faster than the simulated wind speeds. There was a small dip in observed wind speed above 1,031.059 m Mean Sea Level (MSL) right before the observed frontal passage at 0630 UTC, and this was captured in the mid-tower levels by the 30 m LES simulation, although there was also a dip in the wind speed in the near-surface tower levels that was not observed. There are additional dips in wind speed in the WRF simulations around 0800 UTC, just prior to the modeled frontal passage, the same pattern that occurred in the observed frontal passage. The 30 m domain captured these all-level dips in wind speed better than the 1,350 m domain. Overall, the 270 m domain did not capture these dips in wind speed as well as the 1,350 m and 30 m domains.



**Figure 5.30.** Time Series of Wind Speed from Three WRF Domains and the SWiFT Location Tower on May 12, 2014. Approximate time of observed frontal passage is marked with a vertical dashed line.

Vertical profiles of wind direction are shown in Figure 5.31. At the beginning of the simulations, the wind direction and profile shape are similar between all three domains and the observed profile, with the best match being the 270 m and 30 m domains. The direction offset manifests just before the observed frontal passage at 0700 UTC, and the westerly offset of modeled wind direction compared to the northerly observations that was seen in Figure 5.29 is observed in the postfrontal profiles. Wind direction begins to turn more northerly (in agreement with the observations) at about 0930 UTC, after the modeled frontal passage. At 0800 UTC, the 270 m domain shows backing from the surface that was not seen in the other WRF domains or the observed profile.

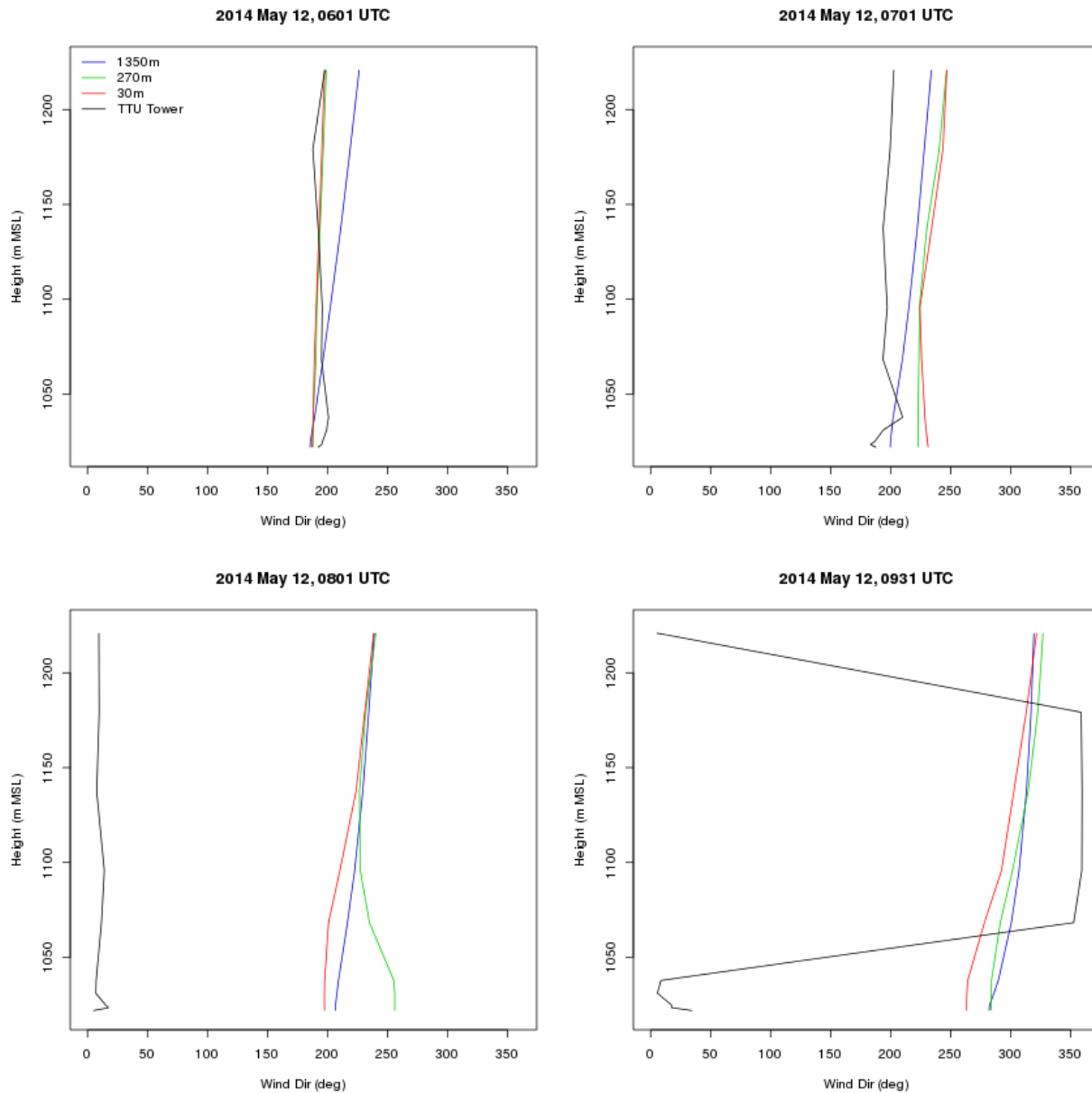


**Figure 5.31.** Vertical Profiles of Wind Direction from Three WRF Domains and the SWiFT Location Tower on May 12, 2014. The top row provides profiles prior to the observed frontal passage and the bottom row provides profiles after the observed frontal passage.

Wind speed (Figure 5.32) profiles were also analyzed and show, in general, that the model did not capture the magnitude of the observed wind speed, being about 5 to 10 m/s different as seen in Figure 5.30. Prior to the observed frontal passage, the higher-resolution domains were closer in magnitude, and to some degree shape, to the observed wind speed profile. After the observed frontal passage, the 1,350 m resolution mesoscale domain had wind speeds closer to the observed (i.e., higher magnitude speeds) than the higher-resolution LES domains. The LES domains still had a speed profile shape that was more representative of the observed wind speed profiles, with an increase in speed with height. The observed wind speeds did increase more quickly in the lower levels than in the simulations; however, the time and strength offsets of the frontal passage in the WRF model likely had an impact on the simulation profiles.

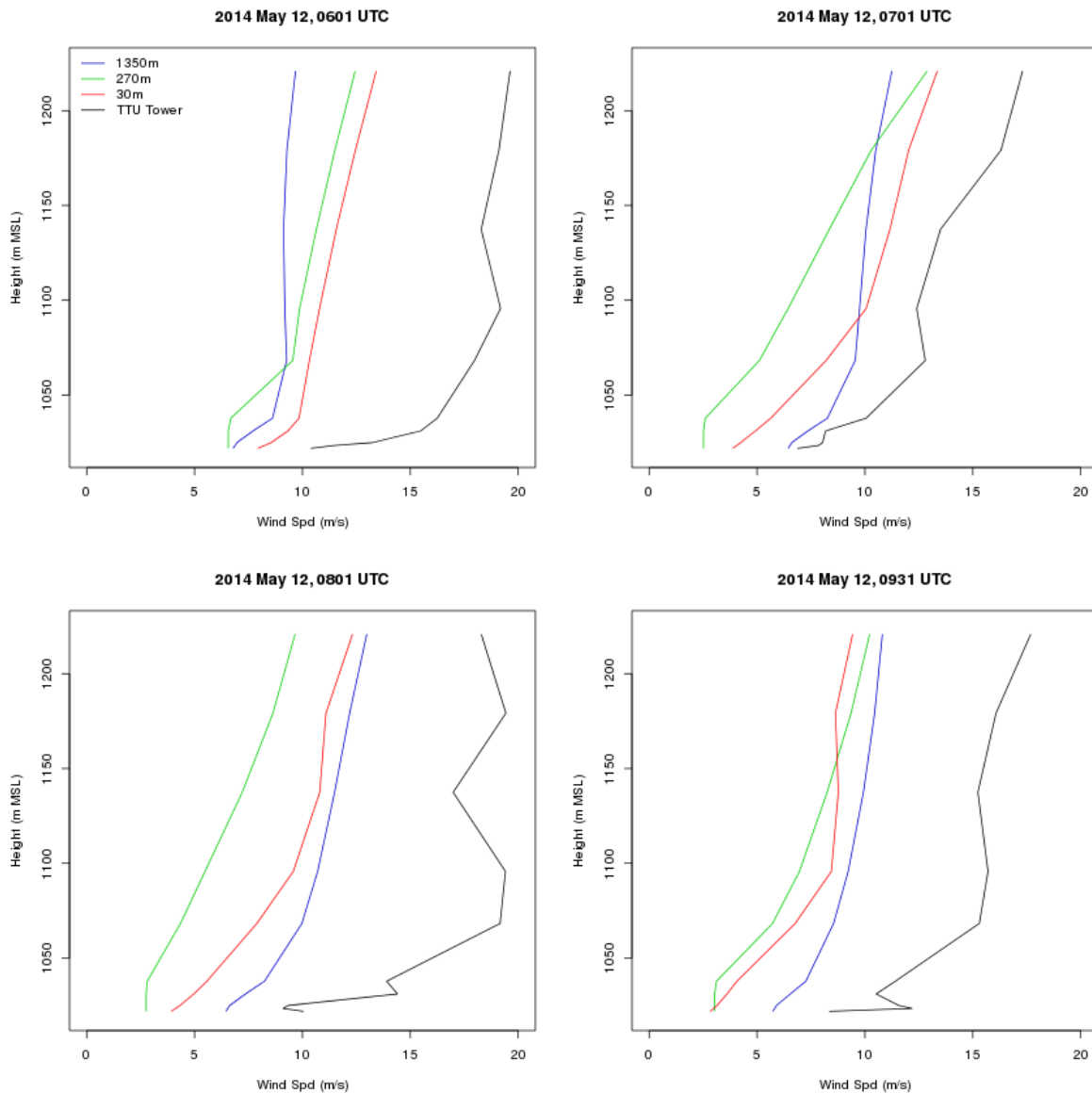


**Figure 5.32.** Vertical Profiles of Wind Direction from Three WRF Domains and the SWiFT Location Tower on May 12, 2014. The top row provides profiles prior to the observed frontal passage and the bottom row provides profiles after the observed frontal passage.

Table 5.1 shows the values of these metrics for each domain size and variable. The values were aggregated across time and vertical levels. Overall, there was a large warm bias of 6 K in the model simulations, which likely correlates with the weaker impact of the front in the model than in the observations. Wind speeds were also lower as noted in the preceding analysis. There was a slight negative (westward) bias in the u-component and slight positive (southerly) bias in the v-component. This is a result of the later frontal passage in the model simulation and the less northerly turn of those winds after the frontal passage compared to the observations. Overall, temperature errors were slightly lower in the 270 m domain than the other domains, wind speed errors were lower in the 1,350 m domain than the others, and u-component errors were lower in the 1,350 m domain whereas v-component errors were lower in the 270 m domain.

**Table 5.1.** Metrics for the May 12 Case. The variables are virtual potential temperature (VPTMP), potential temperature (POT), air temperature (TMP), wind speed (WIND), u-component of the wind (U GRD), and v-component of the wind (V GRD). Units for these are K for temperature, and m/s for wind speeds.

Variable	Domain	ME	MAE	RMSE	CC
VPTMP	1,350 m	6.6	7.7	8.66	0.7
VPTMP	270 m	6	7.34	8.33	0.83
VPTMP	30 m	6.62	7.57	8.49	0.81
POT	1,350 m	7.25	7.71	8.79	0.7
POT	270 m	6.42	7.32	8.47	0.73
POT	30 m	6.96	7.68	8.68	0.7
TMP	1,350 m	7.05	7.43	8.46	0.73
TMP	270 m	6.26	6.99	8.15	0.76
TMP	30 m	6.77	7.36	8.35	0.73
WIND	1,350 m	-4.38	4.4	5.07	0.76
WIND	270 m	-7.01	7.01	7.46	0.76
WIND	30 m	-6.04	6.05	6.53	0.76
U GRD	1,350 m	-0.63	9.33	10.81	0.45
U GRD	270 m	-0.17	11	12.22	0.25
U GRD	30 m	-1.76	10.54	11.64	0.2
V GRD	1,350 m	1.47	5.18	5.85	0.46
V GRD	270 m	1.26	3.45	4.28	0.55
V GRD	30 m	1.86	4.2	5.06	0.53

While the model simulations overall were late on the frontal passage and did not reflect the strength of the front that was observed, the time series and profile analyses did show a slight improvement at the 270 m and 30 m domains over the mesoscale 1,350 m domain, particularly in matching the details of vertical profile shapes. Additional analysis with the LES nested in the mesoscale simulations should be done as this case shows some promise of this method for accurately reflecting vertical distribution of winds.

### 5.6.3 Assessment of Microscale Properties of the Frontal Passage Case

Further assessment of microscale simulations involved in the frontal passage case observed on May 12, 2014 are reported herein. While the ABL in the weakly forced November 8, 2013 diurnal case could be characterized as horizontally homogenous over the simulation domain, the frontal passage case displays an ABL that is distinctly not horizontally homogeneous. The absence of horizontal homogeneity adds a level of complexity to accurate representation of evolution of such an ABL. To better represent the evolution of a heterogeneous ABL, we carried out LES nested within a mesoscale simulation. At present, such “online” nesting can be achieved using the WRF model, but not with SOWFA. As described previously, we used one-way nesting to provide accurate, time-dependent, and spatially varying LBCs to LES. The one-way nesting approach is appropriate when processes resolved on the nested domain do not have a significant effect on the flow on the parent domain. Nested LES was compared to observations and LES over a periodic domain forced with time-dependent profiles of the geostrophic wind and advection tendencies as in the diurnal evolution case discussed previously. Additional complexity results from stable stratification. Under stably stratified conditions, buoyancy acts as a sink of TKE. Because both LESs utilize relatively large grid-cell sizes and the Smagorinsky SGS model, which is absolutely dissipative, it is not possible to resolve a large range of turbulent eddies and maintain a realistic level of turbulence.

Figure 5.33 shows a comparison of the evolution of wind speed over a period of four hours between 0600 and 1000 UTC for observations and 0700 and 1100 UTC for model output. Time periods shifted by an hour are shown for observations and model output for better visual comparison because the mesoscale simulations did not capture the timing of the frontal passage accurately. The nested LES captures significant shear well over all measurement levels, although it underpredicts the mean wind speed. This underprediction can likely be attributed to the underprediction of the wind speed by the parent mesoscale domains. In contrast to the nested LES, the stand-alone LES with periodic LBCs driven by large-scale forcing displays a very different wind speed time evolution with significantly lower wind speed and shear levels over the first 200 m above the surface. The differences between nested and stand-alone LES can be attributed to the type of forcing and, in particular, to the differences in LBCs. While nested simulation allows for heterogeneous conditions over the LES domain, periodic boundary conditions imply homogenous conditions.

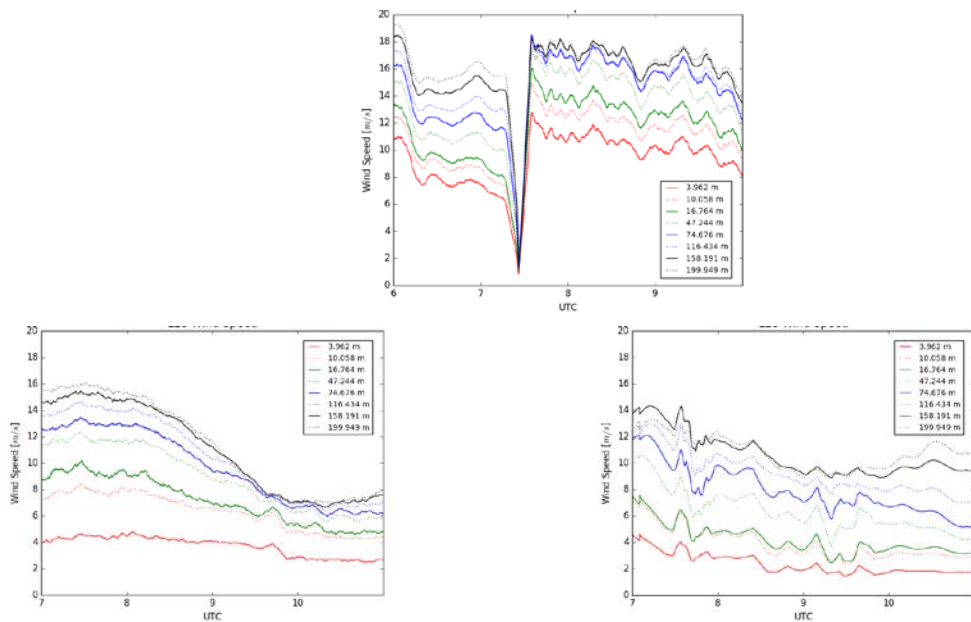


**Figure 5.33.** Wind Speed—Frontal Passage Observed on May 12, 2014; SWiFT Facility Anemometer Measurements (top), WRF-LES with Periodic Boundary Conditions Forced with Output from a Mesoscale Simulation (bottom left), and the WRF-LES Nested in a Mesoscale Simulation (bottom right)

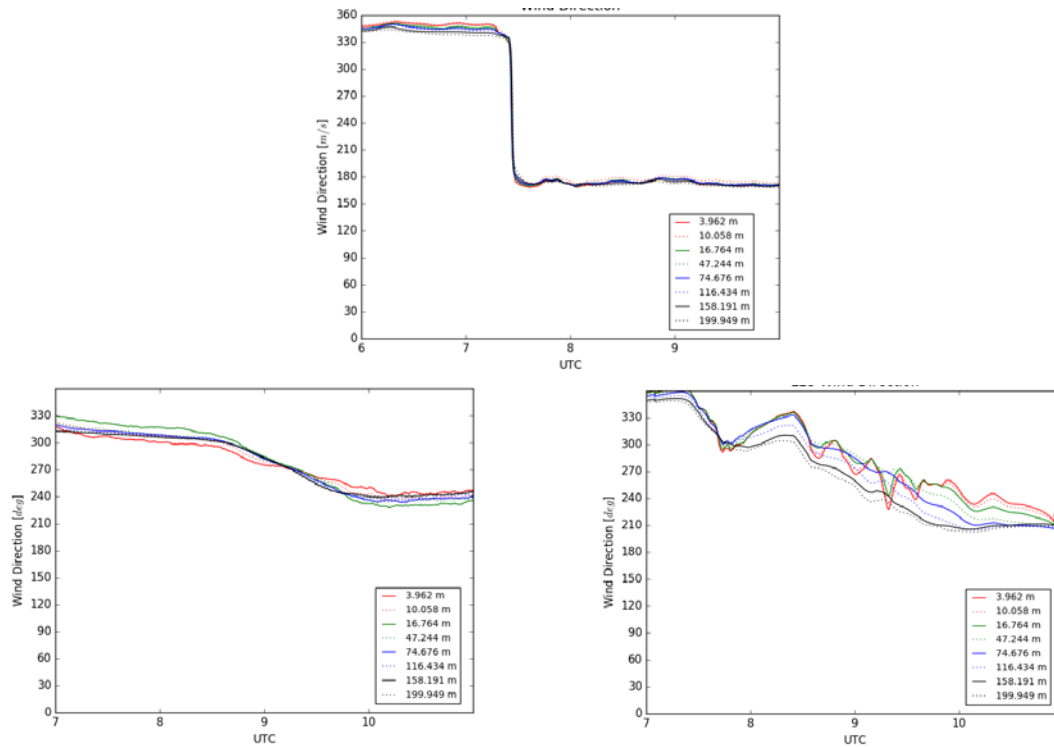


**Figure 5.34.** Wind Direction—Frontal Passage Observed on May 12, 2014; SWiFT Facility Anemometer Measurements (top), WRF-LES with Periodic Boundary Conditions Forced with Output from a Mesoscale Simulation (bottom left), and the WRF-LES Nested in a Mesoscale Simulation (bottom right)

Neither nested nor stand-alone LES predicts the large wind direction change after the frontal passage, as shown in Figure 5.34; however, nested simulation results in wind direction change more consistent with the observed change.

The temperature change resulting from the frontal passage is significantly underpredicted by both nested and stand-alone LES (Figure 5.35). Such a large difference between observed and simulated temperature change can be attributed to the inaccurate large-scale forcing, either by the parent mesoscale domain or the geostrophic wind and advection tendency profiles extracted from the mesoscale simulation.

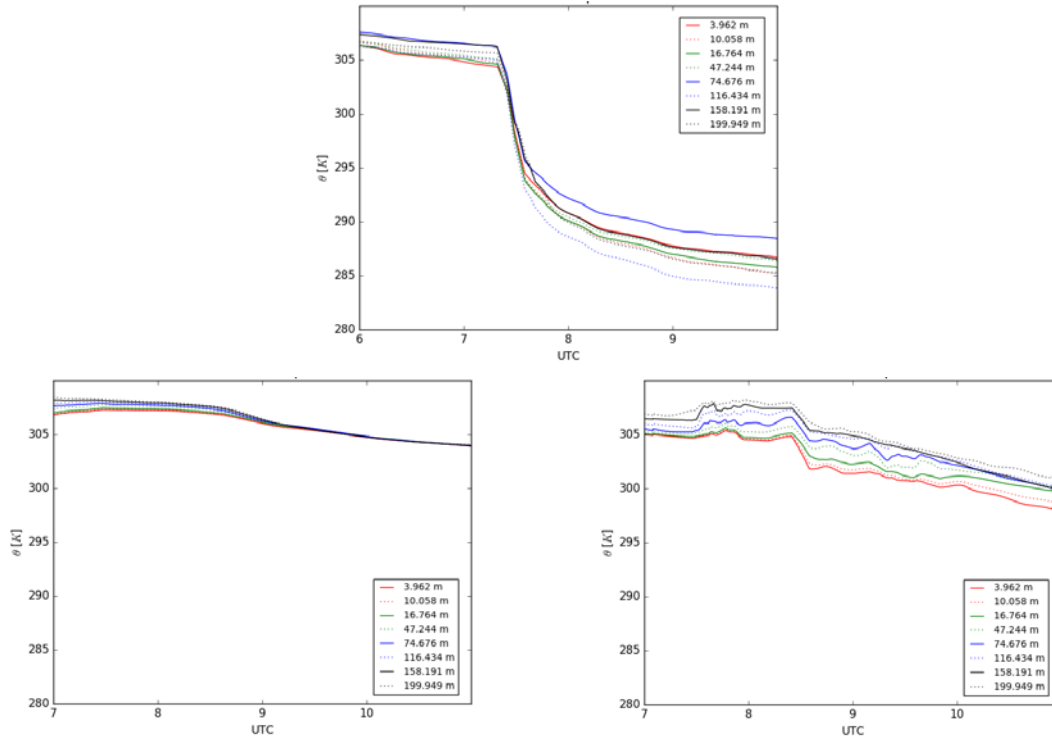


**Figure 5.35.** Temperature—Frontal Passage Observed on May 12, 2014; SWiFT Facility Measurements, WRF-LES with Periodic Boundary Conditions Forced with Output from a Mesoscale Simulation (bottom left), WRF-LES Nested in a Mesoscale Simulation (bottom right)

The TKE evolution shown in Figure 5.36 demonstrates limitations of both LES approaches. Although stand-alone LES results in larger TKE levels before frontal passage and lower levels after its passage, the opposite of what was observed, the nested LES results in intermittent turbulence. Initially, excessively large levels of turbulence are generated as the front approaches, followed by a rapid dissipation of TKE. Such intermittent turbulence bursts can be attributed to the fact that the inflow to the nested LES provided by the parent mesoscale simulation is a smooth flow field without any turbulent eddies. Turbulence develops on the LES nest due to the presence of shear. As turbulence develops, so does turbulent stress (Figure 5.37), resulting in a reduction of shear and consequently, reduction of TKE production, leading to dissipation of TKE. The resulting pulsation of TKE resembles the global intermittence sometimes observed in stably stratified ABLs. In this case, however, it is an artifact of the lack of turbulence at the inflow boundary to the nested LES domain.

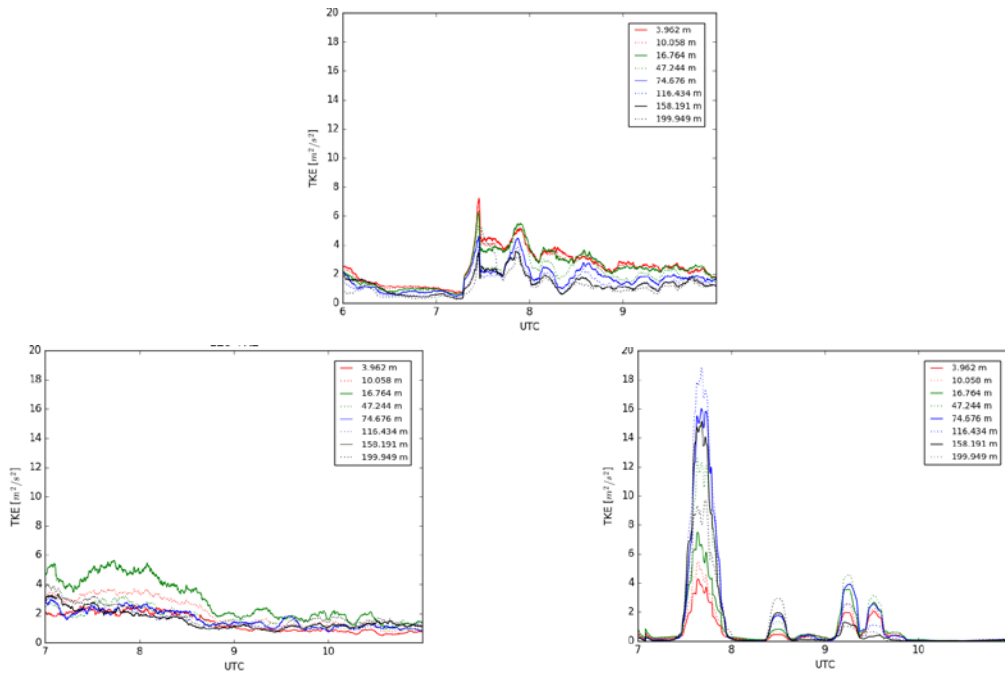


**Figure 5.36.** TKE—Frontal Passage Observed on May 12, 2014; SWiFT Facility Measurements (top), WRF-LES with Periodic Boundary Conditions Forced with Output from a Mesoscale Simulation (bottom left), and the WRF-LES Nested in a Mesoscale Simulation (bottom right)

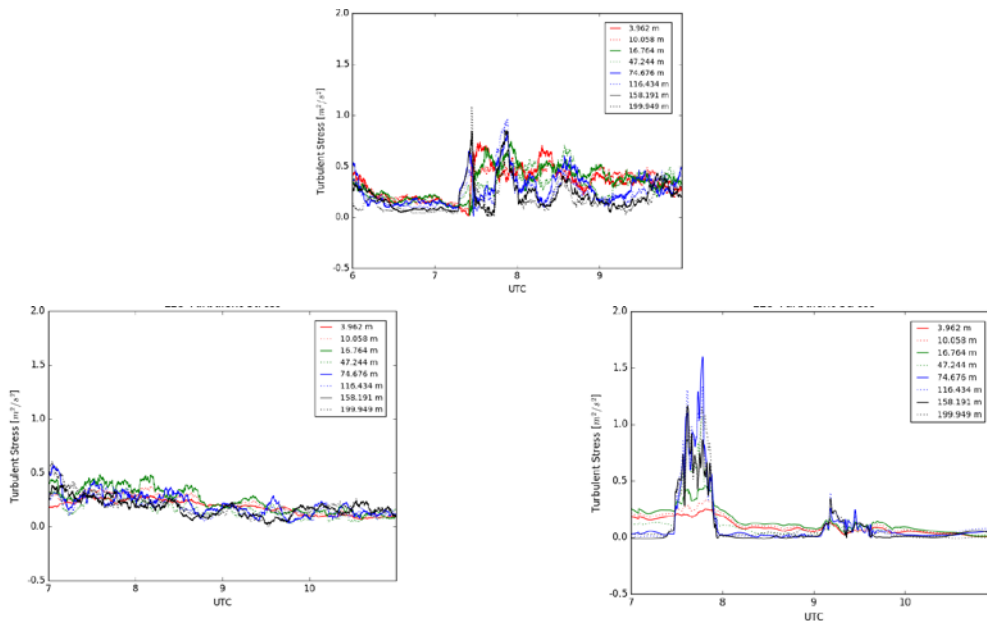


**Figure 5.37.** Turbulent Stress—Frontal Passage Observed on May 12, 2014; SWiFT Facility Measurements (top), WRF-LES with Periodic Boundary Conditions Forced with Output from a Mesoscale Simulation (bottom left), and the WRF-LES Nested in a Mesoscale Simulation (bottom right)

In Figure 5.38, the evolution of turbulent sensible heat flux is presented. The evolution of the flux in LES is consistent with the evolution of a boundary layer from larger downward flux early in the morning toward nearly vanishing flux as morning transition approaches. This evolution is, in general, consistent with observations except for the time interval associated with the frontal passage where measurements display a large variation including attaining positive values.

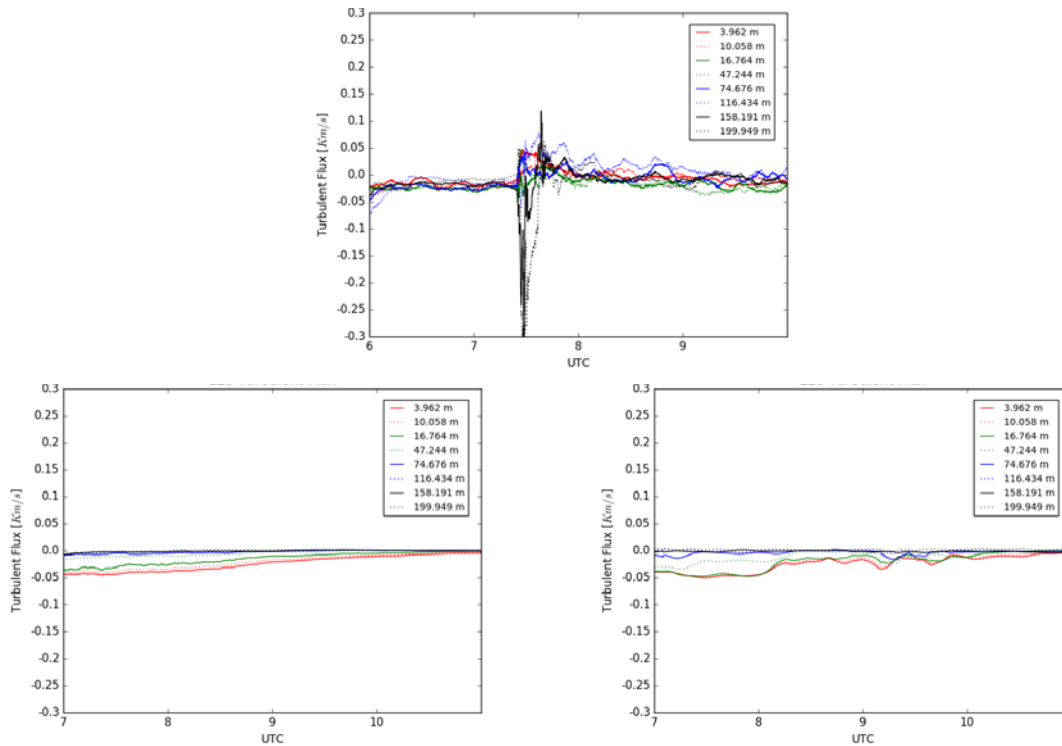


**Figure 5.38.** Turbulent Sensible Heat Flux—Frontal Passage Observed on May 12, 2014; SWiFT Facility Measurements (top), WRF-LES with Periodic Boundary Conditions Forced with Output from a Mesoscale Simulation (bottom left), WRF-LES Nested in a Mesoscale Simulation (bottom right)

Comparison of nested and stand-alone LES forced by large-scale forcing derived from a mesoscale simulation demonstrates advantages of nested simulations that are able to better capture the effects of horizontal heterogeneity of the flow under spatially varying conditions such as those associated not only with a frontal passage, but also with heterogeneous surfaces, such as complex terrain, variable land use, and land-water interfaces. While nested LES can represent the effects of horizontal heterogeneity, this is not sufficient to achieve accurate representation of ABL turbulence due to the absence of resolved turbulence at the inflow to the LES domain. This limitation of a nested LES can be mitigated by employing one of the possible turbulence generation approaches, such as imposing synthetic turbulence at the inflow or perturbing inflow conditions in some way (Mirocha et al. 2014; Muñoz-Esparza et al. 2014 and 2015; section 6.0 of this report).

## 5.7 Spectral Analysis of Canonical ABLs

To further assess the performance of microscale simulation, spectral analysis was carried out on the stand-alone LES based on the case of November 8, 2013. As a result of nearly stationary synoptic forcing, the

wind speed and direction showed little variation over a significant period of time, allowing us to identify time periods associated with convective, neutral, and stable conditions when the ABL could have nearly canonical structure. All the spectra are compared to the theoretical, Kolmogorov  $-5/3$  spectrum.

One-dimensional spectra of three velocity components and temperature are computed for the time period between 1800 and 2000 UTC on November 8, 2013 when atmospheric stability conditions were convective. Two simulations of this period were performed using nested LES and stand-alone LES. The spectra are computed using 11 overlapping 20 min time series obtained from LES and by subsampling the SWiFT facility tower sonic anemometer measurements at 1 Hz. In Figure 5.39, spectra obtained from the stand-alone LES are compared to the observed spectra. Significant differences between the spectra at low frequencies can be attributed to the fact that the LES was forced by time-averaged vertical profiles of geostrophic wind and advection tendencies, which do not have a broad spectrum. Thus, some of the scales of motion larger than the LES domain that affect the microscales in an ABL are not included in the forcing. Spectra of all three velocity components and temperature demonstrate a characteristic high-frequency drop-off. This drop-off is a result of an implicit filter associated with the specific numerical scheme used in an LES. Furthermore, all the spectra show lower energy levels than the observations. The lower energy levels could be attributed to lower surface sensible heat fluxes shown in Figure 5.38.

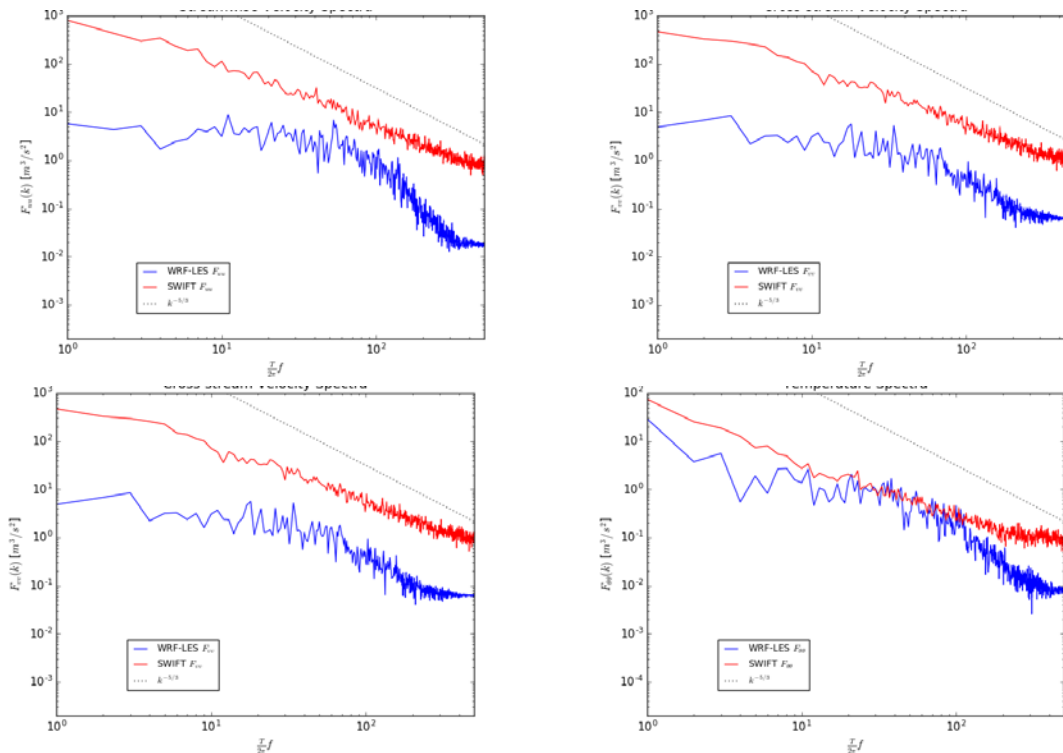


**Figure 5.39.** Comparison of Measured (red) and Simulated (blue) Frequency Spectra under Unstable Stratification; Streamwise Velocity Spectra (top left), Cross-Stream Velocity Spectra (top right), Vertical Velocity Spectra (bottom left), and Temperature Spectra (bottom right). LES was performed using WRF-LES with periodic boundary conditions and forcing derived from a mesoscale simulation.

In Figure 5.40, frequency spectra obtained from the nested LES are compared to observed spectra. One can notice substantially better agreement between simulated and observed spectra at low frequencies corresponding to large-scale motions that are resolved on the parent mesoscale domain. High frequencies display significant drop-off when compared to the observed spectra. In addition to the characteristic high-

frequency drop-off due to the implicit filter, Figure 5.40 shows an example of underdeveloped turbulent flow due to the nonturbulent inflow conditions.

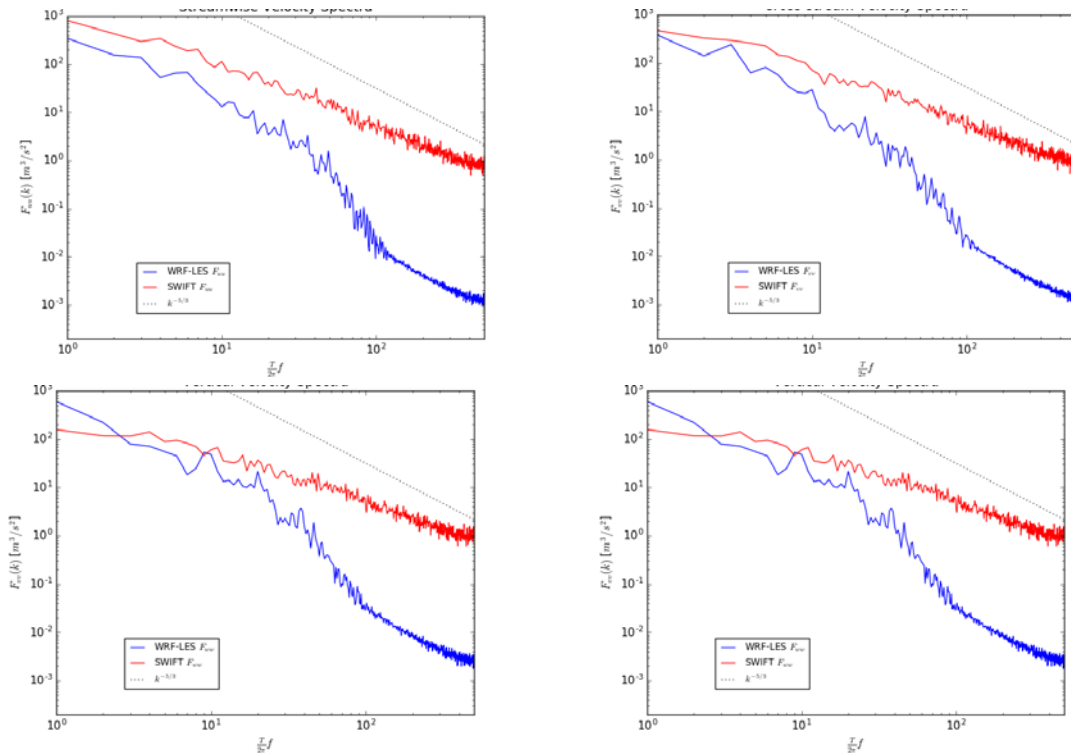


**Figure 5.40.** Comparison of Measured (red) and Simulated (blue) Frequency Spectra under Unstable Stratification; Streamwise Velocity Spectra (top left), Cross-Stream Velocity Spectra (top right), Vertical Velocity Spectra (bottom left), and Temperature Spectra (bottom right). Large-eddy simulation was performed using WRF-LES nested in a mesoscale simulation.

Frequency spectra corresponding to neutrally-stratified atmospheric condition, shown in Figure 5.41 and Figure 5.42, are computed in a similar way as those corresponding to the convective conditions. Near-neutral atmospheric stability conditions associated with the evening transitions were observed between 2130 and 2300 UTC on November 8, 2013. The spectra are again computed using time series obtained from LES and by subsampling the SWIFT facility tower sonic anemometer measurements at 1 Hz. The spectra shown in Figure 5.41 and Figure 5.42 represent an average of eleven spectra computed over overlapping 900 s intervals. Spectra computed using stand-alone LES and nested LES show similar patterns as spectra computed under convective conditions.

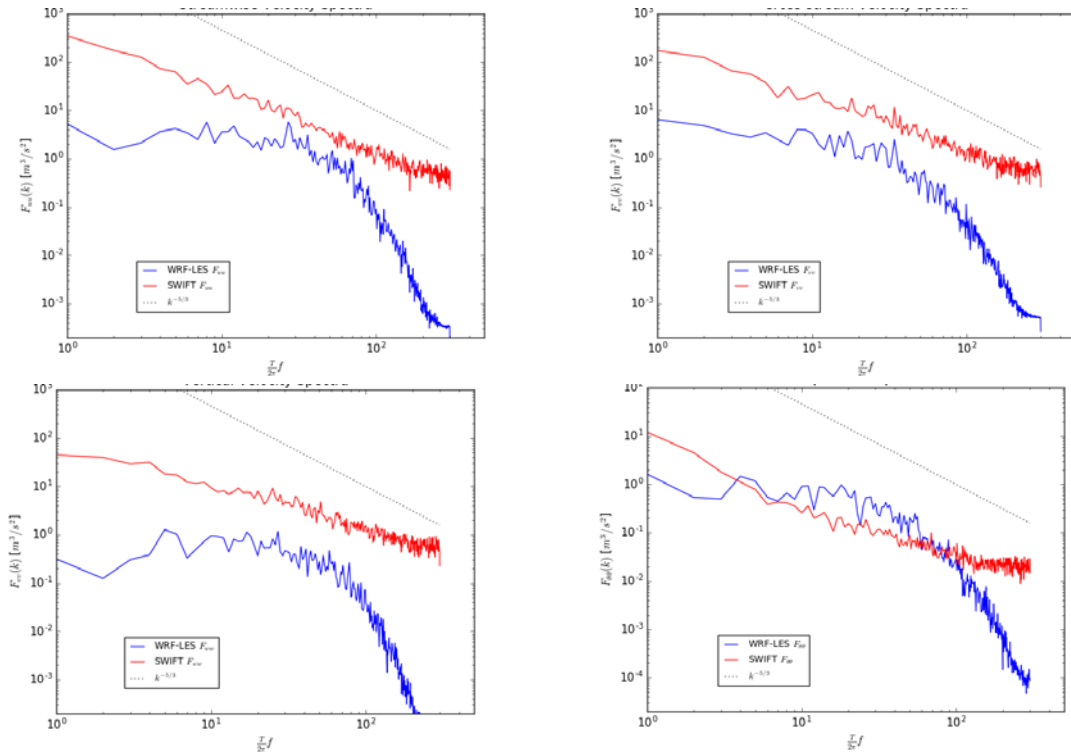


**Figure 5.41.** Comparison of Measured (red) and Simulated (blue) Frequency Spectra under Neutral Stratification; Streamwise Velocity Spectra (top left), Cross-Stream Velocity Spectra (top right), Vertical Velocity Spectra (bottom left), and Temperature Spectra (bottom right). LES was performed using WRF-LES with periodic boundary conditions and forcing derived from a mesoscale simulation.

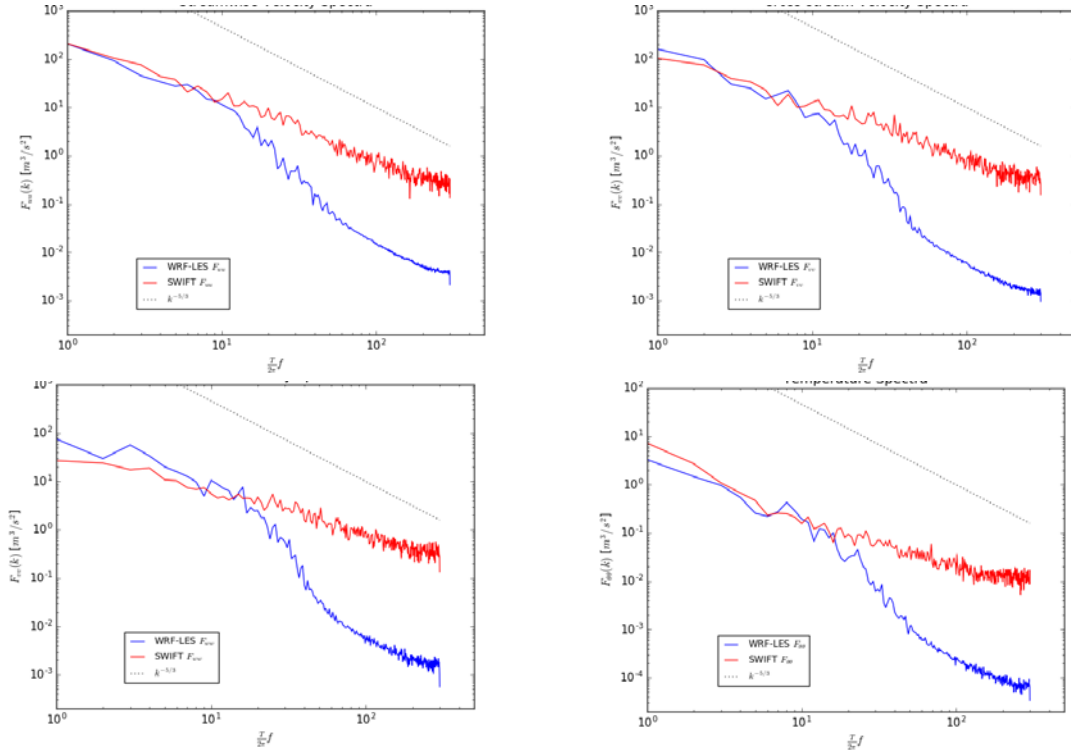


**Figure 5.42.** Comparison of Measured (red) and Simulated (blue) Frequency Spectra under Neutral Stratification; Streamwise Velocity Spectra (top left), Cross-Stream Velocity Spectra (top right), Vertical Velocity Spectra (bottom left), and Temperature Spectra (bottom right). LES was performed using WRF-LES nested in a mesoscale simulation.

For completeness, the team also computed spectra during stably stratified conditions observed between 0400 and 0500 UTC. Again, spectra were computed using 11 overlapping intervals; however, due to reduced boundary layer depth under stable conditions the time intervals were reduced to 600 seconds. As shown in Figure 5.43 and Figure 5.44, the spectral power density levels are significantly lower than those observed. The lower levels of spectral power density in LES are a consequence of underresolved flow due to inadequate grid-cell size. However, to simulate an entire diurnal cycle, a compromise between grid-cell size, domain size, and available computational time must be achieved. For a well-resolved LES of a stably stratified ABL, grid-cell size and time step requirements are prohibitive for a diurnal cycle simulation. Therefore, we used a compromise grid-cell size that may yield a slightly overresolved convective ABL and underresolved stably stratified ABL.

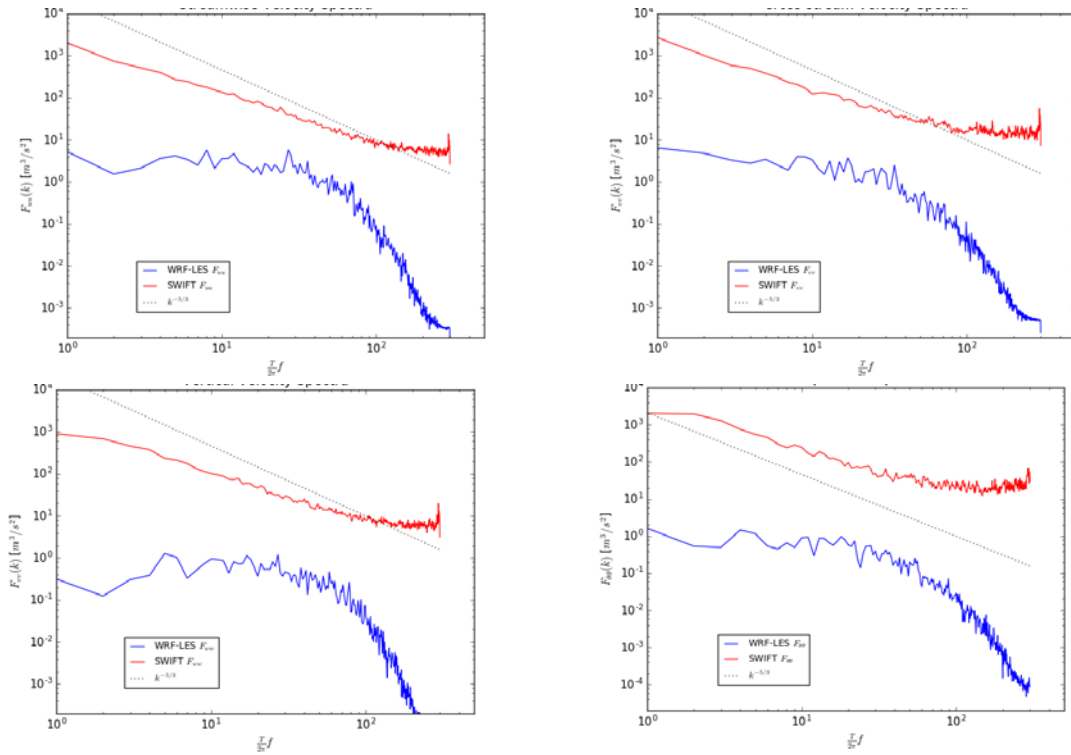


**Figure 5.43.** Comparison of Measured (red) and Simulated (blue) Frequency Spectra under Stable Stratification; Streamwise Velocity Spectra (top left), Cross-Stream Velocity Spectra (top right), Vertical Velocity Spectra (bottom left), and Temperature Spectra (bottom right). LES was performed using WRF-LES with periodic boundary conditions and forcing derived from a mesoscale simulation.

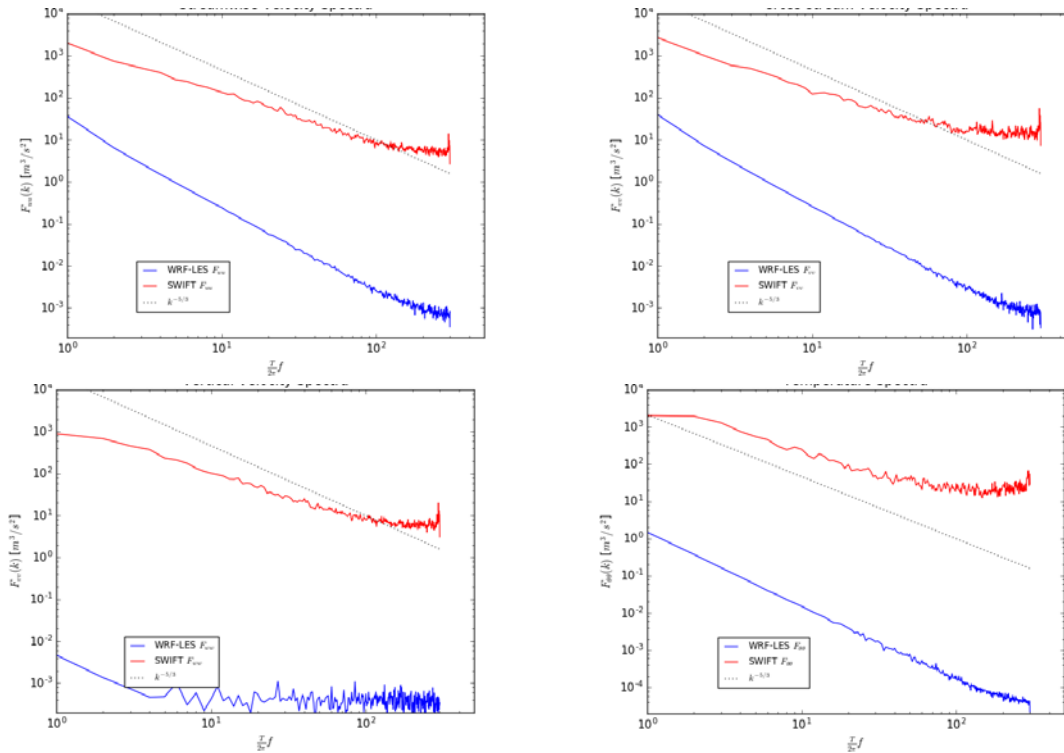


**Figure 5.44.** Comparison of Measured (red) and Simulated (blue) Frequency Spectra under Stable Stratification; Streamwise Velocity Spectra (top left), Cross-Stream Velocity Spectra (top right), Vertical Velocity Spectra (bottom left), and Temperature Spectra (bottom right). Large-eddy simulation was performed using WRF-LES nested in a mesoscale simulation.

The analysis of microscale flow simulations forced by mesoscale simulations, performed either “online” or “offline”, leads us to conclude that both approaches are viable under different conditions. Under nearly stationary synoptic forcing over mostly flat, homogeneous terrain, microscale simulations forced by profiles of time-varying geostrophic wind and advective tendencies produce satisfactory results. However, if the synoptic conditions are not stationary and the domain of interest is not homogeneous (i.e., in the case of complex terrain, heterogeneous land use, or land–water interfaces), LES nested in mesoscale simulations results in more accurate evolution and structure of the ABL flow. However, nesting LES in a parent mesoscale domain introduces additional complexity due to nonturbulent inflow conditions. Simulations of a fully turbulent flow in the nested LES domain can be very slow and require large inflow fetches for turbulence to develop. In order to make nested LES computationally feasible, inflow turbulence generation mechanisms and procedures must be applied.

## 6.0 Turbulence Generation Methods

Recognizing the importance of capturing both the large-scale drivers and resulting small-scale turbulence motions for many wind energy applications, section 5.0 explored internal MMC using stand-alone LES with periodic LBCs, for which turbulence could spin up naturally over time-scales sufficient to either achieve steady state with the imposed mesoscale forcing, or follow the slow evolution of the large-scale forcing fields. However, the constraints imposed by the requirement of periodicity limited the applicability of such approaches. Complementary techniques are required for more complicated terrain settings and meteorological forcing scenarios. The most general MMC approach is to couple the simulation domains not only through internal forcing parameters, but at the lateral boundaries of the microscale domain as well.

One significant obstacle that must be overcome in the replacement of periodic LBCs with mesoscale inflow and outflow is the development of the classical 3D turbulence spectrum within the microscale domain. When replacing periodic LBCs with mesoscale inflow, which does not contain those structures, in the absence of special treatment at the inflow boundaries, a substantial fetch is required for turbulence to spontaneously develop within the microscale domains and equilibrate to a fully-developed cascade. Although fetches can be relatively short during convective conditions due to strong buoyant forcing leading to rapid development of turbulence structures, more frequently occurring weakly convective, neutral, and stable conditions can require fetches on the order of 10 km or more (Mirocha et al. 2013; Muñoz-Esparza et al. 2014, 2015). In the interest of both computational efficiency and the accuracy of the resulting flow field obtained within a reasonable distance from the simulation inlets, it is essential to accelerate turbulence generation and minimize the fetch as much as possible.

The imposition of special forcing at the inlets of the microscale domain to encourage development of the turbulence cascade can reduce the fetch considerably, leading to significant gains in both computational efficiency and solution accuracy at a given downstream distance. One class of treatments entails the addition of realistic turbulent velocity fluctuations to the flow field, essentially imposing a turbulence cascade in balance with the large-scale PBL structure. While these methods achieve the desired reduction of fetch, the distribution and magnitude of the imposed fluctuations is not generally known *a priori*. A typical microscale LES will employ recycling methods (Lund et al. 1998; Wu 2017) or a precursor simulation on a periodic domain (Churchfield et al. 2012; Wu 2017) to develop the turbulence prior to running the main LES. While effective for specific applications, these approaches are not ideal for general MMC applications due to the requirement of an auxiliary computational domain and the additional incurred cost.

The generality of turbulence acceleration can be improved via imposition of flow perturbations that do not require significant auxiliary computation or *a priori* flow information. Herein, two such approaches are investigated. The first approach, TurbSim, utilizes a stochastic turbulence generator originally developed at NREL to assess the relationship between atmospheric turbulence and wind turbine structural fatigue damage (Kelley 2011). This code builds on the Sandia Method (Veers 1988), which produces a turbulent time series for the velocity components on a grid of points encompassing the turbine rotor. The turbulence is assumed to be stationary in this approach. Velocity spectra and coherence are specified as inputs to the method, and are based on either International Electrotechnical Commission (IEC) models or models calibrated with measurements (Jonkman and Buhl 2006). For generalized MMC, this method has been extended to provide turbulence seeding information on the inflow boundaries of the entire microscale computational domain.

The second approach is the stochastic cell perturbation method (Muñoz-Esparza et al. 2015), which is based on seeding the inflow with noncorrelated perturbations, but in a manner that optimally leads to the

generation of a turbulence cascade that is in balance with the large-scale forcing and PBL structure. Mirocha et al. (2013) imposed kilometer-scale velocity perturbations that broke down via the cascade process to produce turbulence that agreed well with results from stand-alone domains using periodic LBCs. Muñoz-Esparza et al. (2014, 2015) improved the perturbation approach considerably by instead imposing stochastic perturbations to only the temperature field, over rectangular horizontal and vertical cells at the domain inflow, with values obtained from the optimal value of the turbulent Eckert number  $Ec = \frac{U_g^2}{c_p \tilde{\theta}_{pm}} = 0.2$ , where  $U_g$  is the geostrophic wind,  $c_p$  is the heat capacity at constant pressure, and  $\tilde{\theta}_{pm}$  represents the range of thermal perturbations. Changing the perturbation values over the advective timescale required for flow to traverse 24 model grid cells results in buoyancy forcing of the correct magnitude and spatiotemporal scale to optimally spawn the rapid development of correlated structures, beginning primarily as hairpin vortex structures near the surface, that rapidly transition to a fully-developed turbulence cascade throughout the ABL. The stochastic cell perturbation approach requires no *a priori* computation of flow characteristics, only the driving geostrophic wind speed, flow speed near the surface (for determination of the advective timescale), and PBL height.

Herein, both the TurbSim and stochastic cell perturbation method are investigated in idealized flow simulations, as described in the following sections.

## 6.1 TurbSim Approach

### 6.1.1 Coupling Framework

Originally, TurbSim was intended to generate turbulent inflow for a wind turbine rotor-sized plane. Because this is a very small region (on the order of 100 m x 100 m, at a 10 m resolution, for example), computational cost was of no concern. For MMC applications, the extent of the inflow plane is on the order of kilometers, resulting in substantial increases in memory usage and computational time (from minutes to tens of hours). As a workaround, smaller TurbSim planes were calculated and tiled to form a complete inlet boundary. The effect of tiling was found to be negligible in the flow field near the inlet.

An additional consideration was given to vertical profiles of the velocity perturbations and their associated turbulence statistics. Because the original application was only intended for application up to a height of approximately 100 m, and only over a small region near the rotor, the statistics of the synthetic turbulence are uniform. Figure 6.1 shows a sample LES profile (dashed curve) and the generic hyperbolic tangent scaling (solid curve) that has been applied in the present work. The tanh function is adjusted so that the synthetic variance is reduced to 10% at the inversion height (in this case, 750 m).

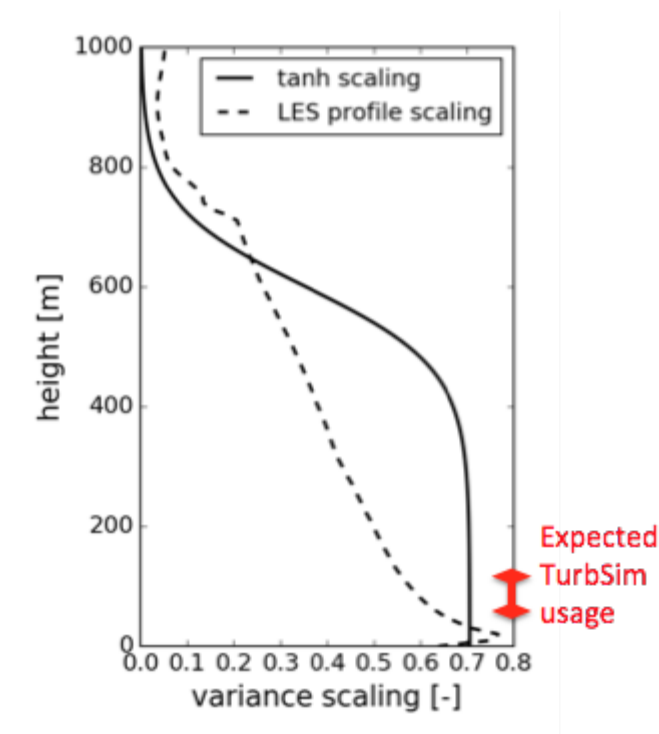


**Figure 6.1.** Scaling of the Synthetic Turbulence Applied to the MMC Coupling as a Function of Height

The tested TurbSim-MMC simulation workflow proceeded as follows.

1. Simulate a 10 min period of TurbSim inflow for a given set of conditions (i.e., the reference velocity at a reference height and turbulence level).
2. Reconstruct the full inflow plane from tiles (if necessary), and subtract out the mean velocity profile to obtain the fluctuations only.
3. Scale the velocity fluctuations on the full inflow plane using the tanh function.
4. Sample the scaled inflow plane at 1-s intervals for use as a time-varying inlet boundary condition in the LES. Spatial interpolation may be necessary to obtain the fluctuations at locations coincident with the LES grid.

### 6.1.2 Coupling Evaluation

An initial test of the approach outlined in section 6.1.1 used LES simulation data obtained from a periodic precursor simulation (Churchfield 2012) to provide a truth case. The motivation for considering an idealized case was to facilitate understanding of the turbulence generation effectiveness without having to characterize and isolate the effects of a nonequilibrium inflow. From the periodic precursor, spatial averages were performed over horizontal planes to provide a mean inflow profile varying with height only. Thus, both an LES-based representative mesoscale inflow and LES-based turbulence statistics are available. For reference, the periodic precursor was sampled and used as inflow to a nonperiodic “main” simulation. The simulated main microscale domain size was 12 km x 4 km x 1 km in the length, width, and height dimensions. Both the precursor and main simulations had a 10 m spatial resolution, typical of microscale simulations.

Test conditions were selected to approximate generic wind farm conditions, including:

- m/s wind speed at 80 m hub height;
- neutral atmospheric stability, with an inversion layer at 750 m; and
- 0.05 m roughness height, approximating generic crops or grassland.

These conditions resulted in a turbulence intensity of approximately 10% at hub height. Note that, while neutral conditions are not necessarily representative of all sites (e.g., SWiFT), this study aims to evaluate the efficacy of velocity perturbations apart from buoyancy effects. Neutral stability remains of interest within the context of nonequilibrium conditions because transition to and from stable and convective conditions necessarily passes through the neutral regime. In addition, for offshore wind energy applications, MMC simulations over the ocean are generally characterized by near-neutral conditions.

For the coupled test cases, the mean precursor profile approximates a smooth mesoscale inflow. Synthetic velocity perturbations from TurbSim were superimposed onto this inflow profile and the resulting flow field was evaluated. A number of metrics were considered, including:

- downstream velocity, turbulence intensity, and shear stress profiles;
- streamwise evolution of turbulence intensity, TKE, and resolved covariance; and
- two-point statistics (e.g., correlation length).

TurbSim calculations used default parameters, assuming that any velocity perturbation with reasonable coherent structure should suffice to accelerate the development of turbulence. The IEC Kaimal turbulence model was used, in conjunction with the IEC coherence model applied only to the streamwise fluctuation component.

### **6.1.3 Results**

The synthetic perturbations with and without coherence were applied in a number of different configurations (Figure 6.2). For example, fine-tuning is possible through modification of the scaling profile described in section 6.1.2. In addition, the fluctuations may be applied over patches rather than individual cell faces in a manner inspired by and analogous to the temperature perturbation approach in Muñoz-Esparza (2014). This has the physical effect of promoting the development of larger turbulent structures closer to the inlet, and has the added benefit of accelerating the TurbSim calculation since a coarser grid can be simulated beforehand.

Results indicate that the correlations in the synthetic turbulence are essential. For instance, Figure 6.2 shows that most cases evaluated are able to qualitatively reproduce the reference profile (black curve), with the exception of the case with uncorrelated inflow (solid blue curve). Moreover, an optimal perturbation patch size appears to exist for a given set of atmospheric conditions, seen by the green curves spanning a range of solutions that includes the reference precursor solution.

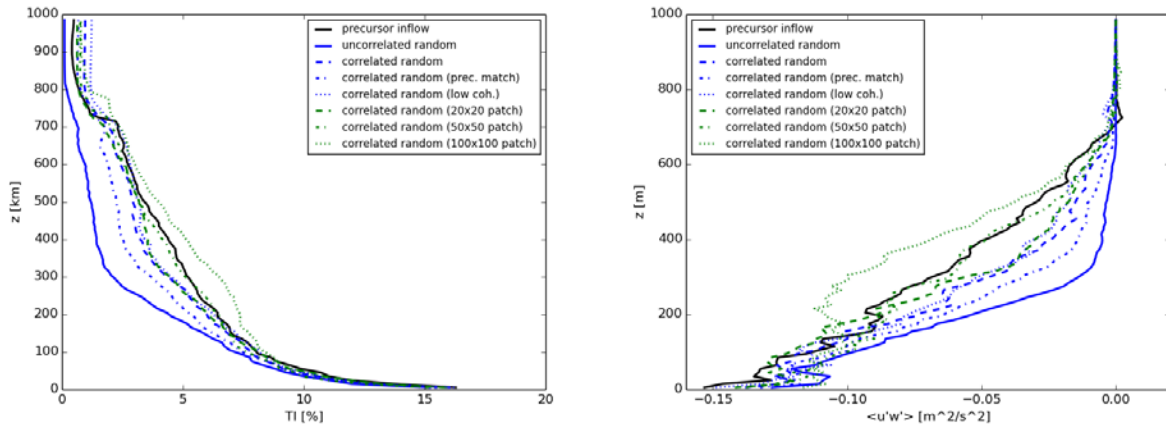


**Figure 6.2.** Downstream (11 km) Profiles of Turbulence Intensity (left) and Reynolds Shear Stress (right) for a Variety of Synthetic Turbulence-Based Perturbation Approaches

Figure 6.3 illustrates the effect of perturbing the inflow. The top image displays the reference solution with a fully-developed inflow (from a periodic precursor) applied at the inlet: no apparent fetch is observed. In contrast, the middle and bottom images both demonstrate MMC-like solutions, simulating a smooth inlet velocity profile superimposed with TurbSim perturbations. In the baseline MMC case (middle), the effect of the tiled inlet plane disappears after the first km; then, the turbulence level and velocity increase up to 2 km, with small turbulence structures forming between 3-5 km; finally, these evolve into larger-scale structures after 6 km. Increasing the perturbation patch size from a single cell face (10 x 10 m) to a patch with four faces (20 x 20 m) promotes the development of larger turbulence structures at a shorter distance downstream from the inlet, as illustrated by the bottom subfigure. In this near-optimal case, similarly-sized structures observed after 6 km downstream in the baseline can be seen earlier around 4 km from the inlet.

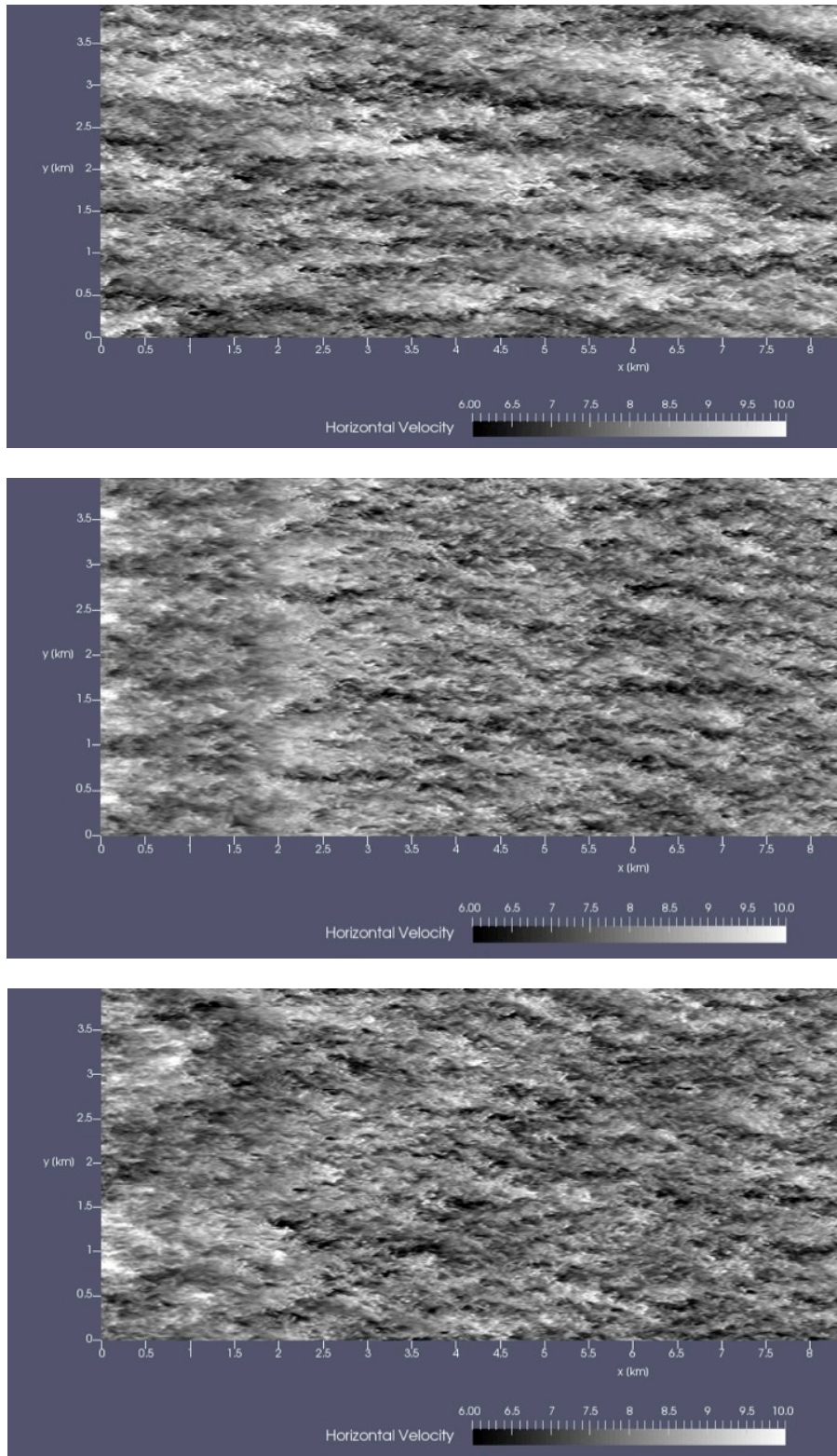


**Figure 6.3.** The Reference Fully-Developed Flow (top), Compared with the Mean Flow Superimposed with Correlated TurbSim Perturbations (middle and bottom) Applied at the Inlet. The middle and bottom fields show a perturbation patch size of 10 x 10 m and 20 x 20 m, respectively.

## 6.2 Stochastic Cell Perturbation Method

Next, the stochastic cell perturbation method of Muñoz-Esparza et al. (2015) is demonstrated under both neutral and weakly convective, geostrophically-forced flow over flat, rough terrain. The computational approach consists of comparing flow statistics from an LES nested directly within a mesoscale domain, within the WRF model, to those of a stand-alone LES domain using periodic LBCs, which is taken to represent the equilibrium solution (following Mirocha et al. 2013 and Muñoz-Esparza et al. 2014, 2015). A schematic of the computational setup is provided in Figure 6.4, showing the rectangular computational domains, aligned approximately in the streamwise flow direction, with the geostrophic wind forcing orientation depicted by the blue arrow.

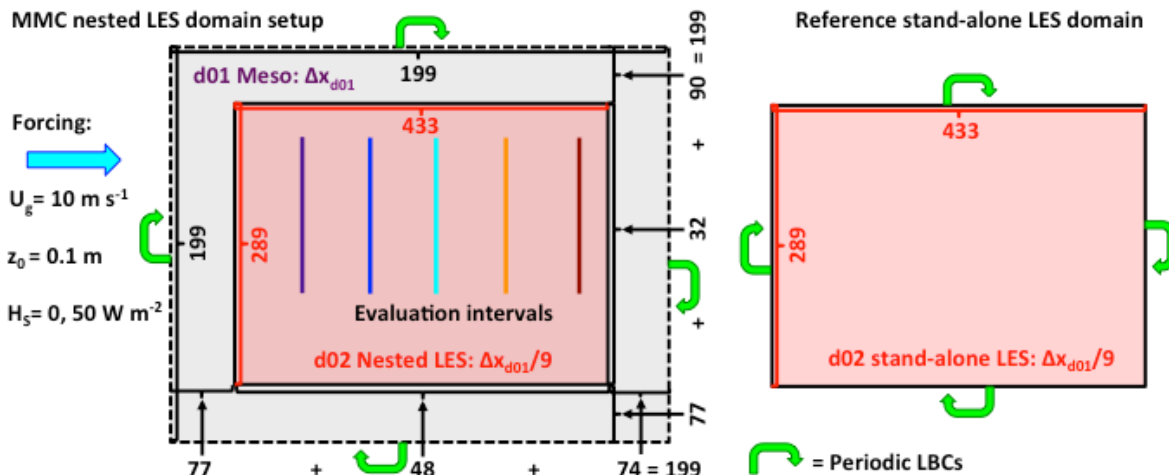


**Figure 6.4.** Computational Setup used to Evaluate the Stochastic Cell Perturbation Method Showing Nested (left) and Stand-Alone LES Domains (right), along with the Number of Grid Cells in each Direction on each Domain, the Location of the Nested LES within the Mesoscale Domain, and Approximate Locations within the Nested Domain from which Flow Statistics were Examined

All simulations were forced with constant values of the geostrophic wind,  $U_g = [u_g, v_g]$ , with  $u_g = 10$  and  $v_g = 0$  m s<sup>-1</sup>, and used flat terrain with a roughness length of  $z_0 = 0.1$  m. Two surface heat flux values of  $H_s = 10$  and  $50$  W m<sup>-2</sup> were applied to represent neutral and moderately convective conditions, with the surface boundary condition applied using the Monin-Obukhov similarity theory (Monin and Obukhov 1954) and stability corrections following Dyer and Hicks (1970). Both the nested and stand-alone LES domains used horizontal and vertical grid spacings of 12 and 6 m, respectively, during neutral conditions, and 24 and 12 m, during convective conditions. Domain depths were 1,506 and 3,012 m for the neutral and convective simulations, with Rayleigh damping applied over the upper 1,000 and 2,000 m. For the nested simulations, the mesoscale domain used the same vertical grid spacing, with a horizontal grid spacing a factor of nine larger than the LES domain. These grid spacings, while smaller than a typical mesoscale simulation, were sufficiently coarse to prevent the development of a turbulence spectrum on the mesoscale domains; therefore, they were representative of an ensemble mean mesoscale profile from which the turbulence cascade would need to develop in a general MMC simulation of this type.

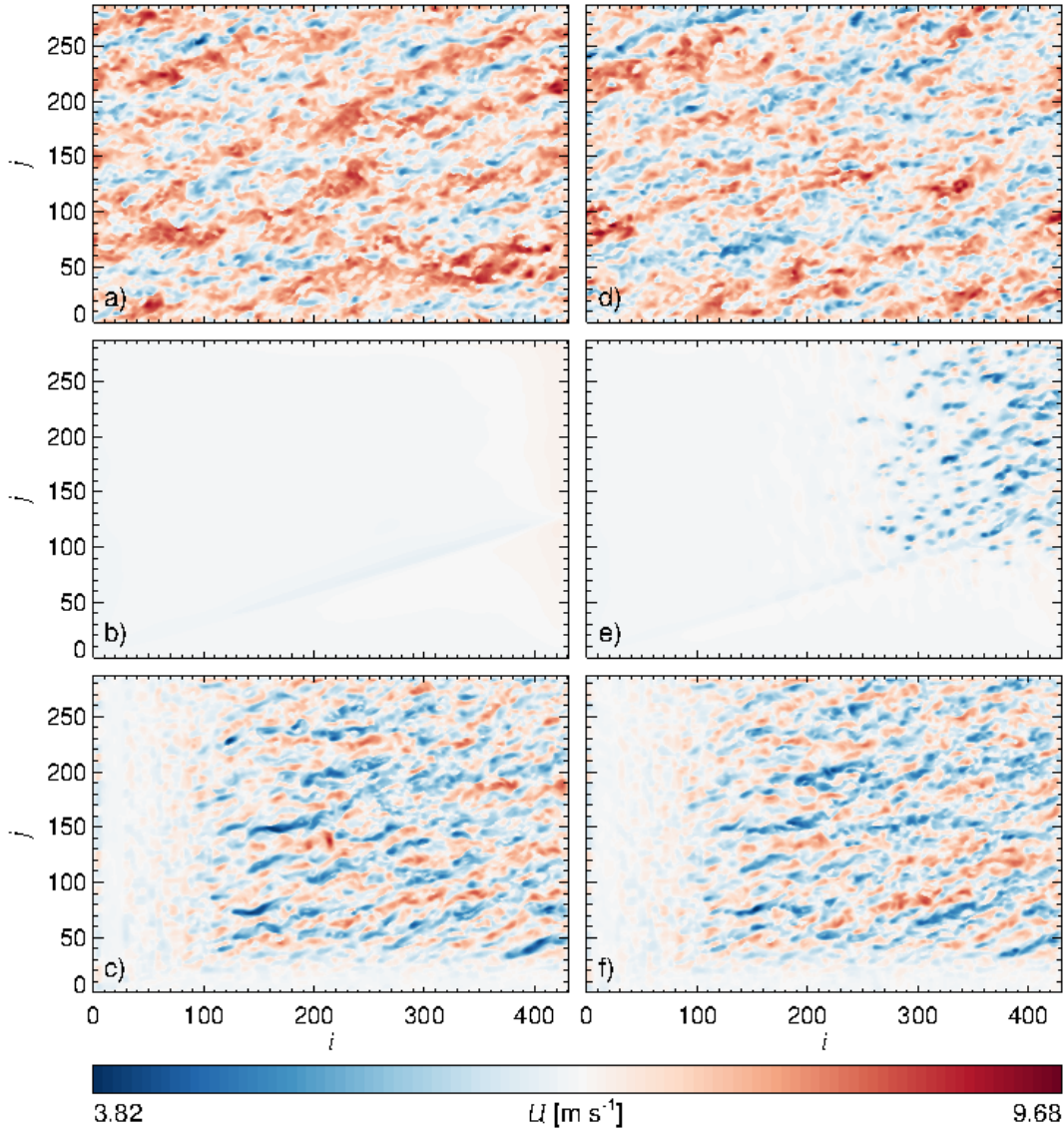
The mesoscale domains were idealized to use periodic LBCs and the same large-scale and surface forcing as that applied to the stand-alone LES, allowing both the mesoscale and stand-alone LES domains to equilibrate to similar solutions. The mesoscale simulation utilized the MYNN2.5 PBL scheme (Nakanishi and Niino 2004), with a view toward compatibility with future developments within the MYNN 2.5

scheme on behalf of related MMC and WFIP2 research efforts. These simulations did not incorporate these new developments, which are still undergoing development and testing. For this study, other modifications were made to the MYNN surface-layer module to accept the imposed idealized forcing, including removal of dependence on the surface skin temperature, which removed the need to also run a land surface model, and use of a standard definition of the Obukhov length that uses the imposed value of  $H_S$ , rather than the existing formulation which used a temperature scale and stability functions.

Two different LES SGS flux models were used: the simple and common Smagorinsky (SMAG; Smagorinsky 1963; Lilly 1967) and the more sophisticated Lagrangian-averaged scale-dependent (LASD; Bou-Zeid et al. 2005) approach. The SMAG model specifies the SGS stresses as  $\tau_{ij} = -2K_M\tilde{S}_{ij}$ , with  $\tilde{S}_{ij} = \frac{1}{2}\left(\frac{\partial\tilde{u}_i}{\partial x_j} + \frac{\partial\tilde{u}_j}{\partial x_i}\right)$  the resolved strain-rate tensor, and  $K_M = (C_S l)^2 |\tilde{S}_{ij}|$  the eddy viscosity, with a tilde specifying a resolved-scale component of the flow.  $C_S$  is a time and space invariant constant, and  $l$  is a length scale. In WRF,  $C_S = 0.18$  and  $l = \sqrt[3]{\Delta x \Delta y \Delta z}$ , where  $\Delta x$ ,  $\Delta y$ , and  $\Delta z$  are the grid spacings in each direction. The corresponding heat flux is given by  $\overline{u_j \hat{\theta}_{v,j}} = -2K_H \frac{\partial \hat{\theta}_v}{\partial x_j}$ , with  $K_H = P_r^{-1} K_M$ . Here,  $P_r^{-1} = 3$  is the inverse of the turbulent Prandtl number, and  $\theta_v = \theta(1 + 0.61q_v)$  the virtual potential temperature, with  $q_v$  the water vapor mixing ratio, and  $\theta = T(p_0/p)^{R/c_p}$  the potential temperature, with  $p$  the pressure,  $p_0 = 1 \times 10^5$  Pa a reference value,  $R = 287$  J kg<sup>-1</sup> K<sup>-1</sup> the dry air gas constant, and  $c_p = 1004$  J kg<sup>-1</sup> K<sup>-1</sup> the specific heat of dry air at constant pressure.

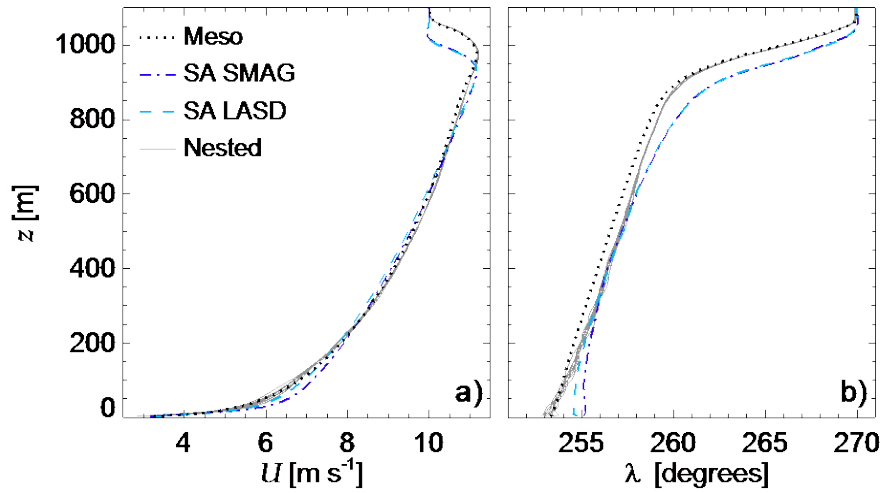
The LASD model uses the basic SMAG formulation, but computes the value of the constant  $C_S$  dynamically, using a two-level filtering procedure that determines how the resolved stresses change across scales, with a power law relation specifying the SGS stresses. This allows dissipation to become very small locally, even where local gradients are large, which cannot occur in the standard SMAG formulation. Although this feature of dynamic SGS models has many benefits, it can lead to numerical instability. To stabilize the procedure, the LASD eddy viscosity coefficients are averaged along fluid pathlines. Because of the tendency of dynamic models to underpredict near wall stresses in finite difference solvers (Chow et al. 2005; Kirkil et al. 2012), SFS stresses near the wall are augmented using the parameterization of Brown et al. (2001) to recover the log law. Further details on the LASD formulation and its implementation into WRF can be found in Bou-Zeid et al. (2005) and Kirkil et al. (2012).

Figure 6.5 shows instantaneous contours of wind speed at approximately 100 m above the surface from each domain during the neutrally-forced simulation. The top, middle, and lower panels show the stand-alone LES, the nested LES with no perturbations, and the nested LES with perturbations. The stand-alone solutions (top) indicate the presence of a fully-developed turbulence cascade throughout the entire domain, with the slight counterclockwise rotation of the flow field relative to the imposed  $U_g$  due to the Coriolis acceleration. The middle panels indicate the motivation for perturbation methods, the slow development of the turbulence cascade within nested LES domains, for which the flow has only the advective timescale within the nest for the cascade to develop. Seeding the nested domain inflow with perturbations (bottom panels) shows accelerated turbulence development, yielding a flow field that appears similar to the stand-alone solutions, within computationally tractable distances from the inflow.



**Figure 6.5.** Plan View Contours of Wind Speed in Stand-Alone and Nested LES Domains at 100 m Above the Surface, from the Convective Simulations, with Stand-Alone Periodic LES (top), Nested Domains with No Perturbations (middle), and via the Cell Perturbation Method (bottom), using both the SMAG (left) and LASD (right) SGS Models

Figure 6.6 shows the mean vertical wind speed (left) and direction (right) profiles within the ABL from the mesoscale, stand-alone LES, and nested LES domains. All domains produce similar distributions, with the mesoscale (black dotted lines) producing slightly deeper mixing than either stand-alone LES (blue dashed lines). Profiles from nested domain simulations at  $i = 400$ , the sampling location furthest from the inlet plane (see Figure 6.4), are also shown, with each grey line showing a slightly different perturbation characteristic. While strongly influencing turbulence characteristics (as described below), changes in perturbation characteristics result in little variability in mean profile characteristics, or from the mesoscale simulation, which constrains the mean flow within the nested domain via forcing at the lateral boundaries.



**Figure 6.6.** Mean Vertical Profiles of Wind Speed (left) and Direction (right) during Neutral Simulations, from Mesoscale (black dotted), Stand-Alone LES (blue dashed), and Nested LES (grey), from  $i = 400$  Grid Cells from the Inflow, using Different Cell Perturbations, as Described in the Text

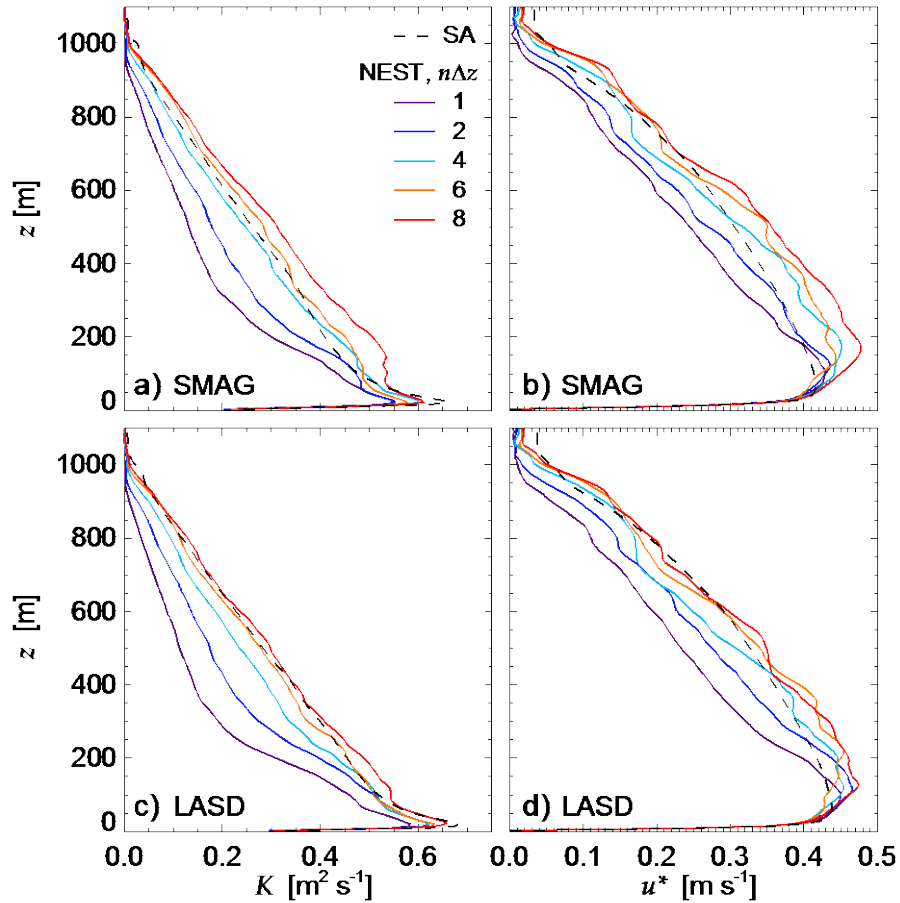
Figure 6.7 shows vertical profiles of the resolved components of the turbulence kinetic energy,  $K = 0.5(\overline{u'^2} + \overline{v'^2} + \overline{w'^2})$  (left) and friction velocity  $u_* = \left[ (\overline{u'w'})^2 + (\overline{v'w'})^2 \right]^{1/4}$  (right), at the same distance ( $i = 400$ ) from the inflow plane as in Figure 6.6. Here, primes indicate local departures from mean values, with overbars indicating averaging over space and time. 10 min averaging is performed over instantaneous output at 1 min increments. The mesoscale and stand-alone LES quantities use spatial averaging over the entire domain (due to periodicity), whereas those from the nested LES are averaged over strips depicted by the colored lines in Figure 6.4, from grid cells  $96 < j < 265$ . The back dashed lines show values from the stand-alone LES, while each color indicates nested domain profiles using perturbations with different values of  $n\Delta z$ , which indicates the number of vertical grid cells over which a perturbation value is held constant, with  $n\Delta z = 1$  indicating unique perturbations at each vertical level. All profiles are averaged over 1 hour (six 10 min averages), and the nested domain profiles are also averaged over the 9 grid cells surrounding each  $i$ -location in the  $i$ -direction (from  $i - 4$  to  $i + 4$ ) to smooth the profiles.

Sensitivity to  $n\Delta z$  is considerable, with the smallest value  $n\Delta z = 1$  showing the greatest underpredictions of both  $K$  and  $u_*$ , relative to the stand-alone values, with decreasing underprediction for increasing values of  $n\Delta z$ , up to values of about  $n\Delta z \cong 4 - 6$  for the SMAG (orange) and  $n\Delta z \cong 6 - 8$  for the LASD (red) simulations, respectively, after which further increases result in overpredictions, especially of  $u_*$ . Whereas for the LASD simulations, the  $n\Delta z$  values that produce the best prediction of  $K$  also produce the best predictions of  $u_*$ , for the SMAG simulations, the  $n\Delta z$  values that produce the best agreement of  $K$  also overpredict  $u_*$ , while those producing the best values of  $u_*$  underpredict  $K$ .

Muñoz-Esparza et al. (2015) found the best performance using a unique stochastic perturbation at each vertical grid index ( $n\Delta z = 1$ ; purple). Possible reasons for discrepancies between their results and those herein include changes to the application of surface boundary condition (we corrected an error in the projection of near-surface deformation elements used by the turbulence models in previous WRF releases), and use of a smaller grid aspect ratio  $\alpha = \Delta h / \Delta z$ , where  $\Delta h$  is the horizontal grid spacing, with  $\alpha \cong 2$  used herein, relative to  $\alpha \cong 4$  used in the previous study. Although a different SGS model was also

used in the previous study, use of the same SGS model in the present study produced similar results to those obtained from the SMAG simulations (not shown).

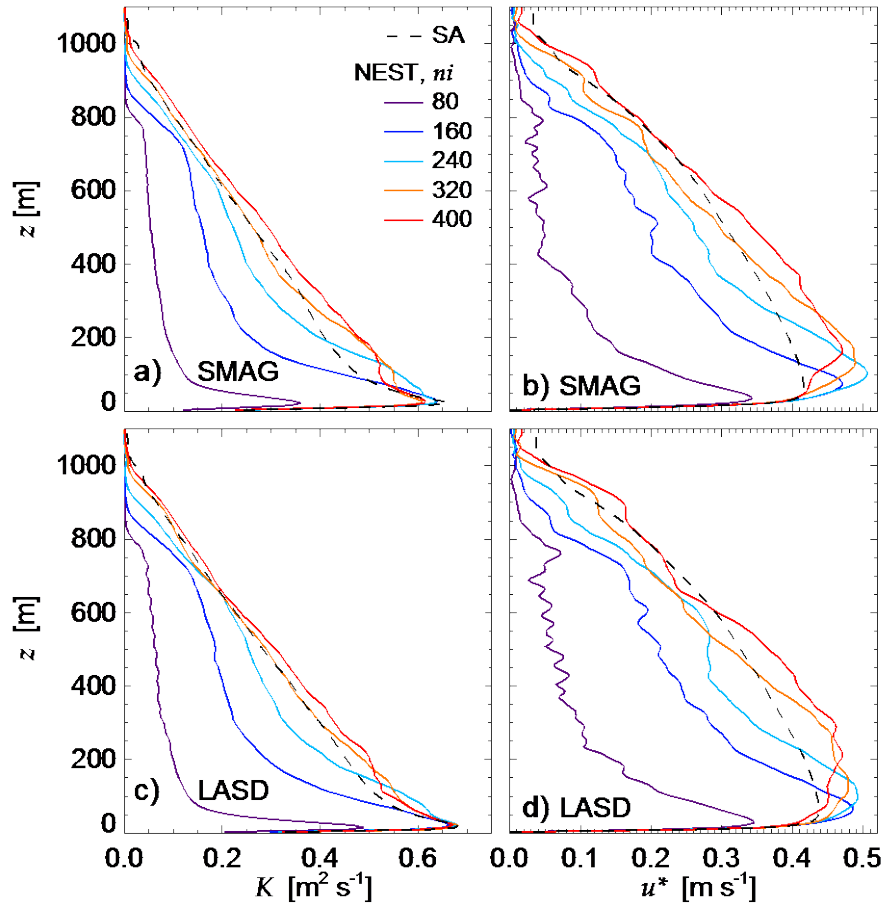
Irrespective of these minor implementation differences, the stochastic perturbation shows rapid development of turbulence characteristics that agree reasonably well with values from a stand-alone periodic domain, especially at heights of interest to wind turbine operations ( $50 < z < 200$  m).



**Figure 6.7.** Vertical Profiles of Resolved Turbulence Kinetic Energy  $K$  (left) and Friction Velocity  $u_*$  (right) on Nested LES Domains (colored) versus the Stand-Alone Value (dashed black) at 400 Grid Cells from the Inflow during Neutral Simulations using Cell Perturbation of Different Vertical Dimensions, as Described in the Text

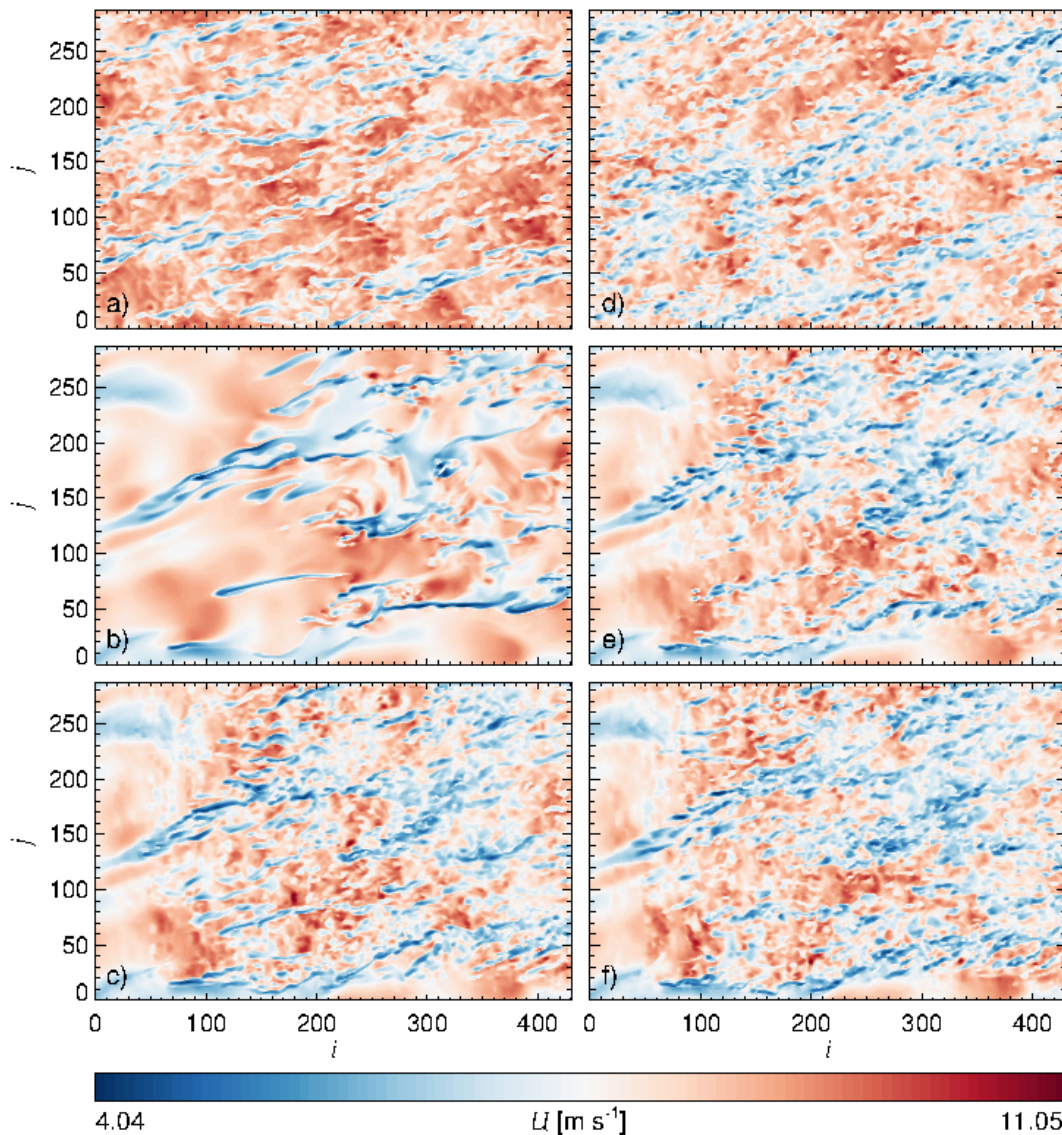
Figure 6.8 shows the evolution of  $K$  (left) and  $u_*$  (right) from simulations using the optimal values of  $n\Delta z = 6$  for the SMAG and  $n\Delta z = 8$  for the LASD simulations, as determined herein, surrounding the 5  $i$ -locations described in relation to Figure 6.7. The perturbations, applied from the surface up to 800 m, produce generally similar evolutions of  $K$  and  $u_*$  through the first two  $i$ -locations using both SGS models, before profile characteristics differentiate. The similarity in near-field characteristics, followed by differentiation farther downstream, indicates how the turbulence model plays only a small role in the formation of the larger-scale turbulence correlations emanating from the initial perturbations, a process governed primarily by buoyancy and nonlinear interactions in the momentum equations, relative to a larger role in the cascade of energy downscale once those large-scale correlations are established. The most significant differences between the simulations is the larger peak  $K$  values near the surface that are maintained over greater distances when using the LASD SGS model, with slightly smaller

overpredictions of  $u_*$  at and just above the near-surface peak. Although both quantities remain slightly underpredicted in the mid-ABL until  $i \approx 360$ , values at heights of most interest to wind turbine operations are reasonably close to the stand-alone values at  $i \cong 240$ . While this distance remains considerable, it is significantly shorter than when in the absence of perturbations (see Figure 6.4).



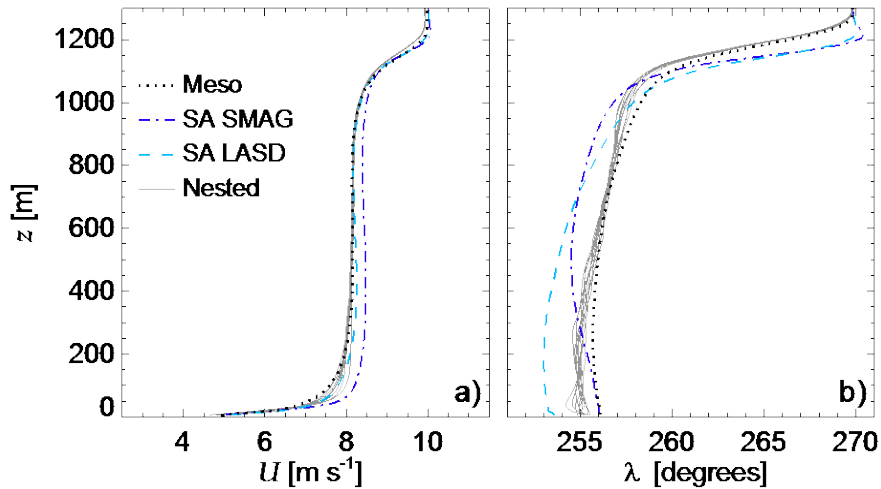
**Figure 6.8.** Vertical Profiles of Resolved Turbulence Kinetic Energy  $K$  (left) and Friction Velocity  $U_*$  (right) on Nested LES Domains (colored) versus the Stand-Alone Value (dashed black) as Function of Inflow Distance, using Cell Perturbation Sizes of  $N\delta z=6$  and 8 from the SMAG (top) and LASD (bottom) SGS Models

Figure 6.9 shows instantaneous contours of the wind speed at approximately 100 m above the surface, from each domain, as in Figure 6.5, from the convective simulation. In contrast to the neutrally-forced simulations, the unperturbed nested domains (middle panels) indicate spontaneous development of the turbulence cascade within a much shorter fetch, with the LASD simulations producing the full spectrum of resolved scales well in advance of the domain midpoint. The introduction of perturbations (bottom panels) indicates a considerable acceleration of turbulence development when applied to the SMAG simulation, but shows only a slight acceleration when using the LASD model.



**Figure 6.9.** Plan View Contours of Wind Speed in Stand-Alone and Nested LES Domains at 100 m above the Surface, as in Figure 6.5, Under Convective Forcing

Figure 6.10 shows mean vertical wind speed (left) and direction (right) profiles within the ABL from the mesoscale, stand-alone LES, and nested LES domains, as in Figure 6.6. All domains again produce similar distributions, with the mesoscale domains (black dotted lines) producing slightly deeper ABLs than either stand-alone LES (blue dashed lines). The SMAG and LASD profiles show greater differences than during neutral conditions, with the LASD producing lower wind speeds and a greater change in wind direction. Profiles from nested domain simulations at  $i = 400$  (grey lines) again show closer agreement with the mesoscale profiles, however, with slightly more turning of the flow near the surface, with each grey line again from a simulation using different perturbation characteristics, as described below.



**Figure 6.10.** Vertical Profiles of Resolved Turbulence Wind Speed (left) and Direction (right), as in Figure 6.6, from the Convective Simulations

Figure 6.11 shows vertical profiles of the resolved components of  $K$  (left) and  $u_*$  (right), as in Figure 6.7, from the convective simulation, at the same distance ( $i = 400$ ) from the inflow plane. All averaging used in computation and display in Figure 6.11 to Figure 6.13 is identical to Figure 6.7 to Figure 6.8.

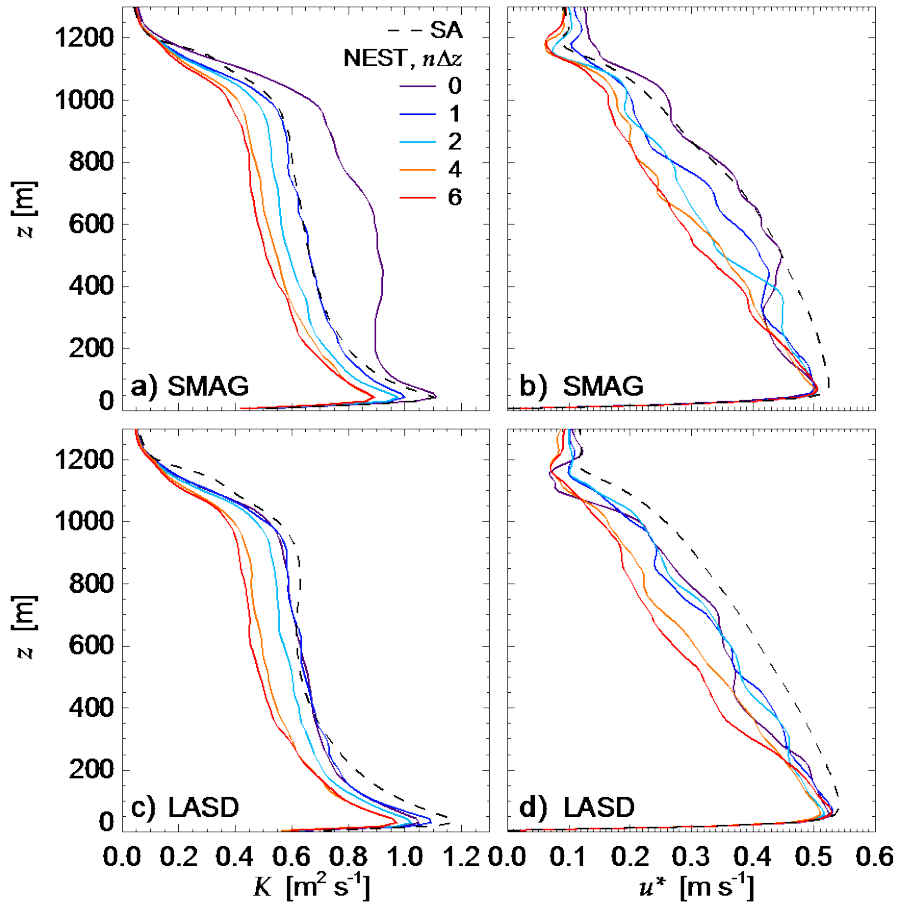
Sensitivity to perturbation depth,  $n\Delta z$ , is again examined, with results from nonperturbed simulations also shown ( $n\Delta z = 0$ , purple). Examination of SMAG simulations shows that the nonperturbed solution exhibits large overpredictions of  $K$  throughout most of the ABL, with excellent prediction of  $u_*$  for  $z > 500$  m, surmounting slightly underpredicted values below. Adding small perturbations significantly improves  $K$ , whereas there is a slight worsening of  $u_*$  for  $z > 500$  m, with small improvements occurring below. Increasing the vertical extents of the perturbations reduces the accuracies of both  $K$  and  $u_*$ , relative to the stand-alone values. Simulations using the LASD produce generally good agreement either using no perturbations, or perturbations with  $n\Delta z = 1$ , with larger perturbations degrading both quantities.

Differences in the efficacy of perturbations during neutral and convective conditions can be understood by considering the evolution of the turbulence production from the growth of initial disturbances through the downscale cascade. During neutral conditions, in the absence of perturbations, vertical shear is the primary process for instigating turbulence motions, resulting first in small vortices that grow very slowly into larger-scale structures through nonlinearities in the governing momentum equations. Adding thermal perturbations excite buoyant motions that rapidly produce large-scale overturning eddies, which subsequently cascade down in scale, filling in the turbulence spectrum much more quickly than the upscale process that occurs in their absence. Patches of  $n\Delta z = 6 - 8$  provide the optimal buoyant inputs to produce large-scale eddies with the correct energy to generate the correct downscale cascade.

During convective conditions, the buoyant driver of large-scale overturning is already present. Once the plumes develop, the downscale cascade naturally fills in the turbulence spectrum. The SMAG SGS model, which is more dissipative, delays production of smaller scales within the cascade, resulting in excessive  $K$  values. Small perturbations of  $n\Delta z = 1$  produce just enough correlations within the inertial subrange to assist the breakdown of these large-scale structures, recovering correct  $K$  values more

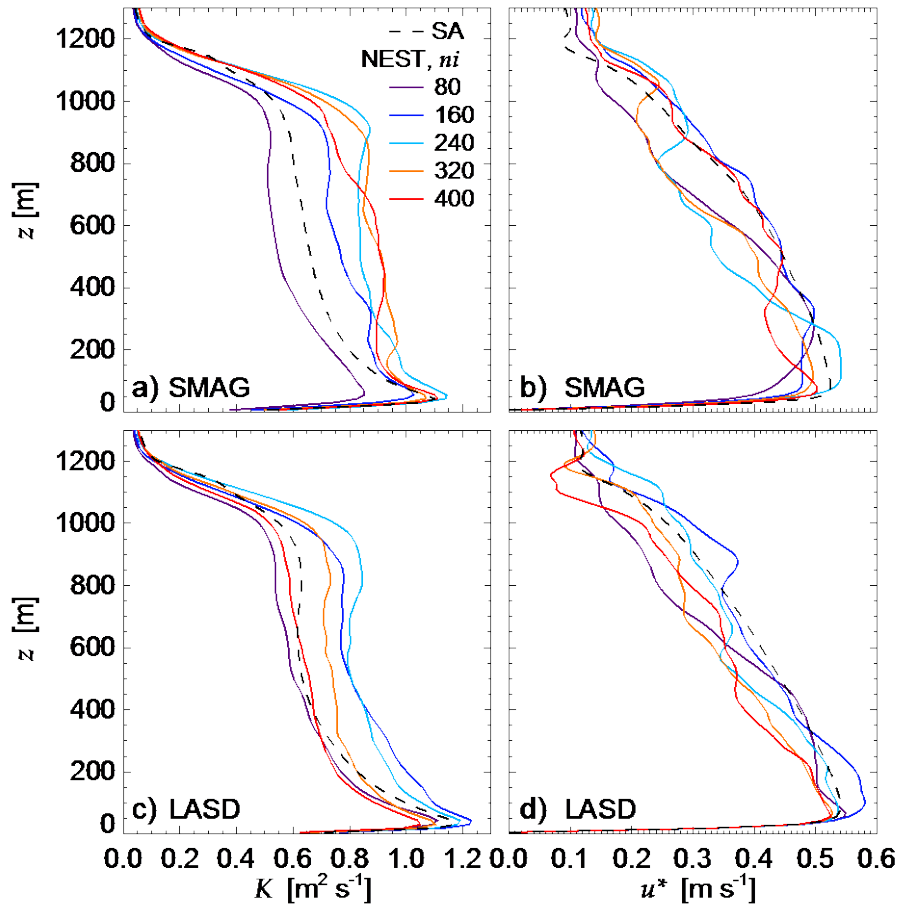
quickly, while also slightly reducing those of  $u_*$ . Larger patches interfere with the formation of the largest buoyant scales, arresting the source of energy for the entire cascade, resulting in smaller  $K$  values overall.

The LASD model, being less dissipative, allows the cascade structures to form more rapidly from the large-scale plumes, which drain energy from those scales, preventing the over-production of  $K$ . The introduction of small perturbations has little impact, as the large-scale driver already in place is robust to small magnitudes. However, larger cells break up the large-scale overturning structures before they can form, resulting in lower energetics overall.



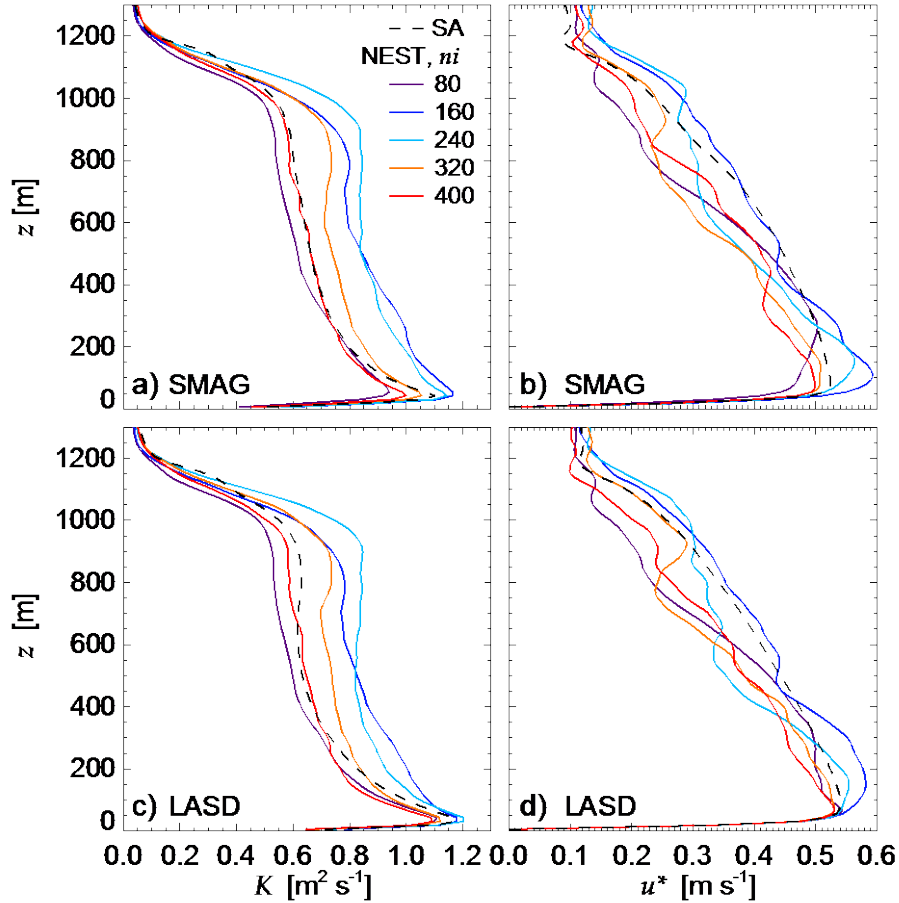
**Figure 6.11.** Vertical Profiles of Resolved Turbulence Kinetic Energy  $K$  (left) and Friction Velocity  $u_*$  (right) as in Figure 6.7, during Convective Conditions

Figure 6.12 and Figure 6.13 reinforce the interpretation discussed previously, showing turbulence development as a function of distance from the inflow, as in Figure 6.8, both without and with perturbations. Results from the SMAG simulations with no perturbations (Figure 6.12a,b) show  $K$  values rapidly exceeding the stand-alone values, and only show signs of beginning to diminish approaching  $i = 330 - 400$  grid cells downstream. Corresponding  $u_*$  values agree well above 500 m, but lag the expected solution below, as previously described. The LASD simulations, on the other hand, feature peak  $K$  values at  $i = 160 - 240$ , after which values decrease toward those of the stand-alone solution. Corresponding  $u_*$  values, while slightly underpredicted, show steadier behavior with distance and agree better with the stand-alone solution at heights relevant to wind turbine airflow interactions.



**Figure 6.12.** Vertical Profiles of Resolved Turbulence Kinetic Energy  $K$  (left) and Friction Velocity  $u_*$  (right), as a Function of Inflow Distance, as in Figure 6.8, from Convective Simulations, with No Perturbations

The addition of small perturbations of  $n\Delta z = 1$  to the SMAG simulations (Figure 6.13a,b) produce a similar initial overshoot of  $K$  values over the first 160 – 240; however, unlike the unperturbed solution, subsequent values diminish rapidly toward the stand-alone values with further distance, with good agreement achieved at  $i = 400$ . Corresponding  $u_*$  values do not agree as well above 500 m, but are similar within the lowest few hundred meters. As described in relation to Figure 6.11, the LASD simulations are only minimally influenced by the addition of small perturbations.



**Figure 6.13.** Vertical Profiles of Resolved Turbulence Kinetic Energy  $K$  (left) and Friction Velocity  $u_*$  (right), as a Function of Inflow Distance, as in Figure 6.12, from Convective Simulations, with Perturbations

### 6.3 Discussion

Each of the two methods of turbulence acceleration investigated herein, the TurbSim method that imposes correlated velocity structures, and the cell perturbation method that imposes uncorrelated stochastic thermal perturbations to the flow field, were shown to effectively reduce fetch length and improve simulated turbulence characteristics in microscale domains forced with mesoscale inflow. Each method contains additional parameters that can be fine-tuned for specific forcing conditions to further improve performance. Herein, it was discovered that the cell perturbation might be improved via optimization of perturbation characteristics for different stability classes. Additionally, use of different perturbation sizes and variously dissipative SGS model formulations provided insights into the process leading to development of the turbulence cascade, which can further aid future development and tuning of the technique. We reiterate that the cell perturbation method requires no *a priori* computation, and any optimization for stability class or other considerations could be parameterized within the perturbation specification, providing a seamless transition during changing meteorological conditions with minimal additional computational overhead. Given that the cell perturbation method was shown to perform as well as or better than various spectral perturbation methods during convective, neutral, and stable conditions (Muñoz-Esparza et al. 2014), including the more elaborate synthetic method of Xie and Castro (2008) (Muñoz-Esparza et al. 2015), which requires *a priori* computation of turbulent stress profiles and

Lagrangian time-scales and is applicable to only neutral conditions, the cell perturbation method shows great promise as a robust, generalizable, and computationally efficient turbulence seeding approach.

The TurbSim method likewise shows promise and produces fetch lengths similar to the cell perturbation method under neutral conditions. This approach uses standard IEC models which, to the authors' knowledge, have never been applied in this context. Both the performance and effectiveness of this approach were found to improve substantially with judicious specification of the perturbation characteristics, as in the cell perturbation approach. Ongoing work focuses on more precise characterization of the fetch length and evaluations of flow fields under diverse atmospheric conditions. For instance, assessments of the coupling effectiveness described in section 6.1.3 will continue with the goal of identifying the quantitative measures that most effectively describe how well an MMC-simulated field will match an equivalent microscale simulation of similar conditions. Experiences from the cell perturbation approach (e.g., turbulence model dissipation characteristics or optimal perturbation depth) can be leveraged for future TurbSim-MMC investigations.

## 7.0 Summary, Context, Next Steps

### 7.1 Summary of Results

The A2e MMC Project has been functioning as a team since mid-March 2015. This team is composed of six DOE laboratories (Argonne, LANL, LLNL, NREL, PNNL, and SNL) and NCAR (as a subcontractor to PNNL, the lead laboratory).

Within the context of a multi-year effort to develop, assess, and provide best practice MMC recommendations for the A2e HPM framework, year 2 effort focused on

- downselecting models for incorporation into the HPM framework,
- selecting and simulating nonstationary cases and developing appropriate assessment metrics to apply,
- examining various coupling procedures to link mesoscale and microscale simulations,
- assessing various methods to initiate turbulence in microscale simulations, and
- studying the impact of the *terra incognita* on the model results.

Section 2.0 of this report details our analysis of models during the first 1.5 years of the project. At the mesoscale, we compared the performance of the WRF model with the MPAS. WRF has many advantages, including

- a large number of users, consisting of several already within the wind energy industry;
- a wide array of physics parameterizations applicable to all atmospheric scales of motion, from global NWP through LES;
- success in many research and operational applications, including wind energy;
- interfaces with a wide range of input data sources and data assimilation techniques;
- a modern, flexible, high-performance computing (HPC) compliant code base; and
- ease of adoption by any experienced CFD or NWP modeler.

For these reasons, and due to the limitations of MPAS described in section 2.0, the MMC team recommends that WRF be used as the base mesoscale model for the A2e systems.

At the microscale, the team assessed three LES models, including WRF-LES, SOWFA, and the HIGRAD LES model. Our goal was to quantify the internal variability of established LES codes and simulation practices to evaluate model coupling approaches from year 2 forward. These three microscale models were compared with varying grid spacings, orders of the advection schemes, turbulence schemes, geostrophic wind speed, roughness height, aspect ratio, and a variety of other parameterizations for convective and neutral conditions in the flat terrain cases from the SWiFT site (Haupt et al. 2015). All models showed success at reproducing some of the basic features of the cases, but all showed discrepancies, particularly in capturing specific profile and turbulence characteristics. In general, the errors in most variables were within the variability of the measurements. Sensitivity to different parameterizations and forcings were evident and reinforced the notion that one must carefully construct the current combination of parameters to correctly model a case. Turbulence quantities and spectra and cospectra were additionally assessed. A major finding was that, when tuned for the cases, the models performed similarly overall, and the differences between models were generally smaller than the variability in the SWiFT tower data that was being used for comparison.

In addition to providing a context for evaluation of MMC techniques, year 1 activities also aided the selection of an appropriate microscale solver for the HPM framework. With the primary consideration for the HFM framework being efficient utilization of emerging exascale computing resources, the HPC team chose to work with the Nalu model. Thus, Nalu is currently being equipped with several of the physics modules and interfaces for wind plant modeling that are already embedded in the SOWFA framework. This enhanced version of Nalu will become the microscale model for the HPM framework.

Note, however, that Nalu, as a stand-alone microscale solver, will still require a robust, high-fidelity method for providing inflow and boundary conditions for the wind plant simulations to be conducted within, with the quality of the Nalu simulations being inextricably bound to the quality of the inflow for the many reasons described throughout this report. The WRF model has been identified as the best starting point to provide high-fidelity mesoscale inflow for Nalu, possessing a sufficiently flexible and extensible HPC-compliant software structure to work within the HPM framework, with potential for considerable improvement in the future. In addition to WRF's ability to provide mesoscale inflow information to Nalu, the MMC team still believes that it may be critical to carry the physics inherent in WRF through the *terra incognita* and into the microscale, as described in the results of section 5.0 of this report. Thus, the MMC team plans to continue to assess how far WRF should be nested before handing off to Nalu in the fully coupled HPM framework that is being developed.

With a view toward a stepwise increase of complexity beyond the canonical, steady flat terrain cases assessed during year 1, this year's activities focused on nonstationary cases over flat terrain (with year 3 efforts targeting nonstationary cases over complex terrain). Section 3.0 of this report describes the nonstationary cases selected for this year's activities, as well as the metrics chosen for their assessment. As in year 1, the test site was the SWiFT facility in West Texas, with two unsteady meteorological cases representing a typical diurnal cycle with a nocturnal LLJ (November 8, 2013) and a frontal passage (May 12, 2014). An additional diurnal cycle case study was selected from the literature.

Section 4.0 describes the use of mesoscale modeling in the *terra incognita*, the range of scales between traditional mesoscale (> about 1 km) and microscale (< about 100 m) simulation for which neither theory or modeling approaches for unresolved turbulence scales are yet mature. There was evidence of impacts related to *terra incognita* issues using traditional subgrid turbulence closure approaches in the mesoscale simulations from about a 1 km resolution and finer. The "noise" in the wind speed (vertical and horizontal), TKE, momentum flux, and temperature indicated these issues. Planar plots displayed increasing spurious rolls in simulations at 333 m and, to a lesser extent at 1 km spacing, when the MYNN boundary layer scheme was utilized, but less so for the YSU scheme. Note that the investigation of *terra incognita* issues was conducted in coordination with A2e-supported development (via WFIP2) of appropriate turbulence closure techniques for that range of scales, and that examination of those closures in the context of MMC is proposed as future work.

The results of modeling the nonstationary diurnal and frontal passage cases at the microscale using different types of coupling mechanisms is presented in section 5.0. Two different classes of MMC were assessed (see section 5.0 for details), reflecting different approaches for specifying the microscale domain's LBCs. For regions with nearly flat terrain, such as the SWiFT facility, spatially uniform but time-dependent meteorological forcing conditions, such as diurnal cycles, can be simulated with periodic LBCs. In this setup, the use of periodic LBCs provides a means to obtain turbulent inflow and outflow, whereas the mesoscale coupling is achieved via linking internal forcing parameters, such as the mean horizontal pressure gradients and advections of momentum and temperature, to mesoscale time variability of those fields. Mesoscale time variability can be obtained either from observations, as one case study examined (GABLS3), or from a separate mesoscale simulation, as exemplified during another case study (November 8 at SWiFT). Significant work was necessary to run the mesoscale model for the SWiFT site

and extract the advective tendencies, pressure gradient forces, vertical planes of data, and surface conditions/fluxes for driving the mesoscale models.

The second method is to couple not only the microscale domain's internal forcing parameters, but also its lateral boundaries, to a mesoscale simulation. The boundary-coupled approach therefore removes the restriction of periodicity and spatial homogeneity of the forcing meteorology, providing a general approach applicable to arbitrary terrain and meteorological conditions. Section 5.0 describes the details of the results of each of these coupling methods.

Although the boundary-coupled approach provided the greatest generality, because the mesoscale flow information providing the lateral boundary information for the microscale domain contained no explicit turbulence information, the approach required methods to accelerate turbulence production at the microscale domain's inflow boundaries.

As such, various inflow perturbation strategies were tried, including the use of stochastic temperature field perturbations, and TurbSim-generated synthetic turbulence, as described in section 6.0. Both methods demonstrated success at generating turbulence with moderate fetch lengths.

## **7.2 Assessment of Modeling Nonstationary Cases**

A formal assessment of the “online” or “offline” coupling methods for the nonstationary cases indicates that both approaches are viable under different conditions. Under nearly stationary synoptic forcing over mostly flat, homogeneous terrain, microscale simulations forced by profiles of time-varying geostrophic wind and advective tendencies produce satisfactory results. However, if the synoptic conditions are not stationary and the domain of interest is not homogeneous (i.e., in the case of complex terrain, heterogeneous land use, or land-water interfaces), LES nested in mesoscale simulations resulted in more accurate evolution and structure of the ABL flow. Nesting the LES in a parent mesoscale domain, however, introduced additional complexity due to a nonturbulent inflow condition. Note that simulations of a fully turbulent flow in the nested LES domain can be very slow and require large inflow fetches for turbulence to develop. In order to make nested LES computationally feasible, inflow turbulence generation mechanisms and procedures must be applied, such as those described in section 6.0.

## **7.3 Context in A2e, Community, and Next Steps**

The MMC team has been working with the DAP team to archive the model data from the selected cases. In addition, the team is collaborating with the IEA Wakebench team to transition the initial cases to their framework, with invitations for the broader community to test their models on the same cases for comparison. During FY16, the MMC team also used the Wakebench GABLS3 case as a validation of the tendency forcing approach to coupling the mesoscale to the microscale.

The emphasis of FY17 modeling efforts is on coupled modeling in complex terrain. To that end, the MMC team is working with the WFIP2 team to identify appropriate cases in the wind region of the Pacific Northwest. Microscale models are not yet optimized for cases in complex terrain, and this will provide an opportunity to move the state-of-the-science forward in collaboration with the WFIP2 team. In particular, we expect to work with the team members who are developing scale-aware and fully 3D boundary layer parameterization that are expected to improve modeling in both the *terra incognita* and in other nonhomogeneous environments, such as complex terrain.

The MMC team also expects to continue working closely with the HPM team during FY17 to assure that the lessons learned from the coupling exercises are included in the new HPM framework. The team has

been extensively documenting the necessity for mesoscale forcing to assure appropriate microscale turbulence features, especially for nonstationary conditions and in complex terrain. The next step is to work in a larger team to transition this knowledge to an environment where it is fully captured in the modeling framework.

The MMC team has been working together quite effectively in collaborative roles. The members have been working together to formulate the appropriate sensitivity studies, then to each take some of the simulations to allow full comparison with a distributed work load. Where one approach appears to be quite effective, the other team members quickly adopt it in their own code. The team is working in full collaboration to produce the best framework available for coupled modeling.

## 8.0 References

- Andren, A., Brown, A. R., Mason, P. J., Graf, J., Schumann, U., Moeng, C.-H., Nieuwstadt, F.T.M., “Large-Eddy Simulation of a Neutrally Stratified Boundary Layer: A Comparison of Four Computer Codes”, *Quarterly Journal of the Royal Meteorological Society*, 120: 1457—1484, 1994.
- Bailey, B. H., “The financial impact of wind plant uncertainty,” NAWEA Symposium, Boulder, CO, Aug. 06, (2013).
- Bosveld, F. C., Baas P., van Meijgaard E., de Bruijn E.I.F., Steeneveld G. J., and Holt-slag A.A.M. (2014). The third GABLS intercomparison case for evaluation studies of boundary-layer models, Part A: case selection and set-up. *Boundary-Layer. Meteorol* 152 133-156, doi: 10.1007/ s10546-014-9917-3
- Bou-Zeid, E., Meneveau, C., and Parlange, M., “A Scale-Dependent Lagrangian Dynamic Model for Large Eddy Simulation of Complex Turbulent Flow”. *Physics of Fluids*, 17(2): 025105, 2005.
- Brown, A. R., Hobson, J. M., Wood, N., “Large-Eddy Simulation of Neutral Turbulent Flow Over Rough Sinusoidal Ridges”, *Boundary-Layer Meteorology*, 91: 411—441, 2001.
- Chen, F., and J. Dudhia, 2001, “Coupling and advanced land surface hydrology model with the Penn State-NCAR MM5 modeling system. Part I: Model implementation and sensitivity,” *Mon. Weather Rev.* 129:569– 585.
- Ching, J., R. Rotunno, M. LeMone, A. Martilli, B. Kosović, P. A. Jimenez, J. Dudhia, 2014: “Convectively Induced Secondary Circulations in Fine-Grid Mesoscale Numerical Weather Prediction Models.” *Mon. Wea. Rev.*, **142**, 3284–3302, doi: 10.1175/MWR-D-13-00318.1.
- Chow, F. K., Street, R. L., Xue, M., and Ferziger, J. H., “Explicit Filtering and Reconstruction Turbulence Modeling for Large-Eddy Simulation of Neutral Boundary Layer Flow. *Journal of the Atmospheric Sciences*, 62(7): 2058—2077, 2005.
- Churchfield, M. J., S. Lee, J. Michalakes, and P. J. Moriarty, 2012. “A numerical study of the effects of atmospheric and wake turbulence on wind turbine dynamics.” *J. Turbul.*, **13**, N14, doi:10.1080/14685248.2012.668191.
- Deardorff, J. W., “Preliminary Results from Numerical Integrations of the Unstable Planetary Boundary Layer”, *Journal of the Atmospheric Sciences: Notes and Correspondences*. 27: 1209—1211, 1970a.
- Deardorff, J. W., “A Numerical Study of Three-Dimensional Turbulent Channel Flow at Large Reynolds Number”, *Journal of Fluid Mechanics*. 41(2): 453—480, 1970b.
- Deardorff, J. W., “Numerical Investigation of Neutral and Unstable Planetary Boundary Layers”, *Journal of the Atmospheric Sciences*, 29: 91—115, 1972.
- Dyer, A. J., and B. B. Hicks, 1970: “Flux-gradient relationships in the constant flux layer”, *Quart. J. Roy. Meteor. Soc.*, **96**, 715–721.
- Fitch, A. C., Olson, J. B., Lundquist, J. K., Dudhia, J., Gupta, A. K., Michalakes, J., “Local and Mesoscale Impacts of Wind Farms as Parameterized in Mesoscale NWP Model”, *Monthly Weather Review*, 140(9): 3017—3038, 2012.
- Jonkman, B. J., and M. L. Buhl, 2006. *TurbSim User’s Guide*, NREL/TP-500-3979.

- Gill, D., and M. Pyle, 2011. "Nesting in WRF." Available at <http://www2.mmm.ucar.edu/wrf/users/tutorial/201107/WRFNesting.ppt.pdf>.
- Haupt, S. E., A. Anderson, L. Berg, B. Brown, M. J. Churchfield, C. Draxl, B. L. Ennis, Y. Fang, B. Kosović, R. Kotamarthi, R. Linn, J. D. Mirocha, P. Moriarty, D. Munoz-Esparaza, R. Rai, W. J. Shaw, 2015: First Year Report of the A2e Mesoscale to Microscale Coupling Project, Pacific Northwest Laboratory Report PNNL-25108, 124 pp.
- Hirth, B., and Schroeder, J., "A Summary of the National Wind Institute Meteorological Measurement Facilities at the Texas Tech University's Reese Technology Center Field Site," Tech. Rep., Texas Tech University, 2014.
- Holton, J. R., *An Introduction to Dynamic Meteorology*, Fifth Edition, Academic Press, 552 pp. 2013. ISBN 9780123848666.
- Jayaraman, B., J. Brasseur, S. E. Haupt, J. Lee, 2016. Deviations from Equilibrium in Daytime Atmospheric Boundary Layer Turbulence arising from Nonstationary Mesoscale Forcing, 69<sup>th</sup> Annual Meeting of the APS Division of Fluid Dynamics, 61 (20), Portland, Oregon, Nov. 22.
- Kain, J. S., 2004, "The Kain–Fritsch convective parameterization: An update," *J. Appl. Meteorol.* 43:170–181.
- Kelly, C. L. and B. L. Ennis, 2016: SWiFT Site Atmospheric Characterization, Sandia National Laboratories Tech Report SAND2016-0216, Albuquerque, NM.
- Kelley, N. D., 2011: *Turbulence-Turbine Interaction: The Basis for the Development of the TurbSim Stochastic Simulator*, NREL/TP-5000-52353.
- Kirkil, G., Mirocha, J., Bou-Zeid, E., Chow, F. K., and Kosovic, B.: *Implementation and Evaluation of Dynamic Subfilter-Scale Stress Models for Large-Eddy Simulation Using WRF*, Monthly Weather Review. 140: 266—284, 2012.
- Kosović, B., "Subgrid-scale Modelling for the Large-Eddy Simulation of High-Reynolds-Number Boundary Layers", *Journal of Fluid Mechanics*, 336: 151—182, 1997.
- Kosović, B., and Curry, J., "A Large Eddy Simulation Study of a Quasi-Steady, Stably Stratified Atmospheric Boundary Layer", *Journal of the Atmospheric Sciences*. 57: 1052—1068, 2000.
- Kotamarthi, V. R., and Y. Feng, 2016: MPAS Atmospheric Boundary Layer Simulation under Selected Stability Conditions: Evaluation using the SWiFT dataset, Argonne National Laboratory Report.
- Lilly, D. K. The representation of small scale turbulence in numerical simulation experiments. In IBM Scientific Computing Symposium on environmental sciences, pages 195–210, Yorktown heights, 1967.
- Linn R. R. and E. Koo, "Determining Effects of Turbine Blades on Fluid Motion," patent No. 7,953,563, submitted on 10-20-2008, issued on 05-31-2011, Los Alamos National Laboratory, (2008).
- Lund, T. S., X. Wu, and K. D. Squires, 1998: Generation of Turbulent Inflow Data for Spatially-Developing Boundary Layer Simulations. *J Comput Phys*, **140**, 233–258, doi:10.1006/jcph.1998.5882.
- Mayor, S. D., Spalart, P. R., Tripoli, G. J., "Application of a Perturbation Recycling Method in the Large-Eddy Simulation of a Mesoscale Convective Internal Boundary Layer", *Journal of the Atmospheric Sciences*, 59(15): 2385–2395, 2002.

- Mehta, D., A. H. van Zuijlen, B. Koren, J. G. Holierhoek, and H. Bijl, “Large-Eddy Simulation of wind farm aerodynamics: A review,” *J. Wind Eng. Ind. Aerodyn.* 133, 1–17 (2014).
- Mirocha, J. D., B. Kosović, M. L. Aitken, and J. K. Lundquist, “Implementation of a generalized actuator disk wind turbine model into the weather research and forecasting model for large-eddy simulation applications,” *J. Renewable Sustainable Energy* 6, 013104-1–013104-19, 2013.
- Mirocha, J. D., B. Kosović, and G. Kirkil, “Resolved turbulence characteristics in large-eddy simulations nested within mesoscale simulations using the Weather Research and Forecasting model,” *Mon. Wea. Rev.* 142, 806–831. doi:10.1175/MWR-D-13-00064.1, 2014.
- Monin, A. S. and A. M. Obukhov, “Basic laws of turbulent mixing in the surface layer of the atmosphere,” *Tr. Akad. Nauk SSSR Geofiz. Inst.* 24, 163–187 (1954); English translation by John Miller, (1959).
- Morgan, B., Larsson, J., Kawai, S., and Lele, S. K., “Improved Low-Frequency Characteristics of Recycling/Rescaling Inflow Turbulence Generation”, *AIAA Journal*, 49(3): 582—597, 2011.
- Muñoz-Esparza, D., B. Kosović, J. Mirocha, and J. van Beeck, 2014: Bridging the Transition from Mesoscale to Microscale Turbulence in Numerical Weather Prediction Models. *Bound.-Layer Meteorol.*, 153, 409–440, doi:10.1007/s10546-014-9956-9.
- Muñoz-Esparza, D., B. Kosović, J. van Beek, and J. D. Mirocha: A stochastic perturbation method to generate inflow turbulence in large-eddy simulation models: application to neutrally stratified atmospheric boundary layers, *Phys.-Fluids* 27, 035102 (2015). Erratum, *Phys.-Fluids* 27, 039901 (2015).
- Nakanishi, M., Niino H. An improved Mellor-Yamada level-3 model with condensation physics: Its design and verification. *Boundary-Layer Meteorology* 2004; 112: 1–31.
- Noh, Y., W. G. Cheon, S.-Y. Hong, and S. Raasch, 2003, “Improvement of the K-profile model for the planetary boundary layer based on large-eddy simulation data,” *Boundary Layer Meteorology* 107:401–427.
- OpenFOAM, The Open Source CFD Toolbox, created by OpenCFD Ltd (ESI Group), distributed online at <http://www.openfoam.com> (2015).
- Pedersen, J. G., M. Kelly, S.-E. Gryning, and B. Brummer, 2013: The effect of unsteady and baroclinic forcing on predicted wind profiles in Large-Eddy Simulations: Two case studies of the daytime atmospheric boundary layer, *Meteorologische Zeitschrift*, 22 (6), 661-674.
- Rai, R. K., L. K. Berg, B. Kosović, J. D. Mirocha, M. S. Pekour, and W. J. Shaw, 2016: Comparison of measured and numerically simulated turbulence statistics in a convective boundary layer over complex terrain. *Bound.-Layer Meteor.*, Accepted.
- Rodrigo, J. S., M. Churchfield, and B. Kosović, 2016a: Atmospheric boundary layer modeling based on mesoscale tendencies and data assimilation at microscale, *Wind Energy Science Discussions* (manuscript submitted to Wind Energy Science), published 19 Aug., do:10.5194/wes-2016-26.
- Rodrigo, J. S., M. Churchfield, and B. Kosović, 2016b: A wind energy benchmark for ABL modelling of a diurnal cycle with a nocturnal low-level jet: GABLS3 revisited, *Journal of Physics: Conference Series* 753, The Science of Making Torque from Wind, doi:10.1088/1742-6596/753/032024.
- Sanderse, B., S. P. van der Pijl and B. Koren, “Review of computational fluid dynamics for wind turbine wake aerodynamics,” *Wind Energy* 14, 799–819 (2011).

- Shaw, W. J., J. K. Lundquist, and S. J. Schreck, “Workshop on Research Needs for Wind Resource Characterization,” *Bull. Amer. Meteorol. Soc.* 90, 535–538 (2009).
- Sauer, J. A. “Towards improved capability and confidence in coupled atmospheric and wildland fire modeling.” PhD thesis, Florida State University, 117 pp. (2013).
- Skamarock, W. C., J. B. Klemp, J. Dudhia, D. O. Gill, D. M. Barker, M. G. Duda, X-Y Huang, W. Wang, and J. G. Powers. “A description of the advanced research WRF version 3,” Report No. NCAR/TN-4751STR, National Center for Atmospheric Research, Boulder, CO (2008).
- Skamarock, W. C., and J. B. Klemp, 2008, “A time-split nonhydrostatic atmospheric model for weather research and forecasting applications,” *Journal of Computational Physics* 227.7:3465–3485.
- Smagorinsky, J. “General circulation experiments with the primitive equations: I. the basic experiment\*.” *Monthly weather review* 91.3 (1963): 99-164.
- The Simulator fOr Wind Farm Applications (SOWFA), created by the National Renewable Energy Laboratory, distributed online at <https://wind.nrel.gov/SOWFA>, (2015).
- Stull, R. B., 1988: An Introduction to Boundary Layer Meteorology, Kluwer Academic Publishers, Boston, MA, 666 pp.
- Tabor, G. T. and Baba-Ahmadi, M. H., “Inlet Conditions for Large Eddy Simulation: A Review”, *Computers and Fluids*, 39(4): 553—567, 2010.
- Talbot, C., Bou-Zeid, E., and Smith, E. “Nested Mesoscale Large-Eddy Simulations with WRF: Performance in Real Test Cases”, *Journal of Hydrometeorology*, 13: 1421—1441, 2012.
- Troldborg N., G. C. Larsen, H. A. Madsen, K. S. Hansen, J. N. Sørensen and R. Mikkelsen, “Numerical simulations of wake interaction between two wind turbines at various inflow conditions,” *Wind Energy* 14, 859–876 (2011).
- Veers, P. S., 1988: *Three-Dimensional Wind Simulation*. Sandia National Laboratories Report, SAND-88-0152.
- Wu, X., 2017: Inflow Turbulence Generation Methods. *Annu. Rev. Fluid Mech.*, **49**, doi:10.1146/annurev-fluid-010816-060322.
- Wyngaard, J. C., 2004: Toward numerical modeling in the “Terra Incognita.” *J. Atmos. Sci.*, **61**, 1816-1826.
- Xie, Z.-T. and Castro I. P., “Efficient Generation of Inflow Conditions for Large Eddy Simulation of Street-Scale Flows”, *Flow, Turbulence, and Combustion*, 81(3): 449—470, 2008.

## **Appendix A**

### **Contributions of Individual Laboratories**



# Appendix A

## Contributions of Individual Laboratories

The MMC project is truly a collaborative effort, with each laboratory taking a share of the effort as well as the team working together to advance the state-of-the-science of mesoscale-microscale coupling. The contributions of the individual laboratories (in alphabetical order) are briefly summarized herein.

**Argonne National Laboratory (Argonne):** Argonne contributed to the selection of the mesoscale model for the mesoscale-microscale modeling project. Argonne evaluated the MPAS model for suitability to this application. Based on these studies, Argonne recommended that MPAS be eliminated from current consideration. It is still in the R&D phase, and produces very large volumes of data owing to its global domain. This makes analysis difficult with the current set of analytical and software tools and is computationally expensive. The model results are comparable to WRF as they both use the same physics. Argonne also performed idealized simulations for a nonstationary diurnal case study using the GABLS3 observational data sets and evaluated the performance of the WRF-LES model in comparison to SOWFA simulations performed by NREL as well as other observations. Argonne developed a design document for building a turbulent seed library that will form the basis for developing and testing an asynchronous coupling strategy for meso- and microscale models. Staff members at Argonne participated in team meetings and in regular teleconferences for discussions about modeling approaches and technical details in simulations

**Lawrence Livermore National Laboratory (LLNL):** LLNL made contributions to several components of the FY16 coordinated science activities. LLNL assisted in identifying case studies from the SWiFT site through analysis of data and discussion with the group. LLNL helped devise a strategy for incorporating mesoscale tendency forcing into microscale simulations with periodic LBCs, including writing a module to ingest the tendencies and interpolate those into the governing equations in WRF. This module was provided to and used by Pacific Northwest National Laboratory (PNNL) and Argonne, and also provided to LANL for assistance in their efforts to incorporate this capability into HIGRAD. LLNL teased out the proper interpretation of the mesoscale forcing parameters for correct incorporation into the microscale codes, and assisted in assessing the performance of the approach, including (in close collaboration with PNNL) identifying the importance of separating mesoscale noise from important baroclinic effects in capturing nocturnal low-level jet characteristics. LLNL also contributed to the investigation of inflow perturbation techniques for turbulence spin up. LLNL contributed the strategy for perturbations assessment via use of both nested and offline periodic LES, with comparison of flow statistics from both the nested-perturbed versus offline simulations, a function of distance from the inflow plane(s) of the nested domain. LLNL also conducted numerous simulations using the stochastic cell perturbation method to evaluate the approach and its sensitivity to both internal control parameters and atmospheric stability. LLNL also contributed (in close collaboration with PNNL) to the interpretation and understanding of the pros and cons of online nested versus offline coupled LES using mesoscale forcing tendencies. LLNL presented MMC-related activities at the American Meteorological Society (AMS) Symposium on Boundary Layers and Turbulence, submitted a journal article involving assessment of vertical nesting in WRF, including investigation of various implementations of surface boundary conditions, led authorship of a journal paper for FY15 microscale MMC activities (draft is currently in review with MMC team), and contributed to several sections of the FY16 project report.

**Los Alamos National Laboratory (LANL):** LANL has contributed to exploring a drag perturbation method in microscale models for turbulence generation, in the context of meso-to-micro model coupling. LANL has been exploring modeling vegetation drag for the heterogeneous ground surface boundary

conditions. Staff members at LANL participated in team meetings and in regular teleconferences for discussions about modeling approaches and technical details in simulations. LANL also attempted nonstationary case simulations in a fully-compressible flow solver and identified some of the technical issues, which could be useful in future implementation of modeling techniques in Nalu, which uses low-Mach-number compressible flow formulations.

**National Center for Atmospheric Research (NCAR):** As a subcontractor to PNNL, NCAR took on project leadership, with Dr. Haupt serving as project Principal Investigator, leading most of the team teleconferences; presenting the project at A2e workshops as well as at the WindTech meeting in Ontario, Canada, and the AMS Symposium on Boundary Layers and Turbulence in Salt Lake City; preparing quarterly reports; and leading this year 2 report. NCAR hosted a team meeting in March where the lab personnel came together to choose cases and finalize the technical approach to modeling the nonstationary cases. NCAR was also responsible for the development of the metrics and the assessment, including developing the metrics plan, and for providing the formal V&V of the model results, which appear in sections 3.0, 4.0, and 5.0 of this report. This required much processing of the SWiFT tower data, including quality control and recalibrating directionality. Model results also required significant postprocessing, including providing code for the modeling teams to output their results in common formats, hosting a model repository, and planning for the long-term data storage with the DAP team. NCAR also supplied modeling advice and guidance. NCAR summarized the results of the assessment and the project overview at that meeting, as well as leading small and large group discussions. NCAR coordinated the planning and assumed leadership for compiling and formatting this report, including writing major portions, although all laboratories contributed to the technical discussions and report writing.

**National Renewable Energy Laboratory (NREL):** NREL researchers have made various contributions to the MMC project. The team helped identify case studies of interest at the SWiFT site through discussion with the entire group and by contributing mesoscale runs to aid in case selection. In the area of mesoscale modeling, subsequent runs were performed by NREL researchers in which important forcing data were extracted and later used by the microscale modelers. NREL staff also performed mesoscale simulations at horizontal resolutions much higher than normally used (down to 333 m), resolutions considered within the *terra incognita*, with a variety of PBL turbulence parameterizations, showing that some of these parameterizations combined with high resolution allow for the formation of spurious flow structures. This points at the growing need for a multi-scale turbulence mesoscale turbulence model. In the area of microscale modeling, NREL researchers developed a method to provide mesoscale forcing to the microscale model using internal source terms. These source terms are derived from the mesoscale model. This method is proving very useful in mesoscale-driven conditions over relatively flat terrain, such as the SWiFT site. NREL also explored a method of forcing the microscale model through the use of mesoscale boundary conditions perturbed with synthetic turbulence generated by the NREL-developed TurbSim code. NREL's work resulted in presentations at the Symposium on OpenFOAM in Wind Energy, the AMS Symposium on Boundary Layers and Turbulence, and the WRF Workshop, along with a future presentation at the annual AMS meeting. NREL researchers are also acting as the link between the A2e MMC Project and the A2e HFM and ExaWind projects.

**Pacific Northwest National Laboratory (PNNL):** Staff members at PNNL have been making important contributions to the MMC project in a number of different areas. PNNL has worked with the project team to identify specific case study periods used in the analysis (section 3.0). PNNL has made contributions to the work focused on identifying issues associated with *terra incognita* (section 4.0) through the analysis of a suite of WRF simulations that apply a range of horizontal resolutions. PNNL staff also contributed simulations made using a coupled WRF model configuration with online coupling between the mesoscale and microscale models. PNNL also contributed simulations using a periodic LES domain that is forced with tendencies derived from the mesoscale WRF model (section 5.0). PNNL's efforts have resulted in

presentations at both the Symposium on Boundary Layers and Turbulence and the American Geophysical Union Fall Meeting, as well as a manuscript that was recently accepted in the journal *Boundary-Layer Meteorology*.

**Sandia National Laboratory (SNL):** SNL operates the SWiFT experimental wind farm facility located in West Texas, where the benchmark diurnal cycle cases were obtained. SNL managed the interaction with TTU for data access and transfer from their NWI historical data sets. SNL additionally provided data processing and analysis of the TTU data, and used the data to identify candidate cases best meeting the desired atmospheric requirements from which the team identified the final cases.



**Pacific Northwest**  
NATIONAL LABORATORY

*Proudly Operated by **Battelle** Since 1965*

902 Battelle Boulevard  
P.O. Box 999  
Richland, WA 99352  
1-888-375-PNNL (7665)

U.S. DEPARTMENT OF  
**ENERGY**

---

[www.pnnl.gov](http://www.pnnl.gov)